Federal University of Espírito Santo – UFES
Technological Center
Master's Degree Program

Superstructure Optimization of Absorption Chillers integrated with a Large Internal Combustion Engine for Intake Air Conditioning

Vitória-ES

2020

Federal University of Espírito Santo – UFES
Technological Center
Master's Degree Program

Superstructure Optimization of Absorption Chillers integrated with a Large Internal Combustion Engine for Intake Air Conditioning

A Thesis submitted for the Master's Degree Program at UFES as partial fulfilment of the requirements on obtaining the Mechanical Engineer Master's Degree title.

André Chun

Supervisor: Prof. PhD. José Joaquim Conceição Soares Santos
Co-supervisor: Prof. PhD. João Luiz Marcon Donatelli

Vitória-ES
2020

Federal University of Espírito Santo – UFES
Technological Center
Master's Degree Program

Superstructure Optimization of Absorption Chillers integrated with a Large Internal Combustion Engine for Intake Air Conditioning

A Thesis submitted for the Master's Degree Program at UFES as partial fulfilment of the requirements on obtaining the Mechanical Engineer Master's Degree title.

Approved work. Vitória-ES, December 9, 2020:

Supervisor - UFES
Prof. PhD.José Joaquim Conceição Soares Santos

Co-Supervisor - UFES
Prof. PhD. João Luiz Marcon Donatelli

Examiner - UFABC
Prof. PhD. Silvia Azucena Nebra de Pérez

Examiner - UFPB
Prof. PhD. Monica Carvalho

Examiner - USP
Prof. PhD. Daniel Alexander Flórez-Orrego

Vitória-ES
2020

I dedicate this master's thesis to my dear family,
in special to my grandmother who is not with us anymore,
and to my Dear and Almighty God,
for giving me the opportunity on achieving this Master's Degree title.

Acknowledgements

I am particularly grateful for the financial support from the Coordination for the Improvement of Higher Education Personnel (CAPES – Brazilian government).

I would like to thank the following companies, TEVISA and LGSA, for their financial sponsorship during CRATOS's R&D project (ANEEL PD-06483-0318/2018) in partnership with the Federal University of Espírito Santo (UFES).

To the Master Degree Program in Mechanical Engineering (PPGEM) at the Federal University of Espírito Santo, I appreciate for supporting my journey in this academic challenge.

I would like to express my very great appreciation to supervisor Prof. PhD. José Joaquim Conceição Soares Santos and co-supervisor Prof. PhD. João Luiz Marcon Donatelli for supporting my career as a specialist in thermal engineering. I definitely learned so much about thermal engineering through your guidance.

I would like to offer my special thanks to the coordinator of CRATOS's R&D project, Prof. PhD. Carla César Martins Cunha, and to my colleague, Bruno Muniz de Freitas Miotto, for the opportunity to learn and share knowledge during these two years of hard work.

I would like to express my deep gratitude to Prof. PhD. Clayton Barcelos Zabeu, thank you for lecturing the GT-Power introductory course at the Mauá Institute of Technology (IMT-SP) and providing the W20V34SG engine modelling in order to adapt, simulate and assist the new case study.

I would like to thank Prof. PhD. Atílio Barbosa Lourenço and MSc. Marcelo Aiolfi Barone for sharing knowledge with good discussions about thermodynamic subjects. I had the opportunity to work with each one of you and I definitely became a better specialist in thermal system design.

My grateful thanks are also extended to Prof. PhD. Rogério Ramos, during your lectures, thank you for encouraging me to seek not only the right answer to a problem but also mastering it to high standard levels. I am also grateful for all wise counsel that kept my mind healthy.

I would also like to thank my dear friends Victor Oliveira de Azevedo, Maria Clara Noguti and Rafael Spinardi, thank you for sharing joy and laughs with me during my most difficult times.

"Dear God, give us strength to accept with serenity the things that can not be changed.
Give us courage to change the things that can and should be changed.
And give us wisdom to distinguish one from the other."
(Admiral Thomas C. Hart)

Abstract

CHUN, A. (2020), *Superstructure Optimization of Absorption Chillers integrated with a Large Internal Combustion Engine for Intake Air Conditioning*, Vitória, 254 p. M.Sc. Thesis - Technological Center, Federal University of Espírito Santo.

This work aims to propose a thermal design for a chilled water system that provides cooling effects and dehumidification process in the intake air, therefore, allowing engine operation under reduced knocking restrictions which implicates in performance enhancement. The reduction of electrical energy demand at the radiator is also investigated as second benefit. The main contribution is to apply superstructure optimization methodology by considering several options of absorption chiller systems integrated to one Wärtsilä 20V34SG engine of 8.7 MW. The superstructure modelling and optimization are carried out in the Engineering Equation Solver (EES) software and two distinct Objective Functions are explored separately. Firstly, it is minimized the chilled water specific cost, and posteriorly, the gross profit is maximized. Furthermore, a detailed exergy analysis is developed for each thermal equipment that composes the optimized thermal system. Finally, an economic feasibility study is also developed. Regarding the main results, the optimal solution in order to reach the maximum profit of 30.7 US$ h^{-1} is a single-effect configuration with high solution heat exchanger in its structure and recovering totally the engine's cooling water while preheating it at the exhaust gases heat exchanger. For the minimum chilled water specific cost of 311.7 US$ ton^{-1}, the best configuration is a half-effect chiller with no solution heat exchangers. The exergy analysis allows to comment that the single-effect chiller concentrates more total exergy losses in the dissipative heat exchangers (29.56%) than the half-effect chiller (22.08%). Notwithstanding, there is more concentration of irreversibility in the half-effect chiller (67.09%) than in the single-effect chiller (48.24%). The exergy efficiency is higher in single-effect chiller, presenting a value of 0.222 against 0.108 of exergy efficiency in half-effect chiller. The engine under a repowered shaft power output of 10.2 MW presents calculated energy efficiency of 45.26% against 44.87% for the rated condition of 8.7 MW. Moreover, the engine exergy efficiency is increased from 43.27% to 43.64%. This repowering application gives a LCOE of 19.2 US$ MWh^{-1} whereas a commercial ORC system under similar conditions presents a LCOE of 57.15 US$ MWh^{-1}. The economic indicators present promising profitable scenario for the studied engine, demonstrating a maximum payback period of 3 years.

Key-words: Superstructure Optimization. Lithium Bromide and Water Absorption Chillers. Internal Combustion Engine. Waste Heat Recovery. Intake Air Conditioning.

Resumo

CHUN, A. (2020), *Otimização por Superestrutura de Chiller por Absorção integrado com um Motor de Grande Porte para Condicionamento do Ar de Admissão*, Vitória, 254 p. Dissertação de Mestrado - Centro Tecnológico, Universidade Federal do Espírito Santo.

Este trabalho objetiva propor um projeto térmico de um sistema de água gelada que fornece efeitos de resfriamento e processo de desumidificação no ar de admissão do motor, portanto, permitindo uma operação sobre condição de restrição reduzida de *knocking* que implica em uma melhora de desempenho. A redução da demanda de energia elétrica no radiador também é investigada como segundo benefício. A principal contribuição é aplicar a metodologia de otimização por superestruturas considerando diversas opções de sistemas de *chiller* por absorção integradas em um motor da Wärtsilä 20V34SG de 8,7 MW. A modelagem e otimização da superestrutura são desenvolvidas no *software Engineering Equation Solver* e duas Funções Objetivo distintas são exploradas separademente. Primeiramente, minimiza-se o custo específico da água gelada, e posteriormente, o lucro bruto é maximizado. Somado a isso, uma análise exergética detalhada é desenvolvida para cada equipamento térmico que compõe o sistema térmico otimizado. Finalmente, um estudo de viabilidade econômica também é realizado. Em relação aos principais resultados, para se alcançar o lucro máximo de 30,7 US$ h^{-1}, a solução ótima é uma configuração de simples-efeito com regenerador de alta em sua estrutura, além de recuperar totalmente a água de resfriamento do motor enquanto preaquecendo no trocador de calor de gases de exaustão. Para o custo específico mínimo de 311,7 US$ ton^{-1}, a melhor configuração é um *chiller* de meio-efeito sem a presença de regeneradores. A análise exergética permite comentar que o *chiller* de simples-efeito concentra mais perdas exergéticas nos trocadores de calor dissipativos (29,56%) do que o meio-efeito (22,08%). Entretanto, há maior concentração de irreversibilidades no *chiller* de meio-efeito (67,09%) do que no simples-efeito (48,24%). A eficiência exergética é maior no simples-efeito, apresentando um valor de 0,222 contra 0,108 de eficiência exergética no meio-efeito. O motor sob condição de repotencialização de 10,2 MW apresenta eficiência energética de 45,26% contra 44,87% da condição nominal de 8,7 MW. Adicionalmente, a eficiência exergética do motor é aumentada de 43,27% para 43,64%. Esta aplicação de repotencialização gera um LCOE calculado de 19,2 US$ MWh^{-1} enquanto que um sistema ORC comercial sobre condições similares apresenta um LCOE de 57,15 US$ MWh^{-1}. Os indicadores econômicos apresentam um cenário promissor para o motor de estudo, demonstrando um período máximo de *payback* descontado de 3 anos.

Palavras-chave: Otimização por Superestrutura. *Chillers* por Absorção. Motor de Combustão Interna. Recuperação de Calor Residual. Condicionamento do Ar de Admissão.

List of Figures

List of Tables

List of symbols

a	Speed of sound for ideal gases
$a_{species}$	Activity for chemical exergy
a_{ij}	Constant for chemical exergy
A	Heat transfer area
A'	Number of moles for oxygen in stoichiometric combustion balance
A/F	Air-Fuel ratio
α	Absolute angle for turbocharger
b	Mass flow rate splitting variable
β	Relative angle for turbocharger
β'	Exchanger compactness for cooling coil
b_{ij}	Constant for chemical exergy
$BMEP$	Brake Mean Effective Pressure
$BSFC$	Brake Specific Fuel Consumption
CF	Correcting factor
CI	Cost Index
$const_k$	Constants for curve fitting in electric generator
COP	Coefficient of Performance
$C_{chiller}$	Chilled water specific cost
c_p	Specific heat at constant pressure
CRF	Capital Recovery Factor
c_v	Specific heat at constant volume
CVU	Variable cost per unit
D'	Coil depth

d_i	Internal diameter
d_k	Parameters for curve fitting in electric generator
dL	Evaporated water mass flow rate
dm	Condensed water mass flow rate
DP	Discounted Payback period
Δ	Variation or difference
ΔT_T	Terminal Temperature Difference
e	Specific exergy in mass basis
$\bar{e}$	Specific exergy in molar basis
ϵ	Effectiveness
η	Efficiency
η_s	Finned-surface weighted efficiency
$\dot{E}$	Exergy rate
f	Fuel-Air ratio
F_{exp}	Expansion factor for economic evaluation
FP	Flow parameter for turbocharger
G	Dry air mass flow rate
h	Specific enthalpy in mass basis
$\bar{h}$	Specific enthalpy in molar basis
h_c	Air convective heat transfer coefficient
H'	Coil height
h_w	Water convective heat transfer coefficient
I	Irreversibility rate in means of exergy
IRR	Internal Rate of Return
k	Ratio between c_p and c_v
K	Proportional weighted value

ξ	Exergy efficiency
L	Water mass flow rate
L'	Coil length
$\dot{L}$	Losses rate in means of exergy
LHV	Lower Heating Value
λ	Excess of air
ln	Natural logarithm
$LCOE$	Levelized Cost of Energy
m	molality
m_i	Equipment coefficient
M	Mach number
$\bar{M}$	molar mass
$\dot{m}$	Mass flow rate
n	Number of ...
N	Rotation speed
n_i	Pump coefficient
NDP	Non-Discounted Payback period
NPV	Net Present Value
NTU	Number of Transfer Units or Tower Characteristic
ν	Dissociation number for the solute in chemical exergy calculation
OCF	Operating cash flow
OF	Objective Function
ω_i'	Humidity ratio for psychrometric chart
ω_i	Angular velocity for turbocharger
p	Pressure
P_f	Price of the fuel

$\dot{P}_{LORM}$	UTE LORM profit rate
p_0	Total pressure
Pe	Perimeter
$p.f.$	Power factor
ϕ	Maintenance factor for cost rate evaluation
Φ'	Relative Humidity for psychrometric chart
Φ	Osmotic coefficient for chemical exergy
π	Total pressure ratio
Q	Heat
Qu	Quality
$\dot{Q}$	Heat transfer rate
r	Radius
R	Ratio of heat transfer between air in contact with water film and water stream over the quantity of heat transfer between humid air stream and air in contact with water film.
ρ	Density
ρ_0	Total density
$\bar{R}$	Universal gas constant
$\dot{R}$	Revenue rate
R^2	Coefficient of determination
RMS	Root Mean Square
s	Specific entropy in mass basis
$\bar{s}$	Specific entropy in molar basis
SR	Stage Reaction for turbocharger
S_L	Longitudinal tube spacing
S_T	Transversal tube spacing
t	Number of years

T	Temperature
T_0	Total temperature
TCI	Total Cost of Investment
τ	Total temperature ratio
U	Overall heat transfer coefficient for each equipment and tangential velocity for turbocharger
v	Specific volume for thermodynamic property
V	Absolute velocity
$\dot{V}$	Volume flow rate
$\sum$	Sum
W	Relative velocity
$\dot{W}$	Work rate
x	Solution mass fraction concentration
X	Parameter of interest
y	molar fraction of species
Z	Purchase cost
$\dot{Z}_i$	Cost rate

List of abbreviations and acronyms

a	Air stream
Ab	Absorber
add	Additional
amb	Ambient
ANEEL	Agência Nacional de Energia Elétrica (Brazilian Electricity Regulatory Agency)
Ar	Argon
ASHRAE	American Society of Heating, Refrigerating, and Air Conditioning Engineers
AuAb	Auxiliary Absorber
AuDe	Auxiliary Desorber
AuSHX	Auxiliary Solution Heat Exchanger
Aup	Auxiliary pump
avg	Average
BTG Pactual	Banking and Trading Group Pactual Anonymous Society
c	Compressor
CAC	Charge Air Cooler
CAPES	Coordenação de Aperfeiçoamento de Pessoal de Nível Superior (Coordination for the Improvement of Higher Education Personnel)
CC	Cooling Coil
ch	Chemical
CHT	Chiller High Temperature
CH_4	Methane
C_2H_6	Ethane
C_3H_8	Propane

C_4H_{10}	Butane
C_5H_{12}	Pentane
C_6H_{14}	Hexane
CLT	Chiller Low Temperature
CMT	Chiller Medium Temperature
Co	Condenser
CO_2	Carbon Dioxide
corr	Corrected
cr	Critical
CRATOS	Chiller as Recovery Alternative Technology for Optimization of Systems
cryst	Crystallization
CT	Cooling Tower
cw	Chilled water
cwAuHX	Chilled water Auxiliary Heat Exchanger
cyl	Cylinder
db	Dry-bulb
De	Desorber
DE	Double-Effect
des	Destroyed
dis	Dissociation
dp	Dew-point for psychrometric chart
dyn	Dynamic
EES	Engineering Equation Solver
eg	Electric generator
ele	Electrical
em	Electric motor

EHX	Exhaust gases Heat Exchanger
Ev	Evaporator
EV	Expansion Valve
ex	Exergy
exp	Expansion
f	Fuel
FUNDAJ	Fundação Joaquim Nabuco (Joaquim Nabuco's Foundation)
g	Exhaust gases
G	Electric Generator
GA	Genetic Algorithm
GT	Gamma Technologies
GDP	Generalized Disjunctive Programming
HCo	High Condenser
HDe	High Desorber
HE	Half-Effect
Hp	High pump
HSHX	High Solution Heat Exchanger
HT	Low Temperature
HX	Heat Exchanger
H_2O	Water
ICE	Internal Combustion Engine
IM	Intake Manifold
IEMA	Instituto Estadual de Meio Ambiente e Recursos Hídricos (State Institute of Environment and Water Resources)
IMT	Instituto Mauá de Tecnologia (Mauá Institute of Technology)
in	Inlet

inc	Increment
IUPAC	International Union of Pure and Applied Chemistry
LCo	Low Condenser
LDe	Low Desorber
LG	Life's Good company
LGSA	Linhares Geração Sociedade Anônima (Linhares Generation Anonymous Society)
LiBr	Lithium Bromide
lm	Log mean
Lp	Low pump
LORM	Luiz Oscar Rodrigues de Melo
LSHX	Low Solution Heat Exchanger
LT	Low Temperature
main	Maintenance
max	Maximum
min	Minimum
ME	Multi-Energy
NCAR	National Center for Atmospheric Research
MINLP	Mixed-Integer Non-Linear Programming
MT	Medium Temperature
NG	Natural Gas
N_2	Nitrogen
NH_3	Ammonia
LO	Lube Oil
O&M	Operation and Maintenance
ope	Operating

ORC	Organic Rankine Cycle
out	Outlet
O_2	Oxygen
p	pump
PETROBRAS	Pétroleo Brasileiro Sociedade Anônima (Brazilian Oil Anonymous Society)
ph	Physical
Pro	Product
rad	Radiator
r/c	Radiation and convection
R&D	Research and Development
ref	Reference
Rea	Reagent
SA	Simulated Annealing
sat	Saturation
SE	Single-Effect
SEDL	Single-Effect with Double-Lift
Sens	Sensible
SEV	Solution Expansion Valve
SP	State of São Paulo
stoich	stoichiometric
t	Turbine
TEVISA	Termelétrica Viana Sociedade Anônima (Thermoelectric Viana Anonymous Society)
ts	Total-to-static
tt	Total-to-total
TV	Thermostatic Valve

3WV	3 Way-Valve
UTE	Unidade Termelétrica (Thermoelectric Unit)
UFES	Universidade Federal do Espírito Santo (Federal University of Espírito Santo)
Vap	Vaporization
w	Water stream
wb	Wet-bulb
WD	Water Distribution
wf	Water film layer
WG	Waste-gate
WHR	Waste Heat Recovery

Contents

1 Introduction

The Brazilian electrical energy matrix is mainly composed by hydroelectric power plants, representing an approximated value of supervised power production around 102.899 GW (60.59%) (ANEEL, 2020). However, since these kind of power plants depend considerably on weather conditions due the necessity of rainfall, it is possible to occur lack of electric power generation (EPE, 2019; FUNDAJ, 2019a).

Since 1993, the Brazilian electrical energy matrix had been facing significant crises in maintaining a secure electric power production on the grid and transmission through base stations around the whole country (FUNDAJ, 2019b). Further, as reported by FUNDAJ (2019c), the major crisis arose in 2001 due long periods of drought weather combined with high dependency on hydroelectric power plants. As a result, the occurrence of great shortages in electric power generation became frequent.

Nevertheless, these electrical energy blackouts had been occurring by other circumstances too, e.g. (i) technical accidents by human error, (ii) failures at power stations, and (iii) unexpected accidents at strategic transmission infrastructures due harmful environmental conditions (FUNDAJ, 2019b). Hence, because of these power outages over the entire country, the Brazilian government decided to overcome these issues by investing in the energy generation sector.

Bearing in mind this scenario, for guaranteeing a safe and functional electrical energy grid, one of the actions from the Brazilian government was to install strategically new thermal power plants powered by reciprocating large internal combustion engines (ICE) around the country.

As a matter of fact, they were majorly designed as simple peaking power plants with low investment cost. By the same token, it was not a concern the implementation of waste heat recovery (WHR) technologies to use possible heat residues (MORASWKI et al., 2017). In short, these thermal power plants were simply forecasted to supply sporadically electrical energy to the grid on periods of dry weather (EPE, 2020). However, it is quite necessary to expose here that some places in Brazil still have poor infrastructure of natural gas distribution for energy generation, for instance, the Amazon state which is located in the north region depends considerably on diesel engines to generate electricity (CRUZ et al., 2004).

The efficient operability under both partial and rated loads is one of the main advantages of reciprocating ICE, being capable on reaching energy efficiencies around 50% (TOLMASQUIM, 2016). Moreover, the engines can be managed into independent groups, allowing to operate under more flexible conditions and deliver only the mandatory

electrical energy to the grid (PETRASSI, 2012).

In agreement with Wärtsilä (2008), a particularity of these thermal power plants driven by ICE is the technological limitation on achieving the manufacturer rated shaft power output due the possible occurrence of knocking phenomena inside the piston-cylinders. One of the factors that causes knocking is the harsh ambient site condition, i.e. hot ambient temperature.

The case study of this work is Luiz Oscar Rodrigues de Melo's thermal power plant, also known as UTE LORM, which is supervised by the LGSA corporation and coordinated by TEVISA company under the management of BTG Pactual financial corporation.

This master's thesis is part of a Research and Development (R&D) project (ANEEL PD-06483-0318/2018), being fully sponsored by TEVISA company. The R&D project is under the Brazilian Electricity Regulatory Agency (ANEEL) rules and it is entitled Chiller as Recovery Alternative Technology for Optimization of Systems (CRATOS). Figure 1 shows the UTE LORM thermal power plant.

Figure 1 – UTE LORM thermal power plant.

Source: Own Authorship.

1.1 Motivation

In Brazil, there are distinct weather conditions due to its diversity and extensive geographic territory. Notwithstanding, at south-east region where the UTE LORM is located, the weather might reach seasons with excessive humidity and hot climate conditions, thereby, impacting negatively the engine performance.

In line with Wärtsilä (2008), spark ignition ICEs are limited by harsh climate condition due knocking effect which is averted through Wärtsilä control system by reducing the brake mean effective pressure ($BMEP$), consequently lowering power output for safe operating condition, i.e. derating.

Despite Wärtsilä engines operate under a broader range of ambient conditions (SANTOIANNI, 2015), an operating recommendation is to keep air temperature in the intake manifold below 45°C, avoiding possible derating condition. However, for places where the climate is hot with high humidity, it is quite difficult to keep simultaneously the intake manifold temperature below 45°C and brake power output at rated condition (8.7 MW).

Furthermore, regarding the Brazilian electrical energy matrix, the scenario had considerably changed along the years. For example, in 2012, the UTE LORM was designed to operate an average of two weeks (3.85%) per year (PETRASSI, 2012). Nevertheless, as the Brazilian electricity demand has been increasing over the years, also allied with a low price of natural gas, the UTE LORM has been operating more than 3.85% of the initial planning in order to ensure a safe and functional electrical energy grid. In 2019, this same thermoelectric power plant had been approximately dispatched fifty weeks (96%) during a period of one year, thus, operating as a base-load plant. As consequence, wasting more heat on the environment through the cooling water and exhaust gases systems. The CRATOS's R&D project was originated due to this story line of the UTE LORM in Brazil.

With this current scenario in mind plus harsh climate condition limiting technologically the engine permits an opportunity to install an absorption chiller for waste heat recovery application on Wärtsilä 20V34SG engine. Then, providing chilled water system for intake air conditioning which allows an operation at reduced knocking conditions inside the piston-cylinders while raising the $BMEP$ simultaneously. In summary, apart from levering the net power output, there is also an opportunity to reduce the operating costs at the radiator by saving some electrical energy demand.

1.2 Objective

This present work aims to integrate one W20V34SG engine at the UTE LORM to a superstructure of absorption chillers, which is set to recover waste heat from the engine and provide simultaneously a chilled water system for intake air conditioning in two steps; (i) precooling and dehumidifying intake air through a cooling coil on compressor upstream, and (ii) increasing intercooling through a chilled water auxiliary heat exchanger on radiator downstream in cooling water circuit. Hence, it is possible to improve the brake efficiency, brake specific fuel consumption ($BSFC$), net power production and some savings on the electrical energy demand at the radiator.

The major goal is to use the superstructure optimization methodology in order

to find both optimal configuration and best parametric conditions of a new thermal system based on lithium bromide and water (LiBr-H_2O) absorption chillers integrated to one W20V34SG engine. Subsequently, the minor goals are to evaluate a detailed exergy analysis of the entire thermal system coupled with the W20V34SG engine and carry out an economic feasibility study to show the best profitable scenario for the UTE LORM.

1.3 Structure

This master's thesis is structured in six chapters, introducing imperative informations about context, motivation and goals in chapter 1. Then, literature surveys of intake air conditioning for ICE, waste heat recovery in ICE, and superstructure optimization are presented in detail in chapter 2. Consecutively, at chapter 3, it is essential to pose fundamentals of absorption chillers and terminology analysis. In chapter 4, it is dedicated to organize the materials and methods of this thesis, presenting in detail the case study, mathematical solvers, superstructure representation, energy and exergy analyses, economic model, and optimization methodology. Finally, results are discussed and commented in chapter 5, followed by the main conclusions and outlooks in chapter 6.

The references are listed at the Bibliography section, and each equipment that composes the integration between the superstructure of absorption chillers and ICE is exposed in Appendix A. In addition, Appendix B organizes the database from GT-Power simulations which are used to predict the operating behavior of Wärtsilä 20V34SG engine. The Appendix C describes chemical exergy calculation for both LiBr-H_2O and fuel. With reference to the historic environment records at the Linhares's city, Appendix D contains some graphs and a brief analysis about the ambient conditions. At last, there are Annex A and Annex B that cover some reliable information about price of natural gas and Wärtsilä technical data, respectively.

2 Literature Survey

In order to pursuit the objective of this work, it is crucial to understand how to build a superstructure modelling integrating several absorption chillers with one engine. Thereupon, this chapter presents a literature review of three essential subjects. Firstly, section 2.1 describes the advantages of applying intake air conditioning for ICE. Subsequently, at the section 2.2, an investigation of waste heat recovery in ICE is reported due the possible usage of waste heats availability. Finally, section 2.3 presents a methodology known as superstructure optimization that is used in thermal system design to find the optimal structure and best parametric conditions.

2.1 Intake Air Conditioning for Internal Combustion Engine

Intake air conditioning in ICEs is a well-known technique that produces more shaft power by filling great air density into piston-cylinders, and its utilization is widely spread. In this master's thesis, it is dedicated a literature review on improving the engine performance by using this classic procedure so called intake air conditioning. In short, there are two different methods to cool the intake air in ICE; direct and indirect charge air cooling. Basically, in the first method the intake air is cooled with ambient air, while in the second approach, water is used to provide cooling effects (KAPSE; ARAKERIMATH, 2017).

A thermodynamic evaluation of a turbocharged diesel engine with intercooling process and combined to an absorption unit showed that there is a relation between the exhaust gases temperature and the intake air temperature. In summary, a colder air provoked a temperature drop on the exhaust gases stream. Thus, the absorption machine produced less cooling effect, impacting directly the intercooling capacity (MOSTAFAVI; AGNEW, 1996c). Furthermore, a second study involving a combined pre and intercooling configurations in the turbocharged diesel engine was developed to investigate the cooling effects in function of the engine parameters and the ambient site conditions. For instance, in case of high ambient temperature it was better to increase precooling temperature difference rather than to raise the intercooling temperature difference (MOSTAFAVI; AGNEW, 1997a).

A theoretical study using thermodynamic laws evaluated the performance of a turbocharged diesel engine combined with an absorption chiller in four different configurations under high ambient temperature of 35°C; (i) no charge air cooler, (ii) with precooler, (iii) with intercooler, and (iv) pre and intercooler. Some parameters such as brake efficiency, power output, and specific fuel consumption were examined for the four different

configurations. The simulation for 2800 RPM assuming no charge air cooler resulted in brake efficiency of 38.8% with power output of 115.1 kW and specific fuel consumption around 210.2 g kWh^{-1}. For pre and intercooler configuration, after simulations maintaining 2800 RPM, it was confirmed that the brake efficiency raised by increasing charge air cooler, presenting a value of 42.84%. Also, the power output increased to 223.6 kW while specific fuel consumption decreased to 201.2 g kWh^{-1} (AGNEW; TALBI; MOSTAFAVI, 1999).

Another similar case study evaluated the four configurations but adding an external air conditioning application (TALBI; AGNEW, 2002). In their results, for 2000 RPM and assuming no charge air cooler, the brake efficiency was 38.51% with power output of 154.8 kW and specific fuel consumption around 211.4 g kWh^{-1}. For pre and intercooler configurations with 2000 RPM, the brake efficiency boosted to 41% with a power output of 167.4 kW and specific fuel consumption around 198.2 g kWh^{-1}.

A study involving natural aspirated diesel engine combined with an absorption refrigeration unit was also investigated for pursuing cooling effects, and it showed to be favourable to combine both equipment (MOSTAFAVI; AGNEW, 1997b). However, when applying precooling process for natural aspirated diesel engine, the specific net power output was higher at a decreased efficiency than a non-precooled configuration (MOSTAFAVI; AGNEW, 1997c).

Engine performance improvements are well common in automobile applications, for instance, a simulation integrating a vehicle ICE with vapour-absorption chiller for intake air cooling showed advantages in engine performance by recovering exhaust gases through a heat exchanger. For coefficient of performance (COP) around 1.10, it was verified an engine efficiency enhancement of 26.95% with a power output of 215.8 kW, whereas for the reference condition, it was assumed an efficiency of 26.25% with power output of 195 kW (MCCARTHY; MADADNIA, 2012).

Kadunic et al. (2014) conducted an experimental bench using a jet-ejector to recover available waste heat from a small gasoline engine, then, providing more cooling effects in the charge air cooler. Thus, they achieved higher engine efficiency by cooling the air below ambient temperature. Also, it was considered a reference for charge air temperature around 60°C, and the advanced ignition timing forward the knock limit alone increased the efficiency in 13%. Moreover, while testing at the operating condition assuming original rich air-fuel ratio, the advanced ignition timing combined with leaner mixtures resulted in efficiency enhancement of more than 18%. Another experimental bench combining turbocharged ICE with jet-ejector for charge air cooling resulted in high power density in means of weight and volume. Therefore, increasing engine efficiency (ZEGENHAGEN; ZIEGLER, 2015).

An integration of a vehicle turbocharged diesel engine with one evaporator heat exchanger was tested in order to aim cooling effects in the intake air. Firstly, the evaporator

was installed in the entry of the compressor, presenting none significant changes in the engines performance. On the other hand, when the evaporator was installed in the exit of the compressor, it provoked a considerable temperature drop in a range of 10 to 20°C. Furthermore, it was achieved a reduction of fuel consumption around 6% with 8% of savings in CO_2 emissions (CIPOLLONE; BATTISTA; VITTORINI, 2017).

Another thermodynamic analysis of ammonia and water (NH_3-H_2O) single-effect absorption chiller integrating a turbocharged diesel engine resulted in cooled ambient temperature around 5°C through an available bottoming waste heat energy in the exhaust gases, reaching a theoretical addition of indicated efficiency of 4% (NOVELLA et al., 2017).

Bearing in mind these different contributions, it is more than sufficient to accept that intake air cooling is an advantage for ICE on reaching high power output, efficiency and less specific fuel consumption. Nevertheless, all of these mentioned works did not show how to avoid the condensation on air stream during cooling process. It is quite consequential to understand and predict how to avoid condensation, and it is directly related to the dew-point of air into intake manifold. The condensation must be avoided at all costs, otherwise, it will be harmful to piston-cylinders.

2.2 Waste Heat Recovery in Internal Combustion Engine

There are several WHR technologies that can use heat residue from industrial facilities. However, in this master's thesis, it is focused to study only absorption chillers recovering waste heat from ICE. The following works show some characteristics of this kind of application.

Regarding the heat losses in ICE, it is possible to recover waste heat from lubricating oil, jacket water and exhaust gases systems through a heat exchanger, producing hot water to drive absorption chillers (WU; WANG, 2006). Notwithstanding, some chillers can be driven directly by steam or exhaust gases too (ASHRAE, 2014).

A theoretical study involving, an integration between absorption machine with supercharged diesel engine, determined using analytical calculations through thermodynamic laws that it was possible to recover waste heat from exhaust gases and use it for cooling purposes (MOSTAFAVI; AGNEW, 1996a). In short, this work evaluated the net power, efficiency and available cooling load in the exhaust gases. Additionally to this framework, a subsequent study was similarly developed considering a turbocharged diesel engine combined with an absorption refrigeration unit. Thus, it was concluded again that there was an opportunity to deliver external cooling load over an acceptance range (MOSTAFAVI; AGNEW, 1996b).

An evaluation comparing four different configurations integrating a turbocharged diesel engine with a single-effect absorption chiller was carried out to investigate the overall efficiency (engine and chiller) and other cycle parameters under a high temperature condition of 35°C. These four configurations are; (i) no charge air cooler, (ii) with precooler, (iii) with intercooler, and (iv) with pre and intercooler. Some interesting results were regarded to exhaust gas temperature which decreased while charge air cooling was increased. This temperature affected the cooling capacity of the chiller, and consequently, the overall efficiency. For example, with no charge air cooler, the overall efficiency and exhaust gases temperature were 50.7% and 1145 K for 2800 RPM, respectively. The pre and intercooling configuration presented lowest overall efficiency (48.94% - 2800 RPM) due the great temperature drop (175 K) in exhaust gases system (AGNEW; TALBI; MOSTAFAVI, 1999). The same behavior was encountered in another similar case study which added an external air conditioning application with the same four configurations (TALBI; AGNEW, 2002).

Besides the theoretical evaluations, it is important to be concerned about practical limitations of this kind of application. As stated in Ryan (2004), the absorption unit must be carefully installed with the cooling water circuit, avoiding derating conditions on both equipment. The absorption chiller has considerable sensitivity to the engine return water temperature. The derating effect is significantly high, thus, some practical solutions are to oversize the absorption chiller to surpass this issue but the drawback obviously comes on high acquisition purchase cost. When interfacing the hot water chiller with the cooling water circuit, it is relevant to note the pressure drop caused by the desorber. Depending on this pressure drop, a booster pump might be unavoidable in order to overcome this extra pressure difference. On the superstructure modelling, it is accounted a booster pump in the hot water circuit.

An experimental study coupling NH_3-H_2O absorption unit to an ICE was carried out by Manzela et al. (2010) who investigated the usage of exhaust gases as primary energy to drive an absorption chiller. In their conclusions once more it was demonstrated that exhaust gases were a potential power source. Moreover, in their experiments, the *COP* was low and the domestic absorption machine did not provide enough cooling capacity. Nevertheless, they suggested to adapt a dedicated absorption unit to match the engine requirements.

Rêgo et al. (2014) conducted an experimental bench involving NH_3-H_2O single-effect absorption chiller with ICE. In this work, engine torque and speed were varied and the cycle parameters of absorption unit were observed during the experimental tests. They controlled successfully the exhaust gases flow to drive the absorption machine. Hence, it was possible to combine effectively NH_3-H_2O single-effect absorption chiller with ICE.

When observing the back pressure on exhaust gas system, it is essential to avoid high

back pressures values. Thereupon, the heat exchanger must be designed to match the engine requirements (ZEGENHAGEN; ZIEGLER, 2015). Another experimental application of engine exhaust gases powering an absorption system showed some proposal heat exchangers to achieve minimum pressure drop, avoiding high back pressure values. Furthermore, it was successfully demonstrated the availability to provide cooling loads through this waste heat recovery application (HILALI; SÖYLEMEZ, 2015).

A variety of systems combining absorption chillers with ICE can be found in the literature, several authors had studied the characteristics of absorption chillers recovering exhaust gases and/or jacket water (LONGO; GASPARELLA; ZILIO, 2005; SALVIANO; MODESTO, 2011; XAVIER et al., 2015; WANG; WU, 2015; NOVELLA et al., 2017).

In this master's thesis, the available cooling water and exhaust gases from Wärtsilä 20V34SG engine are targeted as main heat sources to drive LiBr-H_2O absorption chillers. For the sake of simplicity, instead of using exhaust gases to power directly the absorption units, hot water is produced through a heat exchanger on exhaust gases system. Hence, it is only considered to work with hot water LiBr-H_2O absorption machines (single-effect, half-effect, and single-effect with double-lift).

2.3 Superstructure Optimization

In this work, the state-of-art in superstructure optimization is presented in accordance with several literature reviews, assisting the development in superstructure modelling of absorption chillers integrated with turbocharged spark ignition ICE. According to Henao (2012), superstructure optimization had been carried out for more than three decades by several researchers, engineers, and mathematicians. Moreover, understanding the concept of optimization for energy systems is crucial in defining the state-of-art in superstructure optimization. This concept can be divided into three levels; (i) synthesis level for dealing with configuration, (ii) design level for defining components, and (iii) operation level for rating or partial load condition (FRANGOPOULOS; SPAKOVSKY; SCIUBBA, 2002).

When establishing a system to supply an energy demand for a customer, some important questions rise during the designing phase. For instance, **What is the optimal structure? What is the best parametric conditions?** Usually, these questions are answered by an experienced engineer. However, there are three different methods that can be used to solve the problem and find an optimal solution through an optimization procedure; (i) heuristics and evolutionary search, (ii) reaching pre-determined targets, and (iii) superstructure optimization (FRANGOPOULOS; SPAKOVSKY; SCIUBBA, 2002).

An intrinsic observation must be noticed when applying optimization methodologies in engineering problems; **Can we substitute an experienced engineer, researcher, and specialist for an automatic algorithm with a set of formulas and rules**

for thermal system design? (FRANGOPOULOS; SPAKOVSKY; SCIUBBA, 2002) This question faces the pragmatic thinking about how far these methodologies can solve engineering problems by reducing judgements of an engineer. Notwithstanding, it is still not possible to decide a final optimal solution without a specialist's opinion even using an optimization methodology. In the end, an expert must judge and certify that the final result makes sense.

Superstructure optimization methodology consists on permitting the existence of all components and interconnections, including unreal configurations. Then, a drawback of this method is regarded with high complexities due hard convergence while mathematical algorithms are searching for optimal solutions (FRANGOPOULOS; SPAKOVSKY; SCIUBBA, 2002). In an effort to reduce complexities, Henao (2012) suggests to use only useful components and feasible interconnections, building a rich superstructure. Therefore, this suggestion excludes unnecessary interconnections between components, increasing the chances on searching an optimal solution. One more suggestion from Henao (2012) is related to final structure which must be covered inside the rich superstructure. It means basically that the rich superstructure must embrace as much as possible feasible configurations.

Henao (2012) lists the main aspects to apply superstructure optimization techniques; (i) suitable representation of superstructure, (ii) systematic generation of superstructure, (iii) appropriate modelling of components inside the superstructure, and (iv) proper usage of numerical techniques to solve resultant models. All of these aspects are used in this master's thesis.

Albeit the complexities, the main benefits of superstructure optimization methodology is regarded with the capacity in utilizing any objective function with automatic results of optimal configuration (FRANGOPOULOS; SPAKOVSKY; SCIUBBA, 2002). Furthermore, it allows to consider all interactions between structural, design and operation variables simultaneously (HENAO, 2012).

The task on searching the best solution requires to know what is the level of difficulty. Therefore, depending on the complexities and requirements, one or more optimization criteria can be used on finding the best solution. When evaluating one criterion, it is represented as one objective function but if there are more than one criterion, it is used a multi-objective function to pursuit an optimal solution (FRANGOPOULOS; SPAKOVSKY; SCIUBBA, 2002).

The optimization criterion also depends on what is the priority of each problem. In the case of energy conversion systems, some criteria such as highest thermal efficiency for a given investment, lowest primary cost for a given desirable efficiency, internal parameters matching with external requirement, user friendly start up and shut down aspects allied to control concepts, and high reliability operation with low maintenance cost might be

accounted in the designing phase (ALEFELD; RADERMACHER, 1993).

An evaluation of several systems through superstructure modelling meeting a fixed demand of electricity, steam and mechanical power in synthesis level was developed by using a combinatorial optimization approach known as Simulated Annealing (SA). This combinatorial optimization method has the capacity to handle discrete variables and discontinuous cost functions (MAIA; CARVALHO; QASSIM, 1995). The superstructure modelling had three vapour pressure levels; high, medium and low pressures. Also, between these pressure levels, there were a number of limited equipment (fired and waste heat boilers, gas and steam turbine generators, steam turbines, heaters, pumps, deaerator and vacuum condenser) and interconnections. In their results, despite the fact that SA method showed to be a powerful optimization technique, it did not guarantee the global optimal solution. Moreover, as reported by the authors, if a custom designed equipment is required and costs are continuous functions of the capacities, SA method does not seem to be advantageous. In this master's thesis, the superstructure of absorption chiller has three pressure levels; high, medium and low pressures. Furthermore, it also has a number of limited components and interconnections. However, instead of using SA method, it is selected genetic algorithm to optimize the superstructure.

A superstructure modelling for structural (synthesis level) and parametric (design level) optimization of cogeneration systems was developed by Donatelli (2002) who adopted a strategy involving multi-level approach of the integrated optimization problem. In his work, the first-level problem consisted in decomposing a number of thermoeconomically isolated subsystems from the energy system. These isolated subsystems were subsequently optimized separately by minimizing the specific exergoeconomic costs of the products. In relation to the simulation and optimization tools, IPSEpro sofware was used to simulate the superstructure, and flexible polyhedra known as Neldear-Mead method was used to execute the optimization procedure. The rich superstructure modelling was composed with gas turbines, internal combustion engines, fired and heat recovery boilers, mechanical and absorption chillers, and cooling towers. The utilization of superstructure optimization methodology combined with flexible polyhedra optimization technique reached successfully optimal configuration as well as best parametric condition under several arrangements involving electricity and fuel prices, vapour and chilled water demands, and purchase equipment costs.

Another example using superstructure optimization methodology for combined cycle power plant minimized the cost of the product while both structure and variables of the process were varied during the optimization procedure (KOCH; CZIESLA; TSATSARONIS, 2007). In this superstructure modelling of combined cycle, it was confirmed a limited number of equipment (heat-recovery steam generator, supplementary firing, steam reheat, parallel arrangement of heat exchangers in the gas path, and steam injection into the gas turbine), as

well as, interconnections inside the superstructure. Furthermore, an evolutionary algorithm was used to optimize the superstructure modelling which demonstrated to be a powerful tool on finding optimal structure in synthesis level, and best parametric variables in design level. Also, with respect to complexities, a large superstructure with more decisions variables implicated in more time consuming during the optimization. They used GateCycle software to simulate the superstructure, while a toolbox optimization package in Matlab software optimized the superstructure.

Superstructure modelling for energy supply systems in an urban area was developed through a method combining multi-criterial evolutionary optimizer for structural and operational optimization, and simulation of energy supply systems (heat, electricity and gas) (BOUVY; LUCAS, 2007). The structural and operational optimization were executed at the EpoC tool, while eSim tool simulated the energy system. Inside of the superstructure, it was considered boilers, central condensation combined steam and gas turbine, public supplies for gas and electric energy. The superstructure interfaced the communication between EpoC and eSim tools. In their results, the timing consuming was extremely high, taking 32 days to finish the optimization procedure. Therefore, depending on the size of superstructure, it can take significant computational effort. Nevertheless, the superstructure optimization methodology was successfully applied on finding optimal solutions for energy supply systems.

The concept of superstructure optimization using evolutionary algorithm was also explored by Voll et al. (2012) for superstructure-free synthesis and optimization of distributed energy supply systems. The superstructure involved synthesis level of heating and cooling systems. In their methodology, it was not specified a defined rich superstructure as in the previous works. There were mutation operators for applying generic replacement rules. The parts of the energy supply system were substituted for alternative designs by employing these rules. In order to avoid computational effort due unreal configurations, it was reduced the number of replacement as well as the alternative designs that did not make sense. Additionally, Voll et al. (2012) used an energy conversion hierarchy technique to define efficiently all reasonable connections between the components and the definition of generic replacement rules. The superstructure optimization was successfully applied for distributed energy systems, finding complex solutions such as trigeneration configuration. A second work from the same previous authors applied superstructure-free optimization methodology for thermal power plants (WANG et al., 2015), aiming to avoid complexities and harsh computational time-consuming from conventional superstructure modelling. They engaged the optimization problem with a new mutation rule to synthesize new thermal power plants. In their case study, the problem started from a simple system and forwarded by identifying automatically new complex systems through superstructure-free optimization method.

Wang et al. (2014) carried out a study combining superstructure optimization approach with Mixed-Integer Non-Linear Programming (MINLP) techniques for parametric optimization of supercritical coal-fired power plants. In their methodology, it was used differential evolution approach in the optimization procedure, involving synthesis and design levels of difficulty. Also, the superstructure presented a number of limited equipments (ten feedwater preheaters, up to two reheatings and a secondary turbine with steam extractions), as well as, feasible interconnections. They demonstrated that by applying this combination between superstructure optimization and MINLP techniques, the design trade-off between thermodynamics and economics of energy conversion systems was more effective and showed that more useful information on cost-effective of thermal systems can be delivered by using this method. Another work combined hierarchical and algorithm approaches in order to synthesize efficiently the realistic processes, hence, utilizing the advantage of preliminary screening to create welfare initial estimates and incorporating integrated final flow sheets (MIZSEY; FONYO, 1990).

Bertran et al. (2017) investigated through superstructure optimization methodology new processing routes for sustainable synthesis-design. In their contribution, basically, the optimal processing routes are determined by applying obviously the superstructure optimization. Consecutively, the usage of integrated tools targets to enhance the design aspects. Two specific tools among them are presented and used during the optimization procedure, the first one is related to a database that provides a representation system. The second tool is a software known as Super O which assists the users to formulate and solve the synthesis problem. In short, the Super O software transfers an amount of information from the database between the several tools while involving a library with generic models, thereby, allowing a representation of wide range of possibilities. At last, by defining both selected route and identified targets, it generates new alternatives. Bertran et al. (2017) carried out the superstructure optimization in two case studies; biorefinary and carbon capture-utilization.

A superstructure optimization involving waste recovery technology was carried out by Yu et al. (2017) who used Organic Rankine Cycle (ORC) to recover heat residue from a chemical power plant, presenting optimal net power production while compared to previous results in the literature. In their work, it was developed a superstructure in two steps, firstly it was engaged the structural and operating conditions of the optimization problem. The second step was to target the heat exchanger network through a minimization of the number of heat exchangers in order to maintain the hot utility unchanged.

A superstructure modelling based on vapor compression-absorption cascade refrigeration systems is developed by implementing the models in CONOPT 3 v.3.14W software and optimizing the superstructure on the plataform GAMS v.23.6.5. In their work, an optimal structure was targeted while determining the sizes and the operating

conditions of all system components through the minimization of the total heat transfer area of the system and satisfying the given design specifications. The results showed an optimal solution presenting a total heat transfer area 7.3% smaller than the reference case (MUSSATI; MOROSUK; MUSSATI, 2020).

A review and deep discussion about superstructure optimization methodology expose the challenges and imperatives trends of process synthesis (BARNICKI; SIIROLA, 2004). Additionally, another good review in regard to this subject presents a diversity of methodologies based on superstructure optimization technique combined to mixed-integer programming, multi-objective optimization, optimization under uncertainty, and life cycle assessment (LIU; GEORGIADIS; PISTIKOPOULOS, 2011).

A more recent and vast review about superstructure optimization approaches in process system engineering can be encountered in Mencarelli et al. (2020). Their work covered a survey with several distinct ways to represent the superstructure modelling, emphasizing the existent literature for automated superstructure generation. Furthermore, they discuss deeply the more recent representations, in means of universality, friendly use, and manageability. Regarding the mathematical tools and optimization approaches that are applied in superstructure modelling, Mencarelli et al. (2020) also presents some review about the implications of superstructure representations on the strategies of solving the optimization problem.

Superstructure optimization methodology have been used by several researchers combining mathematical tools in order to solve MINLP problems. For instance, there is a first survey that presented the advances in mathematical programming focused in synthesis and design level of industrial processes using generalized disjunctive programming (GDP) models (GROSSMANN; CABALLERO; YEOMANS, 1999). A second overview of MINLP problems with GDP techniques was presented by Grossmann (2002) who discussed the characteristics of various methods and emphasized an unification analysis from their derivation. Moreover, it was used in another work the GDP technique with alternatives algorithms in MINLP problems (GROSSMANN; RUIZ, 2012). These studies applied this respective techniques with superstructure optimization methodology for synthesis and design of process network.

After researching and studying the contributions of some works from the literature, it is truly feasible to use superstructure optimization in thermal system design. Of course, some considerations are decisive to simplify the original state-of-art of superstructure optimization. A previous work from Chun (2017) already studied means to apply intake air conditioning and recovering waste heat from a large turbocharged diesel engine through absorption chiller by using superstructure optimization. Further, the ISO 15550 and ISO 3046-3 were consulted in order to estimate the engine improvement by correcting the efficiency.

3 Fundamentals and Terminology Analysis

Theoretical concepts and definitions of absorption machines are indispensable for superstructure modelling. The understanding of these fundamentals are primordial to pursuit the objective of this master's thesis.

In this section, basic concepts of absorption cycles are presented in detail. Firstly, it is important to comprehend the relation between absorption unit and external environment.

Refrigeration machine is defined as Type I heat pump when heat transfer is entering into chiller from external environment at high and low temperature levels ($T_{CHT} < T_{HT}$, $T_{CLT} < T_{LT}$), while heat rejection to the external environment is occurring in medium temperature level ($T_{CMT} > T_{MT}$) (HEROLD; RADERMACHER; KLEIN, 2016). Figure 2 represents theoretically three temperature levels for Type I heat pump.

Figure 2 – Basic representation of Type I heat pump.

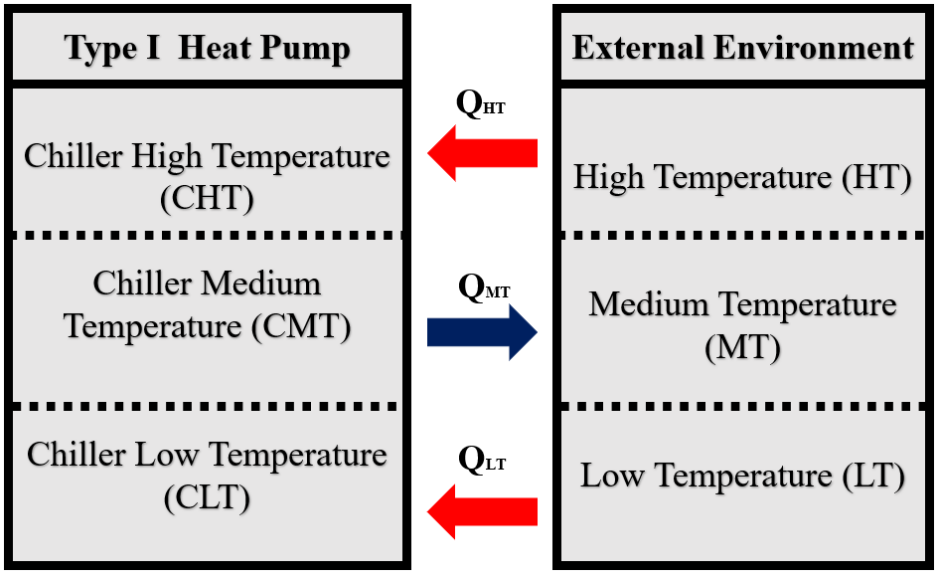

Source: Own authorship.

Several working fluids can be used in Type I heat pumps, e.g. NH_3-H_2O, LiBr-H_2O, methanol, and other organic solvents. In case of absorption chillers, it is commonly used NH_3-H_2O, and LiBr-H_2O (HEROLD; RADERMACHER; KLEIN, 2016). For ensuring good operational functionality, as well as, safety for both environment and human life, these working fluids must present some requirements. For instance, low pressure vapour for absorbent when compared to the working fluid, lowest ratio of the heat capacity of mixture (absorbent and refrigerant) over vaporization heat of the refrigerant, and

finally, the additives for the enhancement of heat and mass transfer should be available without hampering any other characteristics, such as thermal stability, toxicity, and corrosiveness (ALEFELD; RADERMACHER, 1993).

The utilization of LiBr-H_2O as pair of working fluid dominates a majority applications in the market of absorption chillers. Basically, the LiBr works as absorbent while H_2O assumes refrigerant aspects. Also, this working fluid does not allow chilled water temperature at the evaporator below 0°C. Thus, typical applications are in the air-conditioning systems of large buildings (HEROLD; RADERMACHER; KLEIN, 2016).

A crucial particularity of LiBr-H_2O absorption systems is in regard with the phenomenon of crystallization, which can be seen in Figure 3. This phenomenon is caused when the limit of solubility in the mixture is achieved, the solid phase starts to develop due a supersaturation condition of LiBr which means an excess of concentration of LiBr in the mixture.

Figure 3 – Pressure-Temperature-Concentration diagram for LiBr-H_2O solution.

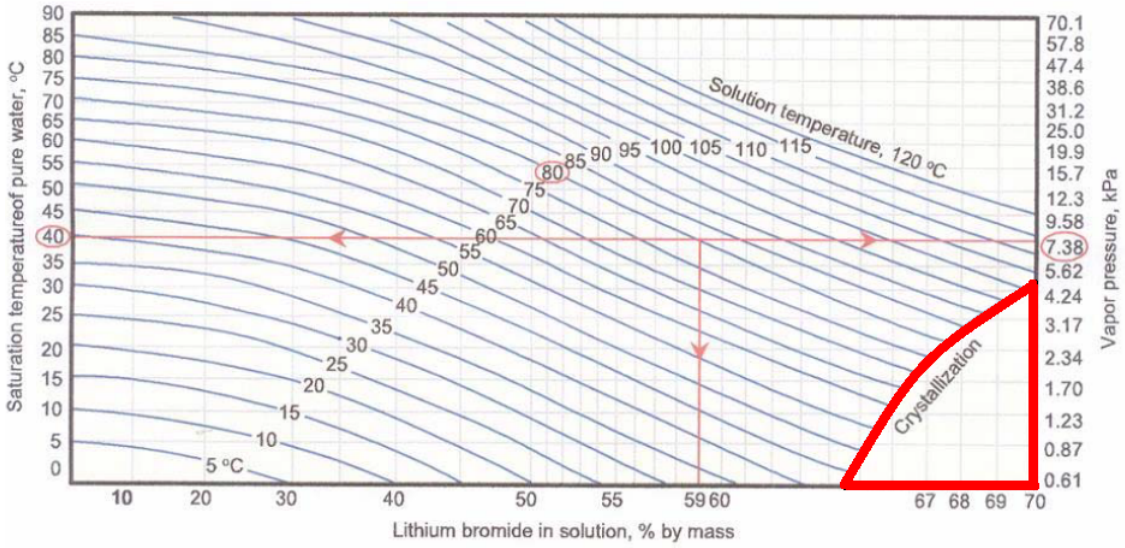

Source: More (2015).

This crystallization effect is a severe drawback because it reduces the solution operating range, blocking the chiller internal piping and stopping the chiller operation. Then, it must be avoided at all costs (ALEFELD; RADERMACHER, 1993; GILANI; AHMED, 2015; HEROLD; RADERMACHER; KLEIN, 2016; MORE, 2015).

Usually, crystallization effect commonly occurs when solution is entering in the absorber due low solution pressure, temperature and high concentration. Therefore, during the thermodynamic modelling, it is adopted two models for averting the crystallization zone in function of the solution mass fraction and temperature, respectively. The first model only

applies for solution stream entering in the absorbers, and it is based at minimum solution enthalpy in function of concentration (ARDEHALI; SHAHRESTANI; ADAMS, 2007). The second model calculates the critical solution concentration in function of temperature, thus, avoiding crystallization at other components such as desorbers and solution heat exchangers (GILANI; AHMED, 2015).

The absorption chillers can be separated into three basic categories; single-effect (SE), double-effect (DE) and advanced-effects (HEROLD; RADERMACHER; KLEIN, 2016). The two common categories that manufacturers had been working in the past years were single-effect and double-effect. Nevertheless, some manufacturers have been advancing recently in absorption chiller technologies, such as low temperature single-effect with double-lift (SEDL) and multi-energy chillers (ME).

The single-effect absorption unit is the simplest category, composing mainly absorber (Ab), desorber (De), condenser (Co), evaporator (Ev), one small pump and two expansion valves, as it can be seen in Figure 4. In addition, it is possible to install a solution heat exchanger (SHX) for increasing *COP*, which is practically around 0.7 (ASHRAE, 2014; HEROLD; RADERMACHER; KLEIN, 2016; MORE, 2015).

Figure 4 – LiBr-H_2O single-effect absorption chiller.

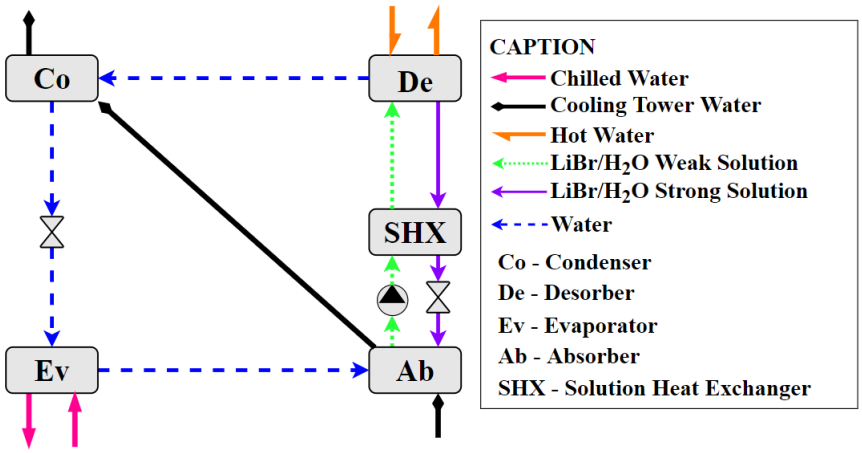

Source: Own Authorship.

This refrigeration machine works with high and low pressure levels. However, it does not consume high electric power demand. The desorber receives thermal energy that drives the absorption system, generating superheated vapour at high pressure which is below the ambient pressure. Also, strong solution at saturated liquid condition leaves the desorber and flows to solution heat exchanger. The condenser receives superheated vapour, rejecting heat to the environment through the cooling water circuit. It is assumed saturated liquid at the exit of the condenser. At evaporator, the liquid-vapour stream enters at low pressure due the expansion valve effect, receiving heat from water and vaporizing

at evaporator outlet to saturated vapour condition. This same saturated vapour at low pressure flows to absorber and mixes with strong solution while rejecting heat to the environment through the cooling water circuit.

The double-effect absorption systems distinguish from single-effect by observing the number of pressure levels, components, and the existence of an internal heat recovering at high condenser (HCo) to low desorber (LDe), as it can be seen in Figure 5. This second category has three pressure levels; high, medium and low pressures.

Figure 5 – Parallel flow LiBr-H_2O double-effect absorption chiller.

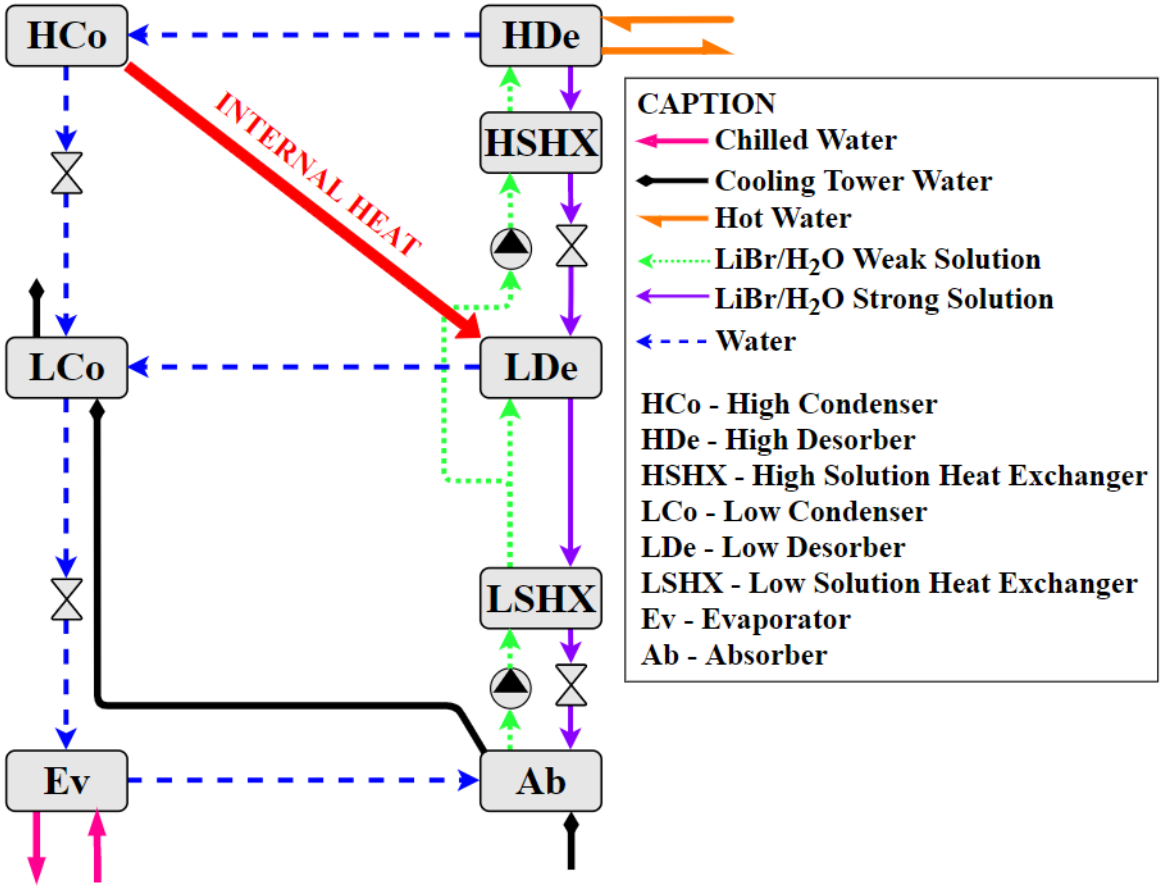

Source: Own Authorship.

High condenser works at high pressure while the low condenser (LCo) is operating under medium pressure. It is relevant to note that low desorber (LDe) is attached to high condenser and recovers internally heat at medium pressure. Also, one more pump, expansion valve and solution heat exchanger (HSHX) might be necessary at high pressure solution stream. The typical *COP* for double-effect absorption units are in a range between 1.0 to 1.4 (HEROLD; RADERMACHER; KLEIN, 2016).

Other configurations of double-effect can be found in the literature and are com-

monly known as series flow. In Figure 6, it is represented two usual series flow; solution to high desorber first and solution to low desorber first (HEROLD; RADERMACHER; KLEIN, 2016).

Figure 6 – Series flow LiBr-H_2O double-effect absorption chiller: solution to low desorber first (a) and solution to high desorber first (b).

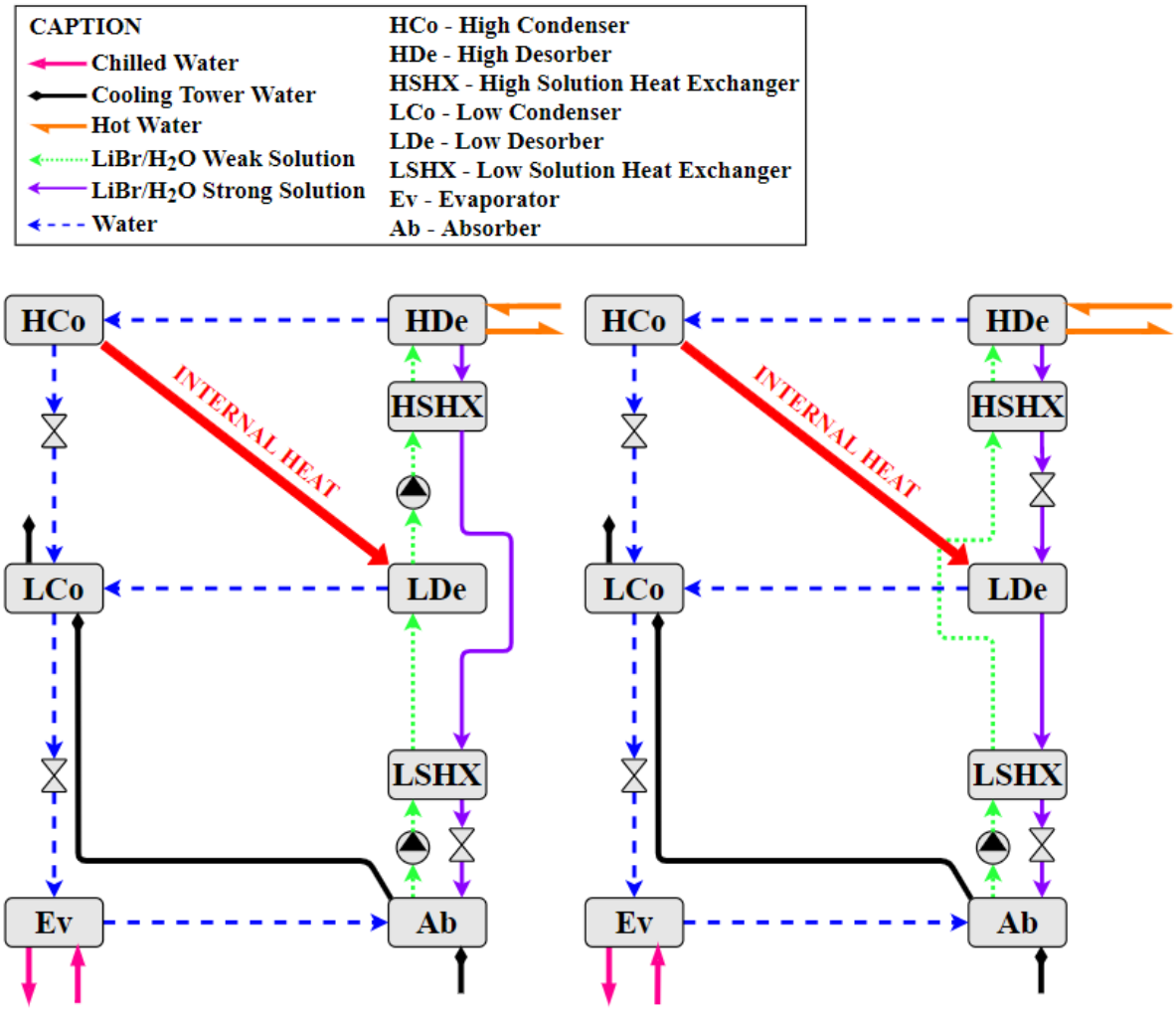

(a) (b)

Source: Own Authorship.

Bearing in mind the number of components, all double-effect configurations present high and low condensers (HCo and LCo), high and low desorbers (HDe and LDe), evaporator (Ev), absorber (Ab), one or two pumps, three or four expansion valves, and finally, one or two solution heat exchangers (HSHX and LSHX). Chun et al. (2018) already studied means to model double-effect superstructures of absorption chillers, but in this master's thesis, it is not accounted to work with such complex configurations.

The third category is ranked as advanced-effects, and most of them are still in testing phase. Notwithstanding, as mentioned before, manufacturers have been improving significantly the absorption system technology.

SEDL absorption chiller is represented in Figure 7, where there are three pressure levels; high, medium and low pressures. The technological key of this configuration is a combination between single-effect and half-effect (HE) systems, aiming to increase heat transfer for low temperature applications of hot water stream around 95°C (LG, 2016).

Figure 7 – Hot water LiBr-H_2O single-effect with double-lift.

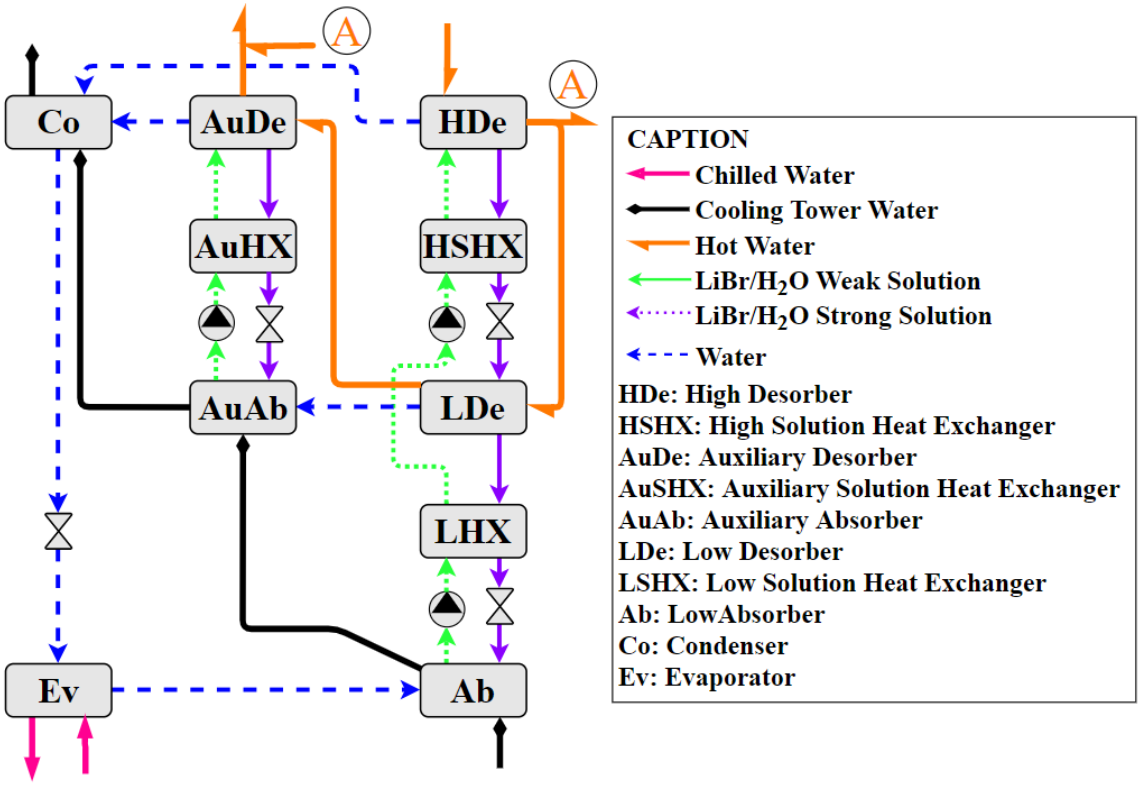

Source: Own Authorship.

The main advantage is a great temperature drop of 40°C in hot water stream and *COP* around 0.8 which is slightly higher than single-effect configuration. Nowadays, there are several manufacturers commercializing this kind of technology (CENTION, 2013; LG, 2016). Furthermore, many researchers investigated low temperature applications using SEDL absorption chiller (FUJII et al., 2017; SCHWEIGLER et al., 1998; YATTARA; YUQUN; MOSA, 2002; YATTARA; ZHU; ALI, 2003). Therefore, it is included in this present work.

Schweigler et al. (1998) created, designed and tested SEDL absoption chiller for partial loads conditions by controlling the mass flow after high desorber. In short, he

was able to work the superstructure definition experimentally. For instance, by observing Figure 7, when hot water mass flow was bypassed to point A, the low desorber, auxiliary absorber (AuAb), auxiliary solution heat exchanger (AuSHX), and auxiliary desorber (AuDe) did not operate under this experimental circumstance. In other words, it means that these components did not exist during the testing phase. Thus, the configuration became a single-effect system.

ME chillers are frequently applied when there are more than one available heat source at the industrial facility. The advantage is to use simultaneously two distinct heat sources in one single ME chiller (BROAD, 2017; YORK, 2016). A basic representation of this configuration can be seen in Figure 8.

Figure 8 – Exhaust gases and hot water LiBr-H_2O multi-energy effect.

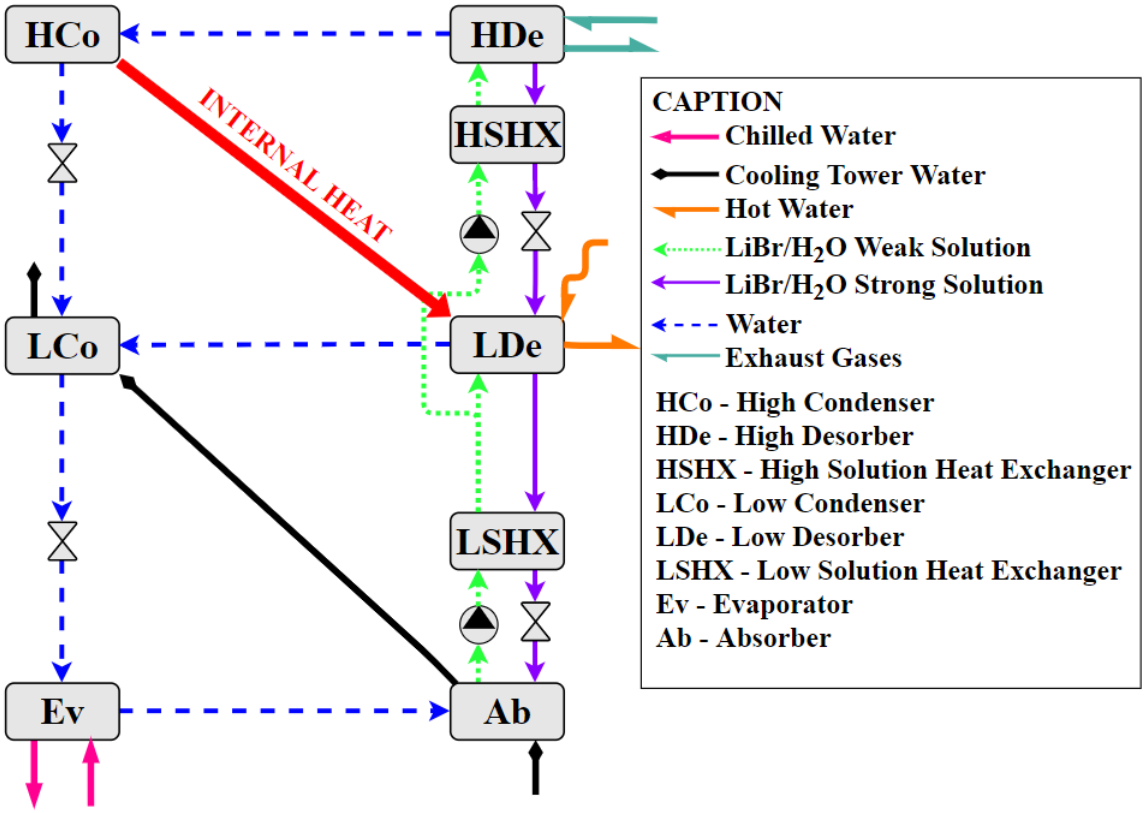

Source: Own Authorship.

ME effect chillers can reach higher *COP* than double-effect chillers, presenting values above 1.4. However, the exhaust gases and hot water temperature must be around 500 and 98°C, respectively (BROAD, 2017).

4 Materials and Methods

In this chapter, it is described the materials and methods that are relevant to this thesis and it is separated into seven sections. The section 4.1 shows the case study, presenting some characteristics and technical information of the UTE LORM power plant. The following section 4.2 presents the main mathematical solvers that are used in this work. The superstructure representation is shown and discussed in section 4.3. The section 4.4 describes the energy analysis for each component that composes the absorption machine. At the section 4.5, an analysis based on the second law of thermodynamics is carried out for each component in order to evaluate the exergy destruction, irreversibility generation, and other thermal losses in means of exergy. The section 4.6 presents an economic model that is used to estimate the acquisition costs of each equipment of the new thermal system. Finally, section 4.7 exposes the optimization methodology in order to find the optimal solution.

4.1 Case study

The UTE LORM is powered with twenty-four Wärtsilä 20V34SG engine of 8.7 MW, being divided into four independent sets composed by six engines, which are fuelled with natural gas from PETROBRAS's gas pipeline (Cacimbas-Vitória) at the Linhares's city, state of Espírito Santo, Brazil (PETRASSI, 2012).

With respect to the major components, according to Wärtsilä (2008), there are two turbochargers and one waste-gate, twenty piston-cylinders, two charge air coolers, one lube oil heat exchanger and two cooling water pumps, as it can be seen in Figure 9 (a).

There are also high temperature (HT) and low temperature (LT) cooling water circuits that cool these components and exchange heat on the radiator. At the UTE LORM, these both cooling water circuits were connected to each other due non-intention on pursuing cogeneration or repowering application. A representation of the power house is shown in Figure 9 (b).

Figure 9 – Wärtsilä 20V34SG engine (a) and a representation of the power house (b).

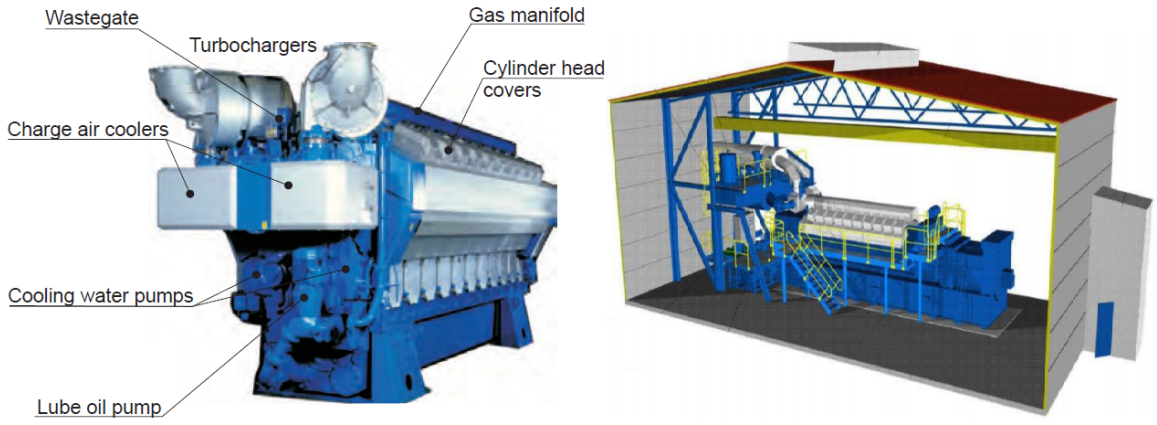

(a) (b) .

Source: Wärtsilä (2008) and Moraswki et al. (2017).

In Figure 10, on the current map, UTE LORM is highlighted among twenty-one thermoelectric power plants driven by sets of reciprocating ICEs on operating mode and connected to the Brazilian electricity grid (IEMA, 2020).

Figure 10 – UTE LORM location in Brazil.

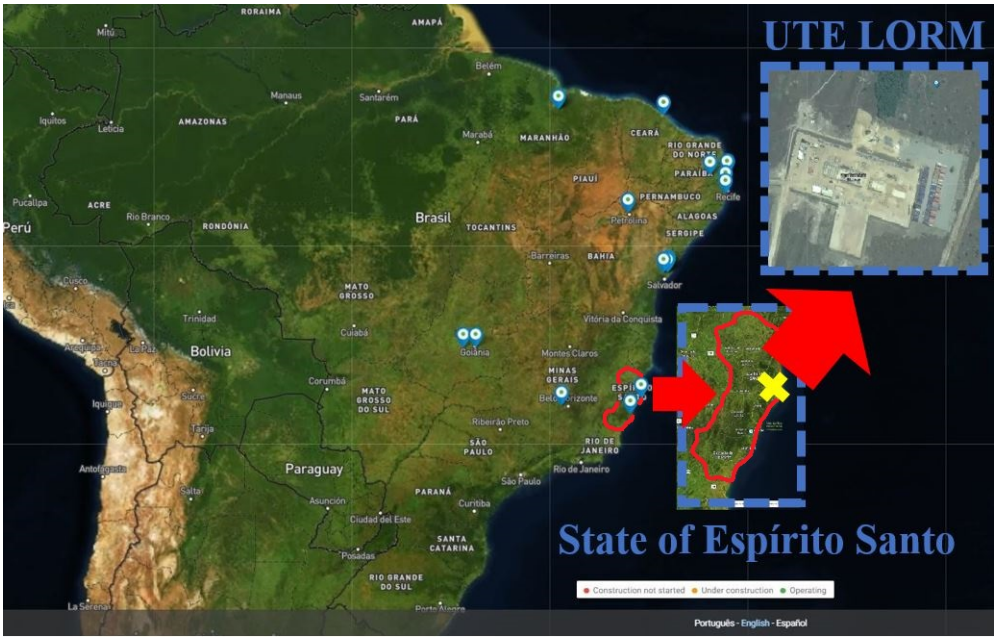

Source: Adapted from IEMA (2020).

Figure 11 represents the schematic of Wärtsilä 20V34SG engine.

Figure 11 – Schematic of Wärtsilä 20V34SG engine including high and low temperature cooling water circuits and radiator.

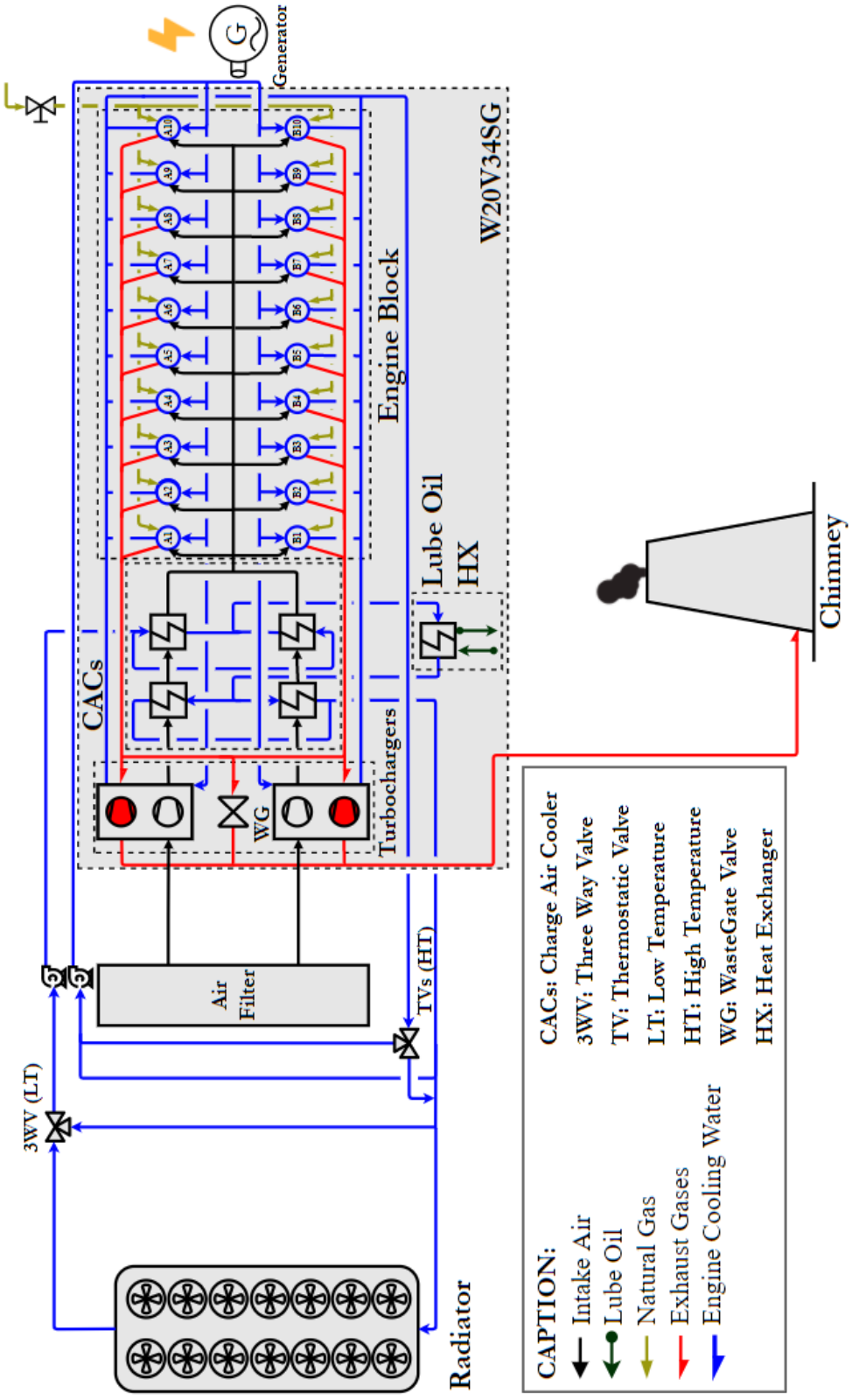

Source: Own Authorship.

4.2 Mathematical Solvers

Basically, two commercial software are used extensively; EES and GT-Power. The EES software is chosen among other mathematical solvers because it solves the block of equations through iterative procedures. Additionally, there are a lot of thermodynamic libraries of several working fluids, such as ideal and real fluids. Figure 12 and Figure 13 show the thermophysical properties and external library routines, respectively.

Figure 12 – EES thermophysical properties.

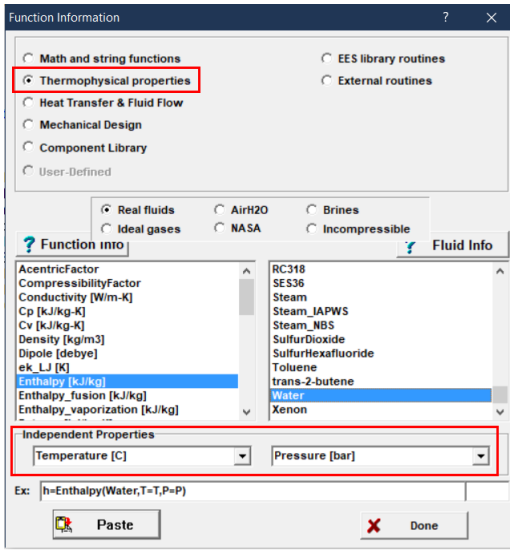

Source: FCHART-EES (2020).

Figure 13 – EES external library routines.

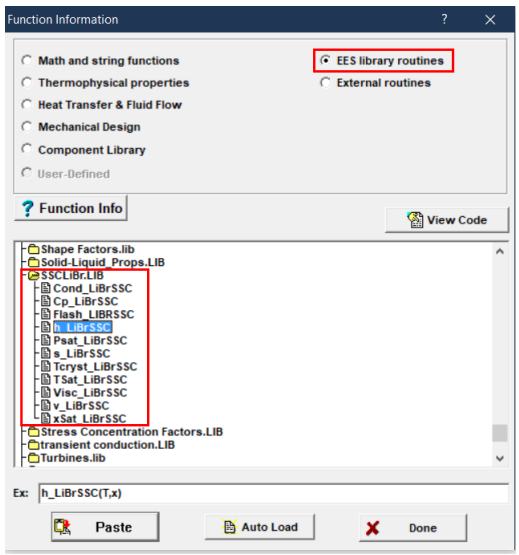

Source: FCHART-EES (2020).

EES software also contains an optimization package, as shown in Figure 14. Note here that the optimization package provides five approaches; Conjugate Directions method, Variable Metric method, Nealder-Mead Simplex method, DIRECT algorithm and Genetic method (FCHART-EES, 2020).

Figure 14 – EES Optimization package.

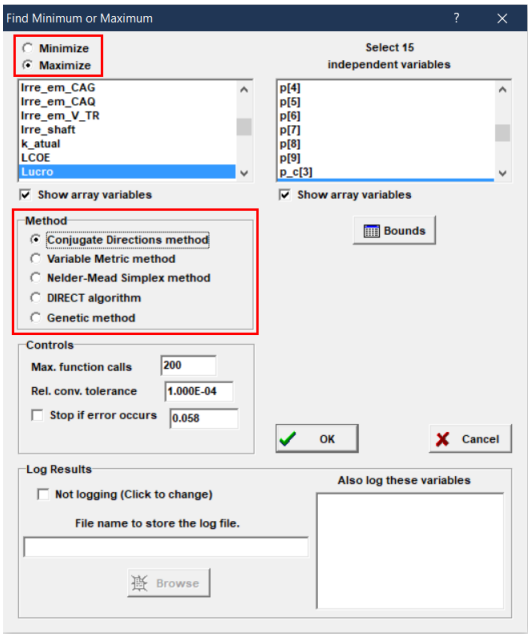

Source: FCHART-EES (2020).

The GT-Power software is necessary because the engine must be simulated under more complex relation involving transient problem. Several simulations are developed in order to generate a great amount of data. The engine performance enhancement is predicted by simulating several scenarios, *BMEP*s varying from 20 to 23.45 bar with a step of 1.15 bar, and defining the intake air temperature on compressor inlet of 12.5°C with 100% of relative humidity.

Hence, the amount of data from GT-Power simulations is used by applying curve fitting in EES software. A polynomial equation of third degree is used for all regression modellings due to its minor value of Root Mean Square (RMS) and R^2 value practically unit, which means a good fitting characteristic with minor local errors.

Moreover, operating data from the site and manufacturer information are necessary to simulate and optimize the superstructure of absorption chillers integrated to one W20V34SG engine. The amount of data that is used in this work can be encountered at the Appendixes and Annexes.

4.3 Superstructure Representation

With respect to the development of superstructure modelling, it is only considered to work with synthesis and design level under an overrating condition.

The combination between ICE and chiller can assume several different configurations, i.e. the rich superstructure involves not only absorption chiller systems but also integrates distinctly the ICE. Hence, it is more complex and increases the level of difficulty.

The low temperature superstructure of absorption chiller recovers engine cooling water at the LT circuit and preheat this amount of water at the exhaust gases heat exchanger which is recovering part of the exhaust gases stream. There are three possible processing routes; (i) only recovering partially or totally the engine cooling water and preheating at the exhaust gases heat exchanger, thus delivering hot water to power the absorption unit, (ii) not recovering engine cooling water and presenting an isolated hot water circuit, (iii) recovering partially or totally the engine cooling water circuit while mixing with some returning water.

Figure 15 presents the structural routes as well as the possibilities of processing routes on the superstructure representation of this master's thesis.

Figure 15 – Possible processing routes on the superstructure representation of absorption chiller integrated to one W20V34SG engine.

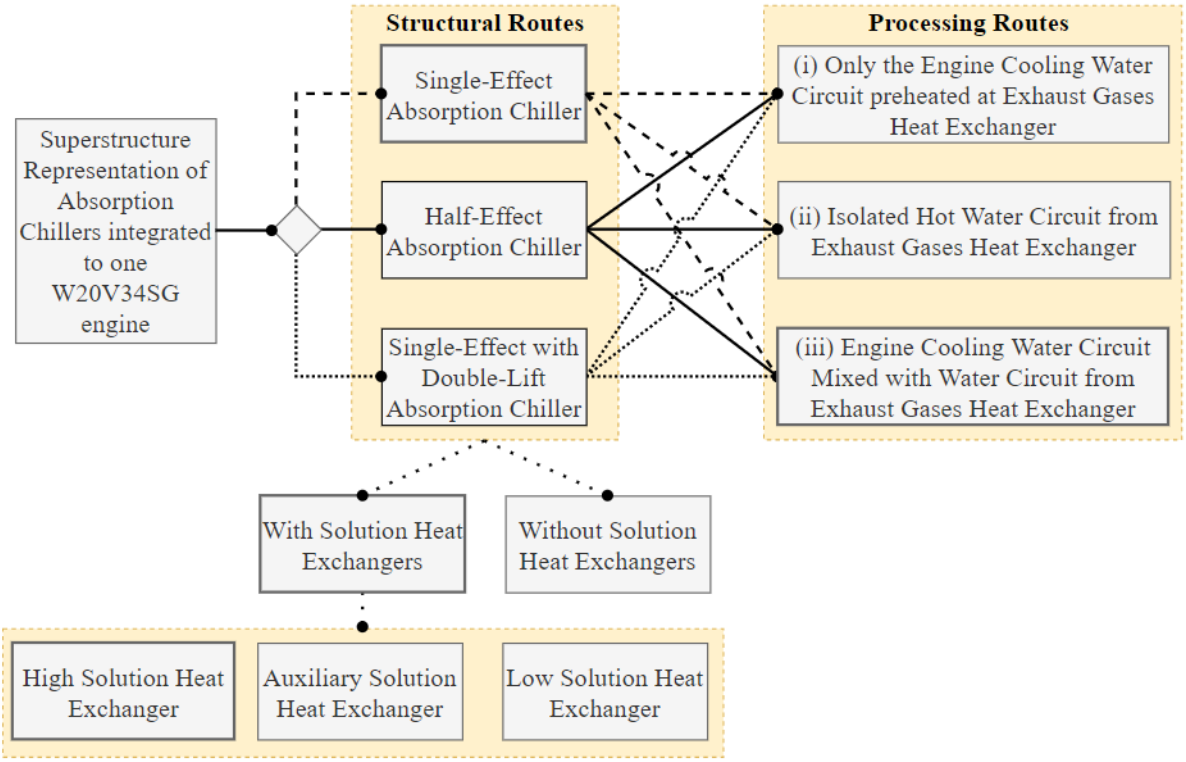

Source: Own Authorship.

4.4 Energy Analysis

This section describes thermodynamic modellings for each component in the superstructure of LiBr-H_2O absorption chiller by applying Herold, Radermacher and Klein (2016) considerations. Moreover, the strategy is to model each heat exchanger by defining variables like terminal temperature difference. Also, conservation of mass and first law of thermodynamics analyses are applied for all components inside of the superstructure.

Figure 16 represents the low temperature superstructure, allowing three configurations of absorption units (SE, SEDL, HE) and a combination among them. An adaptation is made from Schweigler et al. (1998) configuration, where weak solution is simultaneously targeted to low and high desorbers (point 3). This modification permits to add HE structure while SE and SEDL are already taken into account inside the superstructure.

Figure 16 – Low temperature superstructure of hot water LiBr-H_2O absorption chiller.

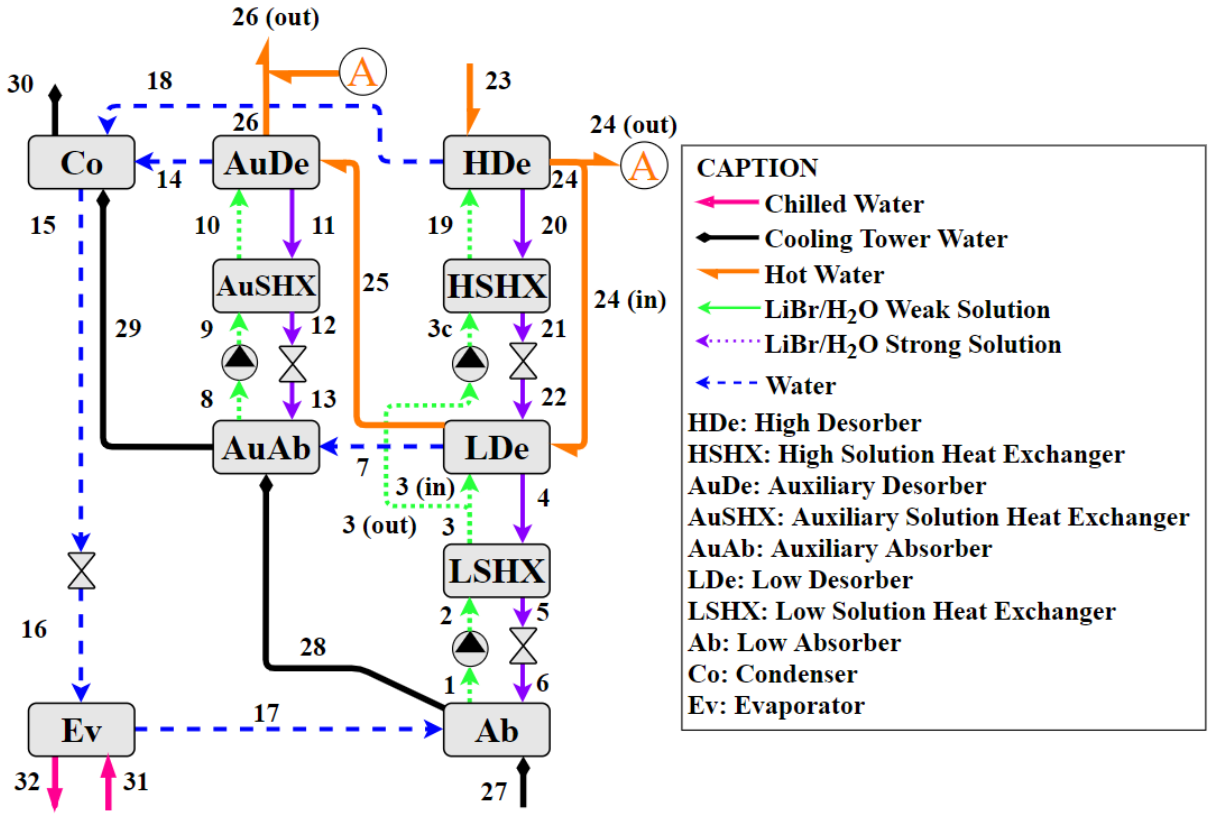

Source: Own Authorship.

It is listed below general assumptions for superstructure modelling of absorption chillers; (i) steady state condition, (ii) adiabatic consideration for all components, (iii) no internal pressure losses for all components, (iv) outlet saturated condition at the mixture for desorber and absorber, and outlet saturated condition for evaporator and condenser,

(v) kinetic and potential energy are negligible, (vi) solution expansion valves are dependent of pressure, temperature and concentration, (vii) cooling tower water is flowing through absorbers and condenser in series, (viii) solution heat exchanger is modeled by using effectiveness method, (ix) crystallization zone is avoided by applying two models from literature, (x) it is assumed constant overall heat transfer coefficients for all components, and (xi) for all water pumps, an isentropic efficiency of 0.8 is assumed.

In Table 1, overall heat transfer coefficients (U_i) are shown as constant values for each component inside the absorption unit.

Table 1 – Overall heat transfer coefficients for each component inside absorption chiller.

Type of Component i	U_i (kW m^{-2} °C^{-1})
Evaporator	1.310
Condenser	2.230
Absorber	1.170
Desorber	1.130
Solution Heat Exchanger	0.130

Source: Adapted from Dixit, Arora and Kaushik (2017).

The cooling water temperatures are defined by cooling tower parameters such as range (5.6°C) and approach (4°C) with ambient site conditions from Appendix D, and hot water inlet temperature (95°C) at the desorber is assumed in accordance with some manufacturers brochure (LG, 2016).

In Figure 17, evaporator produces chilled water for air conditioning purposes, and as previously commented, the temperatures of thermodynamic states at point 31 and 32 are set to 12 and 7°C, respectively. A typical pressure drop of 6 mH_2O in chilled water stream is assumed in accordance with some manufacturers. Regarding the thermodynamic state at point 16, it is considered liquid-vapour condition due expansion valve effect which reduces pressure through an isoenthalpic process. The thermodynamic state at point 17 is assumed saturated vapour condition due the assumption (iv).

Figure 17 – Representation of temperature chart at the evaporator (a) and evaporator heat exchanger with expansion valve (b).

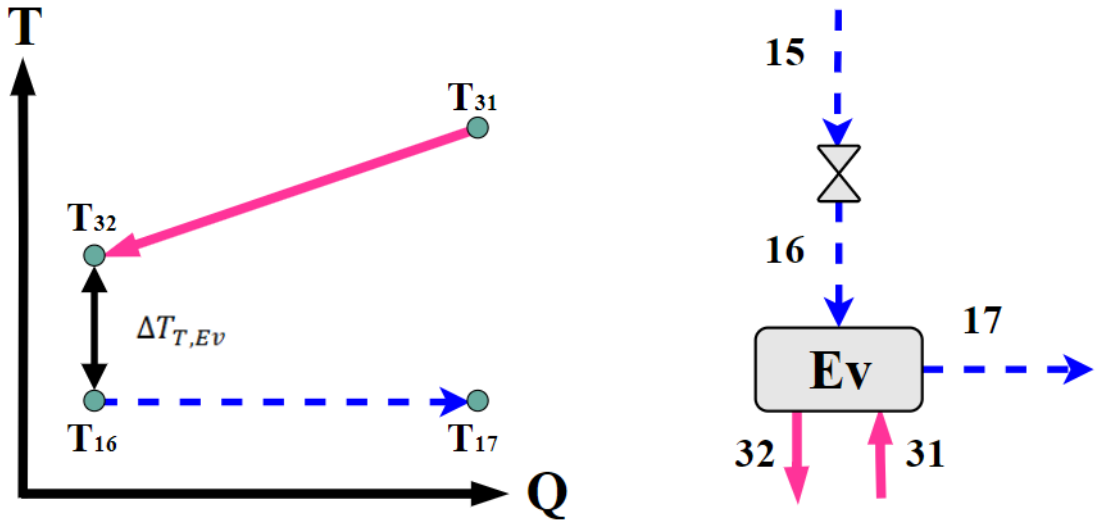

(a) (b)

Source: Own Authorship.

The terminal temperature difference ($\Delta T_{T,Ev}$), as represented in Equation 4.1, is a decision variable and it determines the pressure of the evaporator (p_{Ev}) by using Equation 4.3. Additionally, assumption (iii) allows to set the pressure at point 16 equals to p_{Ev}.

$$\Delta T_{T,Ev} = T_{32} - T_{16} \tag{4.1}$$

$$T_{17} = T_{16} \tag{4.2}$$

$$p_{Ev} = p_{sat}(T_{17}) \tag{4.3}$$

Due assumptions (i), (ii), and (v), the following Equation 4.4 and Equation 4.5 are derived by applying conservation of mass and first law of thermodynamics in the evaporator. In addition, by considering assumption (x) and Equation 4.6 for log mean temperature difference ($\Delta T_{lm,Ev}$) calculation, it is possible to estimate the heat transfer area (A_{Ev}) in Equation 4.7.

$$\dot{Q}_{Ev} = \dot{m}_{16} \cdot (h_{17} - h_{16}) \tag{4.4}$$

$$\dot{Q}_{Ev} = \dot{m}_{31} \cdot (h_{31} - h_{32}) \tag{4.5}$$

$$\Delta T_{lm,Ev} = \frac{(T_{31} - T_{17}) - (T_{32} - T_{16})}{ln\left(\frac{T_{31} - T_{17}}{T_{32} - T_{16}}\right)} \tag{4.6}$$

$$\dot{Q}_{Ev} = U_{Ev} \cdot A_{Ev} \cdot \Delta T_{lm,Ev} \tag{4.7}$$

The temperature chart at the condenser as well as the condenser heat exchanger are represented in Figure 18. In this component, heat rejection to the environment occurs through cooling water. A pressure drop around 2 mH_2O is assumed for cooling water side.

Figure 18 – Representation of temperature chart at the condenser (a) and condenser heat exchanger (b).

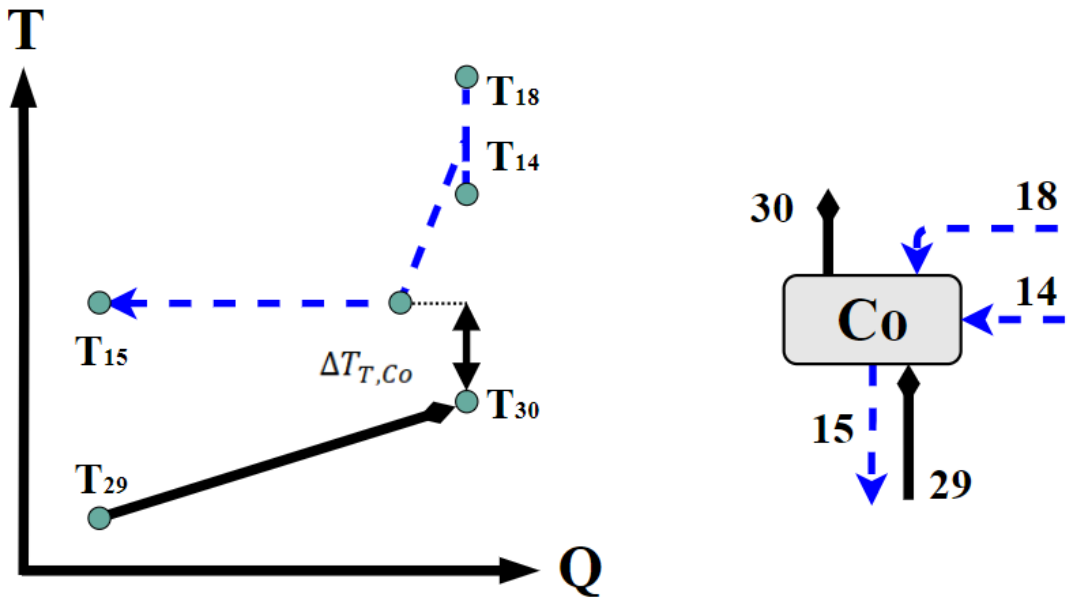

(a) (b)

Source: Own Authorship.

The thermodynamic state at point 30 is defined by the cooling tower parameters such as approach, range and wet-bulb ambient temperature (27.81°C), as represented in Equation 4.8. However, the thermodynamic state at point 29 is calculated by combining the energy balances from all components.

$$T_{30} = T_{wb,amb} + Approach + Range \tag{4.8}$$

With respect to the thermodynamic states at points 14 and 18, two desorbers generate superheated vapour streams which flow directly to the condenser, mixing while entering in this heat exchanger. As stated in Herold, Radermacher and Klein (2016), the thermal energy of superheated vapour could be calculated but more information would be needed. For the sake of simplicity, saturation assumption is considered, approximating the terminal temperature difference ($\Delta T_{T,Co}$) by Equation 4.9.

$$\Delta T_{T,Co} = T_{15} - T_{30} \tag{4.9}$$

Similarly to evaporator and considering assumption (iv), the terminal temperature difference is also a decision variable and it allows to calculate the pressure of the condenser (p_{Co}) by using Equation 4.10. Furthermore, at points 14 and 18, contemplating assumption (iii), the pressures are equal to p_{Co}.

$$p_{Co} = p_{sat}(T_{15}) \tag{4.10}$$

Considering assumptions (i), (ii) and (v), a set of equations that is represented by Equation 4.11 to Equation 4.13 relates the energy balance in the condenser by applying conservation of mass and first law of thermodynamics. Also, by considering assumption (x) and Equation 4.14 for log mean temperature difference ($\Delta T_{lm,Co}$) determination, it is viable to estimate the heat transfer area (A_{Co}) in Equation 4.15.

$$\dot{m}_{15} = \dot{m}_{14} + \dot{m}_{18} \tag{4.11}$$

$$\dot{Q}_{Co} = \dot{m}_{14} \cdot h_{14} + \dot{m}_{18} \cdot h_{18} - \dot{m}_{15} \cdot h_{15} \tag{4.12}$$

$$\dot{Q}_{Co} = \dot{m}_{29} \cdot (h_{30} - h_{29}) \tag{4.13}$$

$$\Delta T_{lm,Co} = \frac{(T_{15} - T_{29}) - (T_{15} - T_{30})}{ln\left(\frac{T_{15} - T_{29}}{T_{15} - T_{30}}\right)} \tag{4.14}$$

$$\dot{Q}_{Co} = U_{Co} \cdot A_{Co} \cdot \Delta T_{lm,Co} \tag{4.15}$$

Other heat exchangers that release heat to the environment through cooling water are low and auxiliary absorbers. These both components receive vapour in different thermodynamic conditions, subsequently, the vapors mix with incoming strong solutions from desorbers and leave as weak solution.

The temperature chart at the low absorber and the flow streams representation are shown in Figure 19.

Figure 19 – Representation of temperature chart at the low absorber (a) and low absorber heat exchanger with low solution pump and solution expansion valve (b).

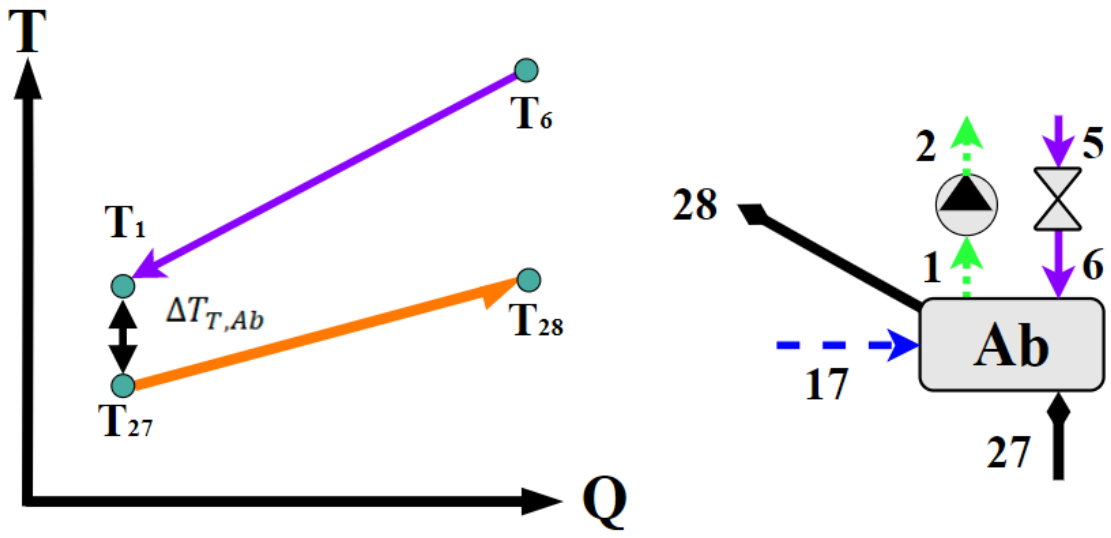

(a) (b)

Source: Own Authorship.

The thermodynamic state of cooling water at point 27 is calculated in function of cooling tower outlet, as represented in Equation 4.16. The efficiency of the cooling water pump is represented as η_p^{CT} whereas the specific volume of the water is described as v_w^{CT}. Also, a pressure drop of 2 mH_2O is adopted for cooling water side.

$$h_{27} - h_{out,w}^{CT} = \frac{v_w^{CT} \cdot (p_{27} - p_{out,w})}{\eta_p^{CT}} \tag{4.16}$$

Due temperature glide on solution side, it is defined the terminal temperature difference ($\Delta T_{T,Ab}$) between temperatures at points 1 and 27, as represented in Equation 4.17. Additionally, it is treated as a decision variable.

$$\Delta T_{T,Ab} = T_1 - T_{27} \tag{4.17}$$

Hence, considering assumptions (iii) and (iv), it is possible to determine the concentration of weak solution at point 1 (x_1) by using Equation 4.19.

$$p_1 = p_6 = p_{17} \tag{4.18}$$

$$p_1 = p_{sat}^{LiBr}(T_1; x_1) \tag{4.19}$$

By applying assumptions (i), (ii) and (v), heat transfer rate on absorber ($\dot{Q}_{Ab}$) is derived from conservation of mass and energy balance, which are represented in Equation 4.20 to Equation 4.22.

$$\dot{m}_1 = \dot{m}_{17} + \dot{m}_6 \tag{4.20}$$

It is important to note here that the lithium bromide mass balance is not executed in this calculation procedure due the over specified number of equations. The lithium bromide mass balance is only accounted at desorbers mass balance, which is discussed posteriorly.

$$\dot{Q}_{Ab} = \dot{m}_{27} \cdot (h_{28} - h_{27}) \tag{4.21}$$

$$\dot{Q}_{Ab} = \dot{m}_{17} \cdot h_{17} + \dot{m}_6 \cdot h_6 - \dot{m}_1 \cdot h_1 \tag{4.22}$$

The log mean temperature difference ($\Delta T_{lm,Ab}$) calculation is represented by Equation 4.23, thus, heat transfer area (A_{Ab}) can be determined through Equation 4.24 since it has considered assumption (x).

$$\Delta T_{lm,Ab} = \frac{(T_6 - T_{28}) - (T_1 - T_{27})}{ln\left(\frac{T_6 - T_{28}}{T_1 - T_{27}}\right)} \tag{4.23}$$

$$\dot{Q}_{Ab} = U_{Ab} \cdot A_{Ab} \cdot \Delta T_{lm,Ab} \tag{4.24}$$

Low solution pump and solution expansion valve are shown in Figure 19. These devices are indispensable to keep the solution streams flowing into the system, basically the low pressure is raised to medium pressure (point 2) through a low solution pump installed at the exit of the absorber (point 1). The power demand at this low solution pump ($\dot{W}_{Lp}$) is practically negligible due low pressure difference. Since pump isentropic efficiency (η_{Lp}) is set 0.6, the following Equation 4.25 and Equation 4.26 are used to determine the temperature at point 2.

$$\dot{W}_{Lp} = \dot{m}_1 \cdot (h_2 - h_1) \tag{4.25}$$

$$\dot{W}_{Lp} = \frac{\dot{m}_1 \cdot v_1 \cdot (p_2 - p_1)}{\eta_{Lp}} \tag{4.26}$$

On the other hand, a solution expansion valve is encountered at absorber inlet (point 6). This device might present flash gas effect in solution stream. Then, a procedure programming code from external library in EES software should be consulted to calculate the temperature and quality (Qu_6) at point 6 assuming an adiabatic process. Furthermore, if it is occurring flash effect through the solution valve, the enthalpy and entropy must be determined by accounting separately each species, H_2O and LiBr.

The LiBr mass fraction in the liquid must be corrected respecting the amount of water that is vaporizing at point 6. Therefore, Equation 4.27 to Equation 4.31 can be used for this purpose.

$$\dot{m}_5^{LiBr} = \dot{m}_5 \cdot x_5 \tag{4.27}$$

$$\dot{m}_6 = \dot{m}_5 \tag{4.28}$$

$$\dot{m}_6^{vapour} = Qu_6 \cdot \dot{m}_6 \tag{4.29}$$

$$\dot{m}_6^{LiBr} = \dot{m}_5^{LiBr} \tag{4.30}$$

$$x_6 = \frac{\dot{m}_6^{LiBr}}{\dot{m}_6 - \dot{m}_6^{vapour}} \tag{4.31}$$

Substituting Equation 4.28, Equation 4.29 and Equation 4.30 in Equation 4.31, it is expressed mass fraction at point 6 as follows:

$$x_6 = \frac{x_5}{1 - Qu_6} \tag{4.32}$$

For calculating enthalpy at point 6, it is used Equation 4.33.

$$h_5 = (1 - Qu_6) \cdot h_6^{LiBr-H_2O} + Qu_6 \cdot h_6^{vapour} \tag{4.33}$$

The same procedure is repeated for entropy determination by Equation 4.34.

$$s_5 = (1 - Qu_6) \cdot s_6^{LiBr-H_2O} + Qu_6 \cdot s_6^{vapour} \tag{4.34}$$

Being aware about crystallization phenomenon after solution expansion valve, it is used a method based on minimum solution enthalpy ($h_{min,i}$) in function of mass fraction (x_i) (ARDEHALI; SHAHRESTANI; ADAMS, 2007), as represented in Equation 4.35.

$$h_{min,i} = -1396.670 + 24 \cdot x_i \tag{4.35}$$

In short, the enthalpy at point 6 must assume higher value than this minimum solution enthalpy to ensure a safe operating zone, avoiding crystallization formation.

In Figure 20, it is shown the temperature chart at the auxiliary absorber and the flow streams representation in this heat exchanger. Also, a pressure drop of 3 mH_2O is adopted in cooling water side.

Figure 20 – Representation of temperature chart at the auxiliary absorber (a) and auxiliary absorber heat exchanger with high solution pump and solution expansion valve (b).

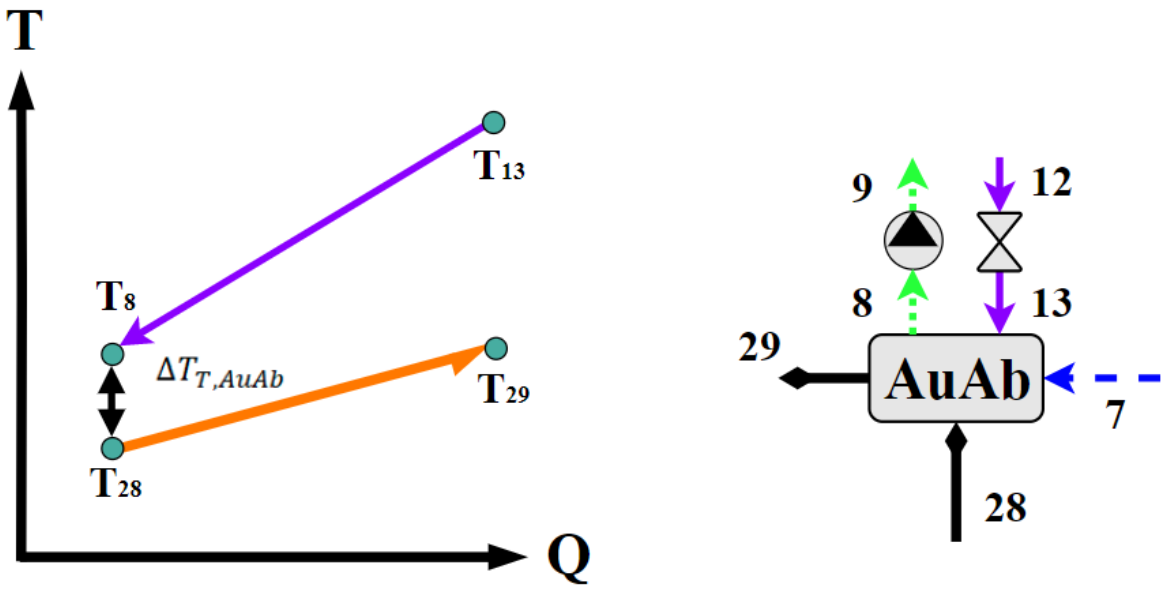

(a) (b)

Source: Own Authorship.

Regarding the auxiliary absorber, the thermodynamic states at points 28 and 29 are calculated by combining the energy balance of all components. The terminal temperature difference at the auxiliary absorber ($\Delta T_{T,AuAb}$) is not enough to determine medium pressure (p_{medium}). In an effort to overcome this issue, medium pressure is treated as decision variable, as represented in Equation 4.36. Thus, the pressures at points 7, 8

and 13 are equal to medium pressure due assumption (iii).

$$p_8 = p_{13} = p_7 = p_{medium} \tag{4.36}$$

The temperature glide on solution side can be seen in Figure 20, thus, the terminal temperature difference is defined as a decision variable to avoid crossed lines between temperatures at points 8 and 28, thus, Equation 4.37 represents this terminal temperature difference at the auxiliary absorber.

$$\Delta T_{T,AuAb} = T_8 - T_{28} \tag{4.37}$$

By considering again assumptions (iii) and (iv), the pressure at the auxiliary absorber outlet (point 8) is defined as saturated liquid solution. Equation 4.38 represents the saturated pressure at the exit of the auxiliary absorber.

$$p_8 = p_{sat}^{LiBr}(T_8; x_8) \tag{4.38}$$

The temperature and concentration at point 8 are determined by a set of equations involving conservation of mass and energy balance in each component that are discussed posteriorly.

By applying assumptions (i), (ii) and (v), heat transfer rate on auxiliary absorber ($\dot{Q}_{AuAb}$) is derived from conservation of mass and energy balance, being represented in Equation 4.39 to Equation 4.41. Furthermore, it is reminded here again that lithium bromide mass balance is not carried out in the auxiliary absorber. The conservations of mass for lithium bromide are all discussed and presented posteriorly at desorbers modelling.

$$\dot{m}_8 = \dot{m}_{13} + \dot{m}_7 \tag{4.39}$$

$$\dot{Q}_{AuAb} = \dot{m}_{28} \cdot (h_{29} - h_{28}) \tag{4.40}$$

$$\dot{Q}_{AuAb} = \dot{m}_7 \cdot h_7 + \dot{m}_{13} \cdot h_{13} - \dot{m}_8 \cdot h_8 \tag{4.41}$$

The log mean temperature difference ($\Delta T_{lm,AuAb}$) calculation is represented by Equation 4.42, thus, heat transfer area (A_{AuAb}) can be determined through Equation 4.43 since it has considered assumption (x).

$$\Delta T_{lm,AuAb} = \frac{(T_{13} - T_{29}) - (T_8 - T_{28})}{ln\left(\frac{T_{13} - T_{29}}{T_8 - T_{28}}\right)} \tag{4.42}$$

$$\dot{Q}_{AuAb} = U_{AuAb} \cdot A_{AuAb} \cdot \Delta T_{lm,AuAb} \tag{4.43}$$

Auxiliary solution pump and auxiliary solution expansion valve are presented in Figure 20. These components are necessary to maintain the solution stream flowing into the system. The isentropic efficiency (η_{Aup}) is assumed around 0.6 and Equation 4.44 and Equation 4.45 depend on solution concentration at point 8 which is not defined yet.

$$\dot{W}_{Aup} = \dot{m}_8 \cdot (h_9 - h_8) \tag{4.44}$$

$$\dot{W}_{Aup} = \frac{\dot{m}_8 \cdot v_8 \cdot (p_9 - p_8)}{\eta_{Aup}} \tag{4.45}$$

In relation to the auxiliary solution expansion valve, the same procedure can be executed for correcting the mass fraction for the amount of water that is vaporizing at point 13. Thus, Equation 4.46 to Equation 4.51 are suggested again for this purpose.

$$\dot{m}_{12}^{LiBr} = \dot{m}_{12} \cdot x_{12} \tag{4.46}$$

$$\dot{m}_{13} = \dot{m}_{12} \tag{4.47}$$

$$\dot{m}_{13}^{vapour} = Qu_{13} \cdot \dot{m}_{13} \tag{4.48}$$

$$\dot{m}_{13}^{LiBr} = \dot{m}_{12}^{LiBr} \tag{4.49}$$

$$x_{13} = \frac{\dot{m}_{13}^{LiBr}}{\dot{m}_{13} - \dot{m}_{13}^{vapour}} \tag{4.50}$$

$$x_{13} = \frac{x_{12}}{1 - Qu_{13}} \tag{4.51}$$

For enthalpy and entropy at point 13, Equation 4.52 and Equation 4.53 are proposed to estimate these properties, respectively.

$$h_{12} = (1 - Qu_{13}) \cdot h_{13}^{LiBr-H_2O} + Qu_{13} \cdot h_{13}^{vapour} \tag{4.52}$$

$$s_{12} = (1 - Qu_{13}) \cdot s_{13}^{LiBr-H_2O} + Qu_{13} \cdot s_{13}^{vapour} \tag{4.53}$$

In auxiliary solution expansion valve, the crystals formation is difficult to occur due low solution concentration. However, it is used a method based on critical solution concentration ($x_{cr,i}$) in function of temperature (T_i) to avert crystallization zone, as represented in Equation 4.54 (GILANI; AHMED, 2015). This methodology is applied to calculate critical concentration at other thermodynamic states, verifying the crystallization formation in each component.

$$x_{cr,i} = 0.0809 \cdot T_i + 61.341 \tag{4.54}$$

In order to ensure none crystallization formation, the solution concentration of each thermodynamic state must have values below critical solution concentration. Nevertheless, it is interesting to discuss that crystallization formation probably occurs at point 6 due high solution concentration combined with low temperature and pressure.

High solution pump and high solution expansion valve follow the same equations and assumptions. The isentropic efficiency (η_{Hp}) is assumed the same of 0.6 and Equation 4.55 and Equation 4.56 depends on solution thermodynamic properties at points 3, 3c and 19 which are not defined yet.

$$\dot{W}_{Hp} = \dot{m}_{out,3} \cdot (h_{3,c} - h_3) \tag{4.55}$$

$$\dot{W}_{Hp} = \frac{\dot{m}_{out,3} \cdot v_3 \cdot (p_{19} - p_3)}{\eta_{Hp}} \tag{4.56}$$

Likewise, the same procedure can be executed for correcting the mass fraction for the amount of water that is vaporizing at point 22. Thus, Equation 4.57 to Equation 4.62 are recommended again for this purpose.

$$\dot{m}_{21}^{LiBr} = \dot{m}_{21} \cdot x_{21} \tag{4.57}$$

$$\dot{m}_{22} = \dot{m}_{21} \tag{4.58}$$

$$\dot{m}_{22}^{vapour} = Qu_{22} \cdot \dot{m}_{22} \tag{4.59}$$

$$\dot{m}_{22}^{LiBr} = \dot{m}_{21}^{LiBr} \tag{4.60}$$

$$x_{22} = \frac{\dot{m}_{22}^{LiBr}}{\dot{m}_{22} - \dot{m}_{22}^{vapour}} \tag{4.61}$$

$$x_{22} = \frac{x_{21}}{1 - Qu_{22}} \tag{4.62}$$

For enthalpy and entropy at point 22, Equation 4.63 and Equation 4.64 are proposed to estimate these properties, respectively.

$$h_{21} = (1 - Qu_{22}) \cdot h_{22}^{LiBr-H_2O} + Qu_{22} \cdot h_{22}^{vapour} \tag{4.63}$$

$$s_{21} = (1 - Qu_{22}) \cdot s_{22}^{LiBr-H_2O} + Qu_{22} \cdot s_{22}^{vapour} \tag{4.64}$$

The power demands at low, auxiliary and high pumps are also almost negligible too, thus, it is important to realize that the power demands in absorption chillers are considerably insignificant.

The next component to be discussed here is the high desorber, as represented in Figure 21.

Figure 21 – Representation of temperature chart at the high desorber (a) and high desorber heat exchanger (b).

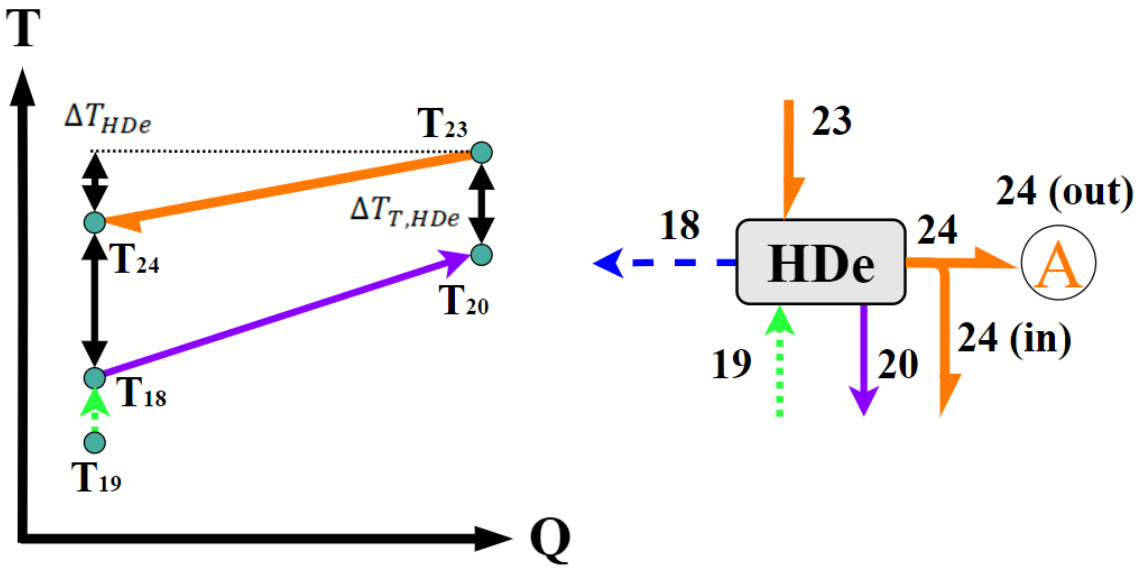

(a) (b)

Source: Own Authorship.

This is the heat exchanger responsible to generate superheated vapour at point 18, which is below ambient pressure, by receiving heat from hot water between points 23 and 24. It is given a hot water temperature at desorber inlet (point 23) of 95°C and a pressure

drop of 1 mH_2O in hot water stream. Furthermore, it can be seen that there is a mass flow rate splitting at point 24, allowing to take out the low desorber from the superstructure. As a consequence, if low desorber does not exist, the auxiliary absorber and the rest of auxiliary components are erased from the superstructure. Therefore, this splitting b_4, as shown in Equation 4.65, is treated as decision variable and by using conservation of mass, as represented in Equation 4.66, it is defined the bypassed mass flow rate ($\dot{m}_{out,24}$).

$$\dot{m}_{in,24} = b_4 \cdot \dot{m}_{24} \tag{4.65}$$

$$\dot{m}_{24} = \dot{m}_{in,24} + \dot{m}_{out,24} \tag{4.66}$$

In this heat exchanger, two more decision variables are temperature difference (ΔT_{HDe}) in hot water stream and terminal temperature difference ($\Delta T_{T,HDe}$), as exposed in Equation 4.67 and Equation 4.68, respectively.

$$\Delta T_{HDe} = T_{23} - T_{24} \tag{4.67}$$

$$\Delta T_{T,HDe} = T_{23} - T_{20} \tag{4.68}$$

An interesting assumption with the thermodynamic behavior of the working fluid in the desorber is regarded with the temperature of thermodynamic state at point 18. Herold, Radermacher and Klein (2016) assume that superheated vapour temperature is in full equilibrium with thermodynamic state of weak solution at point 19. This hypothesis brings a thermodynamic benefit due a temperature glide on the solution side. However, there are other researchers that assume full thermodynamic equilibrium occurring with the strong solution, then, not bringing a thermodynamic benefit.

By contemplating assumptions (iii) and (iv), the strong solution pressure at point 20 (p_{20}) is equal to the pressure of the condenser. Thereupon, it is possible to determine the strong solution concentration (x_{20}) by Equation 4.70.

$$p_{20} = p_{19} = p_{18} = p_{15} \tag{4.69}$$

$$p_{20} = p_{sat}^{LiBr}(T_{20}; x_{20}) \tag{4.70}$$

Following the calculation procedure, using again the assumptions (i), (ii) and (v), it is applied conservation of mass and first law of thermodynamics in the desorber, thus, resulting in Equation 4.71 to Equation 4.74. Repeating the assumption (x), and

Equation 4.75 for log mean temperature difference ($\Delta T_{lm,HDe}$) calculation, it is possible to estimate the heat transfer area (A_{HDe}) in Equation 4.76.

$$\dot{m}_{20} \cdot x_{20} = \dot{m}_{19} \cdot x_{19} \tag{4.71}$$

$$\dot{m}_{19} = \dot{m}_{20} + \dot{m}_{18} \tag{4.72}$$

$$\dot{Q}_{HDe} = \dot{m}_{23} \cdot (h_{23} - h_{24}) \tag{4.73}$$

$$\dot{Q}_{HDe} = \dot{m}_{18} \cdot h_{18} + \dot{m}_{20} \cdot h_{20} - \dot{m}_{19} \cdot h_{19} \tag{4.74}$$

$$\Delta T_{lm,HDe} = \frac{(T_{23} - T_{20}) - (T_{24} - T_{18})}{ln\left(\frac{T_{23} - T_{20}}{T_{24} - T_{18}}\right)} \tag{4.75}$$

$$\dot{Q}_{HDe} = U_{HDe} \cdot A_{HDe} \cdot \Delta T_{lm,HDe} \tag{4.76}$$

The temperature of thermodynamic state at point 19 in weak solution is determined through mass and energy balance by combining all components. The pressure at point 19 is equal to the pressure of the condenser.

In Figure 22, it is represented the temperature chart at the auxiliary desorber and the flow streams representation of this component. It is adopted a pressure drop of 1 mH_2O in hot water stream.

Figure 22 – Representation of temperature chart at the auxiliary desorber (a) and auxiliary desorber heat exchanger (b).

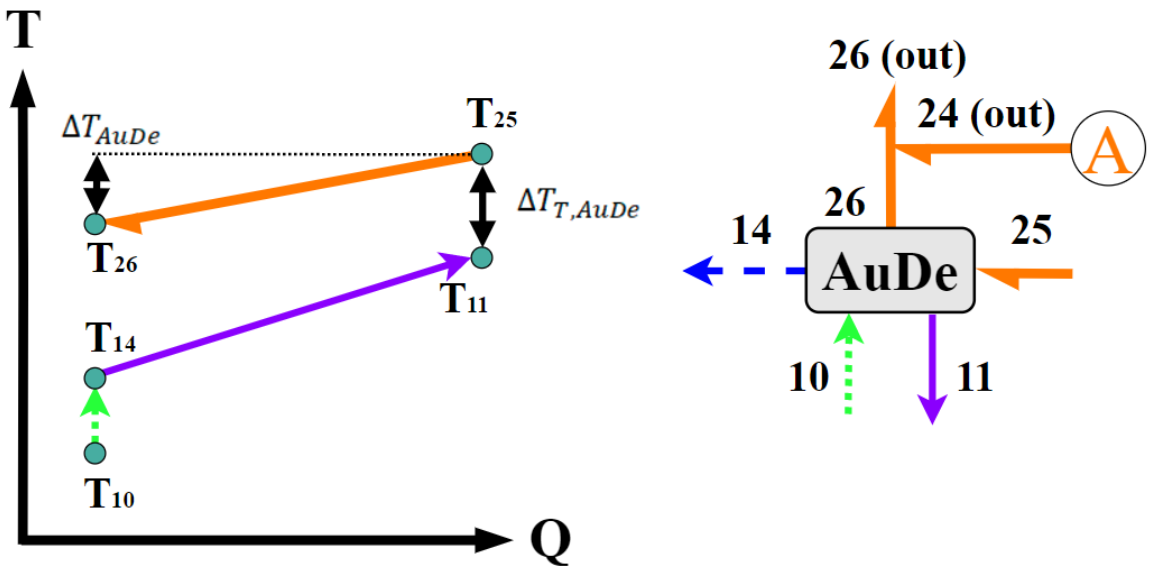

(a) (b)

Source: Own Authorship.

Also, temperature difference (ΔT_{AuDe}) in hot water stream and terminal temperature difference ($\Delta T_{T,AuDe}$) at the auxiliary desorber are considered as decision variables, as it is shown in Equation 4.77 and Equation 4.78, respectively.

$$\Delta T_{AuDe} = T_{25} - T_{26} \tag{4.77}$$

$$\Delta T_{T,AuDe} = T_{25} - T_{11} \tag{4.78}$$

Being mindful that the auxiliary desorber also produces superheated vapour at point 14, as discussed before, the temperature of this thermodynamic state is in equilibrium with weak solution at point 10. Thus, it is repeated all same considerations and equations from high desorber. Additionally, reproducing the same assumptions (iii) and (iv), the following Equation 4.80 determines the strong solution concentration at point 11 (x_{11}).

$$p_{11} = p_{10} = p_{14} = p_{15} \tag{4.79}$$

$$p_{11} = p_{sat}^{LiBr}(T_{11}; x_{11}) \tag{4.80}$$

The heat transfer area (A_{AuDe}) for auxiliary desorber is calculated through Equation 4.86 due same assumption (x) while the heat transfer rate ($\dot{Q}_{AuDe}$) is derived from conservation of mass and energy by contemplating assumptions (i), (ii) and (v), as it is represented by Equation 4.81 to Equation 4.84. The log mean temperature difference ($\Delta T_{lm,AuDe}$) determination is expressed in Equation 4.85.

$$\dot{m}_{11} \cdot x_{11} = \dot{m}_{10} \cdot x_{10} \tag{4.81}$$

$$\dot{m}_{10} = \dot{m}_{11} + \dot{m}_{14} \tag{4.82}$$

$$\dot{Q}_{AuDe} = \dot{m}_{25} \cdot (h_{25} - h_{26}) \tag{4.83}$$

$$\dot{Q}_{AuDe} = \dot{m}_{14} \cdot h_{14} + \dot{m}_{11} \cdot h_{11} - \dot{m}_{10} \cdot h_{10} \tag{4.84}$$

$$\Delta T_{lm,AuDe} = \frac{(T_{25} - T_{11}) - (T_{26} - T_{14})}{ln\left(\frac{T_{25} - T_{11}}{T_{26} - T_{14}}\right)} \tag{4.85}$$

$$\dot{Q}_{AuDe} = U_{AuDe} \cdot A_{AuDe} \cdot \Delta T_{lm,AuDe} \tag{4.86}$$

Similarly to high desorber, the thermodynamic properties of weak solution at point 10 such as temperature is estimated by combining mass and energy balance of all components. Also, the pressure of this weak solution (point 10) is equal to the pressure of the condenser.

The temperature chart at the low desorber and the flow stream representation are presented in Figure 23. In this component, there is an incoming solution stream at point 22 that must be accounted during mass and energy balance.

Figure 23 – Representation of temperature chart at the low desorber (a) and low desorber heat exchanger (b).

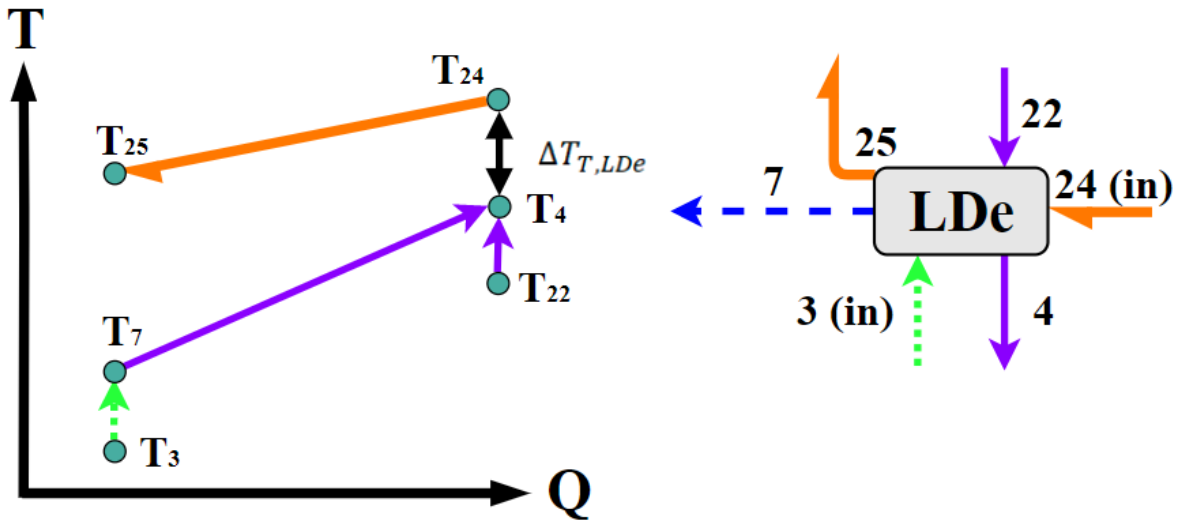

(a) (b)

Source: Own Authorship.

Likewise, low desorber is also discussed here, it has basically the same considerations from high and auxiliary desorbers. Then, a pressure drop of 1 mH_2O is set in hot water stream. As previously commented, superheated vapour at point 7 is in thermodynamic equilibrium with weak solution (point 3).

The temperature difference (ΔT_{LDe}) and terminal temperature difference ($\Delta T_{T,LDe}$) in low desorber are represented by Equation 4.87 and Equation 4.89, respectively. However, only terminal temperature difference in low desorber is set as decision variable.

$$\Delta T_{LDe} = T_{24} - T_{25} \tag{4.87}$$

$$\Delta T_{T,LDe} = T_{24} - T_4 \tag{4.88}$$

In the low desorber, the pressures at points 7, 3 and 4 are equal to the medium pressure due assumption (iii). Adopting assumptions (iii) and (iv) for low desorber, Equation 4.90 determines the strong solution concentration at point 4 (x_4).

$$p_4 = p_3 = p_7 = p_{medium} \tag{4.89}$$

$$p_4 = p_{sat}^{LiBr}(T_4; x_4) \tag{4.90}$$

Once more, by considering assumptions (i), (ii) and (v), the heat transfer rate ($\dot{Q}_{LDe}$) is defined from conservation of mass and first law of thermodynamics, as it is represented by Equation 4.91 to Equation 4.94. Therefore, with assumptions (x), and using log mean temperature difference ($\Delta T_{lm,LDe}$) calculation in Equation 4.95, heat transfer area for low desorber (A_{LDe}) can be estimated through Equation 4.96. The splittings b_3 and b_4 determine the existence of HE or SEDL configurations in the superstructure, respectively. However, only b_4 is treated as decision variable.

$$\dot{m}_{in,3} = b_3 \cdot \dot{m}_3 \tag{4.91}$$

$$\dot{m}_{22} \cdot x_{22} + \dot{m}_{in,3} \cdot x_3 = \dot{m}_4 \cdot x_4 \tag{4.92}$$

$$\dot{Q}_{LDe} = \dot{m}_{in,24} \cdot (h_{24} - h_{25}) \tag{4.93}$$

$$\dot{Q}_{LDe} = \dot{m}_4 \cdot h_4 + \dot{m}_7 \cdot h_7 - \dot{m}_{in,3} \cdot h_3 - \dot{m}_{22} \cdot h_{22} \tag{4.94}$$

$$\Delta T_{lm,LDe} = \frac{(T_{24} - T_4) - (T_{25} - T_7)}{ln\left(\frac{T_{24} - T_4}{T_{25} - T_7}\right)} \tag{4.95}$$

$$\dot{Q}_{LDe} = U_{LDe} \cdot A_{LDe} \cdot \Delta T_{lm,LDe} \tag{4.96}$$

At point 3, after low solution heat exchanger, it is set a splitting b_3 to divide simultaneously weak solution to low and high desorbers. The properties of weak solution (point 3 - in) entering in the low desorber assumes same properties as point 3. Hence, these properties, such as temperature, are determined through a set of equations using conservation of mass and energy balance.

The final components to be mentioned here are three solution heat exchangers and all of them present same objective which is to increase the *COP* by preheating the weak solutions using strong solution streams.

Figure 24 represents the solution heat exchangers for low, medium and high pressures. Using assumption (iii), the pressures are equal for each solution stream.

Figure 24 – Representation of temperature chart at the solution heat exchangers (a) and solution heat exchangers (b).

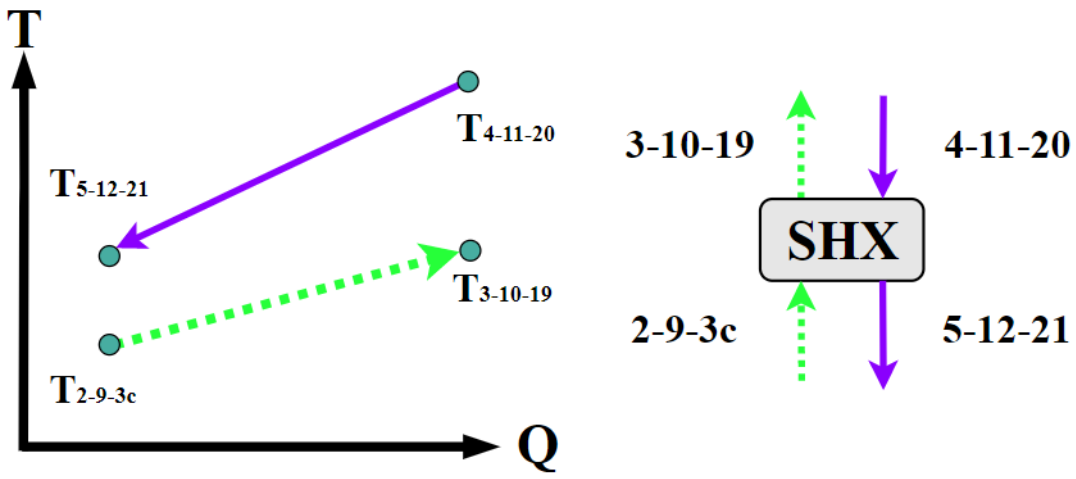

(a) (b)

Source: Own Authorship.

It is assumed that minimum capacitance rate occurs on hot stream (HEROLD; RADERMACHER; KLEIN, 2016). Thus, using effectiveness methodology for each solution heat exchanger, it is defined the following Equation 4.97 to Equation 4.99.

$$\epsilon_{LSHX} = \frac{T_4 - T_5}{T_4 - T_2} \tag{4.97}$$

$$\epsilon_{HSHX} = \frac{T_{20} - T_{21}}{T_{20} - T_{3,c}} \tag{4.98}$$

$$\epsilon_{AuSHX} = \frac{T_{11} - T_{12}}{T_{11} - T_9} \tag{4.99}$$

The effectiveness correlations (ϵ) are important because these variables influence the superstructure parametrically and structurally. For instance, if effectiveness assumes null value, the solution heat exchanger is erased from the superstructure. Otherwise, if it assumes values higher than zero, the solution heat exchanger not only is present inside the superstructure but also assumes parametric characteristic. These effectiveness equations assist to define temperatures at points 3, 3c, 5, 9, 10, 12, 19 and 21.

Repeating the same assumptions (i), (ii), and (v), it is defined through conservation of mass and first law of thermodynamics the Equation 4.100 to Equation 4.105.

$$\dot{Q}_{LSHX} = \dot{m}_2 \cdot (h_3 - h_2) \tag{4.100}$$

$$\dot{Q}_{LSHX} = \dot{m}_4 \cdot (h_4 - h_5) \tag{4.101}$$

$$\dot{Q}_{HSHX} = \dot{m}_{out,3} \cdot (h_{19} - h_{3c}) \tag{4.102}$$

$$\dot{Q}_{HSHX} = \dot{m}_{20} \cdot (h_{20} - h_{21}) \tag{4.103}$$

$$\dot{Q}_{AuSHX} = \dot{m}_9 \cdot (h_{10} - h_9) \tag{4.104}$$

$$\dot{Q}_{AuSHX} = \dot{m}_{11} \cdot (h_{11} - h_{12}) \tag{4.105}$$

The log mean temperature difference ($\Delta T_{lm,LSHX}, \Delta T_{lm,HSHX}, \Delta T_{lm,AuSHX}$) calculations are used again through Equation 4.106 to Equation 4.108.

$$\Delta T_{lm,LSHX} = \frac{(T_4 - T_3) - (T_5 - T_2)}{ln\left(\frac{T_4 - T_3}{T_5 - T_2}\right)} \tag{4.106}$$

$$\Delta T_{lm,HSHX} = \frac{(T_{20} - T_{19}) - (T_{21} - T_{3c})}{ln\left(\frac{T_{20} - T_{19}}{T_{21} - T_{3c}}\right)} \tag{4.107}$$

$$\Delta T_{lm,AuSHX} = \frac{(T_{11} - T_{10}) - (T_{12} - T_9)}{ln\left(\frac{T_{11} - T_{10}}{T_{12} - T_9}\right)} \tag{4.108}$$

Heat transfer area for each solution heat exchanger ($A_{LSHX}, A_{HSHX}, A_{AuSHX}$) can be estimated by considering assumption (x) and using Equation 4.109 to Equation 4.111.

$$\dot{Q}_{LSHX} = U_{LSHX} \cdot A_{LSHX} \cdot \Delta T_{lm,LSHX} \tag{4.109}$$

$$\dot{Q}_{HSHX} = U_{HSHX} \cdot A_{HSHX} \cdot \Delta T_{lm,HSHX} \tag{4.110}$$

$$\dot{Q}_{AuSHX} = U_{AuSHX} \cdot A_{AuSHX} \cdot \Delta T_{lm,AuSHX} \tag{4.111}$$

The thermodynamic states 8, 9, 10, 12, 13, 28 and 29 at auxiliary components are determined by combining mass and energy balance of condenser, absorber, and auxiliary absorber. The thermodynamic states 3, 3c, 19, 21, 22, 5 and 6 at low and high components are calculated by combining mass and energy balance of low desorber, low solution heat

exchanger, low solution expansion valve, high solution pump, high solution heat exchanger, high desorber, and high solution expansion valve. Moreover, the mass flow rates as well as energy fluxes are determined too for each component. Finally, *COP* can be defined as Equation 4.114.

$$\dot{W}_{p,total} = \dot{W}_{Hp} + \dot{W}_{Lp} + \dot{W}_{Aup} \tag{4.112}$$

$$\dot{Q}_{De,total} = \dot{Q}_{HDe} + \dot{Q}_{LDe} + \dot{Q}_{AuDe} \tag{4.113}$$

$$COP = \frac{\dot{Q}_{Ev}}{\dot{Q}_{De,total} + \dot{W}_{p,total}} \tag{4.114}$$

$$\dot{Q}_{Rejection,total} = \dot{Q}_{Co} + \dot{Q}_{AuAb} + \dot{Q}_{Ab} \tag{4.115}$$

The modelling of this superstructure of absorption chillers is not trivial and easy. It took a lot of effort to define each decision variable and what parameters should be used to respect conservation of mass and first law of thermodynamics. Hence, in an effort to guarantee that this superstructure is under the basic conservation laws, Equation 4.116 to Equation 4.118 are applied to certify the obedience of these laws. The value of these metrics ($Error^{Mass}_{Ab,LiBr}$, $Error^{Mass}_{AuAb,LiBr}$, $Error^{Energy}_{System}$) must be always zero.

$$Error^{Mass}_{Ab,LiBr} = \dot{m}_1 \cdot x_1 - \dot{m}_6 \cdot x_6 \tag{4.116}$$

$$Error^{Mass}_{AuAb,LiBr} = \dot{m}_8 \cdot x_8 - \dot{m}_{13} \cdot x_{13} \tag{4.117}$$

$$Error^{Energy}_{Superstructure} = \dot{Q}_{De,total} + \dot{Q}_{Ev} + \dot{W}_{p,total} - \dot{Q}_{Rejection,total} \tag{4.118}$$

The cooling tower, cooling coil, turbocharger, ICE with LT, HT and radiator cooling water, chilled water auxiliary heat exchanger, and exhaust gases heat exchanger are properly exposed at Appendix A, describing in detail the modelling for each equipment.

As the superstructure of absorption chiller is integrated to the W20V34SG engine, there is another decision variable that dictates how much of engine cooling water is used from the Low Temperature (LT) circuit. This decision variable is known as splitting b_5 and it is better presented in section A.4.

Figure 25 shows the entire integration of the superstructure of absorption chillers with the Wärtsilä 20V34SG engine.

Figure 25 – Low temperature superstructure of hot water LiBr-H_2O absorption chiller integrated with Wärtsilä 20V34SG engine.

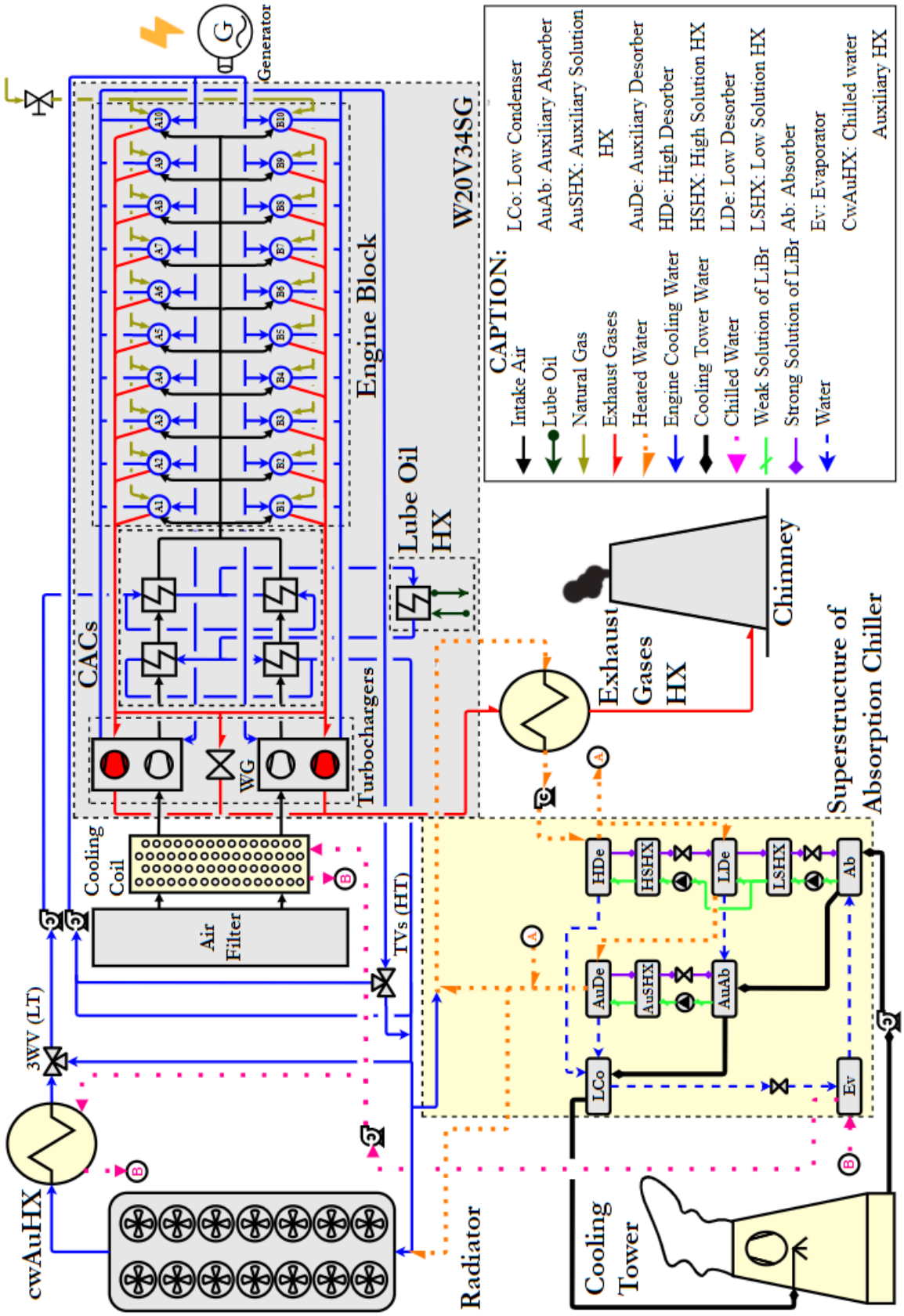

Source: Own Authorship.

4.5 Exergy Analysis

In this section, it is dedicated to apply the second law of thermodynamics in each component. The usage of this law permits to leverage the energy analysis due a better understanding through exergy definition which means energy in its most pure quality (KLEIN; NELLIS, 2012b). When dealing with exergy analysis, it is inevitable to introduce a thermodynamic property known as entropy. In short, it is a measure of the molecular disorder in a system (MORAN et al., 2013). Thereupon, all kind of process escalates the level of disorder, thus, rising entropy generation. As a result, it is followed by an increase of irreversibility during the process.

Comprehending this concept turns out to be a valuable tool to analyse any thermal system. In order to evaluate this entropy generation and how it affects the system, types of processes must be identified e.g. heating, cooling, combustion, mixtures etc. For thermal systems, there are basically two mechanisms that must be investigated for exergy analysis. The first mechanism is physical which depends on temperature and pressure differences, thereupon refereed here as physical exergy (e_{ph}). The second mechanism, known as chemical exergy (e_{ch}), is regarded with the chemical equilibrium of a system at a constant temperature and pressure in a given reference environment (SZARGUT et al., 2015). Equation 4.119 represents the total exergy (e_{total}) into these two exergy terms.

$$e_{total} = e_{ph} + e_{ch} \tag{4.119}$$

It is well known how to treat physical exergy in the literature which can be seen in Equation 4.120. Each thermodynamic state is represented by an index i and T_0 is the reference environment temperature (25°C or 298.15 K at reference pressure of 1 atm).

$$e_{ph} = (h_i - h_0) - T_0 \cdot (s_i - s_0) \tag{4.120}$$

Several researches had carried out exergy analysis of LiBr-H_2O absorption systems in the literature (DIXIT; ARORA; KAUSHIK, 2017; KIM; FERREIRA, 2006; MISRA et al., 2003; MISRA; SAHOO; GUPTA, 2005; PALACIOS-BERECHE; GONZALES; NEBRA, 2012). For LiBr-H_2O chemical exergy evaluation, a methodology from Palacios-Bereche, Gonzales and Nebra (2012) determines the amount of chemical exergy by considering the activity of the constituents and not assuming ideal fluid. The chemical exergy is divided into two parts; standard chemical exergy of pure species (e_{ch}) and exergy destruction due to dissolution process ($e_{ch;dis}$). Equation 4.121 to Equation 4.123 calculate each part in function of standard chemical exergy ($\tilde{\epsilon}^0_{species}$), molar fraction ($y_{species}$), molar mass ($\bar{M}_{sol}$), universal gas constant ($\bar{R}$) and activity of each species ($a_{species}$). With respect to

the calculation of LiBr-H_2O activities as well as other coefficients are presented in detail at Appendix C of section C.1.

$$e_{ch;0} = \frac{1}{\bar{M}_{sol}} \cdot [y_{H_2O} \cdot \tilde{\epsilon}^0_{H_2O} + y_{LiBr} \cdot \tilde{\epsilon}^0_{LiBr}] \tag{4.121}$$

$$e_{ch;dis} = \frac{\bar{R} \cdot T_0}{\bar{M}_{sol}} \cdot [y_{H_2O} \cdot ln(a_{H_2O}) + y_{LiBr} \cdot ln(a_{Libr})] \tag{4.122}$$

$$e_{ch} = e_{ch;0} + e_{ch;dis} \tag{4.123}$$

For cooling coil heat exchanger and cooling tower, chemical compositions on air stream change due to air dehumidification and humidification processes, respectively. Thus, there is chemical exergy that must be accounted during the exergy analysis. Furthermore, fuel with air burning into piston-cylinders provokes chemical reactions, hence, chemical exergy in exhaust gases stream must be accounted during exergy analysis.

For air and exhaust gases streams, the following Equation 4.124 is valid for ideal gases to calculate chemical exergy (e^j_{ch}) in function of chemical molar fractions (y_k), standard reference temperature (T_0), molar mass ($\bar{M}_j$) and universal gas constant ($\bar{R}$). The subscript j refers to air or exhaust gases, while subscript k depends on each species.

$$e^j_{ch} = \frac{\bar{R} \cdot T_0}{\bar{M}_j} \cdot \sum y_k \cdot ln\left(\frac{y_k}{y^e_k}\right) \tag{4.124}$$

The chemical exergy of the fuel ($\dot{E}_f$) is well detailed in Appendix C of section C.2 which discusses properly all calculation procedure for estimating this value. Bearing in mind all these concepts and definitions about exergy analysis, each thermodynamic state can be evaluated in means of exergy flows ($\dot{E}_{total,i}$) by Equation 4.125.

$$\dot{E}_{total,i} = \dot{m}_i \cdot e_{total,i} \tag{4.125}$$

In an effort to analyse each component, an exergy analysis is developed by defining exergy input (Resources), exergy output (Products), and exergy destruction ($\dot{E}_{des}$). Usually, it is understood as exergy input all exergy variation that comes from some available resources to drive the equipment (hot water, fuel, power demand, etc), while exergy output is defined as the desired products (net power, cooling and/or heating loads, etc). For each component, it must be defined carefully what is input and output. Finally, exergy destruction is related to exergy losses and irreversibility of internal process.

Besides that relation, other metrics in terms of exergy can be used for measuring the efficiency of each component. The first metric uses rational exergy efficiency (η_{ex})

by using products and resources, as represented in Equation 4.126. Notwithstanding, for equipment that does not present products, e.g. condenser, absorber, etc. a second metric can be defined by interpreting the exergy efficiency (ξ_{ex}) in terms of total entering exergy flow ($\sum \dot{E}_{entering}$) and total leaving exergy flow ($\sum \dot{E}_{leaving}$), as explicit in Equation 4.127.

$$\eta_{ex} = \frac{Product}{Resource} \tag{4.126}$$

$$\xi_{ex} = \frac{\sum \dot{E}_{leaving}}{\sum \dot{E}_{entering}} \tag{4.127}$$

When evaluating exergy analysis as product and resource, exergy destruction can be expressed into exergy losses ($\dot{L}$) and irreversibility ($\dot{I}$), as shown in Equation 4.128. In Table 2, it is organized the product, resource and exergy efficiency for each component.

$$\dot{E}_{des} = \dot{I} + \dot{L} = Resources - Products \tag{4.128}$$

Table 2 – Defining all product and resource for each component.

Component	Product	Resource	η_{ex}
Evaporator	$\dot{E}_{31} - \dot{E}_{32}$	$\dot{E}_{17} - \dot{E}_{16}$	$\frac{\dot{E}_{31} - \dot{E}_{32}}{\dot{E}_{17} - \dot{E}_{16}}$
Low Desorber	$\dot{E}_7 + \dot{E}_4 - \dot{E}_{in,3} - \dot{E}_{22}$	$\dot{E}_{in,24} - \dot{E}_{25}$	$\frac{\dot{E}_7 + \dot{E}_4 - \dot{E}_{in,3} - \dot{E}_{22}}{\dot{E}_{in,24} - \dot{E}_{25}}$
High Desorber	$\dot{E}_{18} + \dot{E}_{20} - \dot{E}_{19}$	$\dot{E}_{23} - \dot{E}_{24}$	$\frac{\dot{E}_{18} + \dot{E}_{20} - \dot{E}_{19}}{\dot{E}_{23} - \dot{E}_{24}}$
Auxiliary Desorber	$\dot{E}_{14} + \dot{E}_{11} - \dot{E}_{10}$	$\dot{E}_{25} - \dot{E}_{26}$	$\frac{\dot{E}_{14} + \dot{E}_{11} - \dot{E}_{10}}{\dot{E}_{25} - \dot{E}_{26}}$
Low SHX	$\dot{E}_3 - \dot{E}_2$	$\dot{E}_4 - \dot{E}_5$	$\frac{\dot{E}_3 - \dot{E}_2}{\dot{E}_4 - \dot{E}_5}$
High SHX	$\dot{E}_{19} - \dot{E}_{3c}$	$\dot{E}_{21} - \dot{E}_{22}$	$\frac{\dot{E}_{19} - \dot{E}_{3c}}{\dot{E}_{21} - \dot{E}_{22}}$
Auxiliary SHX	$\dot{E}_{10} - \dot{E}_9$	$\dot{E}_{11} - \dot{E}_{12}$	$\frac{\dot{E}_{10} - \dot{E}_9}{\dot{E}_{11} - \dot{E}_{12}}$
Cooling Coil	$\dot{E}^{CC}_{0,a} - \dot{E}^{CC}_{1,a}$	$\dot{E}_{31} - \dot{E}_{32}$	$\frac{\dot{E}^{CC}_{0,a} - \dot{E}^{CC}_{1,a}}{\dot{E}_{31} - \dot{E}_{32}}$
Exhaust gases HX	$\dot{E}^{EHX}_{out,w} - \dot{E}^{EHX}_{in,w}$	$\dot{E}^{ICE}_{out,g} - \dot{E}^{EHX}_{out,g}$	$\frac{\dot{E}^{EHX}_{out,w} - \dot{E}^{EHX}_{in,w}}{\dot{E}^{ICE}_{out,g} - \dot{E}^{EHX}_{out,g}}$
ICE	$\dot{W}_{ICE}$	$\dot{E}_f$	$\frac{\dot{W}_{ICE}}{\dot{E}_f}$

Source: Own Authorship

For dissipative equipment, Equation 4.129 evaluates the irreversibility rate. Each exergy flow as well as exergy efficiency is explicit in Table 3.

$$\dot{I} = \sum \dot{E}_{entering} - \sum \dot{E}_{leaving} \tag{4.129}$$

Table 3 – Defining all exergy flows entering and leaving ($\sum \dot{E}$) for dissipative components.

Component	$\sum \dot{E}$ leaving	$\sum \dot{E}$ entering	ξ_{ex}
Absorber	$\dot{E}_1 + \dot{E}_{28}$	$\dot{E}_{17} + \dot{E}_6 + \dot{E}_{27}$	$\frac{\dot{E}_1 + \dot{E}_{28}}{\dot{E}_{17} + \dot{E}_6 + \dot{E}_{27}}$
Auxiliary Absorber	$\dot{E}_8 + \dot{E}_{29}$	$\dot{E}_7 + \dot{E}_{13} + \dot{E}_{28}$	$\frac{\dot{E}_8 + \dot{E}_{29}}{\dot{E}_7 + \dot{E}_{13} + \dot{E}_{28}}$
Condenser	$\dot{E}_{15} + \dot{E}_{30}$	$\dot{E}_{14} + \dot{E}_{18} + \dot{E}_{29}$	$\frac{\dot{E}_{15} + \dot{E}_{30}}{\dot{E}_{14} + \dot{E}_{18} + \dot{E}_{29}}$
Cooling Tower	$\dot{E}^{CT}_{out,a} + \dot{E}^{CT}_{out,w}$	$\dot{E}^{CT}_{in,a} + \dot{E}_{30} + \dot{W}^{CT}_{fan}$	$\frac{\dot{E}^{CT}_{out,a} + \dot{E}^{CT}_{out,w}}{\dot{E}^{CT}_{in,a} + \dot{E}_{30} + \dot{W}^{CT}_{fan}}$
Radiator	$\dot{E}^{rad}_{out,w} + \dot{E}^{rad}_{out,a}$	$\dot{E}^{rad}_{in,w} + \dot{E}^{rad}_{in,a} + \dot{W}^{rad}_{fan}$	$\frac{\dot{E}^{rad}_{out,w} + \dot{E}^{rad}_{out,a}}{\dot{E}^{rad}_{in,w} + \dot{E}^{rad}_{in,a} + \dot{W}^{rad}_{fan}}$
Chilled Water HX	$\dot{E}_{31} + \dot{E}^{cwAuHX}_{out,w}$	$\dot{E}_{32} + \dot{E}^{cwAuHX}_{in,w}$	$\frac{\dot{E}_{31} + \dot{E}^{cwAuHX}_{out,w}}{\dot{E}_{32} + \dot{E}^{cwAuHX}_{in,w}}$
Low SEV	$\dot{E}_6$	$\dot{E}_5$	1 - $\frac{\dot{m} \cdot (p_5 - p_6)}{\dot{E}_5 \cdot \rho_5}$
High SEV	$\dot{E}_{22}$	$\dot{E}_{21}$	1 - $\frac{\dot{m} \cdot (p_{21} - p_{22})}{\dot{E}_{21} \cdot \rho_{21}}$
Auxiliary SEV	$\dot{E}_{13}$	$\dot{E}_{12}$	1 - $\frac{\dot{m} \cdot (p_{12} - p_{13})}{\dot{E}_{12} \cdot \rho_{12}}$
Refrigerant EV	$\dot{E}_{16}$	$\dot{E}_{15}$	$\frac{\dot{E}_{16}}{\dot{E}_{15}}$

Source: Own Authorship

The exergy efficiency for the absorption system can be evaluated by Equation 4.130.

$$\eta^{chiller}_{ex} = \frac{\dot{E}_{31} - \dot{E}_{32}}{\dot{E}_{23} - \dot{E}_{24} + \dot{E}_{in,24} - \dot{E}_{26} + \dot{W}_{p,total}} \tag{4.130}$$

4.6 Economic Model

In consonance with Boehm (1987), there is a simple methodology that evaluates the equipment purchase cost (Z_i) in function of a reference cost ($Z_{ref,i}$), reference parameter ($X_{ref,i}$), equipment coefficient (m_i), and a variable of interest (X_i), as represented in

Equation 4.131. The $X_{ref,i}$ can assume any equipment parameter such as heat transfer area, mass or volume flow rate, heat loads, power, etc.

$$Z_i = Z_{ref,i} \cdot \left(\frac{X_i}{X_{ref,i}} \right)^{m_i} \tag{4.131}$$

Other researchers also use the same purchase cost equation but with different parameters and coefficients (BEJAN; TSATSARONIS; MORAN, 1996). This simple method allows to determine the purchase cost for any equipment. Hence, all purchase costs of the components inside the new thermal system are calculated by analysing each variable of interest and a set of coefficients for each equipment.

For cooling tower cost evaluation, Boehm (1987) suggests a correction procedure for the purchase cost in function of three correcting factors ($CF_{Approach}$, CF_{Range}, CF_{wb}) which depends on three essential parameters; range, approach and wet-bulb temperature. These correcting factors are presented as curve fittings in Equation 4.132 to Equation 4.134. It is imperative to correct the purchase cost due the sensible influence of each parameter on cooling tower sizing (HENSLEY, 1983). Therefore, Equation 4.135 can be used to calculate the corrected purchase cost of cooling tower ($Z_{CT,Corr}$).

$$CF_{Approach} = 2.19254 - 0.694264 \cdot ln(Approach) \tag{4.132}$$

$$CF_{Range} = 0.451601 \cdot Range^{0.466733} \tag{4.133}$$

$$CF_{wb} = 4.34408 - 1.06326 \cdot ln(T_{wb,amb}) \tag{4.134}$$

$$Z_{CT,Corr} = CF_{Approach} \cdot CF_{Range} \cdot CF_{wb} \cdot Z_{CT} \tag{4.135}$$

In addition, water distribution, pumps and civil foundation are unavoidable for cooling tower operation, then, Boehm (1987) presents a set of data to evaluate these additional costs in cooling tower application.

Regarding the absorption chillers cost evaluation, there are three works that determined the purchase costs of all components inside an absorption machine by applying the same equation from Boehm (1987) (MISRA et al., 2003; MISRA; SAHOO; GUPTA, 2005; DIXIT; ARORA; KAUSHIK, 2017).

Misra et al. (2003) extracted the reference costs from Christian (1977) and used Marshall & Swift economic indexes to correct these costs to year 2000. For pumps and electric motors, it is consulted another study that evaluates the purchase costs of these

small components by considering the efficiency and input power demand (D'ACCADIA; ROSSI, 1998). The following Equation 4.136 and Equation 4.137 are expressed in function of electric motor and pump reference costs ($Z_{ref,i}$), power demands ($\dot{W}_i$), reference power demands ($\dot{W}_{ref,i}$), efficiencies (η_i), and equipment coefficients (m_i and n_i). The pump efficiency for absorption chiller is defined as 0.6 while for electric motor efficiency, it is considered around 0.95.

$$Z_p = Z_{ref,p} \cdot \left(\frac{\dot{W}_p}{\dot{W}_{ref,p}}\right)^{m_p} \cdot \left(\frac{\eta_p}{1-\eta_p}\right)^{n_p} \tag{4.136}$$

$$Z_{em} = Z_{ref,em} \cdot \left(\frac{\dot{W}_{em}}{\dot{W}_{ref,em}}\right)^{m_{em}} \cdot \left(\frac{\eta_{em}}{1-\eta_{em}}\right)^{n_{em}} \tag{4.137}$$

For all components, the reference costs ($Z_{ref,i}^{Actual}$) are updated through Equation 4.138 by consulting economic indexes from Chemical Engineering Plant Cost Index (CEPCI), as it can be seen in Table 4.

$$Z_{ref,i}^{Actual} = Z_{ref,i}^{Before} \cdot \frac{CI_i^{Actual}}{CI_{ref,i}^{Before}} \tag{4.138}$$

Table 4 – Cost index from CEPCI until final September of 2019.

Year	Cost Index
1987	323.8
1997	386.5
2000	394.1
2016	541.7
2017	562.1
2018	591.3
2019	594.9

Source: Vatavuk (2001) and CEPCI (2019)

The economic methodology that is used to update the reference costs might not represent the real value of each component due the technological improvements of each equipment along the years, affecting drastically the purchase cost. Then, it must be noted that this economic model is an approximation and must be compared to real costs.

Table 5 represents the main equipment parameters such as reference purchase costs, component coefficients, variables of interest and the operating ranges that are used for economic evaluation. Therefore, it is determined the purchase cost of each component inside the superstructure of absorption chillers integrated with one ICE, cooling coil, cooling tower, chilled water auxiliary heat exchanger, and exhaust gases heat exchanger.

Table 5 – Reference parameters of all components.

Type of Component i	$Z_{ref,i}$ (US$)	m_i	n_i	$X_{ref,i}$	Range
Evaporator	24,152.00	0.6	–	100	$2 \leftrightarrow 2000$ m^2
Condenser	12,076.00	0.6	–	100	$2 \leftrightarrow 2000$ m^2
Absorber	24,907.00	0.6	–	100	$2 \leftrightarrow 2000$ m^2
Desorber	26,417.00	0.6	–	100	$2 \leftrightarrow 2000$ m^2
Solution HX	18,114.00	0.6	–	100	$2 \leftrightarrow 2000$ m^2
Solution pump	3,170.00	0.26	0.5	10 kW	-
Electric motor	755.00	0.87	1.0	10 kW	-
Cooling Coil	15,875.00	0.6	–	280	$20 \leftrightarrow 2000$ m^2
Cooling Tower	128,607.00	1.0	–	10	$4 \leftrightarrow 60$ m^3 min^{-1}
Cooling Water Distribution	293,959.00	0.7	–	1.0	$0.1 \leftrightarrow 2$ m^3 s^{-1}
Chilled Water Auxiliary HX	38,582.00	0.71	–	100	$2 \leftrightarrow 2000$ m^2
Exhaust gases HX	1745	0.45	–	1	$200 \leftrightarrow 1500$ kW

Source: Adapted from Boehm (1987), D'accadia and Rossi (1998) and Misra et al. (2003).

After determining the purchase cost of each component inside the absorption unit, the total chiller cost ($Z_{total,chiller}$) can be calculated by summing all costs. Subsequently, it is multiplied by an expansion factor ($F_{exp,chiller}$) due other indirect and direct costs. Castillo et al. (2007) presented an installation factor of 3.73 for absorption chiller but in this master's thesis, it is executed an expansion process. Due to this reason, by consulting two typical values of 6.32 and 4.16 for installation and expansion factors, respectively (BEJAN; TSATSARONIS; MORAN, 1996), a proportional calculation gives an expansion factor for absorption chillers around 2.45519. Therefore, the total cost of investment (TCI) can be estimated by Equation 4.139.

$$TCI_{exp} = F_{exp,chiller} \cdot (Z_{total,chiller} + Z_{cwAuHX} + Z_{CC} + Z_{EHX}) + Z_{CT,WD} + Z_{CT,corr} \quad (4.139)$$

In order to estimate the total cost rate ($\dot{Z}_{total}$), Equation 4.140 is extracted from Valero et al. (1994).

$$\dot{Z}_{total} = \dot{Z}_{system} + \dot{Z}_{main} = \frac{TCI_{exp} \cdot CRF + TCI_{exp} \cdot CRF \cdot (\phi_{main} - 1)}{n_{ope}} \quad (4.140)$$

The capital recovery factor (CRF) can be estimated by using Equation 4.141, as follows.

$$CRF = \frac{i_{eff} \cdot (1 + i_{eff})^{20}}{(1 + i_{eff})^{20} - 1} \quad (4.141)$$

Table 6 summarizes the necessary information about effective interest rate (i_{eff}), maintenance coefficient (ϕ_{main}) and number of operating hours (n_{ope}).

Table 6 – Data for estimating total cost rate.

Parameters	Values
i_{eff} (%)	15.0
ϕ_{main}	1.060
n_{ope} (h)	8409.6

Source: Valero et al. (1994) and UTE LORM.

For the operating cost rate ($\dot{Z}_{ope}$), as represented in Equation 4.142, it is related to electrical power demands at the cooling tower fan and for each electrical motor coupled to a pump in the chilled, cooling and hot water circuits, including also absorption chiller pumps. The CVU is represented as the variable cost per unit, and its value is 210 R\$ MWh^{-1} (US\$ 1.00 $\approx$ R\$ 5.38).

$$\dot{Z}_{ope} = CVU \cdot \sum \dot{W}_{ele}^{em} \tag{4.142}$$

Table 7 presents some literature data for evaluating the power demand and electric power consumption for pumps and fan.

Table 7 – Parameters for pumps in water circuits and fan at the cooling tower.

Parameters	Values
$\eta_{w,p}$ (%)	80.0
η_{fan}^{CT} (%)	75.0
η_{em} (%)	95.0
Δp_{fan}^{CT} (kPa)	0.1961

Source: Adapted from Threlkeld (1970).

The profit ($\dot{P}_{LORM}$) is treated as an objective function taking into account economical revenue rates ($\dot{R}_{ICE}$ and $\dot{R}_{rad}$), total cost rate ($\dot{Z}_{total}$) and operating cost rate ($\dot{Z}_{ope}$) as described in Equation 4.145. Equation 4.143 and Equation 4.144 are used to determine these two benefits by defining the price of fuel (P_f) around 0.026 US\$ kg^{-1} (Annex A), $BSFC_{ref}$ of 167.064 g kWh^{-1}, $\dot{W}_{ref,ele}^{ICE}$ of 8545 kW and fan designing electric power of ($\dot{W}_{ref,ele}^{rad}$) of 77.7 kW.

$$\dot{R}_{ICE} = \dot{W}_{ele}^{ICE} \cdot (CVU - BSFC \cdot P_f) - \dot{W}_{ref,ele}^{ICE} \cdot (CVU - BSFC_{ref} \cdot P_f) \tag{4.143}$$

$$\dot{R}_{rad} = CVU \cdot (\dot{W}^{rad}_{ref,ele} - \dot{W}^{rad}_{ele}) \tag{4.144}$$

$$\dot{P}_{LORM} = \dot{R}_{ICE} + \dot{R}_{rad} - \dot{Z}_{total} - \dot{Z}_{ope} \tag{4.145}$$

For economic feasibility evaluation, four usual economic indicators are commonly applied for judging an engineering project. These indicators are Net Present Value (NPV), Non-Discounted and Discounted Paybacks (NDP and DP) periods, and Internal Rate of Return (IRR) (LAPPONI, 2000). They are estimated by defining a constant operating cash flow (OCF) over 20 years which is shown in Equation 4.146.

$$OCF = (\dot{R}_{ICE} + \dot{R}_{rad} - \dot{Z}_{ope} - \dot{Z}_{main}) \cdot n_{ope} \tag{4.146}$$

Net Present Value is quite useful for evaluating the economic feasibility of the project. If NPV is equal or less than zero, the project must be rejected automatically. Nevertheless, in case of NPV higher than zero, the project turns out to be worthy of investment.

$$NPV = -TCI_{exp} + \sum_{t=1}^{20} \frac{OCF_t}{(1 + i_{eff})^t} \tag{4.147}$$

When determining the Internal Rate of Return, the calculation is simply to equalize the NPV equation to a null value, as explicit in Equation 4.148. Usually, the project is only approved when the IRR is greater than the minimum attractive rate.

$$0 = -TCI_{exp} + \sum_{t=1}^{20} \frac{OCF_t}{(1 + IRR)^t} \tag{4.148}$$

Finally, Non-Discounted Payback period can be calculated simply by applying Equation 4.149. This economic indicator can be used as first approach while evaluating the economic feasibility but it is not enough to make the business decision-making.

$$NDP = \frac{TCI}{OCF} \tag{4.149}$$

Concerning the Discounted Payback period estimation, a cash flow table is used to analyse this economic indicator. As the depreciation over time is taken into account on the calculations, DP period is more reliable than the NDP period. Thus, in the result section, it is shown how to define the DP period.

4.7 Formulation of the Optimization Problem

In this section, an optimization method known as Genetic Algorithm (GA) is used to search the optimal solution for superstructure modelling. Further, the main computational programming interface is EES software which already has a package of optimization tool containing a simple GA approach.

With reference to the GA method, it is basically the definition of Darwin theory with applications for optimization problems, imitating the reproduction, crossover and mutation in nature (GOLDBERG, 1989; PARKINSON; BALLING; HEDENGREN, 2013). In agreement with Goldberg (1989), there are four essential characteristics about using GA; (i) the parameter set is used as a coding, (ii) the optimal searching begins with a population, (iii) it uses information from objective function, and (iv) it is used probabilistic transition rules.

As the GA searches for optimal solutions using evolutionary aspects, Amir (2012) summarizes three main advantages; (i) GA approach is capable to deal with problems that have any level of difficulty (linear or nonlinear, defined on discrete, continuous, or mixed search spaces), searching for an optimal solution while handling any kind of objective functions, (ii) GAs can perform global optimum search due recurrence of evolution operators, and finally, (iii) this method can arrange an adaptability to incorporate with domain-dependent heuristics, making an efficient application for a specific problem.

In this master's thesis, it is considered two distinct objective functions using for each one a single optimization criterion which are chilled water specific cost (US dollar per ton of refrigeration) and gross profit rate (US dollar per hour), respectively. The objective functions are going to define the synthesis and design aspects of the optimal absorption unit. However, only the gross profit defines the integration with W20V34SG engine. The chilled water specific cost only accounts the absorption systems.

When dealing with waste heat recovery applications, it is useful to minimize the specific cost in order to achieve the highest production with lowest investment cost. Moreover, the minimization of the specific cost is producing chilled water without meeting the thermal loads of the cooling coil and chilled water auxiliary heat exchanger.

The gross profit is taking account on all acquisition and operating costs, as well as, the dispatch hours of the thermal power plant and the variable cost per unit of electricity. In addition, the production of chilled water is tied to the thermal loads at the cooling coil and chilled water auxiliary heat exchanger.

The superstructure optimization has 15 decision variables, and each one of them is organized in synthesis and/or design levels of influence. Additionally, Table 8 presents the guesses on attempting to solve the optimization problem as well as the search spaces of each decision variable.

Table 8 – Decision variables for superstructure of absorption chillers integrated with one W20V34SG engine.

Decision variable	Synthesis	Design	1^{st} Guess	2^{nd} Guess	Search space (Bounds)
b_4	√	√	0.5	0.7	$0 \leftrightarrow 1$
b_5	√	√	0.5	0.7	$0 \leftrightarrow 1$
ΔT_{HDe} (°C)	√	√	5.0	7.0	$0 \leftrightarrow 20$
ΔT_{AuDe} (°C)	√	√	15.0	13.0	$0 \leftrightarrow 20$
$\Delta T_{T,AuAb}$ (°C)		√	5.0	6.0	$1 \leftrightarrow 10$
$\Delta T_{T,Ab}$ (°C)		√	5.0	4.0	$1 \leftrightarrow 10$
$\Delta T_{T,Co}$ (°C)		√	2.0	3.0	$1 \leftrightarrow 10$
$\Delta T_{T,Ev}$ (°C)		√	3.0	4.0	$1 \leftrightarrow 10$
$\Delta T_{T,HDe}$ (°C)		√	10.0	8.0	$1 \leftrightarrow 15$
$\Delta T_{T,AuDe}$ (°C)		√	3.0	5.0	$1 \leftrightarrow 18$
$\Delta T_{T,LDe}$ (°C)		√	7.0	9.0	$1 \leftrightarrow 18$
ϵ_{HSHE}	√	√	0.5	0.6	$0 \leftrightarrow 1$
ϵ_{AuSHE}	√	√	0.5	0.7	$0 \leftrightarrow 1$
ϵ_{LSHE}	√	√	0.5	0.4	$0 \leftrightarrow 1$
p_{medium} (bar)		√	0.03	0.035	$p_{17} \leftrightarrow p_{15}$

Source: Own Authorship

The optimization procedures account separately two distinct objective functions; (i) chilled water specific cost ($C_{chiller}$), as explicit in Equation 4.150, and (ii) gross profit ($\dot{P}_{LORM}$), as represented in Equation 4.151, respectively.

$$OF_1 = C_{chiller} + Penalty = \frac{Z_{total,chiller}}{\dot{Q}_{Ev}} + Penalty \tag{4.150}$$

$$OF_2 = \dot{P}_{LORM} - Penalty = \dot{R}_{ICE} + \dot{R}_{rad} - \dot{Z}_{total} - \dot{Z}_{ope} - Penalty \tag{4.151}$$

The *Penalty* variable is in regard with the crystals formation in strong solution at point 6 (absorber inlet). During the optimization procedure, the mass fraction can assume higher values than critical mass fraction, therefore, it is penalized in both objectives functions in an effort to avert the crystallization effect. The convergence criterion for each optimization procedure is set by defining an absolute error of 0.1.

In Figure 26, the optimization logic flowchart is presented for both minimization of the chilled water specific cost and maximization of profit.

Figure 26 – Optimization logic flowchart.

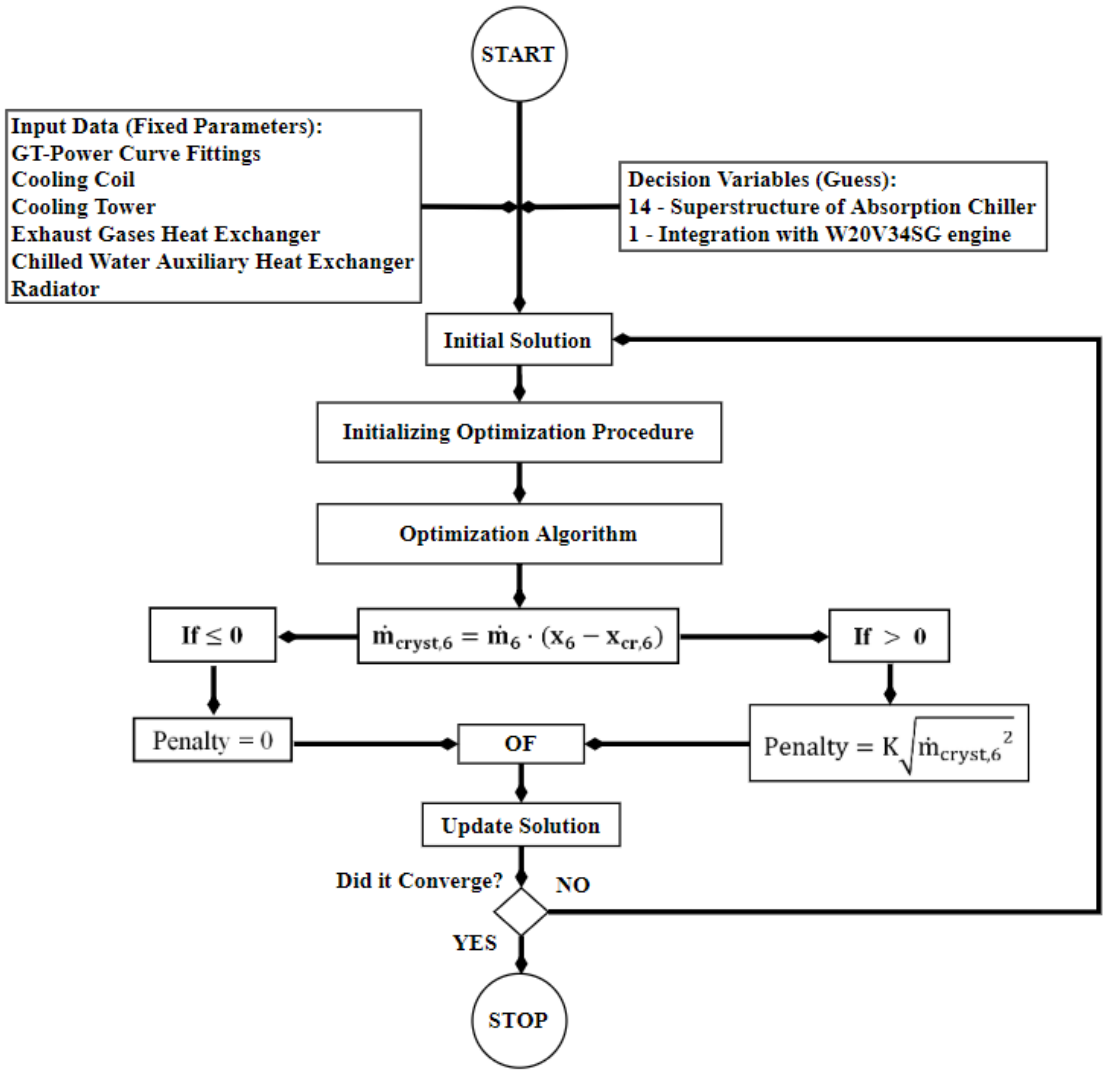

Source: Own Authorship.

The proportional K value is tested during the optimization procedures, and a value of 100 is verified as a good approach in order to converge adequately the optimization procedures.

The GA method from EES is built in a simple coding written by Paul Charbonneau and Barry Knapp at National Center for Atmospheric Research (NCAR), being more specific on FORTRAN-77 optimization subroutine known as PIKAIA (METCALFE; CHARBONNEAU, 2003; METCALFE, 2020; FCHART-EES, 2020). When using this approach, it is required to set the number of individuals, generations and maximum mutation rate, as well as all bounds for each decision variable, as presented in Figure 27.

Figure 27 – GA method in EES optimization package.

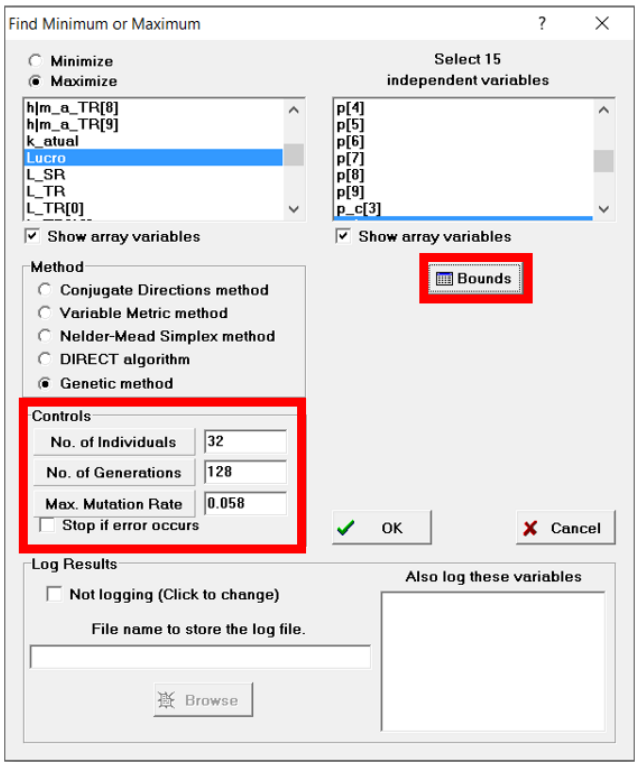

Source: FCHART-EES (2020).

The number of individuals on control setting is defined as 32 while the number of generations is tested for 128 and 256. These values are carefully tested for several trials and errors while optimizing the superstructure modelling. The maximum mutation rate of 0.058 is based on Jong (1975). This GA method from EES software is used to deal with the optimization problem. Notwithstanding, for future works, it might be quite useful to test other optimization methodologies.

5 Results and Discussion

In an effort to discuss properly the results of this master's thesis, three sections are organized to examine each detail of the optimal solutions. Hence, it is firstly presented the optimization results at the section 5.1, secondly, section 5.2 describes a thermodynamic analyses of the optimal solutions. Finally, at the section 5.3, the economic results followed by investment analysis is discussed for the UTE LORM.

Before introducing the results from the optimization problem, it is vital to expose that in this master's thesis the flash effect is neglected at the exit of each solution expansion valve (point 6, 13 and 22). In other words, there are no mass fraction corrections. The reason why it is not developed such corrections regards to unstable mathematical convergences in the external LiBr-H_2O properties functions which need a proper initial guess for each solving procedure (HEROLD; RADERMACHER; KLEIN, 2016; KLEIN; NELLIS, 2012a). The limitation of this simplification implies to treat the solution expansion valves as reversible devices.

There are several academic studies in LiBr-H_2O absorption chillers that did not correct the mass fraction at the exit of solution expansion valves (APRHORNRATANA; EAMES, 1995; DIXIT; ARORA; KAUSHIK, 2017; KAYNAKLI; YAMANKARADENIZ, 2007; MISRA et al., 2003; MISRA; SAHOO; GUPTA, 2005; TALBI; AGNEW, 2000).

The computer machine that is used in this master's thesis has the following settings: ultrabook from LENOVO brand, intel inside core i7, 8 GB of RAM, and 1 hard-disk of 1 TB. The superstructure of absorption chiller integrated with one W20V34SG engine has a total number of 1909 equations with 15 decision variables in EES coding. Regarding the time-consuming, the GA approach from EES optimization package takes an average of 7 hours to process one optimization procedure which has a setting of 128 generations with a population of 32 individuals and maximum mutation rate of 0.058. The superstructure of absorption chiller has a high number of equations as well as a considerable number of decision variables. Hence, the computer machine takes some computational effort to optimize the superstructure.

5.1 Optimization Solutions

A discussion of the results of optimization solutions from both objective functions is presented in detail in this section. Firstly, it is tracked the optimization solution until its optimal convergence for each objective function at the subsection 5.1.1. Subsequently, subsection 5.1.2 presents the values of optimal decision variables for each objective function

as well as an extensive analysis.

5.1.1 Objective Functions

The investigation begins by minimizing the chilled water specific cost of the superstructure of absorption chillers. During the minimization procedures, it is noted that the optimal solutions are reducing the temperature differences at the desorbers to values below 2°C while increasing abruptly the hot water mass flow rate to values above 900 kg s^{-1}. This behavior can be explained by understanding the Table 9, which presents what characteristics each objective function is taking into account during the optimization procedure.

Table 9 – Comparison of each objective function.

Considerations	OF_1 (US$ ton^{-1})	OF_2 (US$ h^{-1})
Power demand of hot water pump		√
Power demand of chilled water pump		√
Power demand of cooling water pump		√
Power demand of the fan at the cooling tower		√

Source: Own Authorship

The chilled water specific cost equation is not considering the amount of power demands from the water pumps in each circuit and the power demand of the fan from cooling tower. This previous analysis allows to understand that the optimization procedures are finding optimal solutions with huge amount of hot water mass flow rate and small temperature differences at the desorbers. In other words, the operating costs from the pumps and fan are not accounted in the minimization procedures.

Despite it is respecting the thermodynamic conservations laws, the great amount of hot water implicates directly in high operating costs and huge piping for each water circuit. In order to avoid this inconvenience, it is decided to minimize the chilled water specific cost under two distinct situations; (i) without any restriction at upper bound of hot water mass flow rate, and (ii) defining a maximum limit of 100 kg s^{-1} at hot water mass flow rate.

The GA method from EES software reaches successfully first local minimum solutions at different generations. When applying the convergence criterion, a few more minimization procedures are needed in order to ensure the lowest minimum value of capital cost per unit of ton for chilled water specific cost.

Table 10 shows the optimal results and the convergence criterion being executed for both first and second guesses under the two distinct situations.

Table 10 – Results of OF_1 (US$ ton^{-1}) until its convergence.

Number of optimization	Without restriction		With restriction	
	1^{st} Guess	2^{nd} Guess	1^{st} Guess	2^{nd} Guess
0	542.7	524.1	542.7	524.1
1	338.5	317.9	370.5	325.2
2	305.4	303.7	333.9	324.1
3	295.3	302.0	320.8	313.3
4	295.3	302.0	318.2	311.7
5	–	–	314.8	311.7
6	–	–	314.8	–

Source: Own Authorship

Figure 28 presents four optimization procedures that are minimizing the chilled water specific cost in function of the number of generations for each guess from Table 8 and under the two distinct situations. Note that the unit of the chilled water specific cost is defined as US dollar per refrigeration ton.

Figure 28 – Four minimization procedures of OF_1.

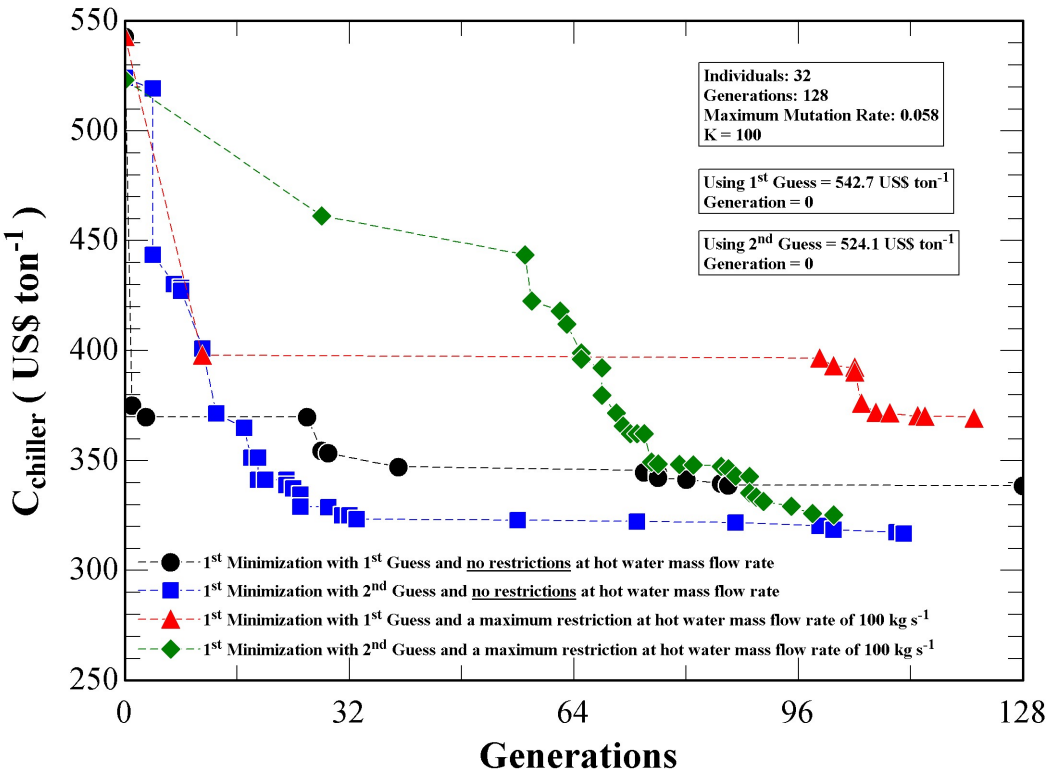

Source: Own Authorship.

The main observation here is about the upper bound restriction of 100 kg s^{-1} at how water mass flow rate. Although this consideration is limiting the minimum solution of OF_1, it is resulting in optimal solutions with more practical engineering meaning. As the hot water is limited by 100 kg s^{-1}, the optimization procedure tries to find a solution without raising abruptly the hot water mass flow rate.

Figure 29 shows the convergence criterion being executed for each minimization procedure. As the minimization of chilled water specific cost is not accounting the operating costs, the optimal results under no restriction are achieving lower values than the optimal solutions under the restriction of 100 kg s^{-1}.

Figure 29 – Minimizing OF_1 until the convergence criterion is satisfied for each guess.

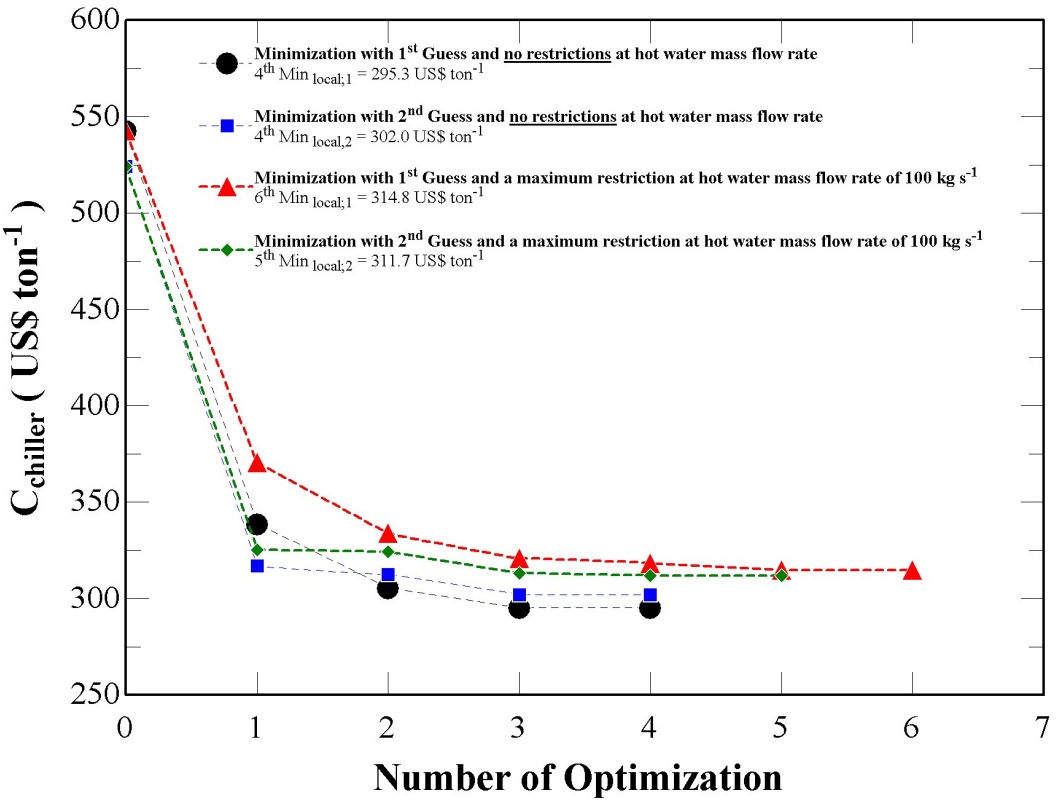

Source: Own Authorship.

In sequence, the maximization of OF_2 is executed by recording the first two optimization procedures in function of the number of generations for each guess from Table 8. For the profit maximization, it is not observed any issue in regard to the hot water mass flow rate, thus, not requiring to limit the upper bound of this calculated parameter.

Table 11 has the optimal results for both first and second guesses while the criterion convergence is equivalently applied for maximizing the OF_2. In this case, the maximization

using second guess reaches a higher value of capital cost per unit of hour than considering the first guess.

Table 11 – Results of OF_2 (US\$ h^{-1}) until its convergence.

Number of optimization	1^{st} Guess	2^{nd} Guess
0	17.8	23.8
1	28.9	29.5
2	29.0	30.5
3	29.4	30.7
4	29.6	30.7
5	30.0	–
6	30.3	–
7	30.3	–

Source: Own Authorship

Figure 30 contains the firsts two local maximum solutions for both distinct guesses at different generations.

Figure 30 – Two maximization procedures of OF_2.

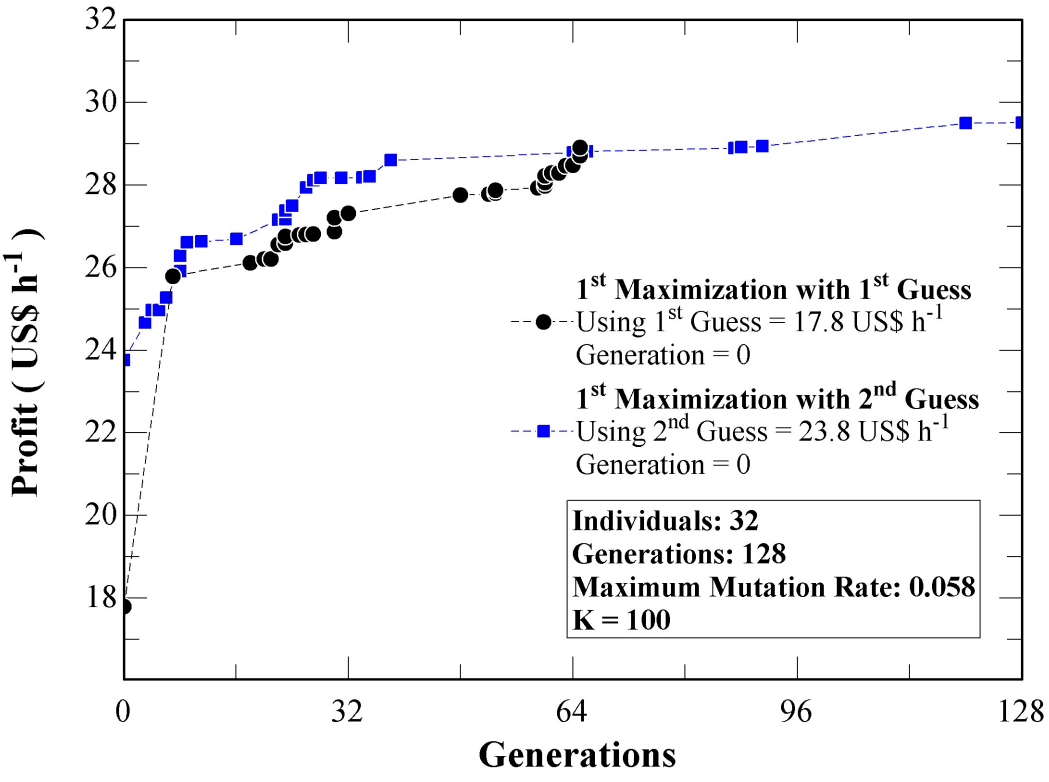

Source: Own Authorship.

Figure 31 shows the convergence criterion being executed for each maximization procedure.

Figure 31 – Maximizing OF_2 until the convergence criterion is satisfied for each guess.

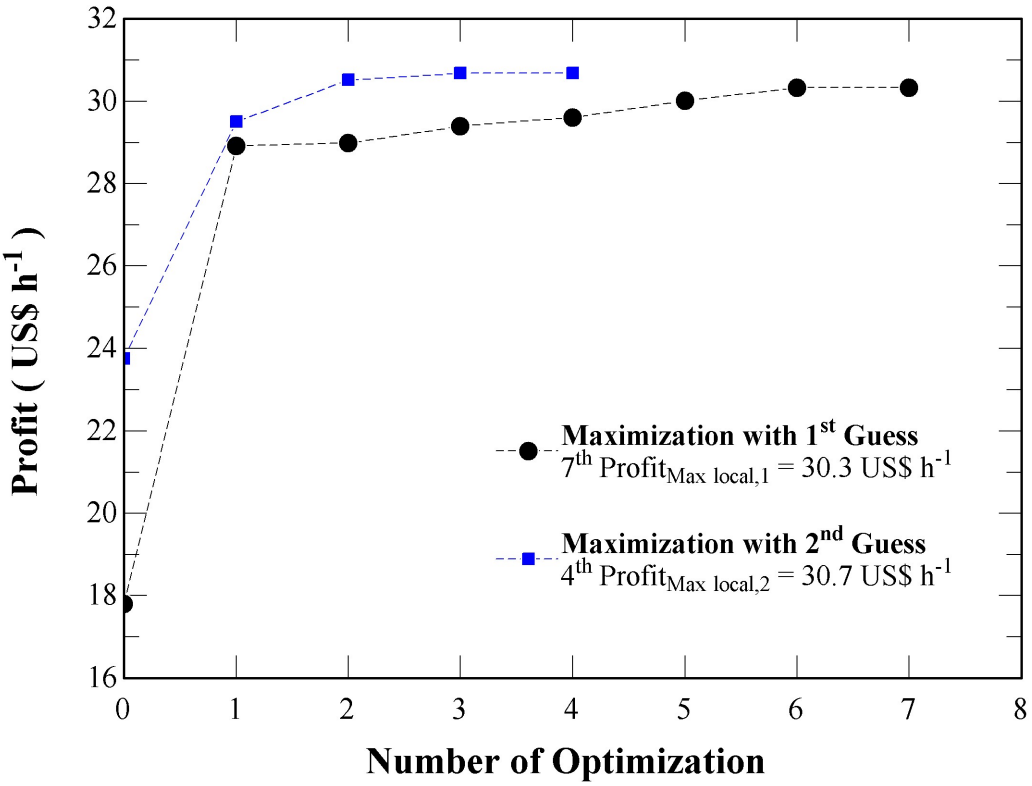

Source: Own Authorship.

5.1.2 Decision Variables

Reminding that there are a total of 15 decision variables, the next results from these optimal solutions regard to the values of each decision variable.

For the sake of simplicity, it is only discussed the best results from both objective functions using each guess from Table 8. Hence, the decision variables in each local minimum solution for chilled water specific cost and each local maximum solution for profit are presented in this subsection.

The optimal decision variables of the minimum optimal solutions using distinct guesses for chilled water specific cost under both different scenarios; non-restricted and restricted hot water mass flow rate, are shown in Table 12. In addition, a comparison between these results is carried out as well as some important calculated parameters are exposed in the same table.

Table 12 – Optimal decision variables for optimal chilled water specific cost.

Decision variable	Without restriction		With restriction	
	4^{th} Min. (1^{st} guess)	4^{th} Min. (2^{nd} guess)	6^{th} Min. (1^{st} guess)	5^{th} Min. (2^{nd} guess)
b_4	0.361	0.725	0.963	1.000
b_5	–	–	–	–
ΔT_{HDe} (°C)	0.000	0.000	0.010	0.002
ΔT_{AuDe} (°C)	1.326	0.858	6.308	6.369
$\Delta T_{T,AuAb}$ (°C)	9.824	7.655	6.866	5.007
$\Delta T_{T,Ab}$ (°C)	3.663	5.358	3.850	3.339
$\Delta T_{T,Co}$ (°C)	6.370	5.544	8.044	6.950
$\Delta T_{T,Ev}$ (°C)	6.670	6.803	6.099	6.810
$\Delta T_{T,HDe}$ (°C)	8.749	3.266	3.107	1.000
$\Delta T_{T,AuDe}$ (°C)	16.139	13.884	16.134	15.719
$\Delta T_{T,LDe}$ (°C)	13.739	14.645	8.750	11.338
ϵ_{HSHX}	0.003	0.062	0.223	0.085
ϵ_{AuSHX}	0.014	0.005	0.003	0.001
ϵ_{LSHX}	0.003	0.011	0.002	0.016
p_{medium} (bar)	0.032	0.030	0.042	0.036
Calculated Parameters	4^{th} Min.	4^{th} Min.	6^{th} Min.	5^{th} Min.
OF_1 (US$ ton^{-1})	295.3	302.0	314.8	311.7
$Z_{total,chiller}$ (US$)	167,326.00	167,433.00	177,142.00	192,859.00
$\dot{Q}_{ev}$ (ton)	566.606	554.412	562.794	618.715
b_3	0.984	0.996	0.997	0.999
ΔT_{LDe} (°C)	1.559	1.048	8.188	8.076
$\dot{m}_{32}$ (kg s^{-1})	94.878	92.836	94.240	103.604
$\dot{m}_{23}$ (kg s^{-1})	1278.491	941.015	92.933	98.638
COP	0.354	0.355	0.363	0.363

Source: Own Authorship

As discussed previously, the minimization procedures that are conducted without restrictions result in huge amounts of hot water ($\dot{m}_{23}$) at the desorbers. These results are not discussed deeply because it does not make sense to evaluate an absorption machine with these great values of hot water mass flow rate. Thus, only the optimization procedures with restriction are discussed in this master's thesis.

With respect to the structural level of the two optimal results from the minimization of chilled water specific cost considering the restriction of 100 kg s^{-1} at hot water circuit, the temperature differences at high desorber (ΔT_{HDe}) are practically nulls (0.010 and 0.002), meaning in non-existence of this component in the final structures. As a result, the high solution heat exchanger plus high solution pump and high expansion valve are erased inside the superstructure. Therefore, the absorption machines result in half-effect configuration as optimal structure. By analysing the splitting b_3, it confirms the half-effect configuration for both optimal structures. The values of 99.7 and 99.9% mean that weak solution at the exit of low solution heat exchanger is flowing directly to low desorber.

Moreover, the effectiveness values of low and auxiliary solution heat exchangers (ϵ_{LSHE} and ϵ_{AuSHE}) are practically zero for both minimum chilled water specific costs, implicating that these components are not necessary. The *COP*s are resulting in equal values of 0.363. The optimal terminal temperature difference of each heat exchanger assumes different value for each optimal solution. Hence, the GA approach can find several combinations between the decision variables for distinct minimum chilled water specific costs.

When analysing the hot water mass flow rate at first and second guesses, it is verified that the restriction is respected, resulting in amounts of 92.933 and 98.638 kg s^{-1}, respectively. The amounts of chilled water are also distinct for each HE structure (92.933 and 98.638 kg s^{-1}), presenting a relative difference of 6.14%. It is interesting to note in these final results that most of the hot water (b_4) is used in the low and auxiliary desorbers for both minimum solutions. As the OF_1 is only dependent on chiller parameters, the decision variable b_5 can be ignored because it is just important when analysing the radiator benefit.

By comparing and evaluating these optimal decision variables from two distinct guesses, lets establish here that the GA method works properly on finding local optimum solutions. Figure 32 presents the final configuration for both minimum chilled water specific costs of 314.8 and 311.7 US$ ton^{-1}.

Figure 32 – HE configuration for both OF_1 of 314.8 and 311.7 US$ ton^{-1}.

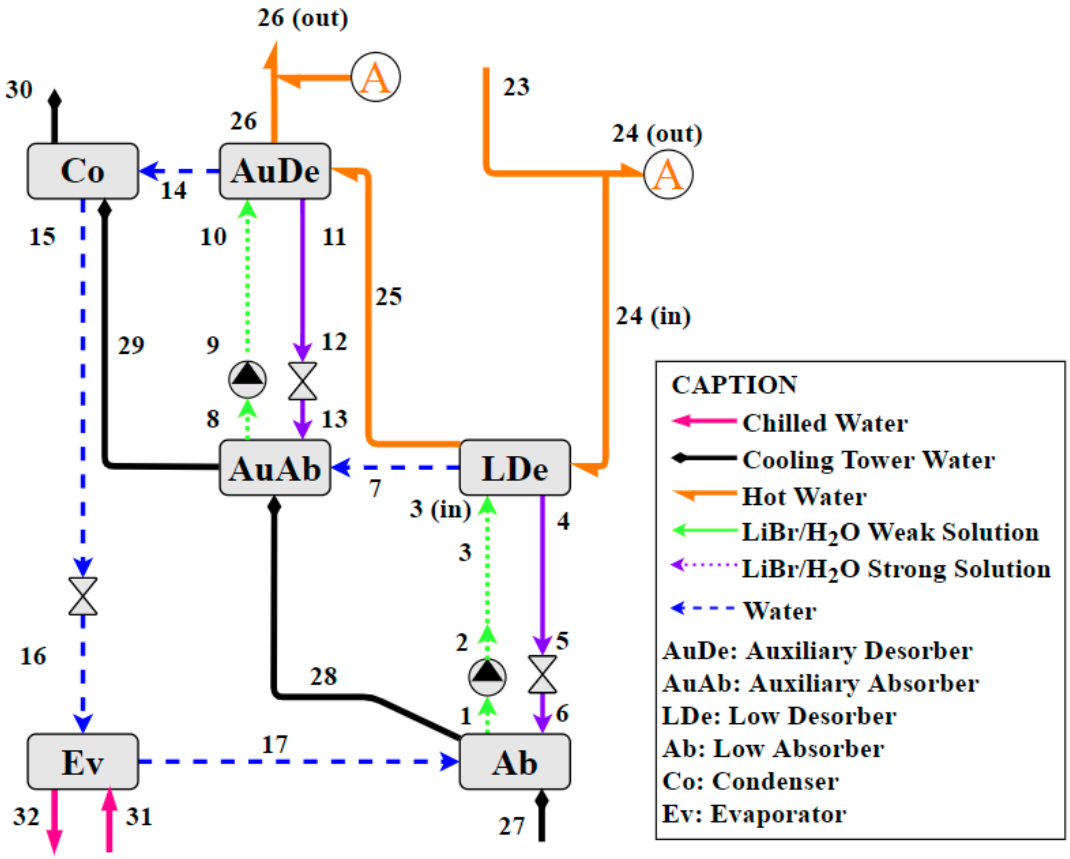

Source: Own Authorship.

As commented previously, it is only discussed the best results of each objective function for each guess from Table 8. Thereupon, for the two optimal profits, Table 13 contains all optimal decision variables.

Lets state here that the superstructure of absorption chillers is now influenced by the radiator benefit during the optimization. Thus, the splitting b_5 must be treated as a decision variable due to its influence on how much of engine cooling water is recovered by the optimal thermal system.

Some extra information are also exposed and analysed in this subsection. For instance, the percentage amounts of chilled water at the cooling coil (b_1), chilled water auxiliary heat exchanger (b_2) and returning hot water at the exhaust gases heat exchanger circuit (b_6) are presented with other calculated parameters.

Table 13 – Optimal decision variables for optimal profit.

Decision variable	7^{th} Maximum (1^{st} guess)	4^{th} Maximum (2^{nd} guess)
b_4	0.072	0.354
b_5	0.999	1.000
ΔT_{HDe} (°C)	16.907	19.694
ΔT_{AuDe} (°C)	0.002	0.001
$\Delta T_{T,AuAb}$ (°C)	5.263	3.798
$\Delta T_{T,Ab}$ (°C)	1.425	1.628
$\Delta T_{T,Co}$ (°C)	1.713	1.888
$\Delta T_{T,Ev}$ (°C)	2.509	1.259
$\Delta T_{T,HDe}$ (°C)	9.440	9.240
$\Delta T_{T,AuDe}$ (°C)	7.232	16.636
$\Delta T_{T,LDe}$ (°C)	4.773	8.952
ϵ_{HSHX}	0.236	0.392
ϵ_{AuSHX}	0.740	0.019
ϵ_{LSHX}	0.000	0.000
p_{medium} (bar)	0.039	0.032
Calculated Parameters	**7^{th} Maximum**	**4^{th} Maximum**
OF_2 (US$ h^{-1})	30.3	30.7
$\dot{R}_{ICE}$ (US$ h^{-1})	51.602	51.602
$\dot{W}_{ICE}$ (kW)	10220	10220
$\dot{W}_{ICE}^{ele}$ (kW)	10016	10016
$\dot{W}_{net}^{ele}$ (kW)	9902.670	9915.384
$BSFC$ (g kWh^{-1})	164.7	164.7
$\dot{R}_{rad}$ (US$ h^{-1})	1.496	1.133
$\dot{W}_{ele}^{rad}$ (kW)	39.380	48.680
N_{rad} (RPM)	689.6	740.2
$T_{in,w}^{rad}$ (°C)	78.1	74.5
$\dot{Z}_{total}$ (US$ h^{-1})	18.340	18.122
$\dot{W}_{total,ope}^{ele}$ (kW)	113.330	100.616
$\dot{Z}_{ope}$ (US$ h^{-1})	4.424	3.927
$C_{chiller}$ (US$ ton^{-1})	331.706	394.331
$Z_{total,chiller}$ (US$)	172,831.00	187,935.00
$\dot{Q}_{ev}$ (ton)	521.037	476.591
b_1	0.457	0.4995
b_2	0.543	0.5005
b_3	0.001	0.1854
b_6	0.599	0.8128
ΔT_{LDe} (°C)	0.173	2.350
$\dot{m}_{32}$ (kg s^{-1})	87.248	79.805
$\dot{m}_{23}$ (kg s^{-1})	38.181	28.177
COP	0.675	0.690

Source: Own Authorship

The profit is optimized for a constant *BMEP* of 23.45 bar, i.e. an increased W20V34SG engine shaft power output generation of 10.220 MW. As the electric generator has an efficiency of 98%, 10.016 MW of electrical energy is delivered to the grid. Furthermore, the repowering application benefits the *BSFC* with a reduction of 2.4 g kWh^{-1}. By defining these two gains, a constant revenue for engine benefit of 51.602 US$ h^{-1} is set as a constant parameter during the optimization. On the other hand, the estimated benefit at the radiator fans depends on its rotational speed, then, the optimization procedure targets to decrease the rotational speed by providing cooling effects on the chilled water auxiliary heat exchanger or/and dropping hot water temperature at the radiator inlet.

The temperature differences on the high desorber are not nulls (16.907 and 19.694°C) for both maximum solutions, presenting a relative difference of 16.48%. Also, splittings b_5 are assuming unit values, implicating that all amount of engine cooling water is heated across the exhaust gases heat exchanger. Then, subsequently, powering the absorption machines. When observing the splittings b_4 (0.072 and 0.354), a majority part of the hot water is by-passed. In addition, by evaluating splittings b_3 (0.001 and 0.1854), the absorption machines have practically none or small amount of weak solution stream entering the low desorber. A comparison involving splittings b_6 (0.599 and 0.8128) allows to analyse that more than 50% of the amount of hot water is flowing to radiator inlet and some quantity of water is returning to exhaust gases heat exchanger.

It is interesting to notice that both optimal solutions of 30.3 and 30.7 US$ h^{-1} are resulting in single-effect absorption chiller as optimal structure in synthesis level. These results can be verified by observing the temperature differences at the auxiliary desorber which are almost null values, implicating in non-existence of all auxiliary components and consequently erasing the low desorber. When analysing the effectiveness values, only the high solution heat exchanger is existing in the final structures. The low solution heat exchanger is also erased due to its null value for both optimal solutions. The optimal terminal temperature difference of each heat exchanger is exposed in Table 13. And again, the GA method can find different combinations between the decision variables for distinct local maximum profits.

The *COP* of SE absorption units are 0.675 and 0.690, which are in accordance with the literature and manufacturer brochure. Regarding the amounts of hot water for both optimal solutions, mass flow rates of 38.181 and 28.177 kg s^{-1} are necessary to power the absorption chillers, showing a relative difference of 26.20%. The chilled water mass flow rate for each maximum profit is 87.248 and 79.805 kg s^{-1}, respectively, presenting a relative difference of 8.53%. As the chilled water temperatures are set 12 and 7°C, these results indeed impact the respective evaporator cooling loads of SE structures which are 521.037 and 476.591 tons. Another important observation regards to chilled water distribution between the cooling coil (b_1) and chilled water auxiliary heat exchanger (b_2), by comparing

both local maximum solutions, the second case uses lesser cooling effect at the chilled water auxiliary heat exchanger. Consequently, saving less energy at the radiator fans.

Concerning the radiator benefits in both optimal solutions from Table 13, it is reached revenues of 1.496 and 1.133 US$ h^{-1} which give fan speeds around 689.6 and 740.2 RPM for SE configurations, respectively. Also, in the first case, evaporator cooling load (521.037 tons) is greater than the second case (476.591 tons), whereas the hot water temperature at the radiator inlet (78.1°C) is higher than the second case (74.5°C).

Other two important metrics that must be observed are the total cost rate ($\dot{Z}_{total}$) and operating cost rate ($\dot{Z}_{ope}$) of the entire system. For first and second cases, the total cost rates involving all equipment are estimated around 18.340 and 18.122 US$ h^{-1} with operating cost rates of 4.424 and 3.927 US$ h^{-1}, respectively. It is verified that the second solution has decreased both metrics in 1.19 and 11.23%, respectively. Figure 33 has a simple interpretation of these two optimal solutions.

Figure 33 – Interpreting the possible optimal solutions: Profit of 30.3 US$ h^{-1} (a) and Profit of 30.7 US$ h^{-1} (b).

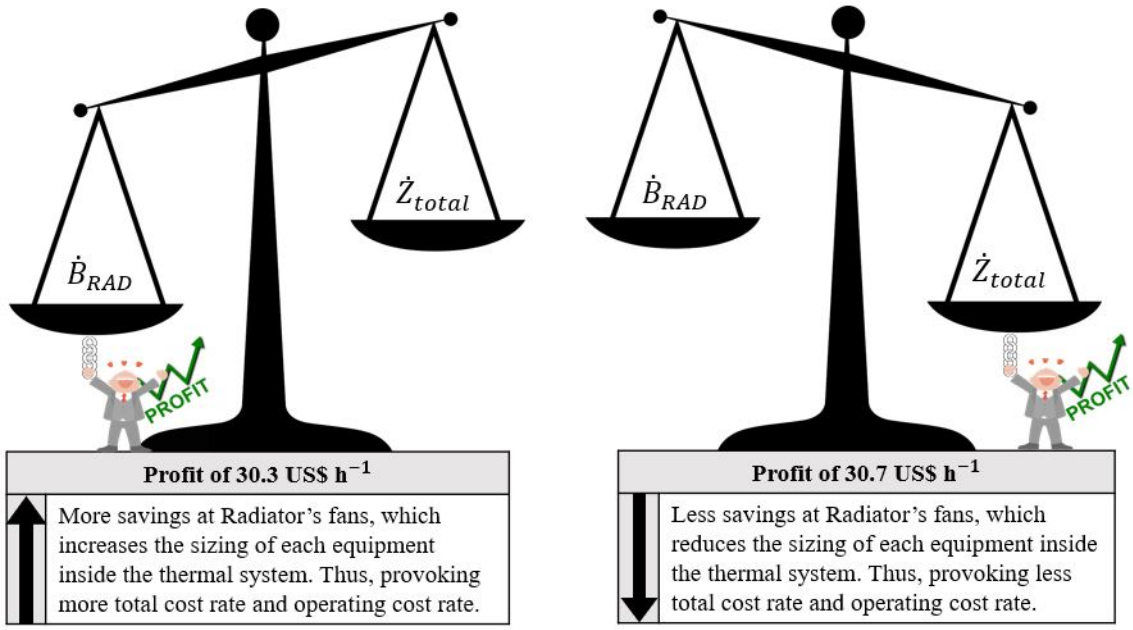

(a) (b)

Source: Own Authorship.

Therefore, as the amount of engine cooling water on radiator is equal for both cases (22.9 kg s^{-1}), the second case reaches highest profit by decreasing the total cost rate instead of saving more energy at the radiator fans.

Besides these results, another comparison that must be explicit here is in regard

with the total chiller cost for each optimal result. For instance, the minimum chilled water specific cost of 311.7 US$ ton^{-1} presents a total cost of US$ 192,859.00. For the maximum profits of 30.3 and 30.7 US$ h^{-1}, the total chiller costs are US$ 172,831.00 and US$ 187,935.00, respectively. Then, it is estimated the chilled water specific cost for each maximum profit. These results are graphically exposed in function of chilled water mass flow rate, as shown in Figure 34.

Figure 34 – Representing four chilled water specific costs in function of $\dot{m}_{32}$.

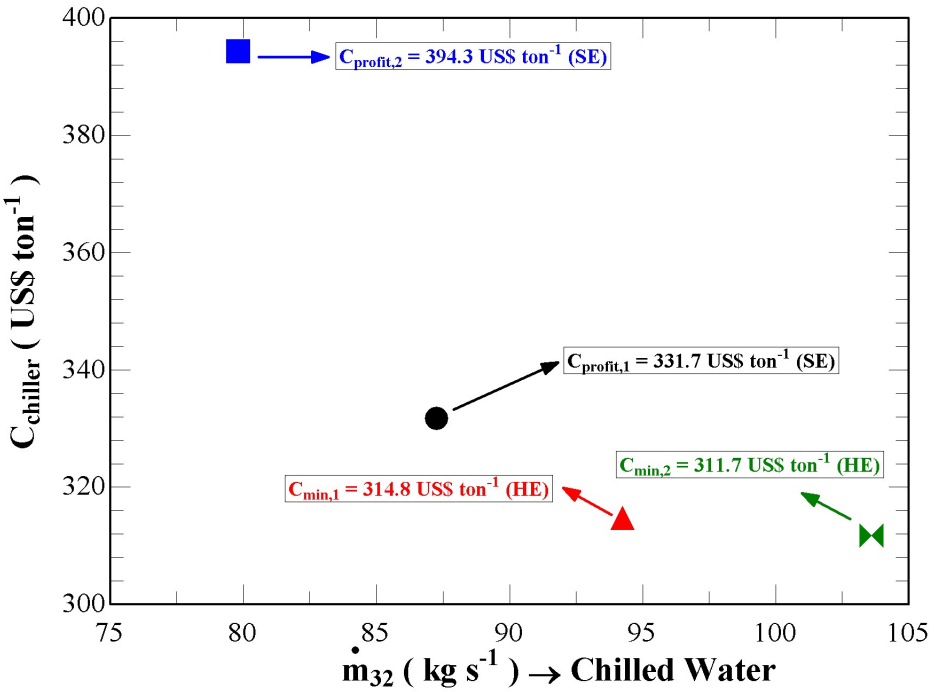

Source: Own Authorship.

A curious behavior is noticed here, the profit maximizations produce lesser chilled water mass flow rates than the chilled water specific cost minimizations. Additionally, the calculated value of the chilled water specific cost for each maximum profit are more expensive.

At last, as we have been discussing deeply the influences of the optimal decision variables as well as of some calculated parameters in the optimal structures, it is vital to present the final SE chiller integrated to one W20V34SG engine and its other equipment. Figure 35 shows the optimal route, while a schematic representation of this respective integration between the SE absorption chiller with W20V34SG engine is shown in Figure 36.

Figure 35 – Optimal route on the superstructure representation of absorption chiller integrated to one W20V34SG engine.

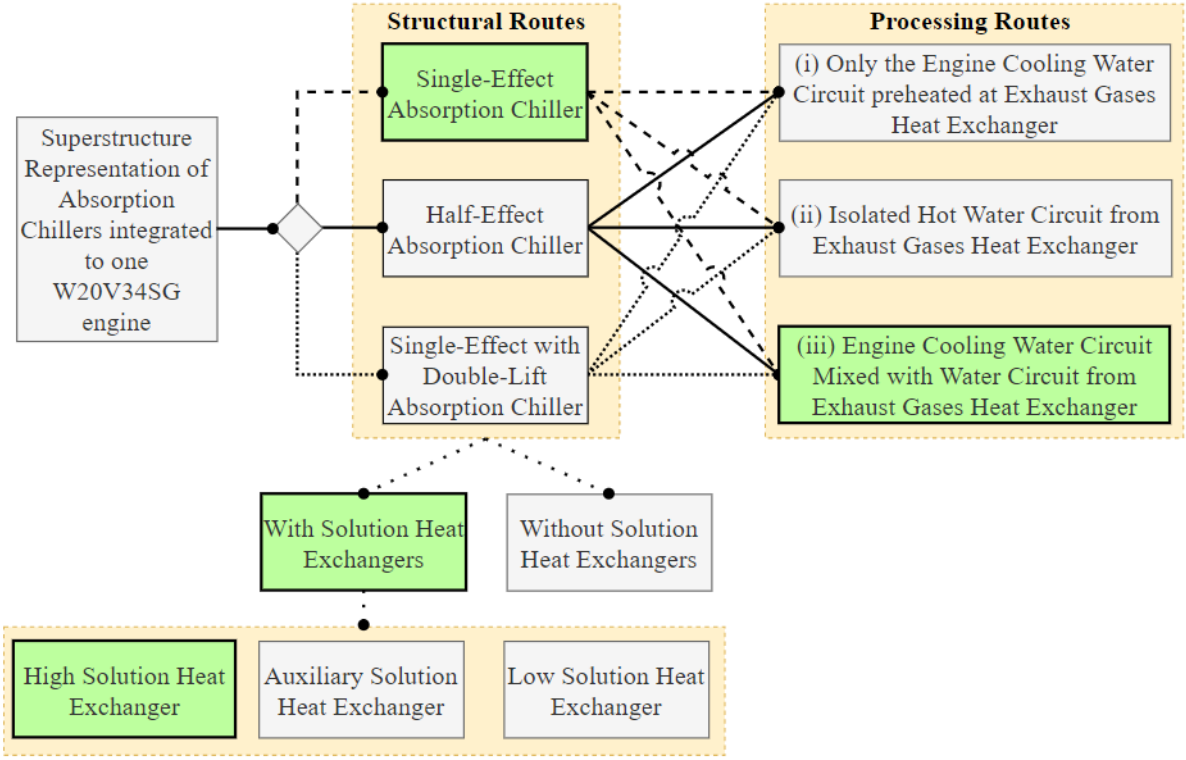

Source: Own Authorship.

From the superstructure optimization perspective, the main result regards to local maximum profit of 30.7 US$ h^{-1} which presents as main optimal configuration in synthesis level the SE chiller with high solution heat exchanger in its structure while integrated to engine cooling water circuit.

Figure 36 – SE configuration for OF_2 of 30.3 and 30.7 US$ h^{-1}.

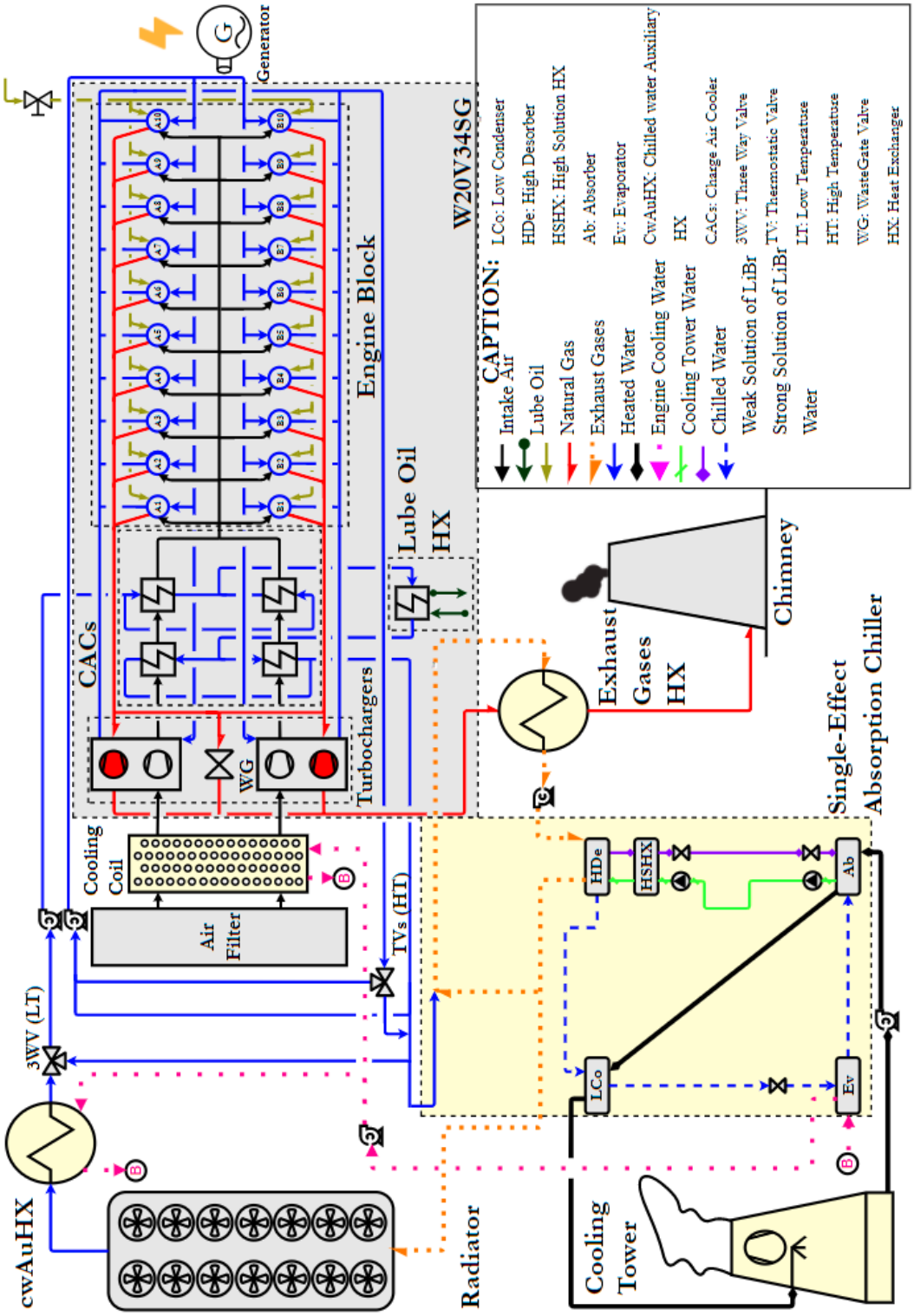

Source: Own Authorship.

5.2 Thermodynamics

Concerning an evaluation of thermodynamic principles in the optimal solutions, the first and second law of thermodynamics in each equipment are applied. All results are well detailed and criticized here, the comprehension of each thermodynamic law is fundamental to ensure a reliable discussion, thereby, this section is dedicated to expose each component in means of energy and exergy analyses.

A comparison involving only the minimum chilled water specific cost (OF_1) of 311.7 US$ ton^{-1} and maximum profit (OF_2) of 30.7 US$ h^{-1} are discussed in this section. Each heat exchanger, expansion valve and pump are presented in an effort to understand thermodynamically what are the differences between them.

The application of the first law of thermodynamics evaluates energy flows such as work and heat for each equipment. As the superstructure modelling of absorption chillers is developed based on energy balances, no matter what the circumstances it must obey the first law.

Table 14 presents three fundamental metrics ($Error^{Mass}_{Ab,LiBr}$, $Error^{Mass}_{AuAb,LiBr}$ and $Error^{Energy}_{Chiller}$) resulting practically in nulls values, hence, guaranteeing that both HE and SE optimal structures are under conservation of mass and energy.

Table 14 – Validating conservation of mass and energy in each absorption chiller.

Metric	Min OF_1 (US$ ton^{-1})	Max OF_2 (US$ h^{-1})
	311.7	30.7
	HE	SE
$Error^{Mass}_{Ab,LiBr}$ (kg s^{-1})	0	0
$Error^{Mass}_{AuAb,LiBr}$ (kg s^{-1})	0	0
$Error^{Energy}_{Chiller}$ (kW)	0	0

Source: Own Authorship

Before introducing the results of energy balance and exergy analysis for each component inside each absorption system, it is primarily checked, with respect to each heat exchanger inside the absorption units, whether each assumed terminal temperature difference is true or false.

The definition of terminal temperature difference can be defined as the value corresponding to the lowest variation between the temperature profiles of hot and cold streams. Conceding that each assumed terminal temperature difference is lower than the terminal temperature difference in its opposite side, the consideration is defined as true statement.

Table 15 contains all the values of the assumed terminal temperature differences of all heat exchanger in each absorption chiller. On the other hand, the terminal temperature differences in their opposite sides are well exposed in Table 16.

Table 15 – Assumed terminal temperature differences of all heat exchangers in each absorption chiller.

$\Delta T_{T,i}$ (°C)	Min OF_1 (US$ ton^{-1})	Max OF_2 (US$ h^{-1})
	311.7	30.7
	HE	SE
Low Absorber	3.339	1.628
Auxiliary Absorber	5.007	3.798
High Desorber	1.000	9.240
Auxiliary Desorber	15.719	16.636
Low Desorber	11.338	8.952

Source: Own Authorship

Table 16 – Terminal temperature differences in their opposite sides of all heat exchangers in each absorption chiller.

$\Delta T_{T,i}^{opposite}$ (°C)	Min OF_1 (US$ ton^{-1})	Max OF_2 (US$ h^{-1})
	311.7	30.7
	HE	SE
Low Absorber	48.857	31.353
Auxiliary Absorber	35.349	20.997
High Desorber	9.114	4.038
Auxiliary Desorber	23.252	19.132
Low Desorber	20.742	17.495

Source: Own Authorship

By comparing both Table 15 and Table 16, it is analysed that there is one false terminal temperature difference occurring at the high desorber heat exchanger for the single-effect chiller. Moreover, this mistake is only verified while optimizing the profit. Fortunately, this misunderstanding does not compromise the mass and energy balances. In contrast, the half-effect configuration presents true terminal temperature differences for all heat exchangers.

When maximizing the profit, the temperature difference at the high desorber (ΔT_{HDe}) increases as much as possible transferring more heat to the mixture. At the same time, the assumed terminal temperature difference in this heat exchanger ($\Delta T_{T,HDe}$) rises simultaneously, thereby, there is an instant that the opposite terminal temperature difference

becomes lower than the assumed terminal temperature difference. Figure 37 has a simple representation of this behavior at the high desorber.

Figure 37 – Terminal temperature difference at the high desorber while maximizing profit (a) and minimizing chilled water specific cost (b).

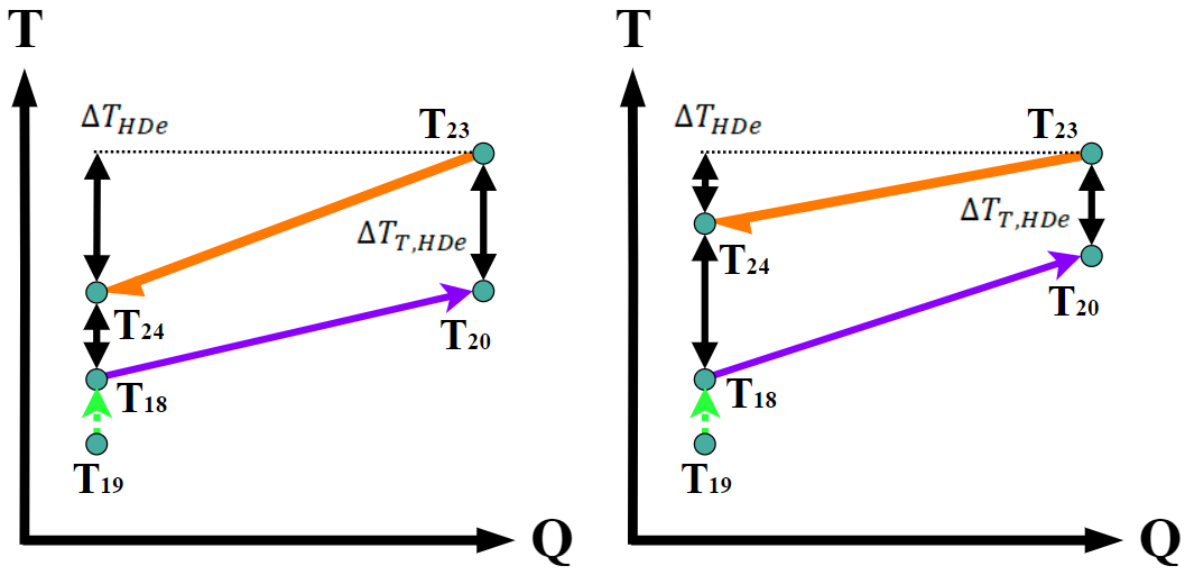

(a) (b)

Source: Own Authorship.

Another critical analysis is related to the mass fraction of each solution stream in the absorption systems. Particularly, as crystallization phenomenon usually occurs on point 6 (strong solution entering the low absorber), this solution stream must be carefully verified for each optimal solution. Then, a penalty is used to always avoid it. Notwithstanding, just to be sure that none crystallization is happening inside the absorption chillers, all solutions streams are checked with their critical mass fractions. Hence, all solution streams must present mass fractions lower than the critical mass fractions.

Table 17 has all calculated mass fractions of each solution stream inside the absorption machine for each optimal solution. A comparison between these values with the critical mass fractions are developed here by analysing Table 18. Thereupon, it is confirmed that none crystallization occurs inside the absorption unit for each optimal solution. This is one of the most crucial results of this master's thesis, this crystallization occurrence must be averted at all costs. Otherwise, it is going to block the flow stream and eventually harm the equipment.

Furthermore, at the low absorber heat exchanger, another method is used to analyse the crystallization formation. The enthalpy of strong solution on point 6 must assume a higher value than the minimum enthalpy that is estimated based on the mass fraction.

Table 17 – Mass fraction of all solution streams.

Properties	Min OF_1 (US\$ ton^{-1})	Max OF_2 (US\$ h^{-1})
	311.7	30.7
	HE	SE
x_1	0.585	0.541
x_2	0.585	0.541
x_3	0.585	0.541
x_4	0.659	0.596
x_5	0.659	0.596
x_6	0.659	0.596
x_8	0.403	0.422
x_9	0.403	0.422
x_{10}	0.403	0.422
x_{11}	0.508	0.444
x_{12}	0.508	0.444
x_{13}	0.508	0.444
x_{19}	0.585	0.541
x_{20}	0.620	0.610
x_{21}	0.620	0.610
x_{22}	0.620	0.610

Source: Own Authorship

Table 18 – Critical mass fraction of all solution streams.

Properties	Min OF_1 (US\$ ton^{-1})	Max OF_2 (US\$ h^{-1})
	311.7	30.7
	HE	SE
$x_{cr,1}$	0.6419	0.6405
$x_{cr,2}$	0.6419	0.6405
$x_{cr,3}$	0.6424	0.6405
$x_{cr,4}$	0.6811	0.6671
$x_{cr,5}$	0.6805	0.6671
$x_{cr,6}$	0.6805	0.6671
$x_{cr,8}$	0.645	0.6648
$x_{cr,9}$	0.645	0.6648
$x_{cr,10}$	0.645	0.6450
$x_{cr,11}$	0.671	0.6590
$x_{cr,12}$	0.671	0.6587
$x_{cr,13}$	0.671	0.6587
$x_{cr,19}$	0.6461	0.6541
$x_{cr,20}$	0.6895	0.6828
$x_{cr,21}$	0.6855	0.6662
$x_{cr,22}$	0.6855	0.6662

Source: Own Authorship

In order to evaluate the energy and exergy analyses in each component, it is presented all thermodynamic states of LiBr-H_2O absorption chiller for each optimal solution. Table 19 to Table 21 show all thermodynamic states for each optimal structure.

Table 19 – Thermodynamic states for hot water HE absorption chiller (311.7 US$ ton^{-1}).

State	$\dot{m}$	p	T	h	h_{min}	s	x	x_{cr}
	(kg s^{-1})	(bar)	(°C)	(kJ kg^{-1})		(kJ kg^{-1} K^{-1})	-	-
1	8.326	0.006	35.2	101.252		0.207	0.585	0.6419
2	8.326	0.036	35.2	101.252		0.207	0.585	0.6419
3	8.326	0.036	35.8	102.502		0.211	0.585	0.6424
3 (in)	8.324	0.036	35.8	102.502		0.211	0.585	0.6419
3 (out)	0.003	0.036	35.8	102.502		0.211	0.585	0.6419
3 (c)	0.003	0.093	35.8	102.502		0.211	0.585	0.6419
4	7.386	0.036	83.7	235.359		0.445	0.659	0.6811
5	7.386	0.036	82.9	233.950		0.441	0.659	0.6805
6	7.386	0.006	82.9	233.950	185.559	0.441	0.659	0.6805
7	0.940	0.036	66.2	2623.783		8.737		
8	4.536	0.036	39.0	80.969		0.365	0.403	0.645
9	4.536	0.093	39.0	80.969		0.365	0.403	0.645
10	4.536	0.093	39.0	81.027		0.365	0.403	0.645
11	3.596	0.093	71.2	154.749		0.492	0.508	0.671
12	3.596	0.093	71.2	154.676		0.492	0.508	0.671
13	3.596	0.036	71.2	154.676		0.492	0.508	0.671
14	0.940	0.093	57.3	2605.844		8.252		
15	0.940	0.093	44.3	185.558		0.630		
16	0.940	0.006	0.2	185.558		0.679		
17	0.940	0.006	0.2	2500.868		9.149		
18	0.000	0.093	85.9	2660.196		8.409		
19	0.003	0.093	40.4	111.376		0.239	0.585	0.6461
20	0.002	0.093	94.0	231.415		0.522	0.620	0.6895
21	0.002	0.093	89.1	222.007		0.496	0.620	0.6895
22	0.002	0.036	89.1	222.007		0.496	0.620	0.6895
23	98.638	4.200	95.0	398.238		1.250		
24	98.638	4.200	95.0	398.232		1.250		
24 (in)	98.638	4.200	95.0	398.232		1.250		
24 (out)	0.000	4.200	95.0	398.232		1.250		
25	98.638	4.100	86.9	364.267		1.157		
26	98.638	4.000	80.6	337.527		1.082		
27	352.945	2.200	31.8	133.485		0.462		
28	352.945	2.000	34.0	142.652		0.492		
29	352.945	1.700	35.8	150.173		0.516		
30	352.945	1.500	37.4	156.617		0.537		
31	103.604	1.600	12.0	50.515		0.180		
32	103.604	1.000	7.0	29.513		0.106		

Source: Own Authorship

The enthalpy and entropy of the water in reference state of 25°C and 1 atm are 104.844 kJ kg^{-1} and 0.367 kJ kg^{-1} K^{-1}, respectively.

Table 20 – Thermodynamic states for hot water SE absorption chiller (30.7 US$ h^{-1}).

State	$\dot{m}$	p	T	h	h_{min}	s	x	x_{cr}
	(kg s^{-1})	(bar)	(°C)	(kJ kg^{-1})		(kJ kg^{-1} K^{-1})	-	-
1	7.744	0.009	33.4	80.948		0.219	0.541	0.6405
2	7.744	0.032	33.4	80.948		0.219	0.541	0.6405
3	7.744	0.032	33.5	80.977		0.219	0.541	0.6405
3 (in)	1.436	0.032	33.5	80.977		0.219	0.541	0.6405
3 (out)	6.308	0.032	33.5	80.977		0.219	0.541	0.6405
3 (c)	6.308	0.071	33.5	80.977		0.219	0.541	0.6405
4	7.029	0.032	66.4	167.201		0.388	0.596	0.6671
5	7.029	0.032	66.3	167.169		0.388	0.596	0.6671
6	7.029	0.009	66.3	167.169	34.532	0.388	0.596	0.6671
7	0.000	0.032	55.5	2603.653		8.730		
8	0.000	0.032	38.8	79.115		0.346	0.422	0.6448
9	0.000	0.071	38.8	79.115		0.346	0.422	0.6448
10	0.000	0.071	39.1	79.880		0.349	0.422	0.6450
11	0.000	0.071	56.3	120.018		0.457	0.444	0.6590
12	0.000	0.071	56.0	119.214		0.455	0.444	0.6587
13	0.000	0.032	56.0	119.214		0.455	0.444	0.6587
14	0.000	0.071	53.8	2599.703		8.356		
15	0.714	0.071	39.3	164.387		0.562		
16	0.714	0.009	5.7	164.387		0.590		
17	0.714	0.009	5.7	2511.072		9.005		
18	0.714	0.071	71.3	2632.787		8.454		
19	6.308	0.071	50.4	115.857		0.330	0.541	0.6541
20	5.594	0.071	85.8	211.132		0.486	0.610	0.6828
21	5.594	0.071	65.3	171.798		0.373	0.610	0.6662
22	5.594	0.032	65.3	171.798		0.373	0.610	0.6662
23	28.177	4.300	95.0	398.246		1.250		
24	28.177	4.000	75.3	315.531		1.019		
24 (in)	9.964	4.000	75.3	315.531		1.019		
24 (out)	18.216	4.000	75.3	315.531		1.019		
25	9.964	4.000	73.0	305.686		0.991		
26	9.964	4.000	73.0	305.681		0.991		
27	177.454	2.200	31.8	133.485		0.462		
28	177.454	1.850	35.0	146.682		0.505		
29	177.454	1.850	35.0	146.682		0.505		
30	177.454	1.500	37.4	156.617		0.537		
31	79.805	1.600	12.0	50.515		0.180		
32	79.805	1.000	7.0	29.513		0.106		

Source: Own Authorship

Table 21 – Specific exergies of each thermodynamic state for each absorption chiller (311.7 US$ ton^{-1} and 30.7 US$ h^{-1}).

	Min OF_1 (US$ ton^{-1}) 311.7 HE			Max OF_2 (US$ h^{-1}) 30.7 SE		
State	e_{ph} (kJ kg^{-1})	e_{ch} (kJ kg^{-1})	e_{to} (kJ kg^{-1})	e_{ph} (kJ kg^{-1})	e_{ch} (kJ kg^{-1})	e_{to} (kJ kg^{-1})
1	0.327	542.118	542.445	0.240	484.515	484.756
2	0.327	542.118	542.445	0.240	484.515	484.756
3	0.369	542.118	542.487	0.241	484.515	484.756
3 (in)	0.369	542.118	542.487	0.241	484.515	484.756
3 (out)	0.369	542.118	542.487	0.241	484.515	484.756
3 (c)	0.369	542.118	542.487	0.241	484.515	484.756
4	9.104	654.940	664.044	5.079	558.337	563.417
5	8.874	654.940	663.814	5.075	558.337	563.417
6	8.874	654.940	663.814	5.075	558.337	563.417
7	23.480	50.252	73.731	5.341	50.252	55.593
8	0.793	334.925	335.718	0.746	353.144	353.890
9	0.793	334.925	335.718	0.747	353.144	353.890
10	0.796	334.925	335.720	0.781	353.144	353.924
11	7.077	444.734	451.811	3.631	374.643	378.274
12	7.067	444.734	451.801	3.555	374.643	378.198
13	7.067	444.734	451.801	3.555	374.643	378.198
14	150.146	50.252	200.398	113.007	50.252	163.258
15	2.417	50.252	52.669	1.287	50.252	51.539
16	-12.285	50.252	37.966	-7.063	50.252	43.188
17	-222.438	50.252	-172.187	-169.118	50.252	-118.866
18	157.464	50.252	207.716	116.700	50.252	166.952
19	0.743	542.118	542.860	2.108	484.515	486.623
20	13.086	593.327	606.413	10.424	578.869	589.293
21	11.369	593.327	604.696	4.732	578.869	583.601
22	11.369	593.327	604.696	4.732	578.869	583.601
23	30.166	50.252	80.417	30.176	50.252	80.427
24	30.164	50.252	80.416	16.279	50.252	66.531
24 (in)	30.164	50.252	80.416	16.279	50.252	66.531
24 (out)	30.164	50.252	80.416	16.279	50.252	66.531
25	24.004	50.252	74.256	14.886	50.252	65.138
26	19.595	50.252	69.847	14.886	50.252	65.137
27	0.441	50.252	50.692	0.441	50.252	50.692
28	0.658	50.252	50.910	0.768	50.252	51.019
29	0.871	50.252	51.123	0.768	50.252	51.019
30	1.093	50.252	51.344	1.093	50.252	51.344
31	1.280	50.252	51.532	1.280	50.252	51.532
32	2.369	50.252	52.621	2.369	50.252	52.621

Source: Own Authorship

As all thermodynamic states are well defined for each absorption chiller, the first thermodynamic results that are sequentially presented here regard to the high desorber. Table 22 exposes energy and exergy analyses of this heat exchanger. For the HE chiller, the high desorber is practically erased from the superstructure because the amount of heat transfer rate and heat transfer area are almost achieving null values.

Table 22 – Thermodynamic analysis at the high desorber.

	Min OF_1 (US$ ton^{-1})	Max OF_2 (US$ h^{-1})
	311.7	30.7
	HE	SE
Energy analysis		
$\dot{Q}$ (kW)	0.650	2330.625
ΔT_{lm} (°C)	3.672	6.284
A (m^2)	0.157	328.215
Exergy analysis		
Product (kW)	–	346.007
Resource (kW)	–	391.553
$\dot{I}$ (kW)	–	45.546
η_{ex}	–	0.884

Source: Own Authorship

By applying the energy balance at the high desorber, it is possible to calculate the main parameters such as log mean temperature difference, heat transfer rate and heat transfer area.

The exergy analysis gives a better understanding of energy in its pure quality. Then, it is evaluated here the product and resource in means of exergy as well as the irreversibility rate and exergy efficiency. For the high desorber heat exchanger, the hot water is treated as resource while the mixture of LiBr-H_2O is defined as product.

As the superheated vapour (point 18) at the exit of high desorber was assumed in full thermodynamic equilibrium with weak solution of LiBr-H_2O (point 19), there is a temperature glide that benefits thermodynamically this heat exchanger by reducing the average thermodynamic temperature difference between the hot and cold streams.

Figure 38 represents the temperature chart versus cumulative heat transfer rate at the high desorber. In summary, the presence of irreversibility can be interpreted as the region between the temperature profiles of hot and cold streams. Thus, as mentioned before, the temperature glide implicates in less irreversibility generation. This graph is extensively repeated for each heat exchanger, assisting the comprehension of thermodynamic analysis.

Figure 38 – Temperature chart of the high desorber in the SE chiller.

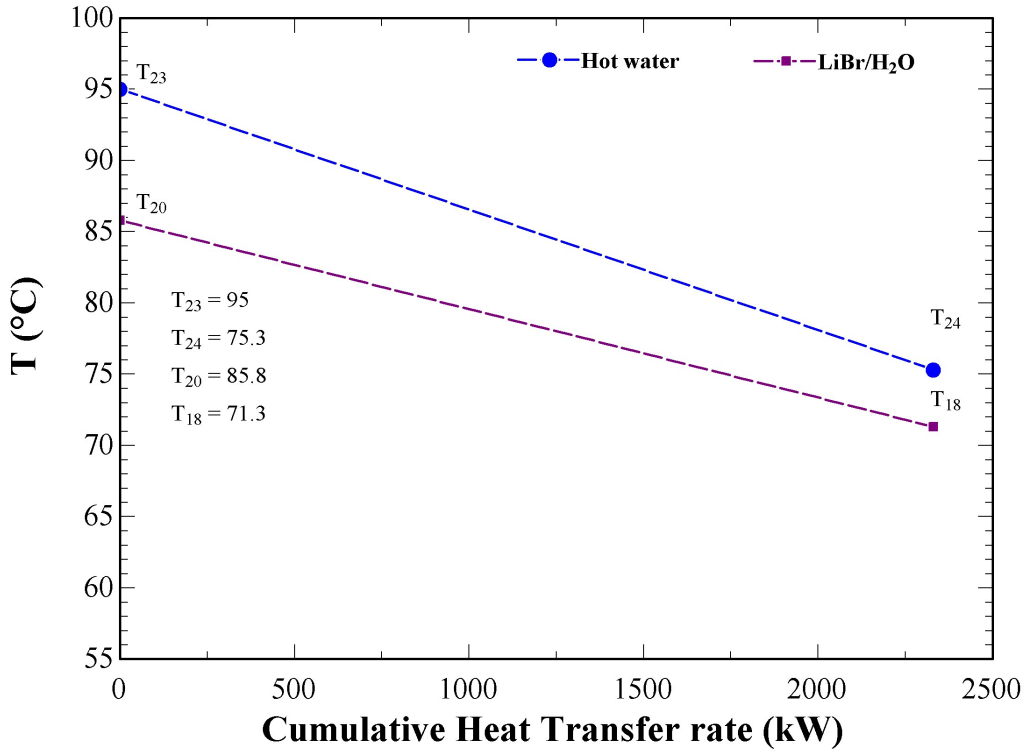

Source: Own Authorship.

Successively, Table 23 has all optimal values of the low desorber heat exchanger for each optimal solution. The SE machine does not use a low desorber in its final configuration due the low heat transfer rate and small heat transfer area.

Table 23 – Thermodynamic analysis at the low desorber.

	Min OF_1 (US$ ton^{-1})	Max OF_2 (US$ h^{-1})
	311.7	30.7
	HE	SE
Energy analysis		
$\dot{Q}$ (kW)	3350.168	98.104
ΔT_{lm} (°C)	15.570	12.750
A (m^2)	190.419	6.809
Exergy analysis		
Product (kW)	457.237	–
Resource (kW)	607.637	–
$\dot{I}$ (kW)	150.360	–
η_{ex}	0.752	–

Source: Own Authorship

In the HE machine, the low desorber recovers more waste heat, as it can be seen in Table 23. When comparing these results against the high desorber in the SE chiller, the heat transfer area of the low desorber is smaller due a high value of log mean temperature difference.

The application of the second law in this heat exchanger provides some reliable information about irreversibility generation. The low desorber inside the HE absorption chiller presents great amount of resource (hot water) and product (mixture of LiBr-H_2O) in means of exergy. Further, as there is more heat transfer rate combined with a high log mean temperature difference, it is expected a great irreversibility generation. In order to comprehend this result, Figure 39 has a representation of the temperature chart versus cumulative heat transfer rate at the low desorber in HE case.

Figure 39 – Temperature chart of the low desorber in the HE chiller.

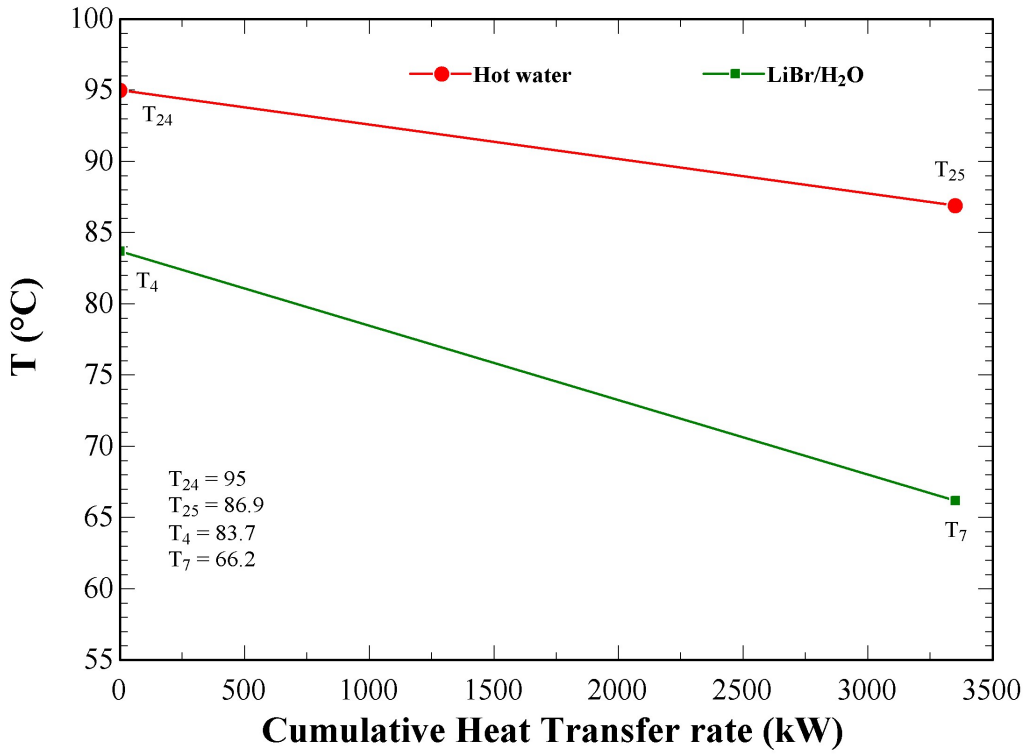

Source: Own Authorship.

The final desorber that is discussed here regards to the auxiliary desorber, the results for each optimal solution are shown in Table 24. The SE chiller also does not have an auxiliary desorber in its final structure. This observation can be verified by evaluating the heat transfer rate which is reaching a low value, thereby, implicating that the heat transfer area is practically null, and as consequence, erasing the auxiliary desorber from

the superstructure.

Table 24 – Thermodynamic analysis at the auxiliary desorber.

	Min OF_1 (US$ ton^{-1})	Max OF_2 (US$ h^{-1})
	311.7	30.7
	HE	SE
Energy analysis		
$\dot{Q}$ (kW)	2637.595	0.049
ΔT_{lm} (°C)	19.240	17.855
A (m^2)	121.316	0.002
Exergy analysis		
Product (kW)	290.350	–
Resource (kW)	434.903	–
$\dot{I}$ (kW)	144.553	–
η_{ex}	0.668	–

Source: Own Authorship

This heat exchanger in the HE chiller is transferring lesser heat transfer rate than the low desorber but at the same time, the log mean temperature difference is increasing simultaneously. Hence, lowering the heat transfer area.

An exergy evaluation is also necessary for this auxiliary desorber in order to analyse the thermal energy in its true quality. Likewise, although there is greater log mean temperature difference in the auxiliary desorber, this heat exchanger generates minor irreversibility rate due a reduced heat transfer rate.

The temperature chart versus cumulative heat transfer rate at the auxiliary desorber is shown in Figure 40, permitting to confirm some of the previous explanations about irreversibility generation. It is seen that in the HE chiller the auxiliary desorber has an increased variation between the temperature profiles. Thereupon, distancing the average thermodynamic temperatures, and consequently, implicating in more irreversibility generation. However, since there is also minor heat transfer rate being transferred in this heat exchanger, it is counterbalancing with less irreversibility generation. Therefore, the region between the temperature profiles is marginally decaying when compared to irreversibility generation at the low desorber.

When comparing the two desorbers of HE chiller against the high desorber of SE machine, the amount of irreversibility in the high desorber is much lower than the low and auxiliary desorbers, as shown in Figure 41. Hence, the HE machine is destroying more exergy during the waste heat recovering process on the hot water stream. In addition, the desorbers in the HE chiller are presenting worst exergy performance.

Figure 40 – Temperature chart of the auxiliary desorber in the HE chiller.

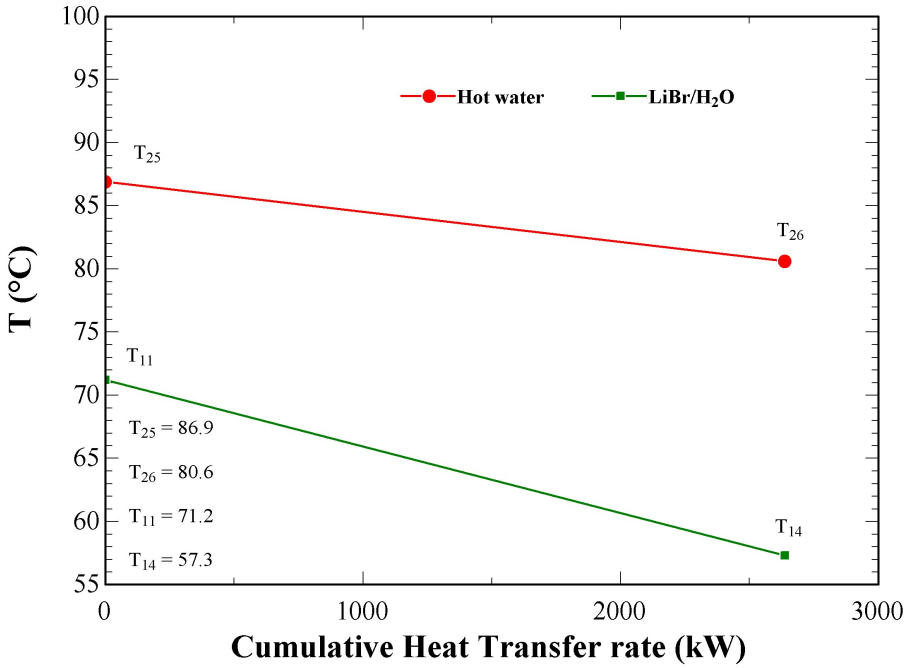

Source: Own Authorship.

Figure 41 – Temperature chart of the desorbers in the HE and SE chillers.

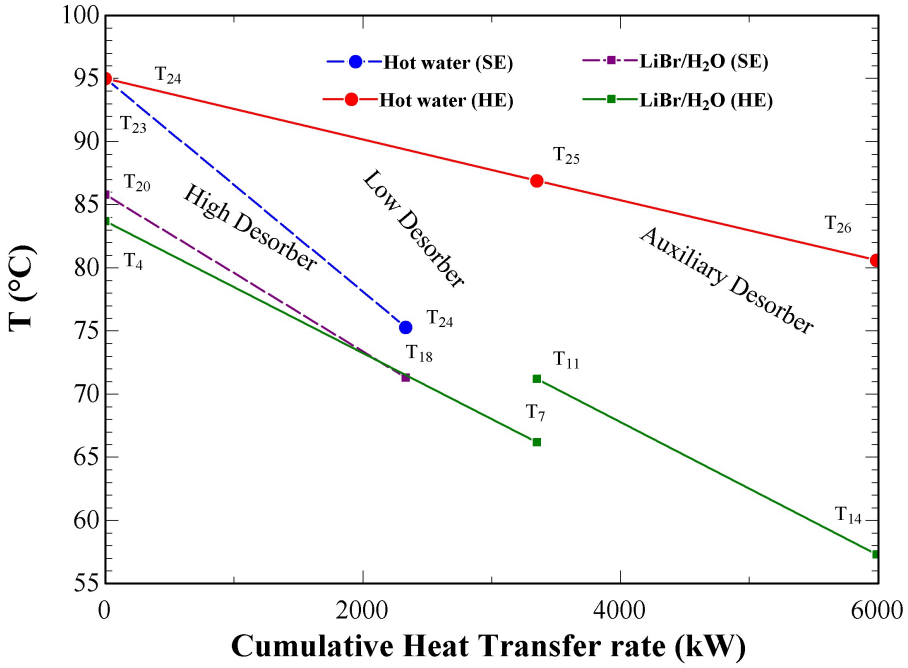

Source: Own Authorship.

The next component that is discussed here refers to the low absorber. This heat exchanger is responsible to reject heat to the environment through the cooling water circuit. Table 25 has all optimal results of the low absorber for each optimal solution.

Table 25 – Thermodynamic analysis at the low absorber.

	Min OF_1 (US$ ton^{-1})	Max OF_2 (US$ h^{-1})
	311.7	30.7
	HE	SE
Energy analysis		
$\dot{Q}$ (kW)	3235.297	2341.796
ΔT_{lm} (°C)	13.136	10.049
A (m^2)	210.504	199.169
Exergy analysis		
$\sum \dot{E}_{leaving}$ (kW)	22484.731	12807.473
$\sum \dot{E}_{entering}$ (kW)	22632.802	12871.166
$\dot{L}$ (kW)	76.784	58.095
$\dot{I}$ (kW)	148.071	63.693
$\dot{E}_{des}$ (kW)	224.855	121.788
ξ_{ex}	0.9935	0.9951

Source: Own Authorship

Conforming to the first law of thermodynamics, the energy analysis shows different results for each optimal solution. The HE solution presents a low absorber with highest heat transfer rate, whereas the SE solution has the lowest heat transfer rate. In numbers, the low absorber in the HE case is transferring heat transfer rate 1.39 times greater than in the SE case. Despite the low absorber has high log mean temperature difference in the HE case, the heat transfer rate is influencing more the sizing of heat transfer area, therefore, resulting in more heat transfer area.

The exergy analysis in this component is also developed in an effort to understand the thermal energy inside the low absorber. Firstly, in the HE case, as there is more heat transfer rate with high log mean temperature difference, it is expected more irreversibility rate as well as exergy losses. The exergy efficiency at the low absorber in the HE machine is resulting in slight detriment when compared to this same heat exchanger in the SE chiller.

By repeating a similar thermodynamic analysis in relation to the temperature chart versus cumulative heat transfer rate at the low absorber for both optimal solutions, it is confirmed that this dissipative heat exchanger in the HE chiller presents an increased irreversibility generation, as represented in Figure 42.

Figure 42 – Temperature chart of the low absorber in the HE and SE chillers.

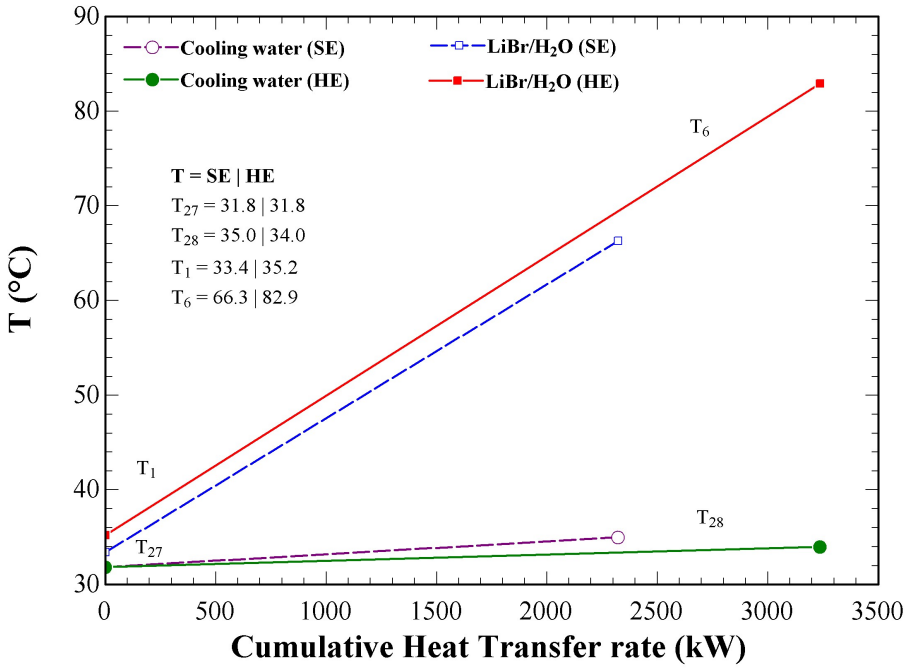

Source: Own Authorship.

The next heat exchanger that is necessary in the HE optimal structure regards to the auxiliary absorber, it also rejects heat to the environment through the cooling water circuit. Table 26 has all optimal results of the auxiliary absorber for each optimal solution.

Table 26 – Thermodynamic analysis at the auxiliary absorber.

	Min OF_1 (US$ ton^{-1})	Max OF_2 (US$ h^{-1})
	311.7	30.7
	HE	SE
Energy analysis		
$\dot{Q}$ (kW)	2654.452	0.049
ΔT_{lm} (°C)	13.851	10.058
A (m^2)	163.798	0.004
Exergy analysis		
$\sum \dot{E}_{leaving}$ (kW)	19566.295	–
$\sum \dot{E}_{entering}$ (kW)	19662.444	–
$\dot{L}$ (kW)	75.155	–
$\dot{I}$ (kW)	96.149	–
$\dot{E}_{des}$ (kW)	171.304	–
ξ_{ex}	0.9951	–

Source: Own Authorship

The SE chiller presents practically null values of heat transfer rate and heat transfer area at the auxiliary absorber, meaning that this heat exchanger is deleted from the superstructure. This result makes sense since SE machine does not need any auxiliary heat exchanger.

By comparing the energy analysis between the low and auxiliary absorbers in HE machine, it is observed that there is less heat being transferred in the auxiliary absorber while the log mean temperature difference is increased simultaneously. The heat transfer area in the auxiliary absorber is following the reduction of heat transfer rate, thus, resulting in a decreased value.

The exergy analysis of auxiliary absorber in the HE machine also presents considerable exergy destruction. Nevertheless, albeit the log mean temperature difference is raised, the reduction of heat transfer rate is simultaneously affecting the irreversibility generation. Therefore, it is registered a minor irreversibility rate in the auxiliary absorber when compared to the low absorber. Regarding the exergy losses, the auxiliary absorber is slightly losing lesser exergy on cooling water circuit than the low absorber.

In Figure 43, the temperature chart versus cumulative heat transfer rate at the auxiliary absorber is graphically presented. As the presence of irreversibility can be interpreted as the zone between the temperature profiles of cold and hot streams, the auxiliary absorber has lower irreversibility generation than the low absorber.

Figure 43 – Temperature chart of the auxiliary absorber in the HE chiller.

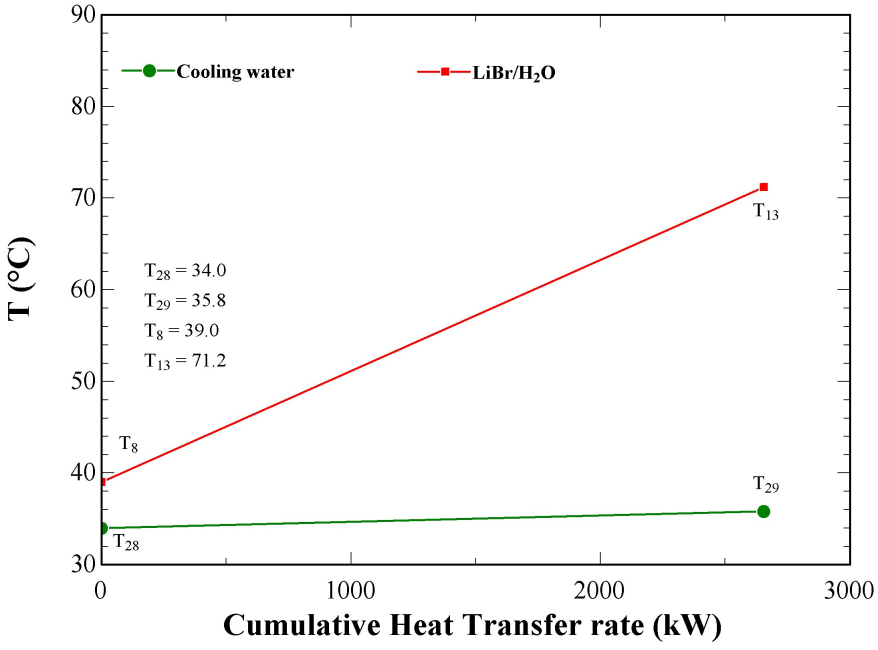

Source: Own Authorship.

The last dissipative heat exchanger that rejects heat to the environment through the cooling water circuit is the condenser. This component is needed in both HE and SE chillers, thereby, Table 27 has all optimal results of the condenser for each optimal solution.

Table 27 – Thermodynamic analysis at the condenser.

	Min OF_1 (US$ ton^{-1})	Max OF_2 (US$ h^{-1})
	311.7	30.7
	HE	SE
Energy analysis		
$\dot{Q}$ (kW)	2274.593	1763.043
ΔT_{lm} (°C)	7.697	2.919
A (m^2)	132.526	270.836
Exergy analysis		
$\sum \dot{E}_{leaving}$ (kW)	18171.262	9148.114
$\sum \dot{E}_{entering}$ (kW)	18231.800	9172.884
$\dot{L}$ (kW)	78.299	57.663
$\dot{I}$ (kW)	60.538	24.770
$\dot{E}_{des}$ (kW)	138.837	82.433
ξ_{ex}	0.9967	0.9973

Source: Own Authorship

In agreement with the energy balance in this heat exchanger, it is verified again the same behavior from previous results at the low absorber which is a condenser releasing highest amount of heat transfer rate in the HE configuration while the SE chiller presents a condenser rejecting lowest heat transfer rate. When comparing these chillers, despite the fact that the heat transfer rate is increased at the condenser in the HE machine, the log mean temperature difference also raises simultaneously, thus, resulting in a reduced heat transfer area. Hence, the HE machine utilizes a smaller condenser than the SE machine.

The exergy analysis at the condenser on both chillers permits to observe that SE case generates lesser irreversibility rate than the HE case. The log mean temperature difference is decreased at the condenser in the SE chiller, thereby, affecting directly the average thermodynamic temperatures difference. Moreover, as the amount of heat transfer rate is reduced in this heat exchanger, the irreversibility generation must decay. The exergy efficiency of the condenser is slightly reduced in the HE case.

The temperature chart of the condenser in Figure 44 allows to analyse a great discrepancy of the region between the temperature profiles, the irreversibility generation as well as the exergy losses in the HE case are increased in this heat exchanger.

The following Figure 45 and Figure 46 represent the temperature chart on each dissipative heat exchanger inside each absorption chiller.

Figure 44 – Temperature chart of the condenser in the HE and SE chillers.

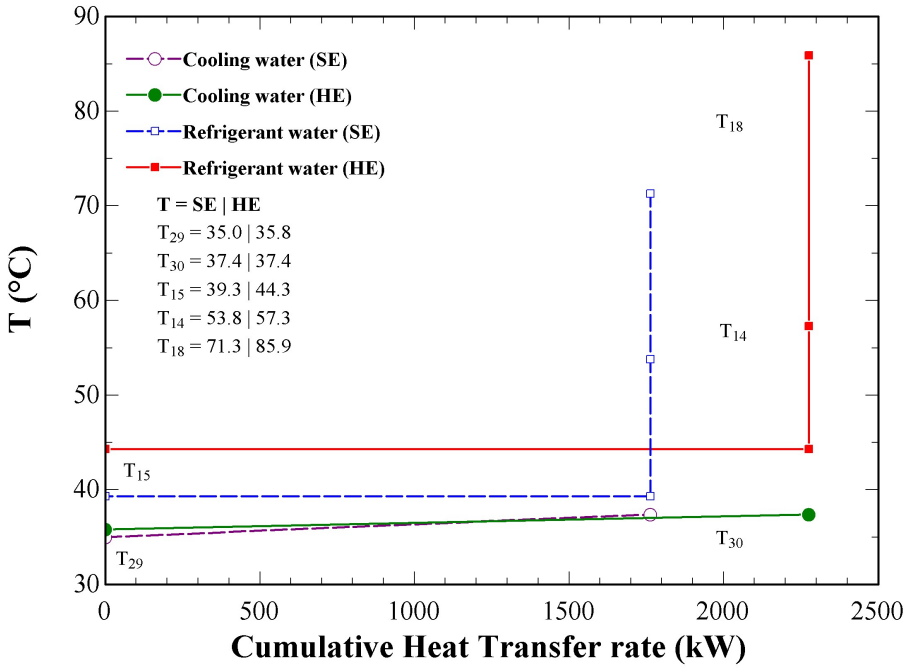

Source: Own Authorship.

Figure 45 – Temperature chart of dissipative heat exchangers in the HE chiller.

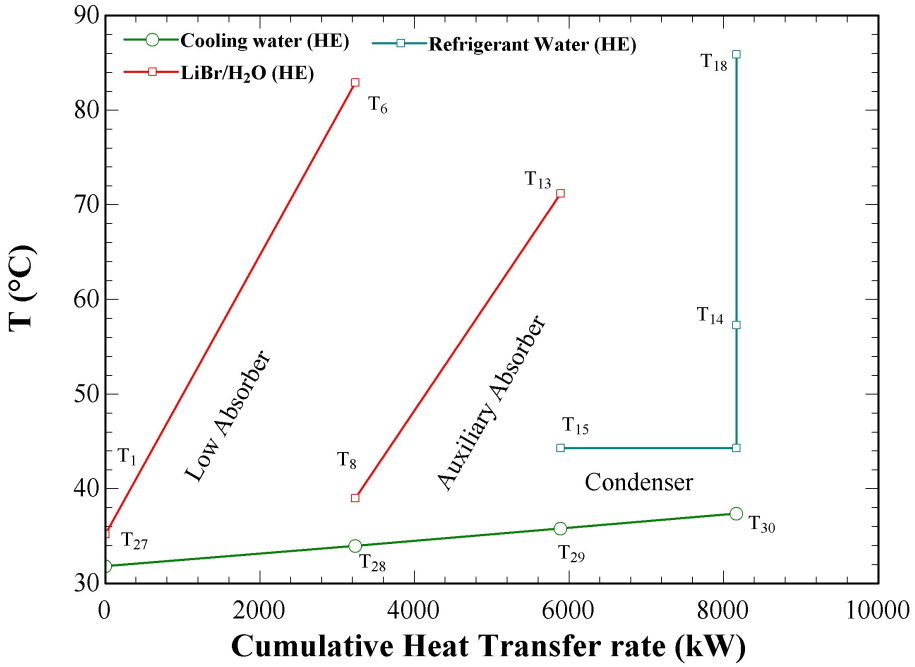

Source: Own Authorship.

Figure 46 – Temperature chart of dissipative heat exchangers in the SE chiller.

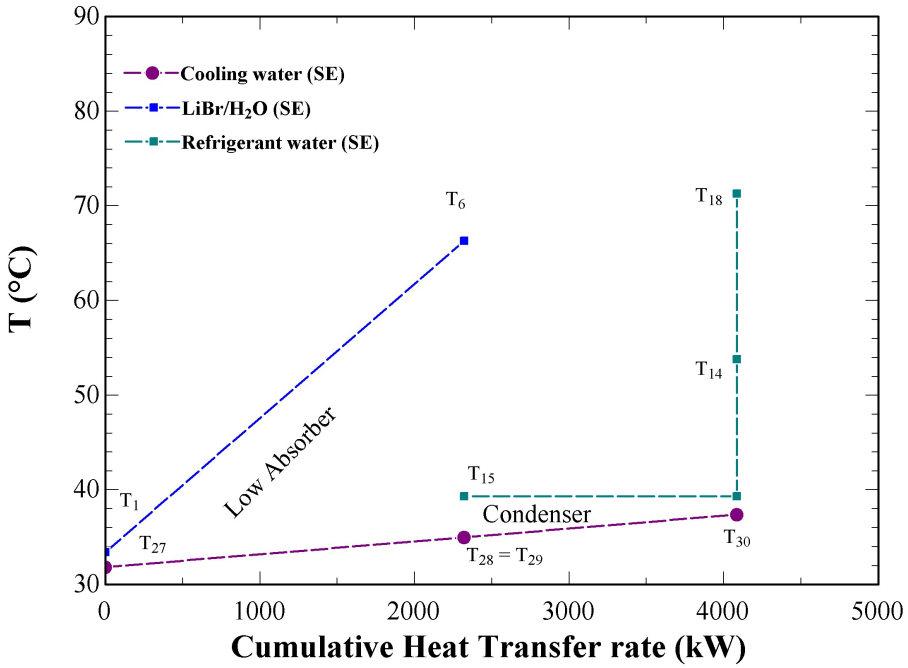

Source: Own Authorship.

The chilled water is produced at the evaporator and it is necessary in all final structures. Table 29 has all optimal results of the evaporator for each optimal solution.

Table 28 – Thermodynamic analysis at the evaporator.

	Min OF_1 (US$ ton^{-1})	Max OF_2 (US$ h^{-1})
	311.7	30.7
	HE	SE
Energy analysis		
$\dot{Q}$ (kW)	2174.593	1676.109
ΔT_{lm} (°C)	9.082	3.118
A (m^2)	182.893	410.330
Exergy analysis		
Product (kW)	112.832	86.914
Resource (kW)	197.502	115.747
$\dot{I}$ (kW)	84.670	28.833
η_{ex}	0.571	0.751

Source: Own Authorship

The HE chiller still remains as the optimal solution to present the evaporator generating highest heat transfer rate. And again, the SE machine has the lowest heat

transfer rate at the evaporator. A comparison between these absorption chillers permits to analyse that the HE unit has an evaporator presenting increased values of heat transfer rate and log mean temperature difference, but as the log mean temperature difference is raised, the heat transfer area is reduced in the HE case. On the other hand, despite there is minor heat transfer rate in the SE case, the heat transfer area raises considerably due a reduction of log mean temperature difference.

Regarding the exergy analysis in the evaporator, there is a decreased irreversibility rate due the reduction of heat transfer rate combined with a low log mean temperature difference in this heat exchanger. The evaporator is assuming better exergy performance in the SE chiller.

Figure 47 shows the temperature chart versus cumulative heat transfer rate at the evaporator in both cases. An evaluation of irreversibility generation is carried out by interpreting the region between the temperature profiles. For the HE case, it is clearly noted that there is a greater irreversibility generation than the SE case.

The analysis of these optimum results allows to verify that different objective functions lead to distinct optimal solutions in energy and exergy magnitudes.

Figure 47 – Temperature chart of the evaporator in the HE and SE chillers.

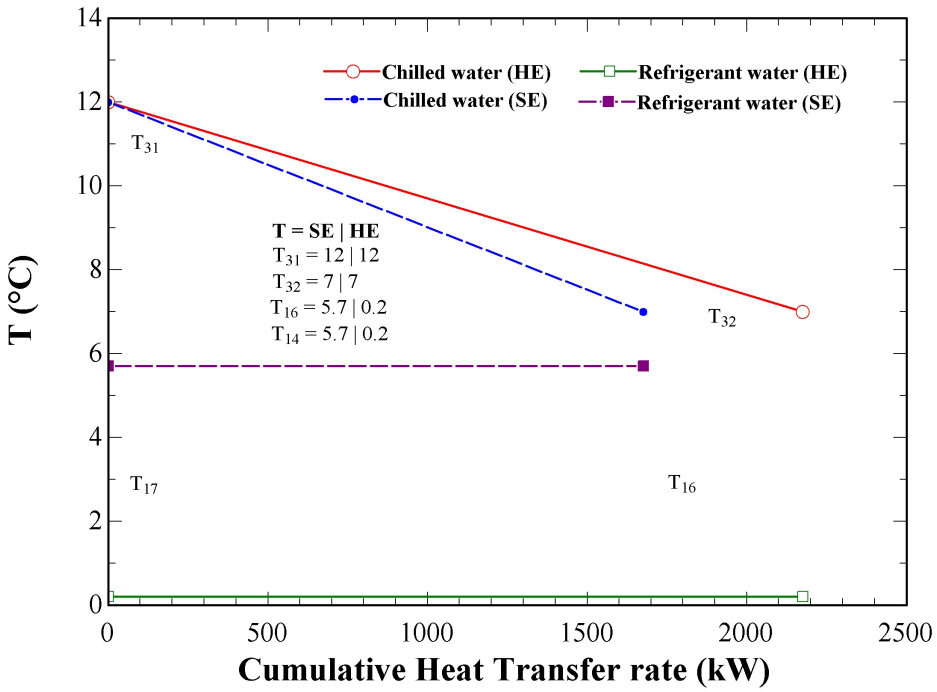

Source: Own Authorship.

The SE chiller needs only the high solution heat exchanger in its final configuration.

The other solution heat exchangers are erased from the superstructure. The HE chiller does not require any solution heat exchanger in its final structure.

Table 29 – Thermodynamic analysis at the high solution heat exchanger.

	Min OF_1 (US$ ton^{-1})	Max OF_2 (US$ h^{-1})
	311.7	30.7
	HE	SE
Energy analysis		
$\dot{Q}$ (kW)	–	220.029
ΔT_{lm} (°C)	–	33.571
A (m^2)	–	50.416
Exergy analysis		
Product (kW)	–	11.776
Resource (kW)	–	31.841
$\dot{I}$ (kW)	–	20.065
η_{ex}	–	0.370

Source: Own Authorship

Figure 48 presents the temperature chart at the high solution heat exchanger in the SE chiller.

Figure 48 – Temperature chart of the high solution heat exchanger in the SE chiller.

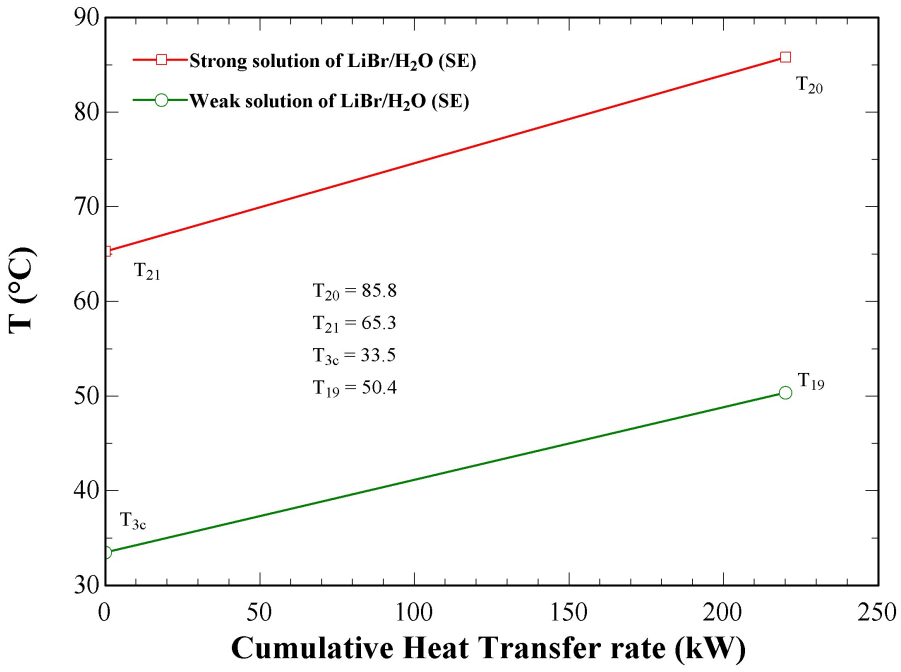

Source: Own Authorship.

The following analysis regards to the refrigerant expansion valve which is responsible to reduce the pressure under an isenthalpic process. Then, it is evaluated the irreversibility rate as well as the exergy efficiency in this dissipative device. Table 30 presents the exergy analysis in the refrigerant expansion valve for each optimal solution.

Table 30 – Thermodynamic analysis at the refrigerant expansion valve.

	Min OF_1 (US$ ton^{-1})	Max OF_2 (US$ h^{-1})
	311.7	30.7
	HE	SE
Exergy analysis		
$\dot{I}$ (kW)	13.817	5.964
ξ_{ex}	0.7208	0.838

Source: Own Authorship

The HE chiller has a refrigerant expansion valve destroying more exergy than in the SE case, presenting a relative difference of 130.83%. Also, the exergy efficiency of the refrigerant expansion valve is decreasing 13.98%.

Being mindful that the solution expansion valves also destroy exergy during the adiabatic process inside the absorption machines, the exergy analysis is also developed for these dissipative devices, as represented in Table 31. The irreversibility rates of low, auxiliary and high solution expansion valves inside the absorption chillers are quite small due the low pressure differences in these dissipative devices. Therefore, the exergy efficiency in each one of them is also practically unit.

Since entropies on the entry and exit of each solution expansion valve are equal in each absorption system, the calculation of the irreversibility rate is based on reversible and isenthalpic processes (APRHORNRATANA; EAMES, 1995).

Table 31 – Thermodynamic analysis at the solution expansion valves.

	Min OF_1 (US$ ton^{-1})	Max OF_2 (US$ h^{-1})
	311.7	30.7
	HE	SE
Exergy analysis		
$\dot{I}_{LSEV}$ (kW)	$1.231 \cdot 10^{-2}$	$9.663 \cdot 10^{-3}$
$\dot{I}_{AuSEV}$ (kW)	$1.330 \cdot 10^{-2}$	–
$\dot{I}_{HSEV}$ (kW)	–	$1.262 \cdot 10^{-2}$
$\xi_{ex_{LSEV}}$	0.9998	0.9997
$\xi_{ex_{AuSEV}}$	0.9995	–
$\xi_{ex_{HSEV}}$	–	0.9995

Source: Own Authorship

Regarding the solution pumps and electric motors, Table 32 presents all optimal results of these components for each optimal solution.

Table 32 – Thermodynamic analysis at the solution pumps and electric motors.

	Min OF_1 (US\$ ton^{-1})	Max OF_2 (US\$ h^{-1})
	311.7	30.7
	HE	SE
Energy Analysis		
$\dot{W}_{Lp}$ (kW)	$2.487 \cdot 10^{-4}$	$1.867 \cdot 10^{-4}$
$\dot{W}_{Aup}$ (kW)	$3.076 \cdot 10^{-4}$	–
$\dot{W}_{Hp}$ (kW)	–	$2.538 \cdot 10^{-4}$
$\dot{W}_{Lem}$ (kW)	$2.618 \cdot 10^{-4}$	$1.965 \cdot 10^{-4}$
$\dot{W}_{Auem}$ (kW)	$3.238 \cdot 10^{-4}$	–
$\dot{W}_{Hem}$ (kW)	–	$2.672 \cdot 10^{-4}$
Exergy Analysis		
$\dot{I}_{Lp}$ (kW)	$2.405 \cdot 10^{-4}$	$1.815 \cdot 10^{-4}$
$\dot{I}_{Aup}$ (kW)	$2.938 \cdot 10^{-4}$	–
$\dot{I}_{Hp}$ (kW)	–	$2.468 \cdot 10^{-4}$
$\dot{I}_{Lem}$ (kW)	$0.131 \cdot 10^{-4}$	$0.098 \cdot 10^{-4}$
$\dot{I}_{Auem}$ (kW)	$0.162 \cdot 10^{-4}$	–
$\dot{I}_{Hem}$ (kW)	–	$0.134 \cdot 10^{-4}$

Source: Own Authorship

For the sake of simplicity, as the irreversibility rates of electric motors are quite small while compared to other main components inside the absorption chiller for each optimal solution, these results are ignored during the thermodynamic analysis.

The next step is to analyse the overall exergy destruction in each absorption unit by gathering all results in one organized spreadsheet, then presenting the necessary information in regard to the exergy fluxes within the components.

Table 33 shows a detailed exergy analysis in order to evaluate the irreversibility, exergy losses, products and resources in means of exergy of each optimal solution. A comparison between them is also exposed in the same table by calculating their percentage values.

With respect to the components that do not exist in each absorption chiller, it is obviously not exposed any information. Therefore, only the existent heat exchangers, solution expansion valves and solution pumps are properly explicit.

Table 33 – Detailed exergy analysis inside the absorption chillers.

	Min OF_1 (US$ ton^{-1}) 311.7 HE		Max OF_2 (US$ h^{-1}) 30.7 SE	
	(kW)	(%)	(kW)	(%)
Irreversibility Analysis				
High Desorber	–	–	45.546	11.63
Low Desorber	150.401	14.43	–	–
Auxiliary Desorber	144.553	13.87	–	–
Low Absorber	148.071	14.20	63.693	16.27
Auxiliary Absorber	96.149	9.22	–	–
Condenser	60.538	5.81	24.770	6.33
Evaporator	84.670	8.12	28.833	7.36
Low SHX	–	–	–	–
Auxiliary SHX	–	–	–	–
High SHX	–	–	20.065	5.12
Refrigerant EV	13.817	1.33	5.964	1.52
Low SEV	$1.2 \cdot 10^{-2}$	$1.2 \cdot 10^{-3}$	$9.7 \cdot 10^{-3}$	$2.5 \cdot 10^{-3}$
Auxiliary SEV	$1.3 \cdot 10^{-2}$	$1.3 \cdot 10^{-3}$	–	–
High SEV	–	–	$1.3 \cdot 10^{-2}$	$3.2 \cdot 10^{-3}$
Low pump	$2.4 \cdot 10^{-4}$	$2.3 \cdot 10^{-5}$	$1.8 \cdot 10^{-4}$	$4.6 \cdot 10^{-5}$
Auxiliary pump	$2.9 \cdot 10^{-4}$	$2.8 \cdot 10^{-5}$	–	–
High pump	–	–	$2.5 \cdot 10^{-4}$	$6.3 \cdot 10^{-5}$
Exergy Losses Analysis				
Low Absorber	76.784	7.37	58.095	14.84
Auxiliary Absorber	75.155	7.21	–	–
Condenser	78.299	7.51	57.663	14.73
Exergy Destruction Analysis				
Low Absorber	224.855	21.57	121.788	31.10
Auxiliary Absorber	171.304	16.43	–	–
Condenser	138.837	13.32	82.433	21.05
Resources Analysis				
High Desorber	–	–	391.553	100.00
Low Desorber	607.637	58.28	–	–
Auxiliary Desorber	434.903	41.72	–	–
Overall Exergy Analysis				
Total Irreversibility	699.470	67.09	188.880	48.24
Total Exergy Losses	230.238	22.08	115.759	29.56
Total Exergy Destruction	929.708	89.18	304.639	77.80
Total Resources	1042.540	100.00	391.553	100.00
Product (Chilled Water)	112.832	10.82	86.914	22.2
$\eta_{ex}^{chiller}$	0.108		0.222	

Source: Own Authorship

A comparison involving only irreversibility in the main components is carried out in Figure 49. Despite the fact that the HE chiller presents in each component more irreversibility rates than in the SE machine, the percentage values follow a different behavior.

Figure 49 – Comparison of irreversibility in percentage values at all main components inside the absorption chillers.

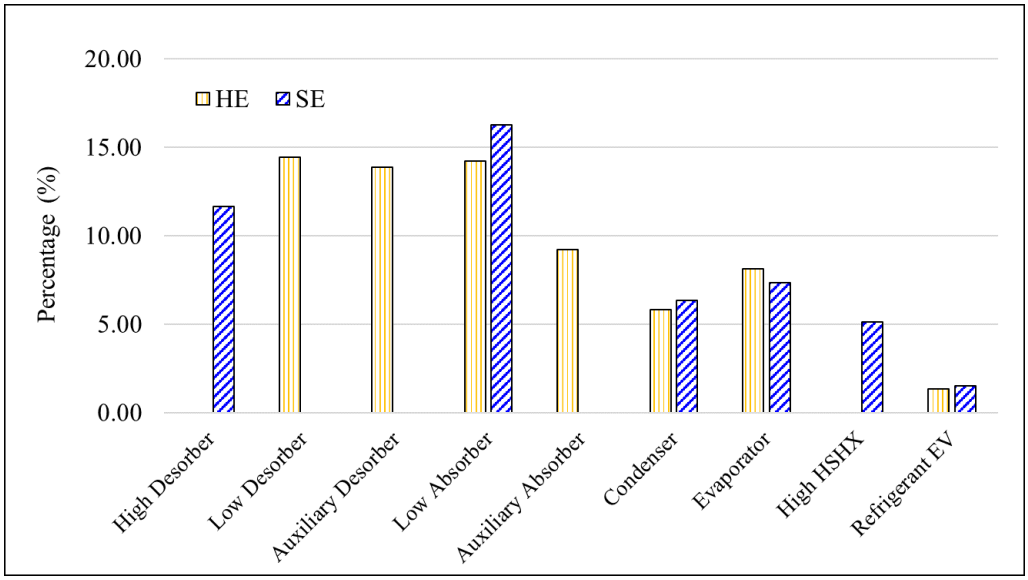

Source: Own Authorship.

The SE chiller concentrates more irreversibility at the low absorber, followed by high desorber, evaporator, condenser, high solution heat exchanger and refrigerant expansion valve. The HE machine has more irreversibility concentration in the following sequence; low desorber, low absorber, auxiliary desorber, auxiliary absorber, evaporator, condenser and refrigerant expansion valve.

When comparing both absorption units, the SE chiller presents low absorber, condenser and refrigerant expansion valve concentrating more irreversibility generation than in the HE case. On the other hand, the HE machine has more irreversibility concentration at the evaporator.

Another observation regards to exergy destruction analysis, the HE machine destroys 3.05 times more exergy while demanding 2.66 times the amount of resource in the SE unit.

A comparison involving only exergy losses of dissipative heat exchangers is shown in Figure 50. The HE chiller has low absorber and condenser presenting lesser percentage values of exergy losses than in the SE case. Moreover, although the HE case presents an extra dissipative heat exchanger that rejects more exergy losses, the sum of percentage values in the HE case does not overpass the sum of percentage values in the SE case.

In short, the SE chiller concentrates more total exergy losses in the dissipative heat exchangers (29.56%) than the HE machine (22.08%).

Figure 50 – Comparison of exergy losses of dissipative heat exchangers.

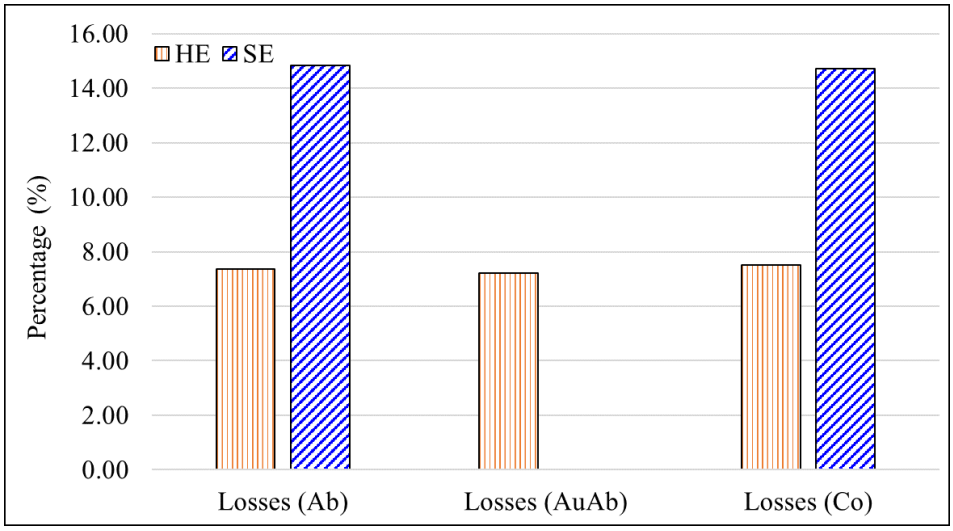

Source: Own Authorship.

An overall exergy analysis inside the chillers is carried out in Figure 51. It is verified that all chiller structures present high percentage values of total irreversibility, followed by the total exergy losses in the dissipative heat exchangers.

Figure 51 – Overall comparison in means of exergy in each optimal solution.

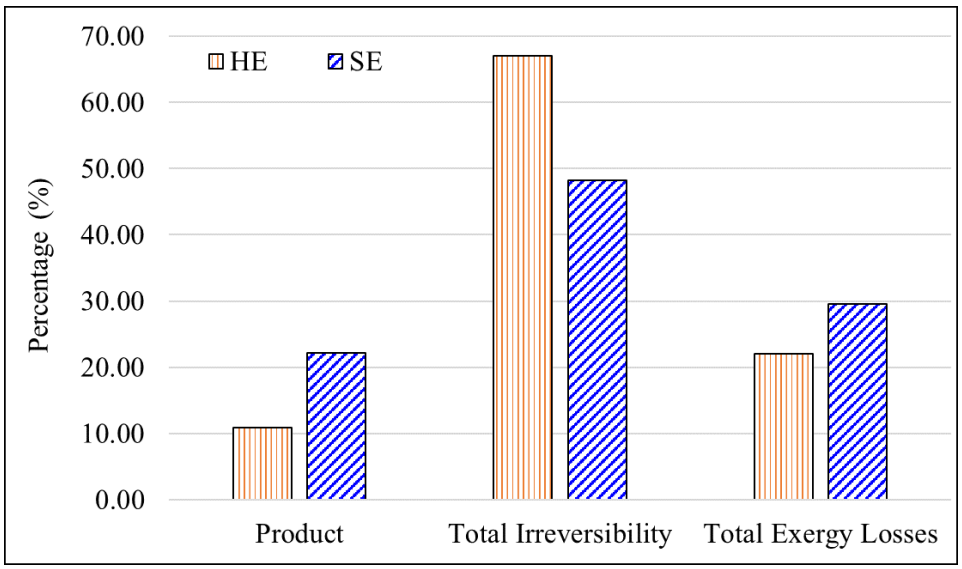

Source: Own Authorship.

The exergy efficiency in the HE configuration is 10.82%, whereas the SE chiller performs better exergy efficiency, presenting a value around 22.2%. A comparison between these chillers shows an interesting result here, the HE unit has more total irreversibility concentration than the SE case. Further, the opposite occurs when looking at the total exergy losses.

Independently of which objective function is considered, all chillers need a cooling tower to reject heat to the environment. The cooling tower modelling is well detailed in section A.1 from Appendix A. Hence, in an effort to evaluate the energy and exergy analyses, all thermodynamic states are explicit in Table 34. Additionally, the thermodynamic states at the cooling tower are graphically presented in Figure 52.

Before introducing the amount of results, it is relevant to note that the input parameters in cooling tower modelling are considered the same values for both optimal cases. Therefore, only the cooling water mass flow rate is changing between the two optimal solutions.

As stated in section A.1, the parameter ratio $L\ G^{-1}$ is assumed unit, implicating that both cooling water (L) and dry air mass flow rates (G) are equal in cooling tower modelling. For the HE and SE chillers, the cooling water mass flow rates at the cooling tower are calculated around 352.945 and 177.454 kg s^{-1}, respectively.

Table 34 – Thermodynamic states at the cooling tower.

State	$\Phi'_{i,a}$	$p_{a,i}$ (bar)	$T_{i,a}$ (°C)	$p_{w,i}$ (bar)	$T_{i,w}$ (°C)	$h_{i,a}$ (kJ kg^{-1})	$h_{i,w}$	$s_{i,a}$ (kJ kg^{-1} K^{-1})	$s_{i,w}$
0	0.780	1.013	31.1	1.013	31.8	88.626	133.336	5.918	0.461
1	0.805	1.013	31.2	1.013	32.4	91.053	135.660	5.926	0.469
2	0.828	1.013	31.4	1.013	32.9	93.481	137.984	5.934	0.477
3	0.848	1.013	31.5	1.013	33.5	95.912	140.308	5.942	0.484
4	0.865	1.013	31.8	1.013	34.0	98.345	142.632	5.950	0.492
5	0.880	1.013	32.0	1.013	34.6	100.781	144.955	5.958	0.499
6	0.894	1.013	32.2	1.013	35.1	103.219	147.279	5.966	0.507
7	0.906	1.013	32.5	1.013	35.7	105.661	149.603	5.974	0.514
8	0.917	1.013	32.8	1.013	36.3	108.106	151.927	5.982	0.522
9	0.926	1.013	33.1	1.013	36.8	110.555	154.250	5.990	0.529
10	0.935	1.013	33.4	1.5	37.4	113.053	156.617	5.998	0.537

Source: Own Authorship

It is interesting to note in Figure 52 that the air at the exit of cooling tower is not completely saturated. The calculated relative humidity at the exit is 93.5% with a dry-bulb temperature of 33.4°C. The specific exergies are exposed consecutively in Table 35.

Figure 52 – Thermodynamic states of cooling tower at the psychrometric chart.

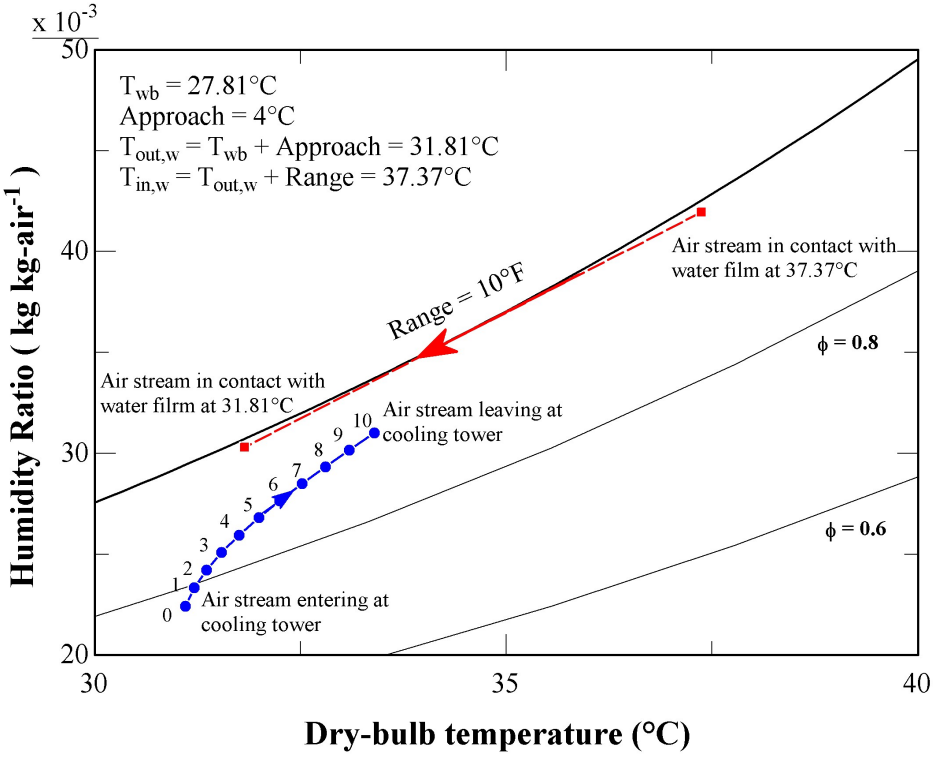

Source: Own Authorship.

Table 35 – Specific exergies at the cooling tower.

State	Fluid	State	T_i (°C)	p_i (bar)	$e_{ph,i}$ (kJ kg^{-1})	$e_{ch,i}$ (kJ kg^{-1})	$e_{to,i}$ (kJ kg^{-1})
10	Cooling Water	in	37.4	1.5	1.093	50.252	51.344
0	Cooling Water	out	31.8	1.013	0.321	50.252	50.573
0	Air	in	31.1	1.013	-0.021	0	-0.021
10	Air	out	33.4	1.013	0.333	0.191	0.524

Source: Own Authorship

By using the information in Table 34 and Table 35, the energy and exergy analyses at the cooling tower for all optimal solutions are evaluated and exposed in Table 36. Since the cooling tower parameters known as range (5.6°C) and approach (4°C) are defined constant for both optimal solutions with a wet-bulb temperature of 27.81°C, the heat transfer rate is directly proportional to cooling water mass flow rate. Bearing in mind about the previous comments, as a matter of fact, the cooling tower is not optimized at all.

Table 36 – Thermodynamic analysis at the cooling tower.

	Min OF_1 (US$ ton^{-1})	Max OF_2 (US$ h^{-1})
	311.7	30.7
	HE	SE
Energy analysis		
$\dot{Q}$ (kW)	8216.957	4131.320
$\dot{W}_{a,flow}$ (kW)	60.795	30.567
$\dot{W}_{w,p}$ (kW)	52.616	26.454
NTU	0.961	0.961
L_{mw} (kg s^{-1})	3.032	1.525
Exergy analysis		
$\sum \dot{E}_{leaving}$ (kW)	18034.171	9067.263
$\sum \dot{E}_{entering}$ (kW)	18175.126	9138.132
$\dot{L}$ (kW)	192.405	96.737
$\dot{I}$ (kW)	140.955	70.869
$\dot{E}_{des}$ (kW)	333.360	167.607
ξ_{ex}	0.9922	0.9922

Source: Own Authorship

By observing Table 36, the HE chiller requires indeed a much bigger cooling tower than the other case due the high amount of heat transfer rate that is released to the environment. Further, the HE chiller is rejecting highest heat transfer rate whereas the SE machine is presenting the lowest heat transfer rate.

An important variable that must be defined is the number of transfer units (NTU), the meaning of this variable is basically related to tower sizing. As the wet-bulb temperature, range, approach and $L\ G^{-1}$ are set constant for both optimization cases, the NTUs must be equals.

Another important result from this energy analysis regards to make up water mass flow rate for each optimal solution, then, depending on the cooling water demand, it might be an undesirable operating cost for cooling tower operation. For the HE case, the make up water mass flow rate at the cooling tower is 3.032 kg s^{-1}. The SE scenario requires 1.525 kg s^{-1} of make up water.

When comparing these previous results, it is analysed that the SE machine uses a cooling tower demanding lesser make up water than in the HE chiller. This analysis is very important due the necessity to figure out where to extract enough source of water at the UTE LORM, thereby, it is reasonable to discuss this issue.

The exergy analysis in cooling tower is also an essential step, allowing to evaluate the exergy performance of this equipment. The Table 36 also presents great values of total exergy leaving and total exergy entering in the HE case which is expected. Moreover, it is

verified that SE chiller uses a cooling tower destroying lesser exergy than in the HE case.

As the temperature values are equal in each optimal solution, the irreversibility generation is directly tied to the quantity of heat transfer rate that is dissipated in this equipment. Regarding the exergy losses rates, it also depends directly on the amount of heat transfer rate at the cooling tower. Thus, as the heat transfer rate is varying with cooling water mass flow rate, it is expected more exergy losses in the HE case.

Figure 53 has a comparison of the temperature chart versus cumulative heat transfer rate at the cooling tower for HE and SE cases. As discussed in previous analyses, the region between the temperature profiles of hot and cold streams regards to the presence of irreversibility, thereupon the cooling tower is presenting more exergy destruction in the HE case by dissipating more heat.

Figure 53 – Temperature chart of cooling tower in HE and SE chillers.

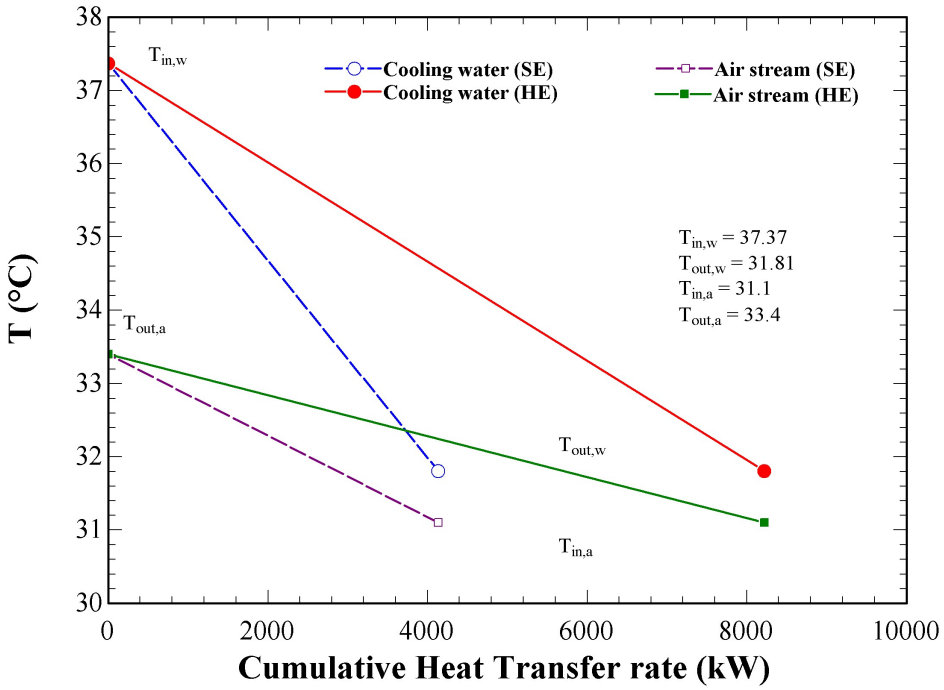

Source: Own Authorship.

The cooling tower also demands electric power in its operating condition in order to maintain an upward air stream by using a fan coupled with an electric motor and a cooling water flowing through a pump that is driven by an electric motor.

For the sake of simplicity, a pressure difference on air stream and fan mechanical efficiency inside the cooling tower are defined as 0.1961 kPa and 0.75, respectively (THRELKELD, 1970), thus, the fan input power is calculated only in function of air

mass flow rate. Table 37 presents the power demands on the air stream, shaft and electric motor as well as the irreversibility rates for each optimal solution.

Table 37 – Thermodynamic analysis of the fan inside the cooling tower ($\eta_{mec,fan} = 0.75$ and $\eta_{em,fan} = 0.95$).

	Min OF_1 (US$ ton^{-1})	Max OF_2 (US$ h^{-1})
	311.7	30.7
	HE	SE
Energy analysis		
$\dot{W}_{a,flow}$ (kW)	60.795	30.567
$\dot{W}_{shaft,fan}$ (kW)	81.060	40.756
$\dot{W}_{em,fan}$ (kW)	85.327	42.901
Exergy analysis		
$\dot{I}_{shaft,fan}$ (kW)	20.265	10.189
$\dot{I}_{em,fan}$ (kW)	4.267	2.145

Source: Own Authorship

When considering the profit as objective function, there are other equipment that must be discussed in this chapter. The cooling coil, exhaust gases heat exchanger and chilled water auxiliary heat exchanger are presented in sequence. Appendix A contains all assumptions and mathematical modelling to predict the thermodynamic states in these heat exchangers. In addition, Appendix D presents a brief data of all historic environmental records at the Linhares's city.

The cooling coil delivers to W20V34SG engine a humid air with wet-bulb temperature of 12.5°C. The ambient condition is assumed with the following settings: dry-bulb temperature of 31.1°C, wet-bulb temperature of 27.81°C and atmospheric pressure of 1 atm.

As it is essential to expose the thermodynamic states as well as the specific exergies, Table 38 presents the thermodynamic states at the cooling coil by using Stoecker and Jones (1985) methodology which is used for energy and exergy analyses.

A second approach from Mansour and Hassab (2012) is utilized to define the geometric aspects such as length, height, depth, number of rolls and other practical informations. Therefore, both methods are combined simultaneously.

Table 38 – Designing the cooling coil by using Stoecker and Jones (1985) methodology.

State	$T_{i,a}$ (°C)	$\Phi'_{i,a}$	$T_{i,cw}$ (°C)	$h_{i,a}$ (kJ kg^{-1})	$h_{i,cw}$ (kJ kg^{-1})	$s_{i,a}$ (kJ kg^{-1} K^{-1})	$s_{i,cw}$ (kJ kg^{-1} K^{-1})
1	31.1	0.780	12.0	88.626	50.515	5.918	0.180
2	29.2	0.819	11.5	83.297	–	5.900	–
3	27.4	0.856	11.0	77.968	–	5.882	–
4	25.6	0.891	10.5	72.640	–	5.864	–
5	23.7	0.923	10.0	67.311	–	5.846	–
6	21.9	0.952	9.5	61.982	–	5.828	–
7	20.0	0.978	9.0	56.653	–	5.810	–
8	18.2	0.999	8.5	51.325	–	5.792	–
9	16.2	1.015	8.0	45.996	–	5.674	–
10	14.3	1.025	7.5	40.667	–	5.666	–
11*	12.3	1.028	7.013	35.338	29.763	5.657	0.1065
*	12.5	1.000	7.013	35.333	29.763	5.736	0.1065

*Correcting the thermodynamic state to saturation line.

Source: Own Authorship

The method from Stoecker and Jones (1985) is presenting fog formation zone at the psychrometric chart, causing a problem on the humid air properties in EES software. Then, thermodynamic values at the exit of cooling coil must be properly corrected. This same issue occurs in Table 39 which provides thermodynamic states for each row in the cooling coil modelling by utilizing Mansour and Hassab (2012) approach. In order to solve this issue, it is corrected the properties of air stream by assuming saturation condition ($\Phi'_a = 1.0$) with the dry-bulb temperature of 12.5°C at the exit of cooling coil.

Table 39 – Designing the cooling coil by using Mansour and Hassab (2012) methodology.

Row	$T_{i,a}$ (°C)	$\Phi'_{i,a}$	$T_{i,cw}$ (°C)	$h_{i,a}$ (kJ kg^{-1})	$h_{i,cw}$ (kJ kg^{-1})	$s_{i,a}$ (kJ kg^{-1} K^{-1})	$s_{i,cw}$ (kJ kg^{-1} K^{-1})
1	31.1	0.780	12.0	88.626	50.515	5.918	0.180
2	26.7	0.849	10.8	76.101	–	5.872	–
3	23.1	0.913	9.9	65.608	–	5.837	–
4	20.1	0.956	9.1	56.897	–	5.808	–
5	17.6	0.984	8.4	49.726	–	5.784	–
6	15.4	0.999	7.8	43.864	–	5.764	–
7	13.7	1.006	7.4	39.103	–	5.663	–
8	12.2	1.008	7.013	35.256	29.763	5.657	0.1065

Source: Own Authorship

At last, Table 40 has the respective specific exergies at the cooling coil. Moreover, regarding the chilled water and dry air mass flow rates, the cooling coil requires 39.861

and 15.523 kg s^{-1}, respectively. The condensed water is estimated around 0.206 kg s^{-1}.

The condensed water that is withdrew in cooling coil heat exchanger can be used as make up water at the cooling tower equipment. However, it is noted that this small amount of condensed water is not sufficient to supply the make up water. Thus, another source of water is required to supply completely the make up water at the cooling tower.

Table 40 – Specific exergies for each thermodynamic state at the cooling coil by using Stoecker and Jones (1985) methodology.

Row	Fluid	State	T_i (°C)	p_i (bar)	$e_{ph,i}$ (kJ kg^{-1})	$e_{ch,i}$ (kJ kg^{-1})	$e_{to,i}$ (kJ kg^{-1})
11	Chilled Water	in	7.013	3	2.566	50.252	52.818
1	Chilled Water	out	12.0	1.6	1.280	50.252	51.532
1	Air	in	31.1	1.013	-0.021	0	-0.021
11	Air	out	12.5	1.013	0.763	0.675	1.438
11	Condensed Water	out	8.953	1.013	-8.950	50.252	41.302

Source: Own Authorship

The thermodynamic states from both methodologies are graphically compared in Figure 54.

Figure 54 – Thermodynamic states of the cooling coil at the psychrometric chart.

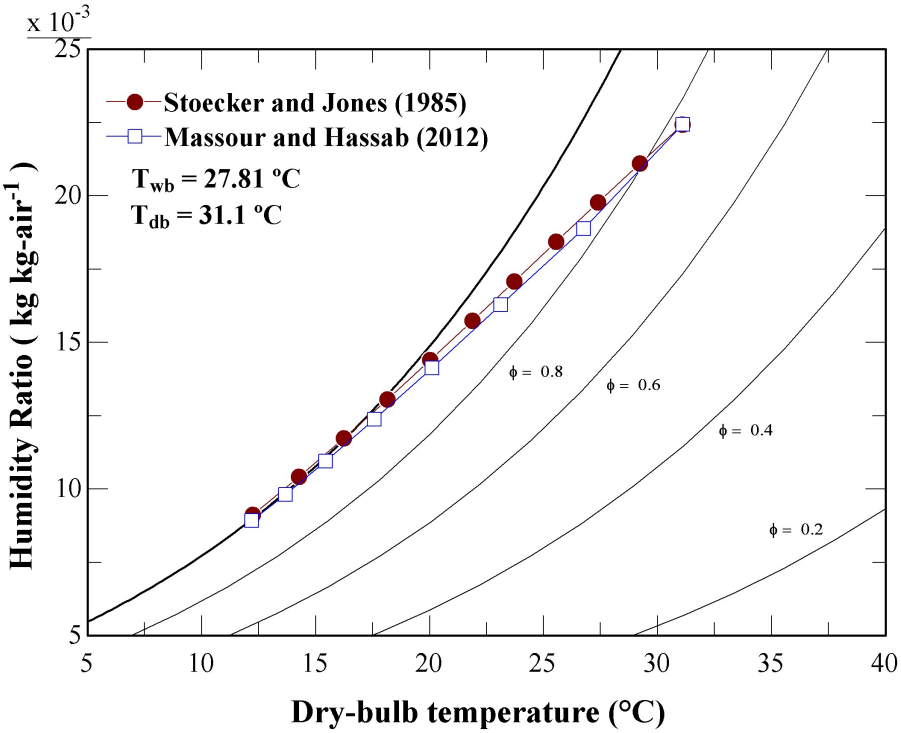

Source: Own Authorship.

In line with the more realistic approach, the total number of 7 rows is imperative to achieve the desired thermodynamic state at the exit of cooling coil. In addition, the height, depth and length are calculated based on practical data, resulting in the respective values of 2.572, 0.209 and 2.688 m.

Unfortunately, a drawback of these geometric results are regarded to the air-filter house due the necessity to fit the cooling coil without exceeding the current dimensions. As the cooling coil is not optimized in this master's thesis, this second approach is just presented in order to provide more practical results.

Concerning the energy and exergy analyses at the cooling coil, Table 41 presents the main thermodynamic results and Figure 55 represents the temperature chart versus cumulative heat transfer rate in this heat exchanger. The cooling coil modelling uses enthalpy potential difference definition combined with thermodynamic laws to determine the heat transfer area and the global heat transfer coefficient.

Table 41 – Thermodynamic analysis at the cooling coil by using Stoecker and Jones (1985) methodology.

	Max OF_2 (US\$ h^{-1})
	30.7
	SE
Energy analysis	
$\dot{Q}$ (kW)	827.201
ΔT_{lm} (°C)	10.716
A (m^2)	776.581
U (kW m^{-2} K^{-1})	0.0994
Exergy analysis	
Product (kW)	31.180
Resource (kW)	51.255
$\dot{I}$ (kW)	20.075
η_{ex}	0.608

Source: Own Authorship

When analysing the exergy on air stream inside the cooling coil, there are some decreasing and increasing exergy variations which can be explained because the standard temperature reference that is adopted during the exergy analysis is 25°C. Basically, the air stream enters the cooling coil and suffers a reduction of exergy until it crosses the reference temperature. From that point, the exergy begins to rise on air stream, resulting in an increased exergy variation.

On the other hand, the chilled water stream is increasing the temperature from 7 to 12°C which implicates that the exergy is reducing. Hence, it is assumed the air stream as product and the chilled water as resource during the exergy evaluation.

Figure 55 – Temperature chart of the cooling coil.

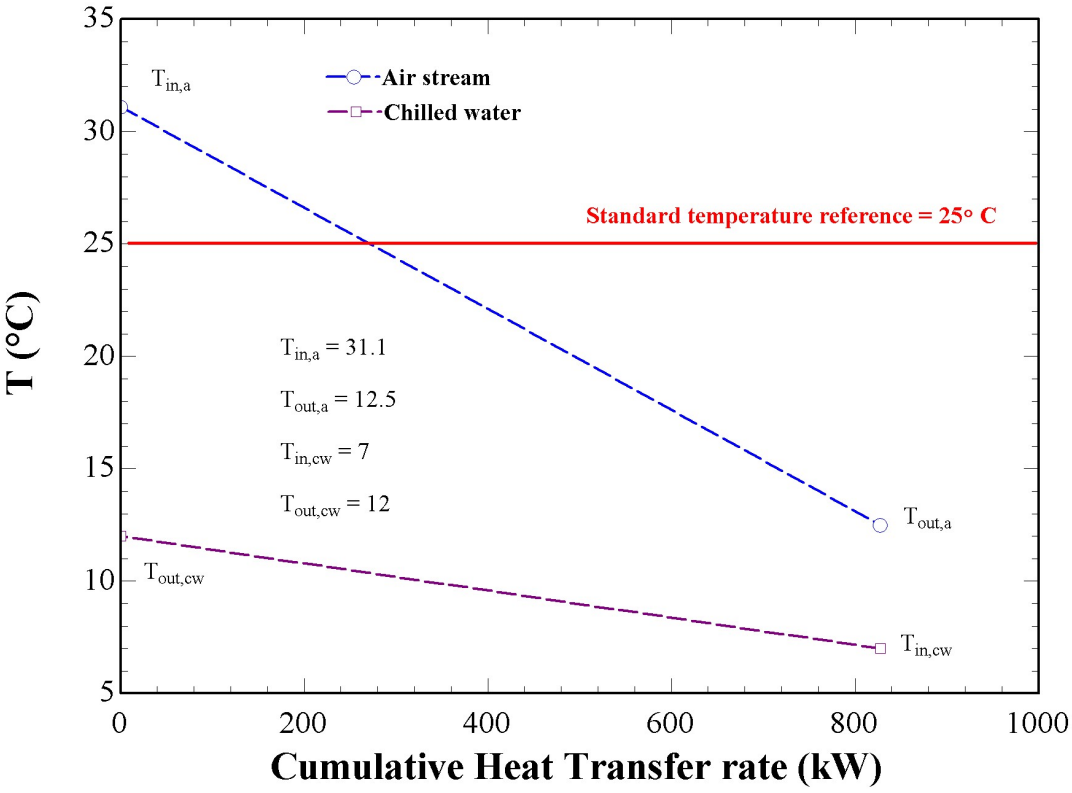

Source: Own Authorship.

The next equipment that must be discussed regards to exhaust gases heat exchanger which recovers part of the exhaust gases stream from W20V34SG engine and produces hot water to drive the absorption unit. Table 42 shows the thermodynamic states of exhaust gases heat exchanger for the local maximum solution.

Table 42 – Thermodynamic states at the exhaust gases heat exchanger.

Structure	Fluid	State	p (bar)	T (°C)	h (kJ kg^{-1})	s (kJ kg^{-1} K^{-1})
	Water	in	4.0	85.38	357.795	1.139
SE	Water	out	2.0	94.97	397.947	1.250
(30.7 US$ h^{-1})	Exhaust Gases	in	1.047	408.71	422.525	0.896
	Exhaust Gases	out	1.047	347.32	352.410	0.788

Source: Own Authorship

Table 43 has all specific exergies for each thermodynamic state in exhaust gases heat exchanger at the local maximum solution.

Table 43 – Specific exergies for each thermodynamic state at the exhaust gases heat exchanger.

Structure	Fluid	State	$\dot{m}$ (kg s^{-1})	e_{ph} (kJ kg^{-1})	e_{ch} (kJ kg^{-1})	e_{to} (kJ kg^{-1})
	Water	in	28.177	22.894	50.252	73.146
SE	Water	out	28.177	29.925	50.252	80.177
(30.7 US$ h^{-1})	Exhaust Gases	in	16.136	155.290	26.097	181.387
	Exhaust Gases	out	16.136	117.308	26.097	143.405

Source: Own Authorship

By using the information in Table 42 and Table 43, it is possible to evaluate the energy balance as well as the exergy analysis at the exhaust gases heat exchanger. Therefore, all calculated parameters from energy and exergy analyses are exposed in Table 44.

Table 44 – Thermodynamic analysis at the exhaust gases heat exchanger.

	Max OF_2 (US$ h^{-1})
	30.7
	SE
Energy analysis	
$\dot{Q}$ (kW)	1131.372
ΔT_{lm} (°C)	287.048
A (m^2)	78.828
Exergy analysis	
Product (kW)	198.117
Resource (kW)	612.865
Wasted exergy at the chimney (kW)	2313.963
$\dot{I}$ (kW)	414.748
$\dot{E}_{des}$ (kW)	2728.711
η_{ex}	0.323

Source: Own Authorship

From the energy analysis, the log mean temperature difference is resulting in a huge value, implicating in low heat transfer area.

An exergy analysis is also repeated here for the exhaust gases heat exchanger. The hot water stream is defined as product and the exhaust gases stream as resource.

As the log mean temperature difference is assuming a great value, it is expected a huge amount of irreversibility in this heat exchanger. Regarding the wasted exergy at the

chimney, it must be accounted as exergy destruction. This component has a low exergy efficiency due high irreversibility generation.

Figure 56 shows the representation of the temperature chart versus cumulative heat transfer rate at the exhaust gases heat exchanger.

Figure 56 – Temperature chart of the exhaust gases heat exchanger.

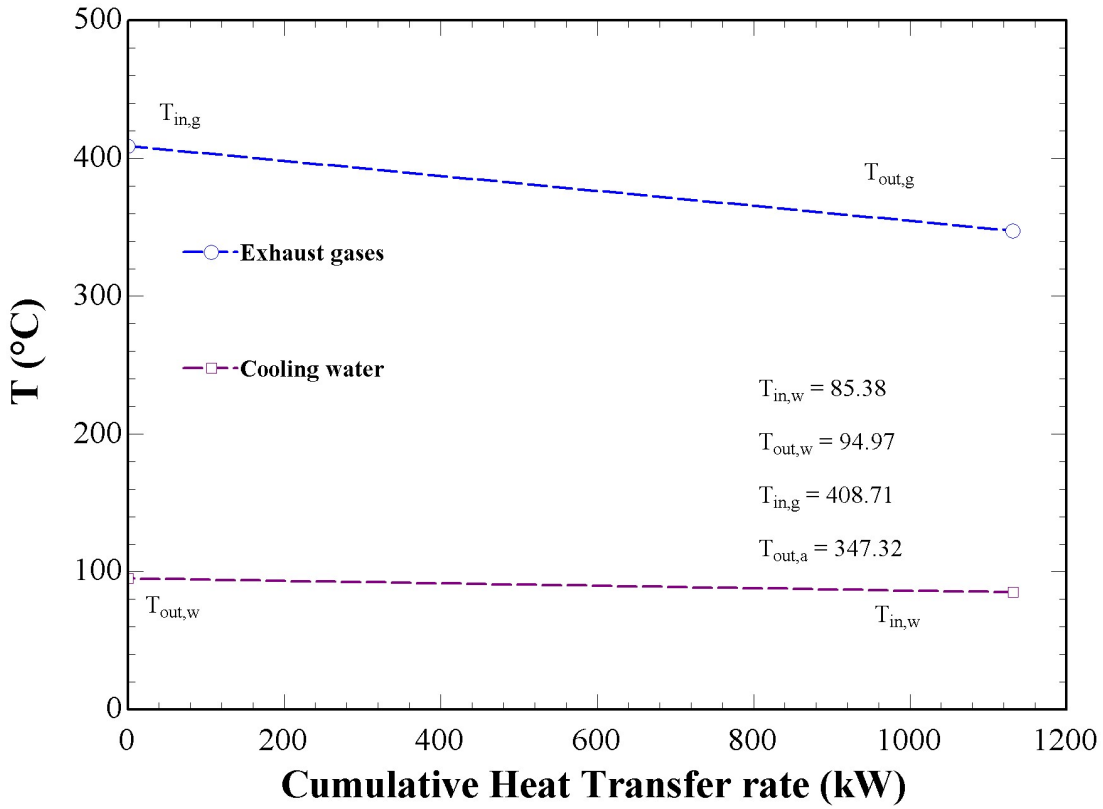

Source: Own Authorship.

The next discussion is about the chilled water auxiliary heat exchanger. Table 45 and Table 46 have the thermodynamic states and specific exergies that are necessary in order to evaluate the energy and exergy analyses in this component, respectively. Thus, all calculated parameters are shown in Table 47.

Table 45 – Thermodynamic states at the chilled water auxiliary heat exchanger.

Structure	Fluid	State	p (bar)	T (°C)	h (kJ kg^{-1})	s (kJ kg^{-1} K^{-1})
SE (30.7 US$ h^{-1})	Chilled Water	in	3.0	7.013	29.763	0.1065
	Chilled Water	out	1.6	12.0	50.515	0.180
	Cooling Water	in	4.0	42.1	176.496	0.600
	Cooling Water	out	4.0	33.4	140.298	0.483

Source: Own Authorship

Table 46 – Specific exergies for each thermodynamic state at the chilled water auxiliary heat exchanger for local maximum solutions.

Structure	Fluid	State	$\dot{m}$ (kg s^{-1})	e_{ph} (kJ kg^{-1})	e_{ch} (kJ kg^{-1})	e_{to} (kJ kg^{-1})
SE (30.7 US$ h^{-1})	Chilled Water	in	39.945	2.566	50.252	52.818
	Chilled Water	out	39.945	1.280	50.252	51.532
	Cooling Water	in	22.900	2.267	50.252	52.519
	Cooling Water	out	22.900	0.787	50.252	51.039

Source: Own Authorship

By evaluating the energy analysis at the Table 47, there is an amount of heat transfer rate that is rejected on chilled water stream, assisting the radiator. Hence, bringing some energy savings at the radiator fans.

The log mean temperature difference in this heat exhanger is resulting in high value, implicating in small heat transfer area.

Further, when analysing the exergy fluxes in this component, both exergy variations in the cooling water and chilled water streams are decaying which mean that there is no product. The exergy variations are completely destroyed inside this heat exchanger, thereupon, the irreversibility rate can be calculated by summing them.

As this heat exchanger is a dissipative component, the exergy efficiency is defined as the total exergy leaving divided by the total exergy entering.

Table 47 – Thermodynamic analysis at the chilled water auxiliary heat exchanger.

	Max OF_2 (US$ h^{-1})
	30.7
	SE
Energy analysis	
$\dot{Q}$ (kW)	828.954
ΔT_{lm} (°C)	28.193
A (m^2)	29.402
Exergy analysis	
$\sum \dot{E}_{leaving}$ (kW)	3227.221
$\sum \dot{E}_{entering}$ (kW)	3312.502
$\Delta \dot{E}_{Cooling}$ (kW)	33.917
$\Delta \dot{E}_{Chilled}$ (kW)	51.364
$\dot{I}$ (kW)	85.281
ξ_{ex}	0.9743

Source: Own Authorship

Figure 57 – Temperature chart of chilled water auxiliary heat exchanger.

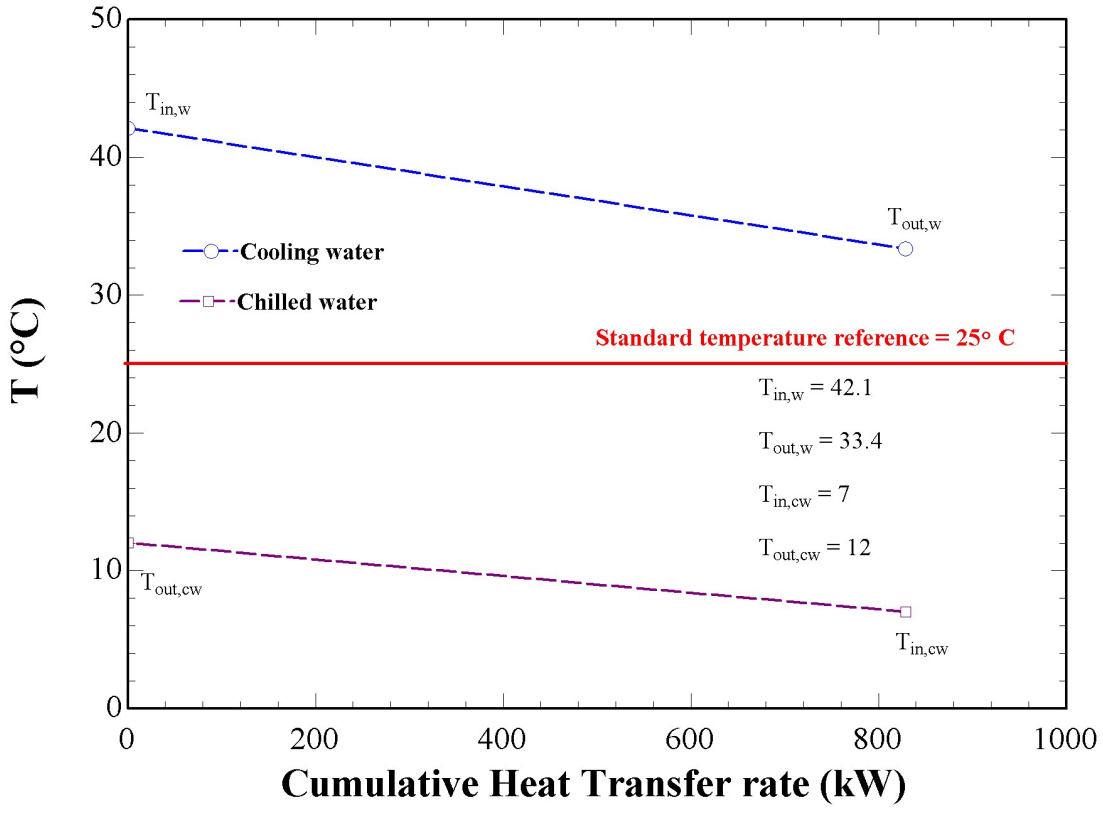

Source: Own Authorship.

The W20V34SG engine is also affected by the new thermal system that is proposed in this master's thesis. Therefore, it is fundamental to discuss how this integration is influencing the energy and exergy distribution in the W20V34SG engine.

One of the subjects that is targeted in this thesis regards to radiator savings, thus, it is firstly presented a brief energy analysis in this component. Reminding that the auxiliary heat exchanger assists the cooling effects at the radiator, it is investigated how much of exergy is destroyed as well as the exergy efficiency in the radiator.

The energy and exergy analyses at the radiator component are carried out based on information from Table 48 and Table 49.

Table 48 – Thermodynamic states at the radiator.

Structure	Fluid	State	p (bar)	T (°C)	h (kJ kg^{-1})	s (kJ kg^{-1} K^{-1})
SE (30.7 US$ h^{-1})	Air	in	1.013	31.1	88.626	5.918
	Air	out	1.013	58.0	116.852	6.007
	Cooling Water	in	4.0	74.5	312.051	1.009
	Cooling Water	out	4.0	42.1	176.496	0.600

Source: Own Authorship

Table 49 – Specific exergies for each thermodynamic state at the radiator.

Structure	Fluid	State	$\dot{m}$ (kg s^{-1})	e_{ph} (kJ kg^{-1})	e_{ch} (kJ kg^{-1})	e_{to} (kJ kg^{-1})
SE (30.7 US$ h^{-1})	Air	in	109.977	-0.021	0	-0.021
	Air	out	109.977	1.664	0	1.664
	Cooling Water	in	22.900	15.780	50.252	66.032
	Cooling Water	out	22.900	2.267	50.252	52.519

Source: Own Authorship

The thermodynamic analysis at the radiator is shown in Table 50, presenting a great amount of thermal energy being released at the environment. It is seen that the radiator has a reduction in its rotation speed, presenting an electrical energy saving around 29.02 kW.

The exergy analysis shows that this heat exchanger destroys a considerable amount of exergy, resulting in an low exergy efficiency when compared to other dissipative heat exchangers. The temperature profiles at the radiator is explicit in Figure 58.

Table 50 – Thermodynamic analysis at the radiator ($\eta_{em}^{inverter} = 1$).

	Max OF_2 (US$ h^{-1})
	30.7
	SE
Energy analysis	
$\dot{Q}$ (kW)	3104.208
ΔT_{lm} (°C)	13.517
$A_{manufacturer}$ (m^2)	10126
U (kW m^{-2} K^{-1})	0.02268
$\dot{W}_{fan}$ (kW)	48.680
N_{fan} (RPM)	740.2
Exergy analysis	
$\sum \dot{E}_{leaving}$ (kW)	1385.646
$\sum \dot{E}_{entering}$ (kW)	1558.503
$\dot{L}$ (kW)	185.267
$\dot{I}$ (kW)	172.857
$\dot{E}_{des}$ (kW)	358.124
ξ_{ex}	0.8891

Source: Own Authorship

Figure 58 – Temperature chart of radiator.

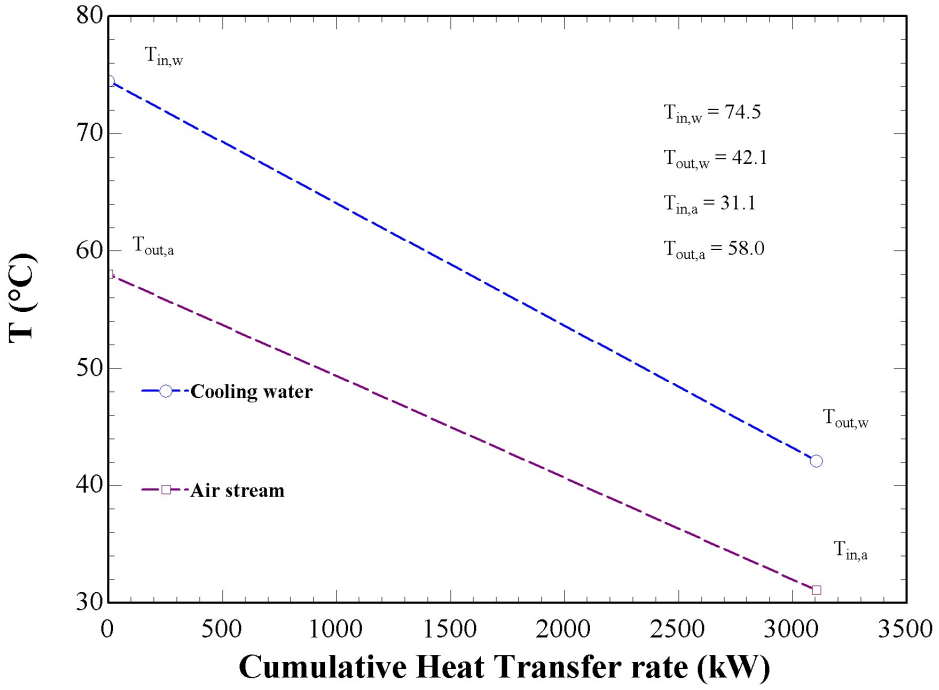

Source: Own Authorship.

Figure 59 summarizes the cooling water being cooled through radiator and chilled water auxiliary heat exchanger.

Figure 59 – Temperature chart at the radiator and chilled water auxiliary heat exchanger.

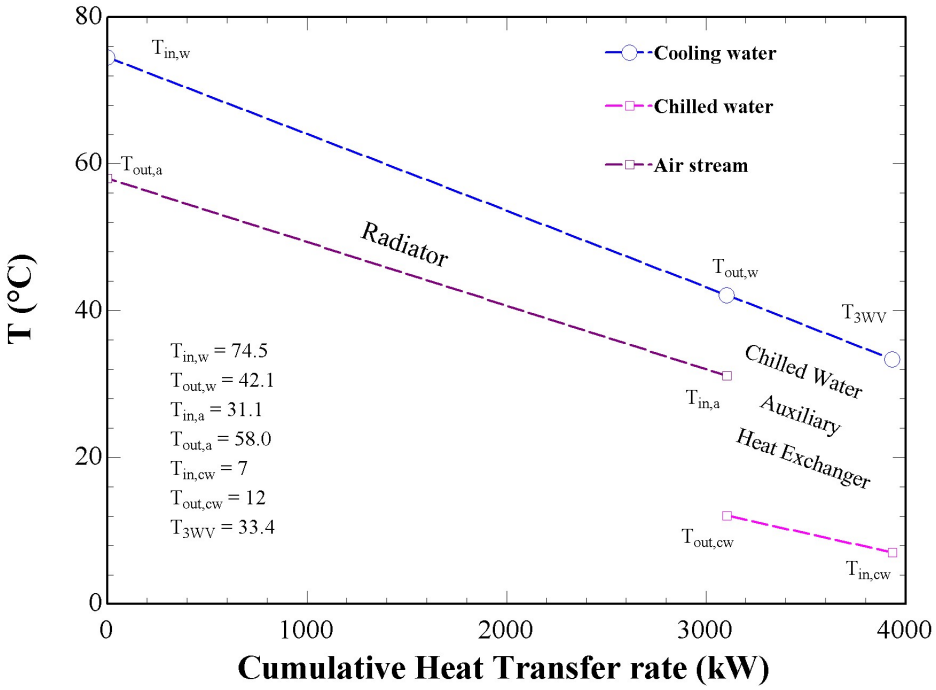

Source: Own Authorship.

The thermal system requires three additional pumps to maintain the water stream flowing in each independent circuit. First of all, the cooling tower needs a centrifugal pump to overcome the head of the cooling water circuit. The same logic applies to chilled water circuit which presents another pump supplying enough work in order to keep the water stream flowing through the heat exchangers and mechanical devices. And thirdly, as the hot water circuit is integrated to the engine cooling water, a booster pump is necessary to overcome the extra pressure difference caused by the exhaust gases heat exchanger and other devices on the flowing patch.

It is important to remember that the HE case does not minimize the electric power demands of each electric motor coupled to the water pumps. Table 51 presents the results in regard to each pump and electric motor.

Table 51 – Thermodynamic analysis of each water pump for each optimal solutions.

	Min OF_1 (US$ ton^{-1})			Max OF_2 (US$ h^{-1})		
	311.7			30.7		
	HE			SE		
Water circuit	cooling	chilled	hot	cooling	chilled	hot
$\Delta\dot{E}_{flow}$ (kW)	42.327	20.388	23.629	21.281	15.705	7.057
$\dot{W}_p$ (kW)	52.616	25.904	28.199	26.454	19.954	8.421
$\dot{W}_{em}$ (kW)	55.385	27.267	29.683	27.846	21.004	8.865
$\dot{I}_p$ (kW)	10.289	5.516	4.570	5.173	4.249	1.364
$\dot{I}_{em}$ (kW)	2.769	1.363	1.484	1.392	1.050	0.444
$\eta_{ex,p}$	0.8045	0.7871	0.8379	0.8045	0.7871	0.8379

Source: Own Authorship

By analysing Table 51, the HE case needs water pumps and electric motors demanding more shaft power and electric power, respectively. As the thermodynamic states around the cooling water pump are equal for both cases, the input power estimation is only varying with the mass flow rate in each circuit. Moreover, the exergy efficiency of cooling water pump does not change in any case due to the same reason. The chilled and hot water pumps also obey the same previous logic, thus, only modifying in function of mass flow rate in each circuit.

The exergy analysis permits to observe the irreversibility rate in each pump, then, as the HE case requires bigger water pumps and electric motors than in the SE case, the irreversibility generation these components must follow by presenting greater values.

The W20V34SG engine is influenced by the new thermal system, thus, it is important to analyse how the energy and exergy fluxes are occurring in this equipment. One of the goals of this master's thesis is to enhance the engine performance, thereby, the optimization procedures are set for *BMEP* equal 23.45 bar, which mean a shaft power output around 10220 kW or electric power output of 10016 kW ($\eta_{eg}^{ICE} = 0.98$).

The brake engine efficiency for rated shaft power output of 8716 kW (*BMEP* of 20 bar) is 44.87%, consuming a fuel mass flow rate of 0.405 kg^{-1}. When increasing the *BMEP* to 23.45 bar (10220 kW of shaft power output), there is an efficiency enhancement of 0.39% with an extra fuel consumption of 0.0658 kg s^{-1}.

Moreover, a brochure from the manufacturer is consulted in an effort to define the heat losses rates of the engine. The mass flow rate of natural gas is calculated around 0.4708 kg s^{-1}, and with an estimated *LHV* of 47965 kJ kg^{-1}, the amount of energy is equal to 22583 kW. The heat losses distribution of the engine are well presented in Table 52.

Table 52 – Energy rate balance and thermodynamic states for W20V34SG engine at the shaft power output of 10220 kW ($\eta_{ICE}^{brake} = 45.26\%$) integrated with SE chiller.

	Heat Losses		$\dot{m}$	T_{in}	T_{out}	h_{in}	h_{out}
	(kW)	(%)	(kg s^{-1})	(°C)	(°C)	(kJ kg^{-1})	(kJ kg^{-1})
Exhaust Gases	6818	30.19	16.136	–	408.71	–	422.525
CACs (air)	2643	11.70	15.523	204.6	39.4	233.329	63.088
Block (Water)	1530	6.77	30.040	76.0	88.1	318.439	369.365
Lube Oil	1050	4.65	–	–	–	–	–
R/C	322	1.43	–	–	–	–	–

Source: Own Authorship

Figure 60 presents the energy flow sheet on W20V34SG engine in Sankey diagram. By using the first law of thermodynamics, it seems that there is a great opportunity to recover thermal energy on exhaust gases stream.

Nevertheless, as the energy analysis does not provide enough information about the entropy generation, it is crucial to execute a proper exergy analysis. The application of the second law will confirm precisely and truly the energy availability.

Figure 60 – Energy rate flow sheet of W20V34SG engine in Sankey diagram.

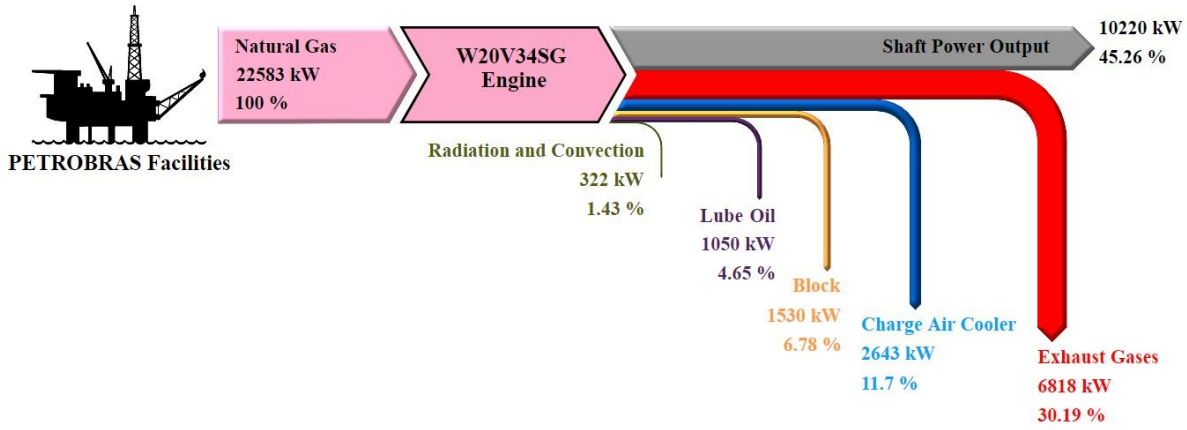

Source: Own Authorship.

Figure 61 presents the exergy flow sheet on W20V34SG engine, representing in a simple manner the thermal energy sources in their true forms. The chemical exergy of natural gas ($e_{ch,f}$) is determined on Appendix C as 49739.121 kJ kg^{-1}, thus, the total chemical exergy rate in natural gas is calculated by just multiplying the mass flow rate of natural gas with the previous value, resulting in 23417 kW. Therefore, the engine exergy efficiency is calculated around 43.64% against 43.27% of the rated condition of 8.7 MW, presenting an exergy efficiency improvement of 0.37%.

In addition, when evaluating the available thermal energy on exhaust gases stream, the energy analysis gives an amount of 6818 kW (30.19%). Notwithstanding, the total exergy rate on exhaust gases stream assumes a value of 2926.828 kW, which represents 12.499% of the total exergy rate from natural gas. These results prove that there is minor exergy availability on exhaust gases stream when compared with energy analysis in this same engine.

The exergy rate at the engine cooling water is also calculated and its value is approximately 529.739 kW (2.262%). Therefore, the irreversibility and other exergy losses of the engine are estimated by subtracting the shaft power output, cooling water and exhaust gases exergy rates from the quantity of chemical exergy of natural gas, thereby, resulting approximately in 9740.4 kW (41.60%).

It is important to repeat here that the optimal solution sets the engine cooling water to flow directly and fully to exhaust gases heat exchanger, being preheated to 95°C before entering the SE chiller. Hence, the SE machine is recovering exergy rates from both cooling water and exhaust gases streams.

Figure 61 – Exergy rate flow sheet of W20V34SG engine.

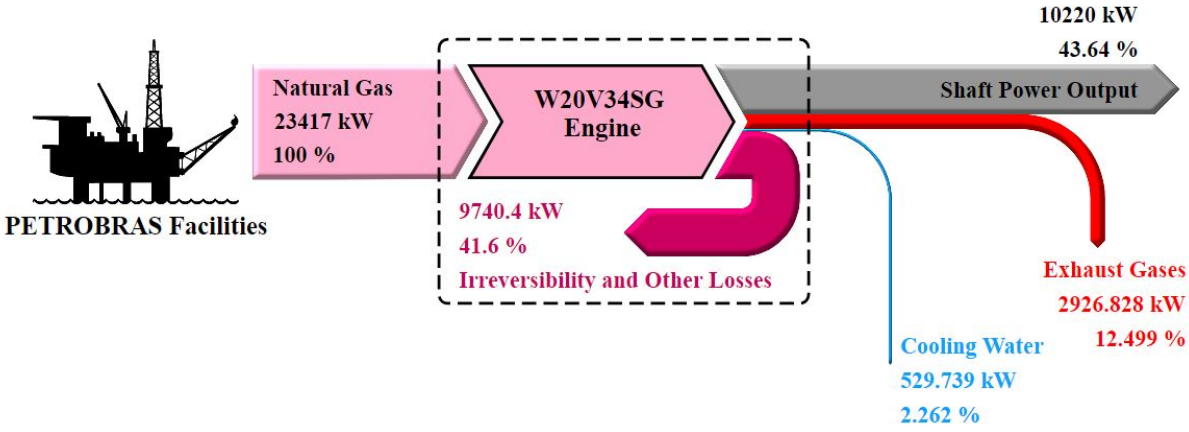

Source: Own Authorship.

The importance on evaluating each internal and external heat exchanger as well as other components and equipment that are imperative in the thermal system regards to the fact that it is possible to investigate, track and map each exergy flow such as irreversibility rates, exergy losses, and work in an exergy flow sheet. Hence, this task permits to analyse with confidence the energy in its true quality in each component.

Firstly, it is discussed the exhaust gases heat exchanger which wastes 2313.963 kW of exergy rate and generates 414.749 kW of irreversibility. Then, producing 198.117 kW of hot water to power the SE unit.

Since the incoming exergy rate from booster pump in hot water circuit is 7.057 kW, it is possible to define the amount of exergy that is recovered from the engine cooling water. Thus, as the high desorber presents a total resource in means of exergy around 391.553 kW, the exergy rate from engine cooling water is calculated by excluding 198.117 and 7.057 kW from this previous value, resulting in 186.377 kW.

Besides this amount of recovered exergy on engine cooling water, a small part of the exergy is destroyed at the radiator, presenting a value of 309.444 kW. Further, a portion of 33.917 kW of the amount of exergy on engine cooling water is destroyed due the cooling effect from chilled water auxiliary heat exchanger. Thus, the rest of exergy rate is determined around 9740.7 kW which is completely destroyed by the engine. Regarding the electrical energy demand at the radiator fans, an input power of 48.68 kW is required from the grid. As the UTE LORM usually operates the radiator under full load speed, the electrical energy demand at the radiator is 77.7 kW, thereby, representing an electrical energy saving of 29.02 kW.

When recalling the exergy analysis in the SE chiller, there is a total exergy destruction rate of 304.639 kW that is divided into irreversiblity and exergy losses. Firstly, lets discuss about the exergy losses rate of 115.759 kW which is destroyed at the cooling tower. Besides this dissipative heat exchanger presents irreversibility and exergy losses rates, it also demands electric power to drive the cooling water pump and fan. For instance, the pump increases the exergy rate in cooling water circuit by 21.281 kW due the necessity to overcome the head of this system.

Moreover, the fan at the cooling tower demands 42.901 kW of electric power which implicates in 40.760 kW of shaft power, then, delivering 30.567 kW of work on air stream. Hence, the cooling tower destroys in means of thermal and mechanical exergy a total amount of 167.607 kW.

In relation to the chiller irreversibility rate, it is estimated from previous exergy analysis in the SE machine, resulting in 188.880 kW. This quantity of irreversibility is resulted by subtracting the amount of product and total exergy losses from the resource.

As discussed before, the amount of product in means of exergy is 86.914 kW. However, another pump is needed in order to overcome the head of the chilled water system, thereupon, the amount of exergy rate is increased by the pump which adds 15.705 kW. Therefore, there is a total amount of exergy rate of 102.619 kW in the chilled water stream.

The auxiliary heat exchanger and cooling coil utilize the quantity of exergy rate from chilled water stream as a resource to provide cooling effects. Notwithstanding, the auxiliary heat exchanger does not present a product, destroying all incoming exergy rates. The cooling coil presents a product due the increasing of exergy variation on air stream.

The chilled water auxiliary heat exchanger uses 51.364 kW of exergy rate from the chilled water stream, provoking a reduction in means of exergy on the engine cooling water around 33.916 kW, thus, generating 85.281 kW of irreversibility rate.

The cooling coil uses 51.255 kW of exergy rate to produce 31.180 kW in means of exergy for intake air cooling, then, the irreversibility rate is determined around 20.075 kW.

Table 53 has a detailed exergy destruction analysis in each equipment, presenting each percentage value in regard to the chemical exergy of the fuel (23417 kW - 100%).

Table 53 – Exergy destruction analysis in each isolated equipment.

	Max OF_2 (US$ h^{-1}) 30.7 SE	
Isolated Unit	$\dot{E}_{des,i}$	
	(kW)	(%)
SE Chiller	304.639	1.30
Cooling Tower	167.607	0.72
Chilled Water Auxiliary HX	85.281	0.36
Fan and Electric Motor	12.334	0.05
Cooling Water Pump and Electric Motor	6.565	0.03
Booster Pump and Electric Motor	1.808	0.01
Chilled Water Pump and Electric Motor	5.299	0.02
Cooling Coil	20.075	0.09
W20V34SG Engine with Electric Generator	13401	57.23
Radiator	358.124	1.53
Exhaust Gases HX	2728.711	11.65
Thermal system with W20V34SG engine	13550.3	57.87

Source: Own Authorship

Figure 62 shows the energy flow sheet of the entire thermal system integrated to the W20V34SG engine. In sequence, Figure 63 presents a detailed exergy distribution. These flowsheets are showing each percentage value of energy and exergy rates in each component by comparing with the incoming chemical energy and exergy rates of natural gas, respectively.

Figure 62 – Energy rate flow sheet of the thermal system coupled to W20V34SG engine in Sankey diagram.

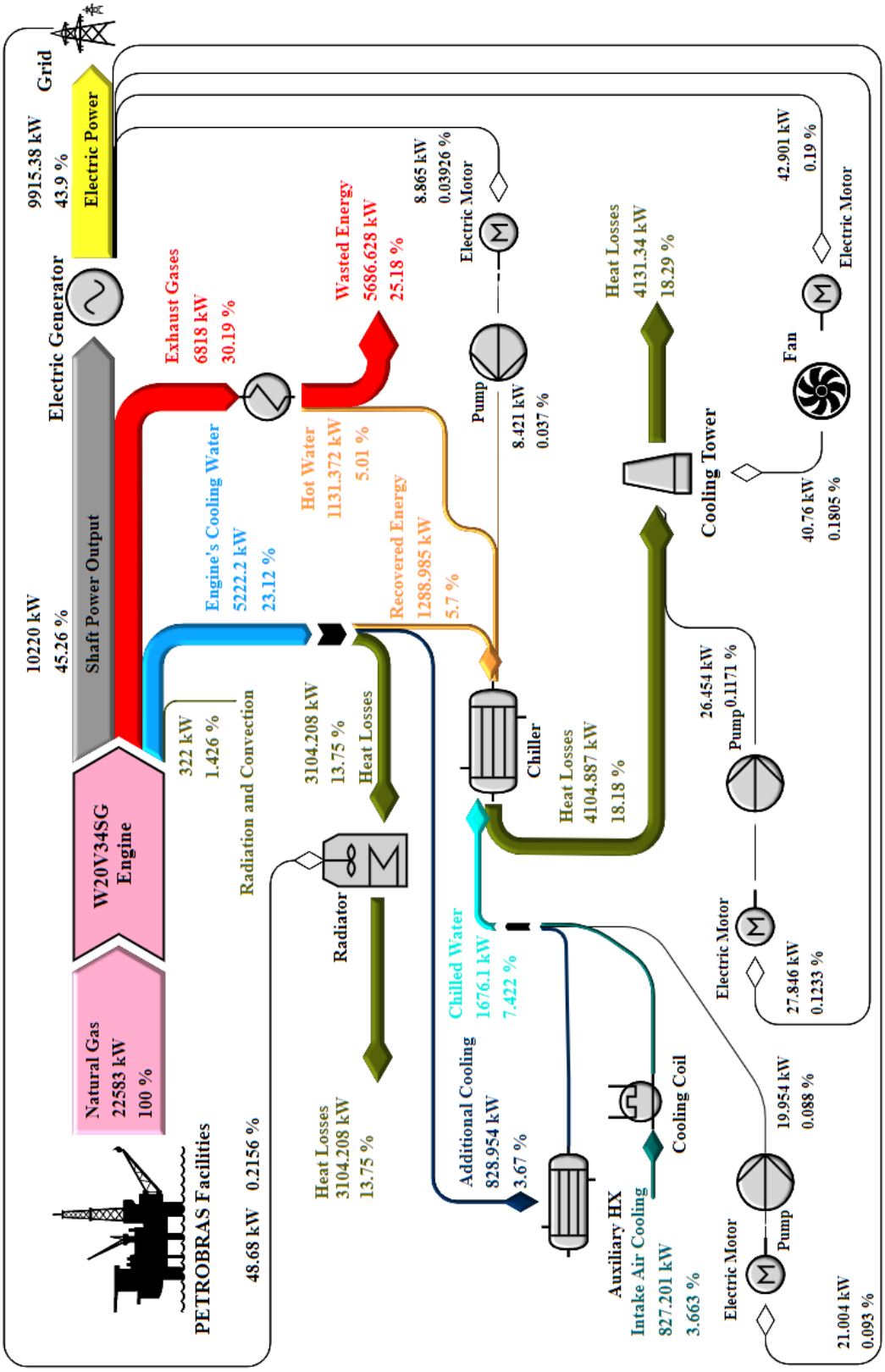

Source: Own Authorship.

Figure 63 – Exergy rate flow sheet of the thermal system coupled to W20V34SG engine for SE chiller.

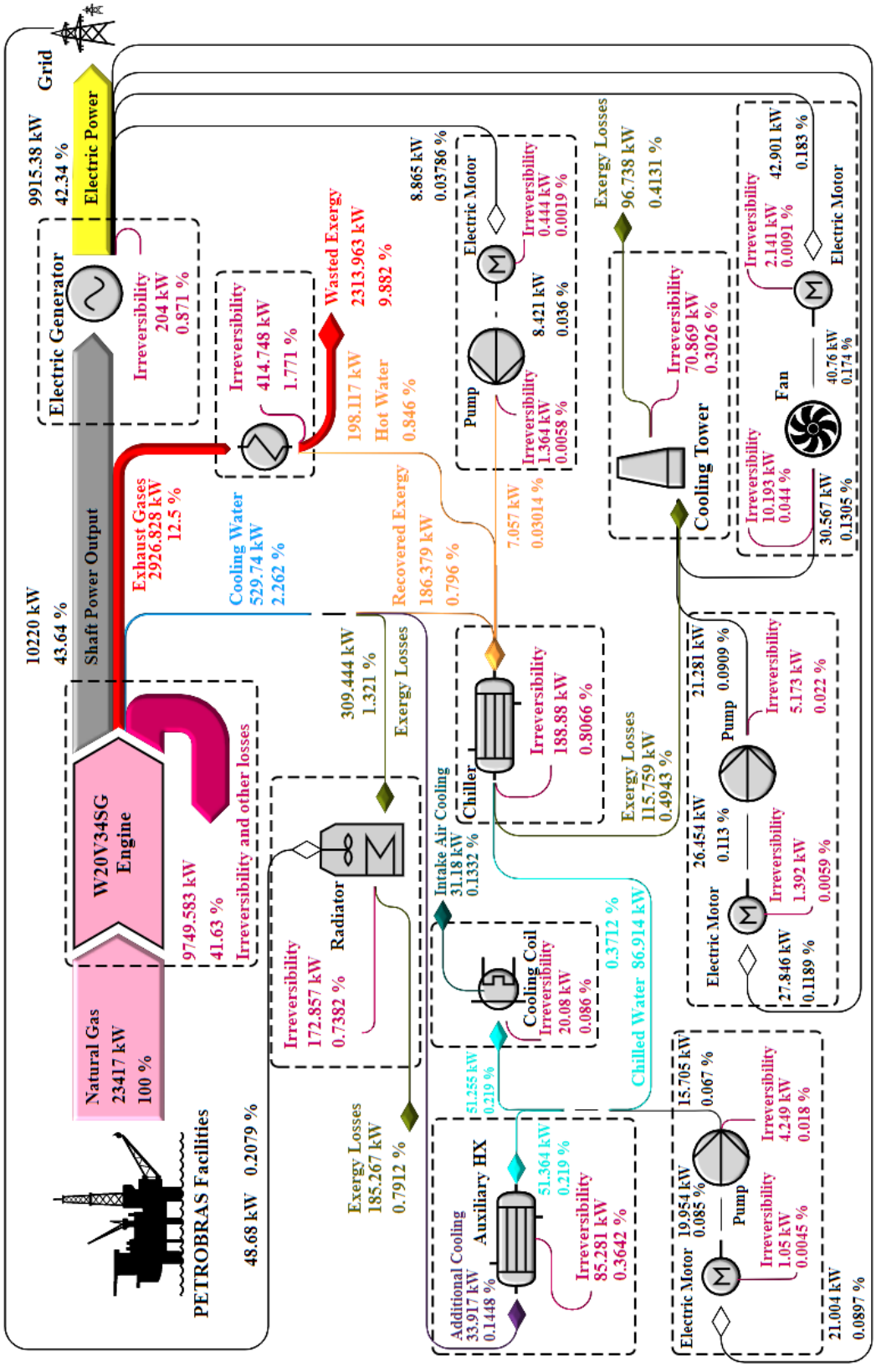

Source: Own Authorship.

For *BMEP* of 23.45 bar, it has been shown that the engine shaft power output is 10220 kW with a *BSFC* of 164.7 g kWh^{-1}. As a matter of fact, a safe operating condition inside the piston-cylinders must be checked, thereby, the peak pressure is calculated around 184.4 bar which is based on GT-Power simulations. This peak pressure is below the manufacturer limit of 186 bar. Further, the mass flow rate of exhaust gases on waste-gate valve is estimated around 0.218 kg s^{-1}, it means that the turbochargers are not losing control at the waste-gate valve.

5.3 Economics

The economic evaluation of each optimal solution is also an essential part of the main results. Before introducing this respective discussion about each equipment cost. Table 54 presents all purchase costs of each equipment for both HE and SE chillers.

Table 54 – Purchase costs of all equipment in each optimal solution.

	Min OF_1 (US\$ ton^{-1})		Max OF_2 (US\$ h^{-1})	
	311.7		30.7	
	HE		SE	
Type of Component i	Z_i (US\$)	(%)	Z_i (US\$)	(%)
Evaporator	34,696.00	17.99	56,343.00	29.98
Condenser	14,299.00	7.41	21,956.00	11.68
Auxiliary Absorber	33,489.00	17.36	∅	∅
Low Absorber	38,930.00	20.19	37,658.00	20.04
High Desorber	∅	∅	53,898.00	28.68
Auxiliary Desorber	29,664.00	15.38	∅	∅
Low Desorber	38,878.00	20.16	∅	∅
High Solution HX	∅	∅	12,010.00	6.39
Auxiliary Solution HX	∅	∅	∅	∅
Low Solution HX	∅	∅	∅	∅
High Solution pump	∅	∅	248.00	0.13
Auxiliary Solution pump	261.00	0.14	∅	∅
Low Solution pump	247.00	0.13	229.00	0.12
Chiller Cost Residue (∅)	2,395.00	1.24	5,593.00	2.98
Total Chiller Cost	192,859.00	100.00	187,935.00	100.00

Source: Own Authorship.

The chiller cost residue (∅) in Table 54 regards to all components that are not accounted in the final structures. Reminding that EES software is a mathematical tool that just proceeds by calculating a set of equations. The solution heat exchangers that are erased in HE and SE chillers present non-null values on heat transfer area calculations. Hence, implicating in some residues on the economic evaluations.

It is interesting to observe here that the total chiller cost of HE chiller is more expensive (US$ 192,859.00) than the SE chiller (US$ 187,935.00). A comparison between these both chillers shows different purchase costs for each component. The HE chiller presents more expensive purchase costs on the following sequence; low absorber, low desorber, evaporator, auxiliary absorber, auxiliary desorber, and condenser. In the SE chiller, the purchase costs are organized in descending order as follows; evaporator, high desorber, low absorber, condenser and high solution heat exchanger.

When comparing these two different results, the purchase costs of evaporator and condenser are increased in the SE chiller while the low absorbers are practically resulting in same values.

The purchase costs of solution pumps are quite small when compared to the heat exchangers. Although there is a specific equation to determine the purchase costs of electric motors, the required electric powers are practically resulting in null values which implicate in smaller purchase costs. Figure 64 exposes a comparison of the main purchase costs as percentage values.

Figure 64 – Comparison of the main purchase costs inside the absorption chillers.

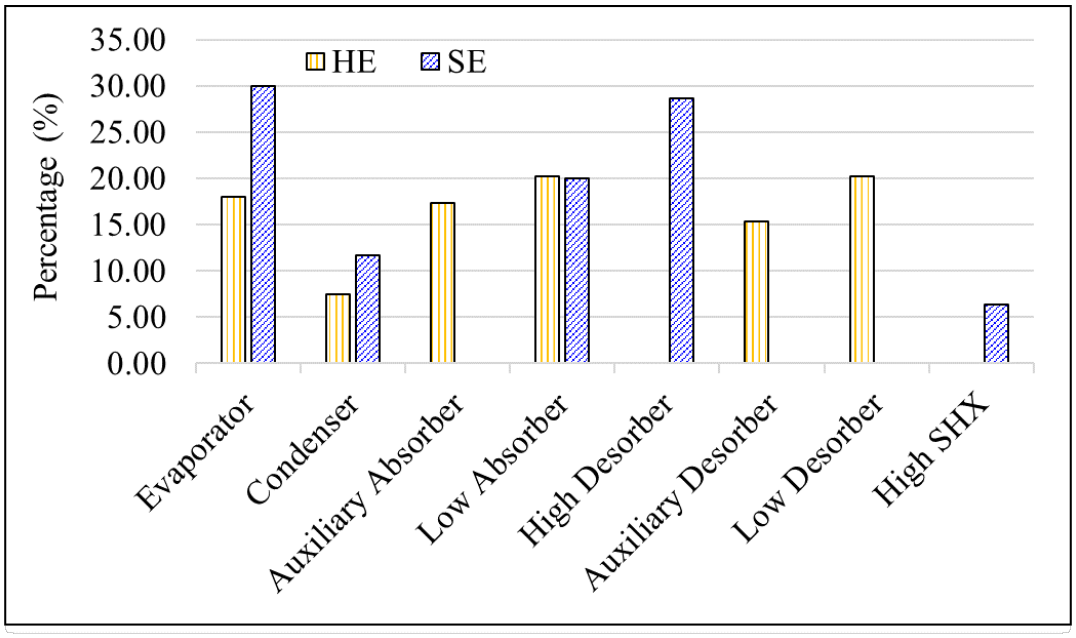

Source: Own Authorship.

Table 55 has the purchase costs of all equipment in the thermal system. The SE absorption chiller corresponds to 51.27% of the total cost of investment. Secondly, the cooling tower and cooling water distribution are representing 25.06%. The exhaust gases heat exchanger, chilled water auxiliary heat exchanger and cooling coil sum 23.67%.

Table 55 – Purchase costs of all equipment in the thermal system.

	Min OF_1 (US$ ton^{-1})		Max OF_2 (US$ h^{-1})	
	311.7		30.7	
	HE		SE	
Equipment i	Z_i (US$)	(%)	Z_i (US$)	(%)
SE Chiller	192,859.00	–	187,935.00*	51.27
Cooling Coil	–	–	29,278.00*	7.99
Chilled Water Auxiliary HX	–	–	16,179.00*	4.41
Exhaust gases HX	–	–	41,306.00*	11.27
Cooling Tower	273,573.00	–	137,547.00	15.29
Cooling Water Distribution	192,859.00	–	87,928.00	9.77
$TCI_{literature}$	–	–	899,911.00	100.00

*These costs must be summed and multiplied by the expansion factor of 2.45519.

Source: Own Authorship.

Figure 65 presents a comparison between these equipment in means of percentage values.

Figure 65 – Comparison of each equipment purchase cost in the thermal system.

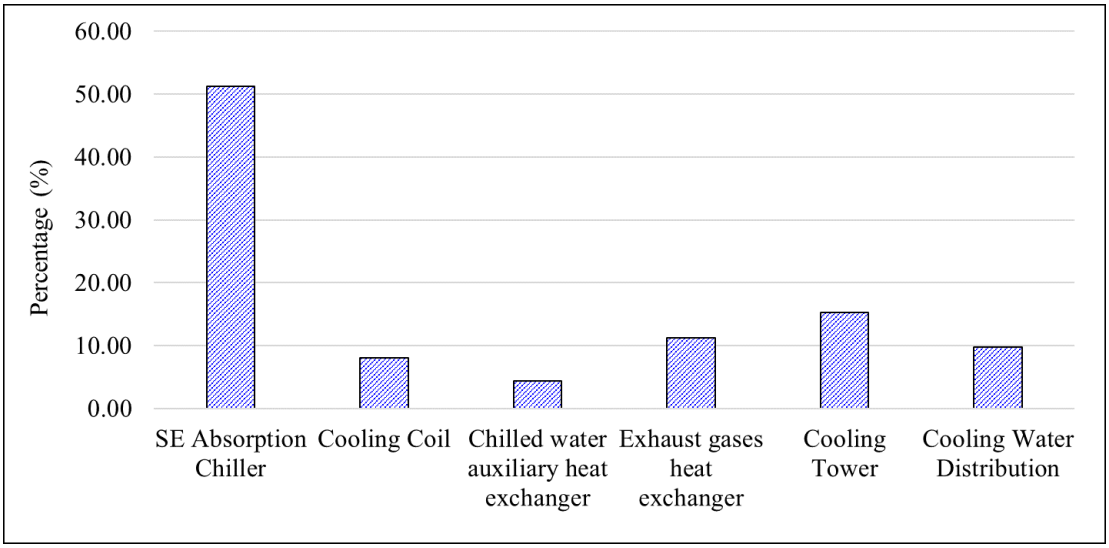

Source: Own Authorship.

During the R&D project, it is firstly contacted a company "A" to request the preliminary budget of the installation of this new thermal system at the UTE LORM. Secondly, the commercial representatives of Life's Good company in Brazil are also contacted in order to request only the SE chiller budget. Table 56 presents the comparison of SE chiller cost between this study with the budgets of each company.

Table 56 – Comparison of purchase costs of SE chiller with manufacturer budget.

	Z_i (US$)	TCI (US$)
SE Chiller (Literature)	187,935.00	899,911.00
SE Chiller (Company "A")	125,000.00	782,500.00*
SE Chiller (Life's Good)	180,000.00	–

*It does not consider the indirect costs of instrumentation and control systems.

Source: Own Authorship.

As there is additional electric power output from W20V34SG engine, it is calculated the Levelized Cost of Energy ($LCOE$) of the entire integration between the new thermal system with one engine.

The extra fuel consumption is calculated around 0.0658 kg s^{-1} ($P_f = 0.026$ US$ kg^{-1}) which gives a fuel cost rate of 6.178 US$ h^{-1}. By acknowledging this previous value with the total cost (investment expenditure) and operating cost of the thermal system based on SE chiller, the $LCOE$ for 20 years of this additional electric power generation is estimated around 1.92 ¢US$ kWh^{-1} by using Equation 5.1.

$$LCOE = \frac{TCI_{t=0} + \sum_{t=1}^{20} \frac{Z_{O\&M,t} + Z_{fuel,t}}{(1+i_{eff})^t}}{n_{ope} \cdot \sum_{t=1}^{20} \frac{\dot{W}_{ele,add,t}}{(1+i_{eff})^t}} \tag{5.1}$$

In the year of 2018, the TEVISA company requested a commercial budget to a company with the intention to acquire an Organic Rankine Cycle (ORC) powered with hot water that would be produced by the exhaust gases from Wärtsilä diesel engine of 9 MW at the UTE VIANA thermoelectric power plant. By using the information from Table 57, the $LCOE$ of this alternative waste heat recover application was calculated around 5.715 ¢US$ kWh^{-1}.

Table 57 – Calculating $LCOE$ for 20 years.

	SE optimal result	Commercial ORC system
$\dot{W}_{ele,add}$ (kW)	1471	144
TCI (US$)	899,911.00	409,762.00
Z_{fuel} (US$)	51,837.00	–
$Z_{O\&M}$ (US$)	41,654.00	3,740.00
i_{eff} (%)	15.0	15.0
$LCOE$ (US$ MWh^{-1})	19.20	57.15

Source: Own Authorship.

When comparing both technologies, although the SE optimal result presents more

investment expenditure and greater operation and maintenance costs, it is generating more additional power output. Hence, the $LCOE$ of this repowering application on W20V34SG engine is more competitive than the hot water ORC system.

5.3.1 Investment Scenario for UTE LORM

This master's thesis is part of a R&D project (ANEEL PD-06483-0318/2018) in partnership between UFES and UTE LORM, thereby, it is interesting to discuss the investment scenario by applying the economic indicators. In an effort to discuss the investment scenario for the UTE LORM, it is necessary to define a cash flow over 20 years, assuming 96% (8409.6 hours) of operating dispatch condition. The cash flow rate for maximum solution of 30.7 US$ h^{-1} is equal to 47.782 US$ h^{-1}. Therefore, Table 58 presents the cash flow under operating condition of 8409.6 hours over 20 years.

Table 58 – Cash flow under operating condition of 8409.6 hours over 20 years.

		Max OF_2 (US$ h^{-1}) 30.7 SE	
Year	Capitals (US$)	Present Value (US$)	Accumulated Present Value (US$)
0	(899,911.00)	(899,911.00)	(899,911.00)
1	401,828.00	349,416.00	(550,495.00)
2	401,828.00	303,840.00	(246,655.00)
3	401,828.00	264,209.00	17,554.00
4	401,828.00	229,747.00	–
5	401,828.00	199,780.00	–
6	401,828.00	173,722.00	–
7	401,828.00	151,062.00	–
8	401,828.00	131,358.00	–
9	401,828.00	114,225.00	–
10	401,828.00	99,326.00	–
11	401,828.00	86,370.00	–
12	401,828.00	75,105.00	–
13	401,828.00	65,308.00	–
14	401,828.00	56,790.00	–
15	401,828.00	49,383.00	–
16	401,828.00	42,941.00	–
17	401,828.00	37,340.00	–
18	401,828.00	32,470.00	–
19	401,828.00	28,235.00	–
20	401,828.00	24,552.00	–

Source: Own Authorship

The economic indicators are well presented in Table 59. For local maximum solution of 30.7 US$ h^{-1}, the investment scenario is very attractive, the NPV is more than one and a half million dollars. By considering a minimum attractive rate of 15% at the UTE LORM, the IRR turns out to be considerably promising. The NDP and DP periods demonstrate that the investment would be paid less than three years, thereupon, matching

the business requirements of this R&D project which is a maximum limit of 5 years.

Table 59 – Economic indicators for maximum solution.

	Max OF_2 (US\$ h^{-1})
	30.7
	SE
NPV (US\$)	1,615,267.00
IRR (%)	44.62
NDP (Years)	2.24
DP (Years)	2.93

Source: Own Authorship

The investment scenario is very promising, nevertheless, the investors must have a great initial capital. As the assumed conversion reference between the Brazilian and United States monetary system is R$ 5.38 to US$ 1.00, the total cost of investment would be around R$ 4,841,521.18.

A sensitivity investment analysis is also a fundamental step in order to evaluate the risks of this engineering enterprise. Thereupon, the operating dispatch hours and CVU are varied in this analysis. The dispatch is simulated in a range of 2000 to 8409.6 hours with a step of 500 hours. The historic record of CVU variation at the UTE LORM presents minimum and maximum values of 150 and 350 R$ MWh^{-1}, respectively. Table 60 to Table 62 show all simulations that are executed under these previous CVUs.

Table 60 – Simulating for CVU of 150 R$ MWh^{-1} in a range of 2000 to 8406.9 hours.

Operating Dispatch Number of Hours	$\dot{Z}_{total}$ (US\$ h^{-1})	Profit (US\$ h^{-1})	NPV (US\$)	IRR (%)	NDP (Years)	DP (Years)
2000	76.201	-42.978	-538,031.00	2.517	15.56	195,14
2500	60.961	-27.738	-434,055.00	5.359	12.09	129.76
3000	50.800	-17.577	-330,067.00	7.909	9.88	88.24
3500	43.543	-10.320	-226,091.00	10.269	8.36	59.53
4000	38.100	-4.877	-122,114.00	12.498	7.24	38.50
4500	33.866	-0.644	-18,131.00	14.635	6.39	22.42
5000	30.479	2.743	85,844.00	16.703	5.71	13.93
5500	27.708	5.514	189,818.00	18.721	5.17	10.70
6000	25.399	7.823	293,806.00	20.700	4.72	8.81
6500	23.445	9.777	397,781.00	22.650	4.34	7.55
7000	21.770	11.452	501,754.00	24.577	4.02	6.62
7500	20.320	12.903	605,714.00	26.486	3.74	5.90
8000	19.050	14.173	709,689.00	28.382	3.50	5.34
8409.6	18.122	15.100	794,864.00	29.927	3.32	4.94

Source: Own Authorship

Table 61 – Simulating for CVU of 210 R$ MWh^{-1} in a range of 2000 to 8406.9 hours.

Operating Dispatch Number of Hours	$\dot{Z}_{total}$ (US$ h^{-1})	Profit (US$ h^{-1})	NPV (US$)	IRR (%)	NDP (Years)	DP (Years)
2000	76.201	-27.393	-342,918.00	7.606	10.11	92.53
2500	60.961	-12.152	-190,165.00	11.052	7.94	51.56
3000	50.800	-1.992	-37,400.00	14.245	6.53	25.11
3500	43.543	5.265	115,354.00	17.280	5.55	12.78
4000	38.100	10.708	268,109.00	20.214	4.82	9.21
4500	33.866	14.942	420,868.00	23.079	4.26	7.32
5000	30.479	18.329	573,621.00	25.898	3.82	6.10
5500	27.708	21.099	726,373.00	28.685	3.46	5.26
6000	25.399	23.409	879,136.00	31.451	3.17	4.63
6500	23.445	25.362	1,031,888.00	34.200	2.92	4.12
7000	21.770	27.037	1,184,640.00	36.939	2.70	3.73
7500	20.320	28.488	1,337,381.00	39.669	2.52	3.41
8000	19.050	29.758	1,490,133.00	42.394	2.36	3.13
8409.6	18.122	30.686	1,615,267.00	44.624	2.24	2.93

Source: Own Authorship

Table 62 – Simulating for CVU of 350 R$ MWh^{-1} in a range of 2000 to 8406.9 hours.

Operating Dispatch Number of Hours	$\dot{Z}_{total}$ (US$ h^{-1})	Profit (US$ h^{-1})	NPV (US$)	IRR (%)	NDP (Years)	DP (Years)
2000	76.201	8.974	112,343.00	17.222	5.56	12.89
2500	60.961	24.214	378,912.00	22.298	4.40	7.75
3000	50.800	34.375	645,490.00	27.213	3.64	5.68
3500	43.543	41.632	912,059.00	32.044	3.11	4.51
4000	38.100	47.075	1,178,628.00	36.831	2.71	3.75
4500	33.866	51.308	1,445,201.00	41.593	2.40	3.21
5000	30.479	54.695	1,711,768.00	46.343	2.16	2.81
5500	27.708	57.466	1,978,335.00	51.084	1.96	2.50
6000	25.399	59.775	2,244,907.00	55.823	1.79	2.25
6500	23.445	61.729	2,511,474.00	60.559	1.65	2.04
7000	21.770	63.403	2,778,039.00	65.293	1.53	1.88
7500	20.320	64.865	3,044,602.00	70.025	1.43	1.74
8000	19.050	66.125	3,311,169.00	74.759	1.34	1.62
8409.6	18.122	67.052	3,529,541.00	78.636	1.27	1.53

Source: Own Authorship

The first result from this sensitivity investment analysis is the total cost rate ($\dot{Z}_{total}$) profile in function of the number of operating dispatch hours. As the SE chiller is kept the same structure for all CVUs, there is only one total cost rate profile.

Figure 66 – Total cost rate in function of CVU and operating dispatch hours.

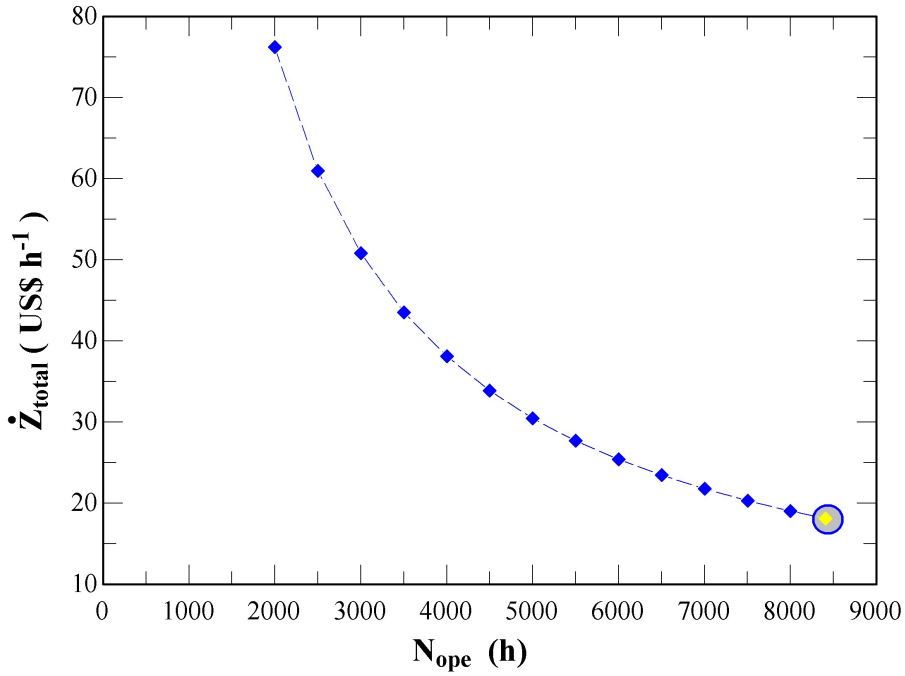

Source: Own Authorship.

The second result is about the profit rate profile in function of CVU and the number of operating dispatch hours. The investment scenario is highlighted with yellow color inside a gray circle.

In Figure 67, when assuming a CVU of 150 R$ MWh^{-1}, the profit is reduced considerably. Also, in order to maintain a profitable scenario, the operating dispatch hours must be greater than 5000 hours. As the CVU is increased to 210 R$ MWh^{-1}, there is a broader profitable range above 3500 hours. The third scenario of 350 R$ MWh^{-1} increases significantly the profit rate, resulting always in profitable condition no matter the operating dispatch hour.

The economic indicators are well represented in Figure 68 to Figure 71, the NPV must follow always the profit sign, i.e. if it is positive, the NPV must be positive. In Figure 67, when analysing only the NPV, the project can be judged similarly to the profit rate.

Moreover, the minimum attractive rate is 15% at the UTE LORM, then, by evaluating Figure 68, the IRR follows the NPV behavior which is an approval condition under the same range of operating dispatch hours. Therefore, presenting IRRs values above the minimum attractive rate of 15%.

Figure 67 – Profit rate in function of CVU and operating dispatch hours.

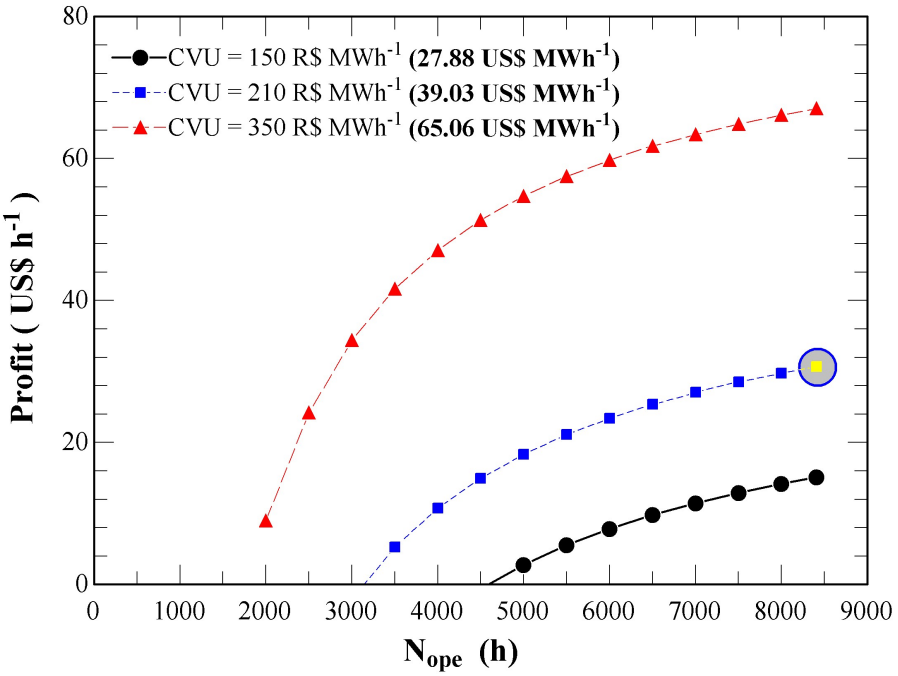

Source: Own Authorship.

Figure 68 – NPV in function of CVU and operating dispatch hours.

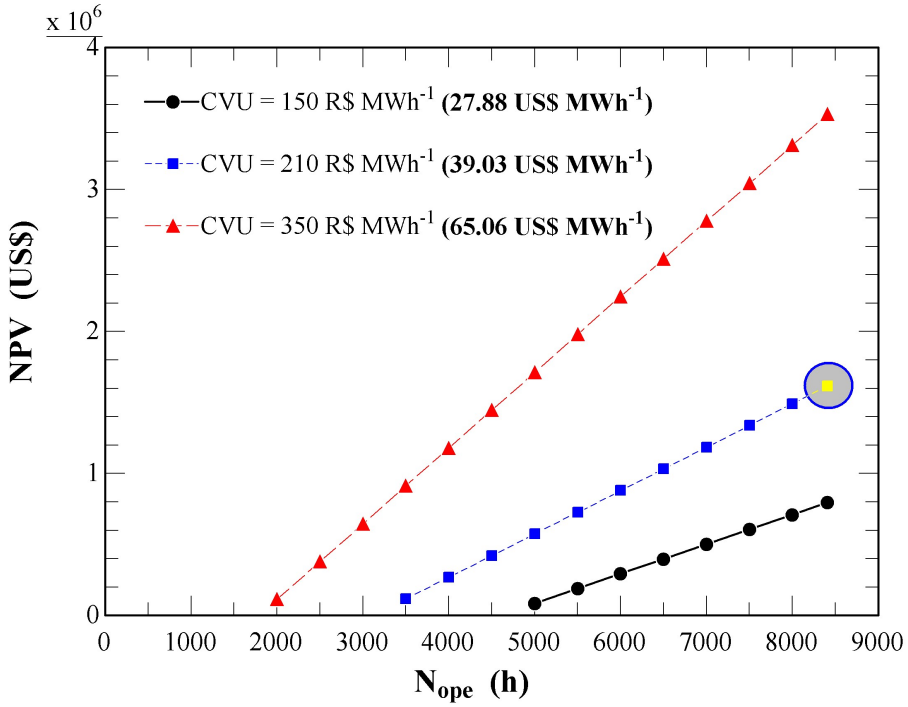

Source: Own Authorship.

Figure 69 – IRR in function of CVU and operating dispatch hours.

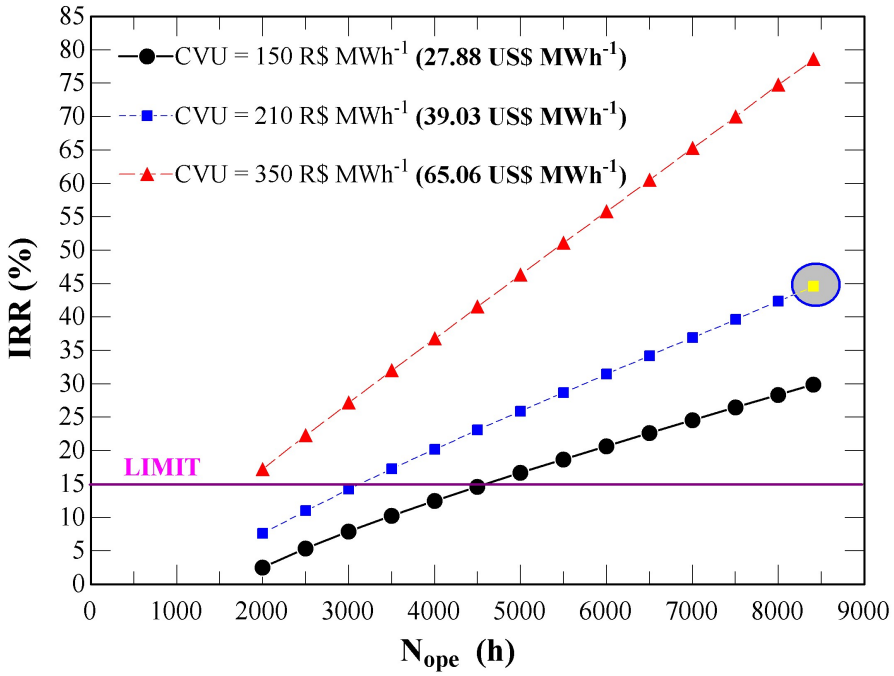

Source: Own Authorship.

However, there are other requirements such as NDP and DP periods that must be taken into account during the business analysis. Hence, it is developed and discussed a sensitivity analysis in relation to these both economic indicators.

Figure 70 presents the NDP periods in function of CVU and operating dispatch hours. The NDP period analysis already limits the business project for CVU of 150 R$ MWh^{-1} and operating dispatch hours below 6000 hours. Further, for CVU of 210 R$ MWh^{-1}, the operating dispatch hours must be higher than 4000 hours in an effort to ensure 5 years limit. The CVU of 350 R$ MWh^{-1} respects this boundary condition if the operating dispatch hours is above 2500 hours.

Figure 71 has the same evaluation for DP periods in function of CVU and operating dispatch hours. The difference regards that this analysis is more reliable for business risks because it takes into account the cash flow depreciation over time. Repeating a similar analysis, when the CVU is 150 R$ MWh^{-1}, the DP period is only approved for 8409.6 hours. For CVU of 210 R$ MWh^{-1}, the investment is only worthy for operating dispatch hours above 6000 hours. Finally, the CVU of 350 R$ MWh^{-1} requires an operating dispatch hours above 3500 hours to guarantee a maximum DP period of 5 years limit. The DP period is reducing the range of operating dispatch hours than the other economic indicators, hence, it is fundamental to consider this variable for business decision-making.

Figure 70 – NDP period in function of CVU and operating dispatch hours.

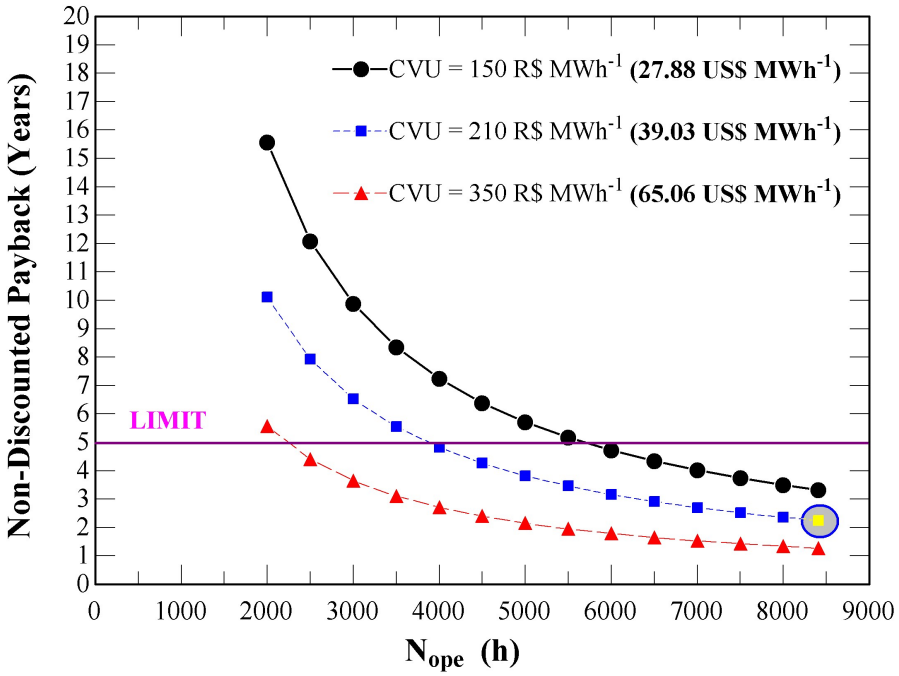

Source: Own Authorship.

Figure 71 – DP period in function of CVU and operating dispatch hours.

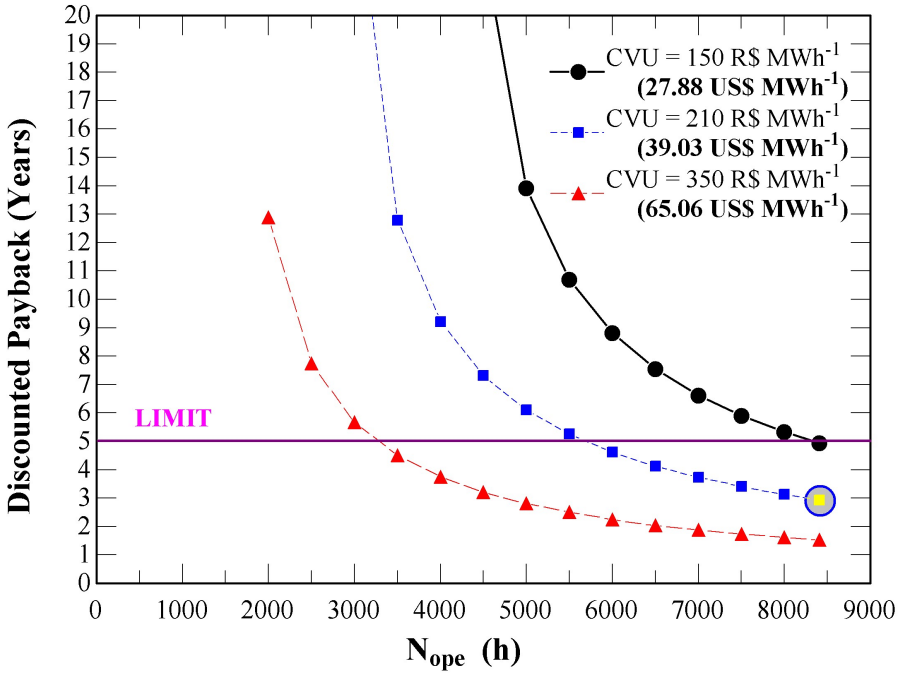

Source: Own Authorship.

6 Conclusion and Outlook

In this master's thesis, the main contribution is to use a methodology known as superstructure optimization in order to define the optimal configuration and best parametric conditions for the new thermal system. A low temperature superstructure of absorption chillers integrated to one W20V34SG engine provides cooling effects on the intake air while recovering heat from the exhaust gases and hot water streams. The possible structures that are taken into account are single-effect, half-effect and single-effect with double-lift.

In this work, two distinct objective functions are studied in order to investigate the optimization behaviors. During the first optimization analysis involving chilled water specific cost (OF_1), a restriction at the upper bound of hot water mass flow rate of 100 kg s^{-1} is set due the excess increasing of this amount of water while the temperature differences at the desorbers are decreasing abruptly. Hence, all minimizations of chilled water specific cost are carried out by applying this restriction in order to search for reasonable and feasible solutions from the structure and parametric levels. It is important to comment that the chilled water specific cost minimization does not take account the power demand of each electric motor. During the minimization, there is no final user for the chilled water production.

The minimization procedure also leads to encounter the HE absorption chiller without the existence of solution heat exchangers as the best structure in synthesis level. However, when analysing the optimum parametric conditions in design level, this half-effect chiller uses a huge amount of hot water to power the absorption machine which is very undesirable because increases the piping and interferes directly on the necessary room at the power house.

The second objective function (OF_2) presents in synthesis level the best structure as SE absorption chiller with the existence of high solution heat exchanger in its structure. Furthermore, this scenario presents an integration, between SE chiller with the W20V34SG engine, using all engine cooling water that is heated at the exhaust gases heat exchanger. This equipment is recovering part of the available thermal energy on engine exhaust gases stream. During the maximization, the production of chilled water must meet the cooling load demands from the cooling coil and the auxiliary heat exchanger.

As the SE unit is producing lower amount of chilled water (79.805 kg s^{-1}) than the HE machine (103.604 kg s^{-1}), it means that the maximum profit does not require the same amount of chilled water from the minimum specific cost. Thus, in summary, the HE unit could meet cooling thermal loads for more than one engine.

The exergy analysis in the HE machine shows highest irreversibility concentration in the low desorber, whereas the SE chiller concentrates more irreversibility generation in the low absorber. When comparing these two distinct chillers, the dissipative heat exchangers inside the SE absorption chiller concentrates more exergy losses (29.56%) than the HE unit (22.08%). Notwithstanding, the overall exergy analysis shows that the HE unit concentrates more irreversibility (67.09%) than the SE chiller (48.24%).

For a competitive scenario against another WHR technology, a comparison is carried out between the SE machine against an ORC system proposal, and it is demonstrated that the thermal system based on SE chiller has a lower $LCOE$ than the ORC proposal. Moreover, the repowering application allows an engine energy and exergy efficiency enhancement of 0.39% and 0.37%, respectively.

A sensitivity investment analysis at the UTE LORM is also carried out in this present thesis, the economic indicators are all studied by varying the CVU and operating dispatch hours. The discounted payback period is presenting more crucial influence over the range of operating dispatch hours. Thus, for business decision-making, it is highly recommended to use the discounted payback as major economic indicator.

For the Brazilian energy matrix scenario, the results of this master's thesis allow to note that the gross profit seems to be more advantageous as objective function than the chilled water specific cost. It can be justified because the profit takes account on dispatch hours of the thermal power plant, variable cost per unit of electricity, operating and acquisition costs, and ultimately it gives a final purpose to the chilled water production which is meeting the thermal load demands of the cooling coil heat exchanger and chilled water auxiliary heat exchanger.

Although the optimization strategy worked properly to accomplish the objectives, there are three main limitations that must be highlighted here. Firstly, great amount of non-linear mathematical equations overwhelms the EES software during the solving procedures. Secondly, LiBr-H_2O thermophysical properties in the external routines of EES library require good initial guesses for determining feasible solutions. Unfortunately, because of these two limitations, it is not possible to optimize the superstructure of absorption chillers and correct simultaneously the mass fractions due the flash effects on the exit of the solution expansion valves (points 6, 13 and 22).

For the sake of simplicity, flash effect is neglected in this work, thus, implicating in no need to correct the mass fraction. The solution expansion valves are treated as reversible devices which are not true in practice. Notwithstanding, it is not a huge mistake or even violate any thermodynamic laws or fundamentals. Usually, irreversibility generation in the solution expasion valves are quite small due to low pressure differences.

The third main limitation is related to the GA method from EES optimization

package, in short, optimal solutions are successfully found through this method but it takes great computational effort to optimize the superstructure of absorption chiller integrated to the engine.

For future works, a list of suggestions are presented below:

(i) It is recommended to correct the mass fractions at the exit of solution expansion valves, as explicit in section 4.4. It is necessary because the solution expansion valves are treated as reversible devices in this thesis.

(ii) Concerning the economic evaluation, it is also suggested to consult manufacturer cost as a more reliable reference. The economic methodology that is utilized in this master's thesis uses literature reference to estimate all purchase costs. Therefore, there is a chance that some of these acquisition costs are quite inaccurate.

(iii) Bearing in mind all the efforts to model each equipment in Appendix A, there are some observations in regard to the turbocharger modelling. As this master's thesis proposes to leverage the engine performance, it is fundamental to predict how the turbocharger is going to react under more severe operating condition. Then, it is suggested to model the turbocharger as a real machine by utilizing geometric data and compressible analysis combined with triangle velocities. The reason to develop such more complex modelling bounces back on ensuring a safe operating condition. In the absence of compressor map and turbine map, it is quite dangerous to operate the turbocharger without acknowledging the surge and stall regions. Thus, in order to overcome this issue, a more detailed modelling is suggested in section A.3.

(iv) As the turbocharger needs a better and more realistic modelling, the charge air cooling modelling in W20V34SG engine must be treated accordingly to the designing parameters combined with more complex relations involving heat transfer and fluid mechanics concepts. In this thesis, it is used conservation laws to predict the thermodynamic states on air stream. A drawback of this approach is basically related on not accounting an off-design behavior at the charge air coolers. Due to this reason, the cooling effect of chilled water auxiliary heat exchanger on engine cooling water will probably be limited by the off-design behavior.

(v) The usage of EES software is good enough to achieve the goal of this master's thesis, but other optimization methodologies are highly recommended to search for new optimal solutions. Moreover, better mathematical solvers that are more robust under great amount of non-linear mathematical equations are also recommended.

(vi) The global heat transfer coefficient of each heat exchanger must be calculated accordingly to the designing parameters combined with heat transfer and fluid mechanics concepts.

(vii) The multi-energy and double-effects chillers can be added in the superstructure

of absorption chillers, increasing the complexities. Hence, this new superstructure will recover heat sources from high and low temperatures sources.

(viii) The frequency inverter at the radiator fans must be properly treated in order to account the energy losses. In this master's thesis, for the sake of simplicity, the efficiency of frequency inverter was defined as an unit value.

(ix) The cooling coil and cooling tower must be optimized with the superstructure of absorption chiller integrated with the W20V34SG engine. In addition, more realistic modellings are highly recommended in order to predict the geometric dimensions of these equipment.

(x) The operating cost of the makeup water in the cooling tower must be evaluated.

Bibliography

AGNEW, B.; TALBI, M.; MOSTAFAVI, M. Combined power and cooling, an analysis of the combined diesel-absorption cycle. *Applied Thermal Engineering*, Elsevier, v. 19, n. 10, p. 1097–1105, 1999.

ALEFELD, G.; RADERMACHER, R. *Heat conversion systems*. [S.l.]: CRC press, 1993.

AMIR, V. Optimization the rankine cycle with genetic algorithm. In: *Proceedings of the 2nd International Conference on Mechanical, Production and Automobile Engineering (ICMPAE'2012)*. [S.l.: s.n.], 2012. p. 225–228.

ANEEL. *BIG - Banco de Informações de Geração*. 2020. Disponível em: <https://www2.aneel.gov.br/aplicacoes/capacidadebrasil/capacidadebrasil.cfm>.

APRHORNRATANA, S.; EAMES, I. W. Thermodynamic analysis of absorption refrigeration cycles using the second law of thermodynamics method. *International journal of refrigeration*, Elsevier, v. 18, n. 4, p. 244–252, 1995.

ARDEHALI, M.; SHAHRESTANI, M.; ADAMS, C. C. Energy simulation of solar assisted absorption system and examination of clearness index effects on auxiliary heating. *Energy conversion and management*, Elsevier, v. 48, n. 3, p. 864–870, 2007.

ARSP. *RESOLUÇÃO ARSP Nº 028, DE 25 DE ABRIL DE 2019*. 2019. Disponível em: <https://arsp.es.gov.br/>.

ASHRAE. Refrigeration, chapter 18. *American Society of Heating, Refrigerating, and Air Conditioning Engineers, Atlanta*, 2014.

BARNICKI, S. D.; SIIROLA, J. J. Process synthesis prospective. *Computers & Chemical Engineering*, Elsevier, v. 28, n. 4, p. 441–446, 2004.

BASKHARONE, E. A. *Principles of turbomachinery in air-breathing engines*. [S.l.]: Cambridge University Press, 2006.

BEJAN, A.; TSATSARONIS, G.; MORAN, M. *Thermal design and optimization*. [S.l.]: John Wiley & Sons, 1996.

BERTRAN, M.-O. et al. A generic methodology for processing route synthesis and design based on superstructure optimization. *Computers & Chemical Engineering*, Elsevier, v. 106, p. 892–910, 2017.

BOEHM, R. F. *Design analysis of thermal systems*. [S.l.]: Wiley New York, 1987.

BOUVY, C.; LUCAS, K. Multicriterial optimisation of communal energy supply concepts. *Energy conversion and management*, Elsevier, v. 48, n. 11, p. 2827–2835, 2007.

BROAD. *BROAD XII NON-ELECTRIC CHILLER MODEL SELECTION AND DESIGN MANUAL*. [S.l.], 2017.

CASTILLO, J. C. Á. et al. Cost estimation of using an absorption refrigeration system with geothermal energy for industrial applications in el salvador. United Nations University, 2007.

CENTION. *SAB-LW Series Single Effect Double Lift Hot Water Driven Absorption Chiller*. [S.l.], 2013.

CEPCI. Economic indicators. 2019. Disponível em: <https://www.chemengonline.com/site/plant-cost-index/>.

CHRISTIAN, J. *Central cooling: Absorptive chillers*. [S.l.], 1977.

CHUN, A. *Otimização de uma Superestrutura de Chillers por Absorção para a Recuperação de Calor Residual em Motores de Combustão Interna.* Trabalho de Conclusão de Curso — Bachelor Thesis, Federal University of Espírito Santo, Espírito Santo, Brazil, 2017.

CHUN, A. et al. Thermoeconomic optimization of absorption chiller superstructures for an internal combustion engine; waste heat recovery and cold-water applications. In: ENCIT 2018. [S.l.], 2018.

CIPOLLONE, R.; BATTISTA, D. D.; VITTORINI, D. Experimental assessment of engine charge air cooling by a refrigeration unit. *Energy Procedia*, Elsevier, v. 126, p. 1067–1074, 2017.

CRUZ, R. W. A. d. et al. Avaliação da introdução de cogeração no sistema isolado do interior do estado do amazonas. [sn], 2004.

D'ACCADIA, M. D.; ROSSI, F. de. Thermoeconomic optimization of a refrigeration plant. *International Journal of Refrigeration*, Elsevier, v. 21, n. 1, p. 42–54, 1998.

DIXIT, M.; ARORA, A.; KAUSHIK, S. Thermodynamic and thermoeconomic analyses of two stage hybrid absorption compression refrigeration system. *Applied Thermal Engineering*, Elsevier, v. 113, p. 120–131, 2017.

DIXON, S. L.; HALL, C. *Fluid mechanics and thermodynamics of turbomachinery*. [S.l.]: Butterworth-Heinemann, 2013.

DONATELLI, J. *Otimização estrutural e paramétrica de sistemas de cogeração utilizando superestruturas*. Tese (Doutorado) — Doctoral Thesis, COPPE/Federal University of Rio de Janeiro, Rio de Janeiro, RJ, Brazil, 2002.

EPE. *Cenário de crise hídrica amplia discussão sobre segurança energética | Reportagem Especial do canal energia*. 2019. Disponível em: <http://www.epe.gov.br/pt/imprensa/noticias>.

EPE. *Expansão de Geração: Fontes*. 2020. Disponível em: <http://www.epe.gov.br/pt/areas-de-atuacao/energia-eletrica/expansao-da-geracao/fontes>.

FCHART-EES. *www.fchart.com/ees/*. 2020. Disponível em: <http://www.fchart.com/ees/eeshelp/cnt.htm>.

FOX, R. W.; PRITCHARD, P. J.; MCDONALD, A. T. *Introdução À Mecânica Dos Fluidos* . [S.l.]: Grupo Gen-LTC, 2012.

FRANGOPOULOS, C. A.; SPAKOVSKY, M. R. V.; SCIUBBA, E. A brief review of methods for the design and synthesis optimization of energy systems. *International Journal of Thermodynamics*, v. 5, n. 4, p. 151–160, 2002.

FUJII, T. et al. Cycle simulation and prototyping of single-effect double-lift absorption chiller. In: *12th International Heat Pump Conference, Rotterdam*. [S.l.: s.n.], 2017.

FUNDAJ. *Situação dos Principais Reservatórios do Brasil – 27/12/2019a*. 2019a. Disponível em: <https://www.fundaj.gov.br/index.php/a-questao-energetica/11610-situacao-dos-principais-reservatorios-do-brasil-27-12-2019>.

FUNDAJ. *Relembre os apagões mais recentes no Brasil*. 2019b. Disponível em: <https://www.fundaj.gov.br/index.php/a-questao-energetica/10110-relembre-os-apagoes-mais-recentes-no-brasil-2>.

FUNDAJ. *Pouca chuva leva hidrelétricas a menor nível desde 2014*. 2019c. Disponível em: <https://www.fundaj.gov.br/index.php/a-questao-energetica/11612-pouca-chuva-leva-hidreletricas-a-menor-nivel-desde-2014>.

GILANI, S. I.-u.-H.; AHMED, M. S. M. S. Solution crystallization detection for double-effect libr-h2o steam absorption chiller. *Energy Procedia*, Elsevier, v. 75, p. 1522–1528, 2015.

GOLDBERG, D. *Genetic Algorithms in Search, Optimization, and Machine Learning*. [S.l.]: Addison Wesley, Reading, Massachusetts, 1989.

GROSSMANN, I. E. Review of nonlinear mixed-integer and disjunctive programming techniques. *Optimization and engineering*, Springer, v. 3, n. 3, p. 227–252, 2002.

GROSSMANN, I. E.; CABALLERO, J. A.; YEOMANS, H. Advances in mathematical programming for automated design, integration and operation of chemical processes. *Korean J. Chem. Eng*, v. 16, p. 407–426, 1999.

GROSSMANN, I. E.; RUIZ, J. P. Generalized disjunctive programming: A framework for formulation and alternative algorithms for minlp optimization. In: *Mixed Integer Nonlinear Programming*. [S.l.]: Springer, 2012. p. 93–115.

HENAO, C. A. *A superstructure modeling framework for process synthesis using surrogate models*. Tese (Doutorado) — Doctoral Thesis, The University of Wisconsin-Madison, 2012.

HENSLEY, J. C. *Cooling tower fundamentals*. [S.l.]: Marley Cooling Tower Company, 1983.

HEROLD, K. E.; RADERMACHER, R.; KLEIN, S. A. *Absorption chillers and heat pumps*. [S.l.]: CRC press, 2016.

HEYWOOD, J. B. *Internal combustion engine fundamentals*. [S.l.]: McGraw-Hill Education, 2018.

HILALI, I.; SÖYLEMEZ, M. S. An application of engine exhaust gas driven cooling system in automobile air-conditioning system. *Isi Bilimi ve Teknigi Dergisi/Journal of Thermal Science & Technology*, v. 35, n. 1, 2015.

IEMA. *IEMA lança Plataforma de Energia e estudos sobre termoelétricas*. 2020. Disponível em: <https://ecoa.org.br/iema-lanca-plataforma-de-energia-e-estudos-sobre-termoeletricas/>.

INMET. *MINISTÉRIO DA AGRICULTURA, PECUÁRIA E ABASTECIMENTO*. 2020. Disponível em: <http://www.inmet.gov.br/portal/index.php?r=estacoes/estacoesAutomaticas>.

JONG, K. A. D. Analysis of the behavior of a class of genetic adaptive systems. 1975.

KADUNIC, S. et al. Increased gasoline engine efficiency due to charge air cooling through an exhaust heat driven cooling system. *MTZ worldwide*, Springer, v. 75, n. 1, p. 58–65, 2014.

KAPSE, R.; ARAKERIMATH, R. R. Study and comparison of charge air cooling techniques their effects on efficiency of automobile engine. *International Journal of Engineering Research and Technology*, IJERT, v. 6, p. 196–201, 2017.

KARSTADT, S. et al. Effect of water droplets caused by low pressure egr on spinning compressor wheels. In: *19th Supercharging Conference Dresden*. [S.l.: s.n.], 2014.

KAYNAKLI, O.; YAMANKARADENIZ, R. Thermodynamic analysis of absorption refrigeration system based on entropy generation. *Current Science*, v. 92, 02 2007.

KIM, D.; FERREIRA, C. I. A gibbs energy equation for libr aqueous solutions. *International journal of refrigeration*, Elsevier, v. 29, n. 1, p. 36–46, 2006.

KLEIN, S.; NELLIS, G. Mastering ees. *f-Chart software*, 2012.

KLEIN, S.; NELLIS, G. *Thermodynamics*. [S.l.]: Cambridge University Press, 2012.

KLOPPERS, J. C. *A critical evaluation and refinement of the performance prediction of wet-cooling towers*. Tese (Doutorado) — Doctoral Thesis, Stellenbosch: University of Stellenbosch, 2003.

KOCH, C.; CZIESLA, F.; TSATSARONIS, G. Optimization of combined cycle power plants using evolutionary algorithms. *Chemical Engineering and Processing: Process Intensification*, Elsevier, v. 46, n. 11, p. 1151–1159, 2007.

KORPELA, S. A. *Principles of turbomachinery*. [S.l.]: Wiley Online Library, 2011.

KRÖGER, D. G. *Air-cooled heat exchangers and cooling towers*. [S.l.]: PennWell Books, 2004. v. 1.

LAPPONI, J. C. Projetos de investimento: construção e avaliação do fluxo de caixa. *São Paulo: Lapponi*, v. 7, 2000.

LG. *LG HVAC SOLUTION ABSORPTION CHILLER*. [S.l.], 2016.

LIU, P.; GEORGIADIS, M. C.; PISTIKOPOULOS, E. N. Advances in energy systems engineering. *Industrial & Engineering Chemistry Research*, ACS Publications, v. 50, n. 9, p. 4915–4926, 2011.

LONGO, G. A.; GASPARELLA, A.; ZILIO, C. Analysis of an absorption machine driven by the heat recovery on an ic reciprocating engine. *International Journal of Energy Research*, Wiley Online Library, v. 29, n. 8, p. 711–722, 2005.

MAIA, L.; CARVALHO, L. V. D.; QASSIM, R. Synthesis of utility systems by simulated annealing. *Computers & Chemical Engineering*, Elsevier, v. 19, n. 4, p. 481–488, 1995.

MANSOUR, M. K.; HASSAB, M. Thermal design of cooling and dehumidifying coils. In: *Heat Exchangers–Basics Design Applications*. [S.l.]: InTech, 2012.

MANZELA, A. A. et al. Using engine exhaust gas as energy source for an absorption refrigeration system. *Applied energy*, Elsevier, v. 87, n. 4, p. 1141–1148, 2010.

MCCARTHY, T. J.; MADADNIA, J. Exhaust heat energy recovery through use of absorption cooling of internal combustion engine intake air. In: AMERICAN SOCIETY OF MECHANICAL ENGINEERS DIGITAL COLLECTION. *ASME 2012 Heat Transfer Summer Conference collocated with the ASME 2012 Fluids Engineering Division Summer Meeting and the ASME 2012 10th International Conference on Nanochannels, Microchannels, and Minichannels*. [S.l.], 2012. p. 165–171.

MENCARELLI, L. et al. A review on superstructure optimization approaches in process system engineering. *Computers & Chemical Engineering*, Elsevier, p. 106808, 2020.

METCALFE, T. *MPIKAIA - Parallel Genetic Algorithm*. 2020. Disponível em: <http://www.hao.ucar.edu/Public/about/Staff/travis/mpikaia/>.

METCALFE, T. S.; CHARBONNEAU, P. Stellar structure modeling using a parallel genetic algorithm for objective global optimization. *Journal of Computational Physics*, Elsevier, v. 185, n. 1, p. 176–193, 2003.

MISRA, R.; SAHOO, P.; GUPTA, A. Thermoeconomic evaluation and optimization of a double-effect h 2 o/libr vapour-absorption refrigeration system. *International Journal of Refrigeration*, Elsevier, v. 28, n. 3, p. 331–343, 2005.

MISRA, R. et al. Thermoeconomic optimization of a single effect water/libr vapour absorption refrigeration system. *International Journal of Refrigeration*, Elsevier, v. 26, n. 2, p. 158–169, 2003.

MIZSEY, P.; FONYO, Z. Toward a more realistic overall process synthesis—the combined approach. *Computers & chemical engineering*, Elsevier, v. 14, n. 11, p. 1213–1236, 1990.

MORAN, M. J. et al. *Fundamentals of engineering thermodynamics*. [S.l.]: John Wiley & Sons, 2013.

MORASWKI, P. A. et al. Repotenciação da ute viana por meio do aproveitamento do calor rejeitado. In: *IX CITENEL*. [S.l.: s.n.], 2017.

MORE, A. J. 40 lessons on refrigeration and air conditioning from iit kharagpur. *IIT Kharagpur*, 2015.

MOSTAFAVI, M.; AGNEW, B. Thermodynamic analysis of combined diesel engine and absorption refrigeration unit—supercharged engine. *Applied Thermal Engineering*, Elsevier, v. 16, n. 6, p. 509–514, 1996a.

MOSTAFAVI, M.; AGNEW, B. Thermodynamic analysis of combined diesel engine and absorption unit—turbocharged engine. *Applied thermal engineering*, Elsevier, v. 16, n. 10, p. 845–850, 1996b.

MOSTAFAVI, M.; AGNEW, B. Thermodynamic analysis of combined diesel engine and absorption unit-turbocharged engine with intercooling. *Applied thermal engineering*, Elsevier, v. 16, n. 8-9, p. 733–740, 1996c.

MOSTAFAVI, M.; AGNEW, B. *Thermodynamic analysis of charge air cooling of diesel engine by an exhaust gases operated absorption refrigeration unit-Turbocharged engine with combined pre and inter cooling*. [S.l.], 1997a.

MOSTAFAVI, M.; AGNEW, B. Thermodynamic analysis of combined diesel engine and absorption refrigeration unit—naturally aspirated diesel engine. *Applied thermal engineering*, Elsevier, v. 17, n. 5, p. 471–478, 1997b.

MOSTAFAVI, M.; AGNEW, B. Thermodynamic analysis of combined diesel engine and absorption refrigeration unit—naturally aspirated engine with precooling. *Applied thermal engineering*, Elsevier, v. 17, n. 6, p. 593–599, 1997c.

MUSSATI, S. F.; MOROSUK, T.; MUSSATI, M. C. Superstructure-based optimization of vapor compression-absorption cascade refrigeration systems. *Entropy*, Multidisciplinary Digital Publishing Institute, v. 22, n. 4, p. 428, 2020.

NOVELLA, R. et al. Thermodynamic analysis of an absorption refrigeration system used to cool down the intake air in an internal combustion engine. *Applied Thermal Engineering*, Elsevier, v. 111, p. 257–270, 2017.

PALACIOS-BERECHE, R.; GONZALES, R.; NEBRA, S. A. Exergy calculation of lithium bromide–water solution and its application in the exergetic evaluation of absorption refrigeration systems libr-h2o. *International Journal of Energy Research*, Wiley Online Library, v. 36, n. 2, p. 166–181, 2012.

PARKINSON, A. R.; BALLING, R.; HEDENGREN, J. D. Optimization methods for engineering design. *Brigham Young University*, v. 5, 2013.

PERRY, R. H.; GREEN, D. W.; MALONEY, J. O. *Perry's Chemical Engineer Handbook*. [S.l.]: McGraw-Hill, 1997.

PETRASSI, P. *Relatório do Ensaio de Desempenho*. [S.l.], 2012.

RÊGO, A. et al. Automotive exhaust gas flow control for an ammonia–water absorption refrigeration system. *Applied Thermal Engineering*, Elsevier, v. 64, n. 1-2, p. 101–107, 2014.

RYAN, W. Driving absorption chillers using heat recovery. *ASHRAE Journal*, American Society of Heating, Refrigeration and Air Conditioning Engineers, Inc., v. 46, n. 9, p. S31, 2004.

SALVIANO, L.; MODESTO, M. Simulation of the coupled between an absorption refrigeration system (h2o-nh3) and a turbo-charged diesel engine. In: *21 st Brazilian Congress of Mechanical Engineering October*. [S.l.: s.n.], 2011. p. 24–28.

SANTOIANNI, D. Power plant performance under extreme ambient conditions. *Wärtsilä Technical Journal: In Detail*, n. 1, p. 22–27, 2015.

SCHWEIGLER, C. J. et al. Operation and performance of a 350 kw (100 rt) single-effect/double-lift absorption chiller in a district heating network. *ASHRAE Transactions*, American Society of Heating, Refrigeration and Air Conditioning Engineers, Inc., v. 104, p. 1420, 1998.

STANFORDIII, H. W. *HVAC water chillers and cooling towers: fundamentals, application, and operation*. [S.l.]: CRC Press, 2016.

STOECKER, W. F.; JONES, J. W. *Refrigeração e ar condicionado*. [S.l.]: McGraw-Hill do Brasil, 1985.

SZARGUT, J. et al. *Towards an international reference environment of chemical exergy 1–21*. 2015.

TALBI, M.; AGNEW, B. Exergy analysis: an absorption refrigerator using lithium bromide and water as the working fluids. *Applied Thermal Engineering*, Elsevier, v. 20, n. 7, p. 619–630, 2000.

TALBI, M.; AGNEW, B. Energy recovery from diesel engine exhaust gases for performance enhancement and air conditioning. *Applied thermal engineering*, Elsevier, v. 22, n. 6, p. 693–702, 2002.

THRELKELD, J. L. *Thermal environmental engineering*. [S.l.]: Prentice Hall, 1970. v. 11.

TOLMASQUIM, M. *Energia Termelétrica: Gás Natural, Biomassa, Carvão, Nuclear*. [S.l.]: Empresa de Pesquisa Energética, ISBN 978-85-60025-05-3, 2016.

TURTON, R. K. *Principles of turbomachinery*. [S.l.]: Springer Science & Business Media, 2012.

VALERO, A. et al. Cgam problem: definition and conventional solution. *Energy*, Elsevier, v. 19, n. 3, p. 279–286, 1994.

VATAVUK, W. M. Updating the ce plant cost index. 2001.

VOLL, P. et al. Superstructure-free synthesis and optimization of distributed industrial energy supply systems. *Energy*, Elsevier, v. 45, n. 1, p. 424–435, 2012.

WANG, J.; WU, J. Investigation of a mixed effect absorption chiller powered by jacket water and exhaust gas waste heat of internal combustion engine. *International Journal of Refrigeration*, Elsevier, v. 50, p. 193–206, 2015.

WANG, L. et al. Superstructure-free synthesis and optimization of thermal power plants. *Energy*, Elsevier, v. 91, p. 700–711, 2015.

WANG, L. et al. Parametric optimization of supercritical coal-fired power plants by minlp and differential evolution. *Energy Conversion and Management*, Elsevier, v. 85, p. 828–838, 2014.

WäRTSILä. *Wärtsilä 34SG Power Plant Product Guide*. [S.l.], 2008.

WU, D.; WANG, R. Combined cooling, heating and power: A review. *progress in energy and combustion science*, Elsevier, v. 32, n. 5-6, p. 459–495, 2006.

XAVIER, B. H. et al. Cogeneration with internal combustion engine and absorption refrigeration system (ars) operating with natural gas: technical, economical and environmental issues. In: *23rd ABCM International Congress of Mechanical Engineering. December*. [S.l.: s.n.], 2015. p. 6–11.

YATTARA, A.; YUQUN, Z.; MOSA, M. Theoretical analysis on the economico-performance of solar single-efect double-lift (se/dl) absorption refrigeration system. *Journal of Applied Sciences*, v. 2, n. 9, p. 916–921, 2002.

YATTARA, A.; ZHU, Y.; ALI, M. M. Comparison between solar single-effect and single-effect double-lift absorption machines (part i). *Applied Thermal Engineering*, Elsevier, v. 23, n. 15, p. 1981–1992, 2003.

YORK. *YORK Commercial and Industrial HVAC 2016*. [S.l.], 2016.

YU, H. et al. Process integration and superstructure optimization of organic rankine cycles (orcs) with heat exchanger network synthesis. *Computers & Chemical Engineering*, Elsevier, v. 107, p. 257–270, 2017.

ZABEU, C.; MARTELLI, A.; PENARANDA, A. *Projeto de P&D "Diagnóstico de Problemas, Otimização da Combustão e Balanceamento da Potência de Cilindros de Motores a Gás Natural"*. [S.l.], 2008.

ZEGENHAGEN, M.; ZIEGLER, F. Feasibility analysis of an exhaust gas waste heat driven jet-ejector cooling system for charge air cooling of turbocharged gasoline engines. *Applied energy*, Elsevier, v. 160, p. 221–230, 2015.

Appendix

APPENDIX A – Thermal System

In this Appendix A, a detailed description of each equipment modelling using mass and heat transfer, thermodynamics and fluid mechanics concepts is presented accordingly to some references in the literature, manufacturer brochures, GT-Power simulations and UTE LORM database.

A.1 Cooling Tower

In this section A.1, the cooling tower is presented as counter-flow configuration with induced draft, as shown in Figure 72. The humid air and water streams flow vertically in opposite directions (KRÖGER, 2004; STANFORDIII, 2016).

Figure 72 – Counter-flow cooling tower with induced draft.

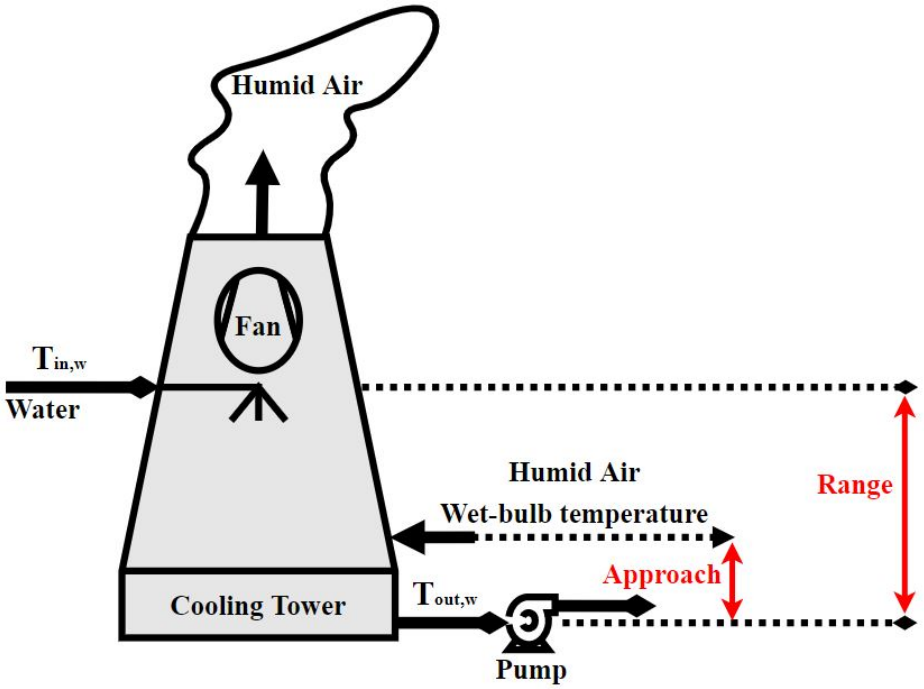

Source: Own Authorship.

There are mainly five parameters in cooling tower modelling that must be explicit; tower characteristic (NTU), $L\ G^{-1}$, *approach*, *range* and wet-bulb temperature (PERRY; GREEN; MALONEY, 1997). The first parameter is regarded to the tower sizing, also known as number of transfer units or tower characteristic. The second parameter $L\ G^{-1}$ is water mass flow rate (L) divided by air mass flow rate in dry basis (G). The third parameter

(*approach*) is the difference between water temperature leaving the tower ($T_{out,w}$) and wet-bulb temperature ($T_{in,wb}$) entering the tower, as represented in Equation A.1. *Range* is the difference between inlet and outlet water temperatures at the tower, as explicit in Equation A.2. Finally, wet-bulb temperature is dependent on ambient conditions.

$$approach = T_{out,w} - T_{in,wb} \tag{A.1}$$

$$range = T_{in,w} - T_{out,w} \tag{A.2}$$

The cooling tower modelling is based on mass and heat transfer using enthalpy potential difference, basic thermodynamic and a linear discretization technique (STOECKER; JONES, 1985), as shown in Figure 73.

Figure 73 – Discretization in the cooling tower modelling.

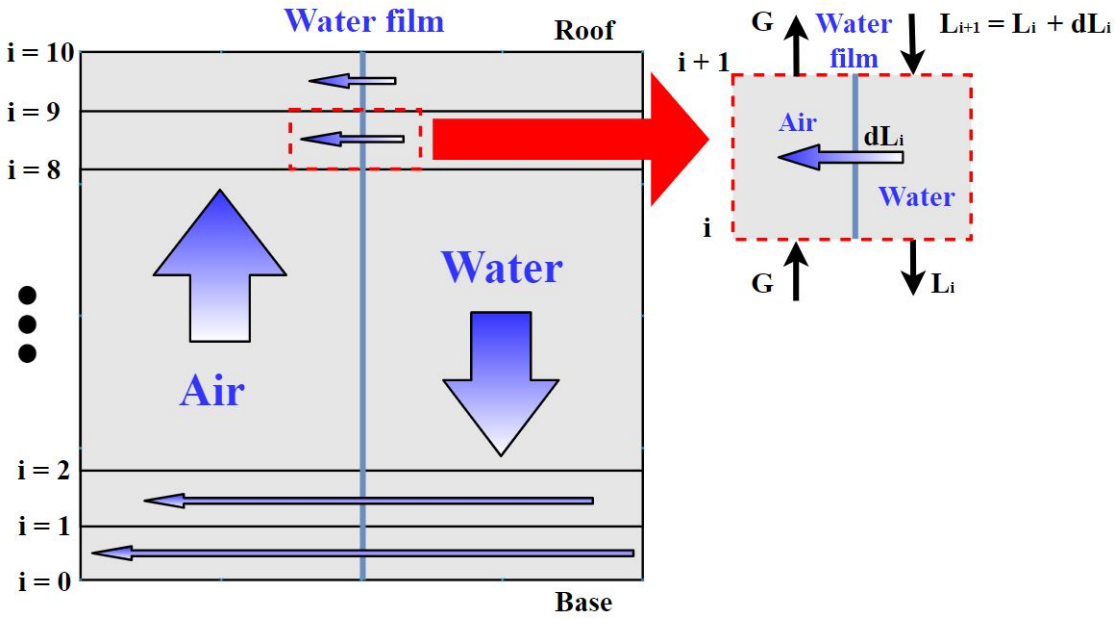

Source: Own Authorship.

The following considerations are set to simplify and support the modelling: (i) steady state, (ii) kinetic and potential energy are negligible, (iii) no pressure losses in each discretization, (iv) humid air in contact with water film is in saturated condition, (v) water droplets leaving the tower due induced draft are not accounted in this modelling, (vi) humid air stream is not considered saturated at the tower outlet, (vii) evaporation process is considered, thus, mass balance must be corrected for water mass flow in each discretization, (viii) Lewis number is unit.

In consonance with Stoecker and Jones (1985), it is set a linear discretization technique, then, the temperature difference for each increment (ΔT_{inc}) is calculated by Equation A.3 which is in function of desired number of increments (n_{CT}), and inlet and outlet water temperatures ($T_{in,w}$ and $T_{out,w}$).

$$\Delta T_{inc} = \frac{T_{in,w} - T_{out,w}}{n_{CT}} \tag{A.3}$$

The next step is to determine the water temperature ($T_{i+1,w}$) and temperature of air in contact with the water film ($T_{i+1,wf}$) for each increment, as shown in Equation A.4 and Equation A.5, respectively.

$$T_{i+1,w} = T_{i,w} + \Delta T_{inc} \tag{A.4}$$

$$T_{i+1,wf} = \frac{2 \cdot T_{i,w} + \Delta T_{inc}}{2} \tag{A.5}$$

Applying mass and energy balance for each increment as well as potential enthalpy difference, it is possible to determine the thermodynamic state of humid air stream in each increment outlet. The corrected mass flow rate for water-vapour (dL_i) and liquid water (L_{i+1}) are explicit by Equation A.6 and Equation A.7, respectively.

$$dL_i = G \cdot (\omega'_{i+1,a} - \omega'_{i,a}) \tag{A.6}$$

$$L_{i+1} = L_i + dL_i \tag{A.7}$$

The make up water mass flow rate (L_{mw}) can be estimated by summing all mass flow increments, thus, Equation A.8 represents this simple calculation step.

$$L_{mw} = \sum_{i=0}^{n_{CT}-1} dL_i \tag{A.8}$$

First law of thermodynamics is applied in sequence, as represented in Equation A.9.

$$G \cdot (h_{i+1,a} - h_{i,a}) = L_{i+1} \cdot h_{i+1,w} - L_i \cdot h_{i,w} \tag{A.9}$$

Subsequently, the potential enthalpy difference is used for determining the tower characteristic for each increment (NTU_i) which is defined in Equation A.10 to Equation A.12.

$$\frac{h_c \cdot A}{c_{pu}} \cdot \left[\frac{h_{i+1,a} + h_{i,a}}{2} - \left(\frac{h_{i+1,wf} + h_{i,wf}}{2} \right) \right] = L_{i+1} \cdot h_{i+1,w} - L_i \cdot h_{i,w} \tag{A.10}$$

$$NTU_i = \frac{h_c \cdot A}{c_{pu}} \cdot \frac{1}{L_{i+1}} \tag{A.11}$$

$$NTU_i = \left[h_{i+1,w} - \left(1 - \frac{dL_i}{L_{i+1}}\right) \cdot h_{i,w}\right] \cdot \frac{1}{\left[\frac{h_{i+1,a} + h_{i,a}}{2} - \left(\frac{h_{i+1,wf} + h_{i,wf}}{2}\right)\right]} \tag{A.12}$$

By using sensible heat transfer rate and potential enthalpy difference definition, the temperature of air stream in each increment outlet ($T_{i+1,a}$) is calculated by Equation A.13.

$$T_{i+1,a} - T_{i,a} = \frac{h_c \cdot A}{G \cdot c_{pu}} \cdot \left[\frac{h_{i+1,a} + h_{i,a}}{2} - \frac{h_{i+1,wf} + h_{i,wf}}{2}\right] \tag{A.13}$$

The total heat transfer rate ($\dot{Q}^{CT}_{total}$) across the cooling tower can be calculated by Equation A.14. For each increment, the vaporization heat ($\dot{Q}^{CT}_{i,Vap}$) and sensible heat ($\dot{Q}^{CT}_{i,Sens}$) rates are defined by Equation A.15 to Equation A.18.

$$\dot{Q}^{CT}_{total} = L \cdot (h_{n_{CT-1},w} - h_{0,w}) \tag{A.14}$$

$$h_{i,support} = f(AirH_2O; T_{i+1,a}; \omega'_{i,a}; p_{i,a}) \tag{A.15}$$

$$\dot{Q}^{CT}_{i,Vap} = G \cdot (h_{i+1,a} - h_{i,support}) \tag{A.16}$$

$$\dot{Q}^{CT}_{i} = L_{i+1} \cdot h_{i+1,w} - L_i \cdot h_{i,w} \tag{A.17}$$

$$\dot{Q}^{CT}_{i,Sen} = \dot{Q}^{CT}_{i} - \dot{Q}^{CT}_{i,Vap} \tag{A.18}$$

The input data are presented in Table 63 and some simulations are developed to analyse the humid air stream across the cooling tower.

Table 63 – List of input data for cooling tower modelling.

approach (°C)	4.0
range (°C)	5.6
$T_{wb,amb}$ (°C)	27.0
$T_{db,amb}$ (°C)	35.0
p_{amb} (atm)	1.0
$L\ G^{-1}$	1.0
n_{CT}	10

Source: Own Authorship.

As the water temperature is calculated by using the input parameters, its temperature chart is presented in Figure 74. The first result from this cooling tower modelling is in regard to the calculation of air stream temperature which is quite interesting due a change direction in sensible heat across the cooling tower.

Figure 74 shows that at the base (i = 0) the air stream has a higher temperature than water stream until increment 5, thus, transferring heat from air to water. Notwithstanding, after increment 5, the water temperature starts to become greater than air stream temperature, hence, transferring heat from water to air.

Figure 74 – Temperatures of air and water streams across cooling tower.

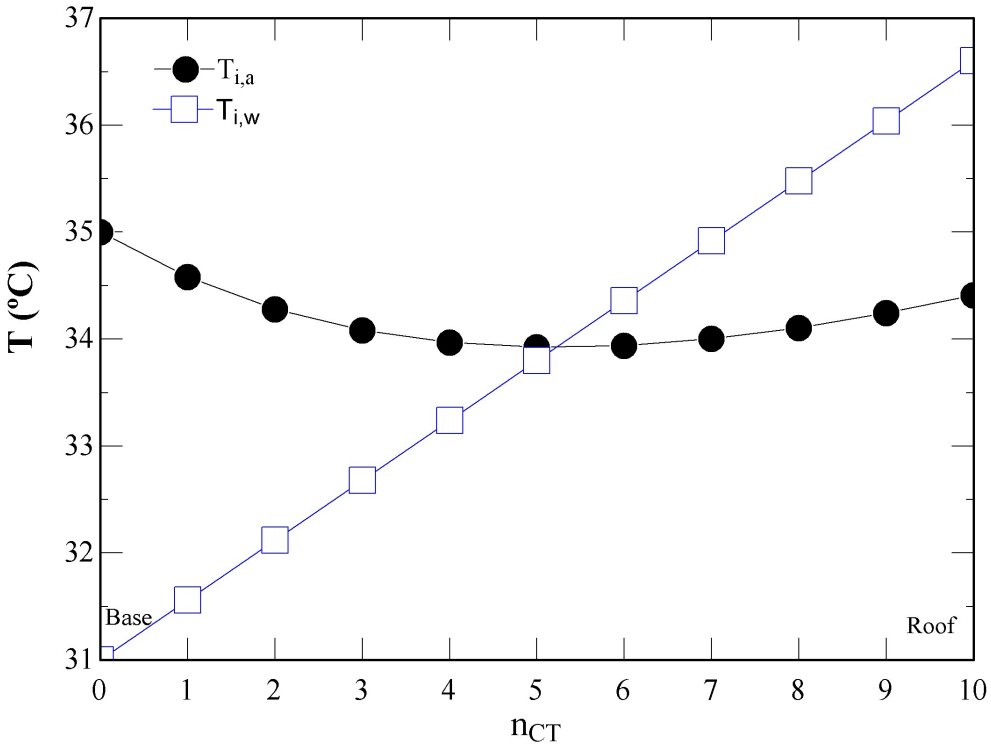

Source: Own Authorship.

The sensible heat changes direction at the same increment 5, as it can be seen in Figure 75. Thereupon, the modelling is responding accordingly to the mass and heat transfer by using potential enthalpy difference.

Another observation about this result is the amount of vaporization heat on the bottom of cooling tower that is higher than the top. By analysing this behavior, it can be presumed that there are more water-vapour evaporating nearly at the base.

Therefore, in Figure 76, it can be confirmed that indeed water-vapour is highest at the first increment (i = 0) due highest vaporization heat.

Figure 75 – Vaporization and sensible heat transfer rates across cooling tower.

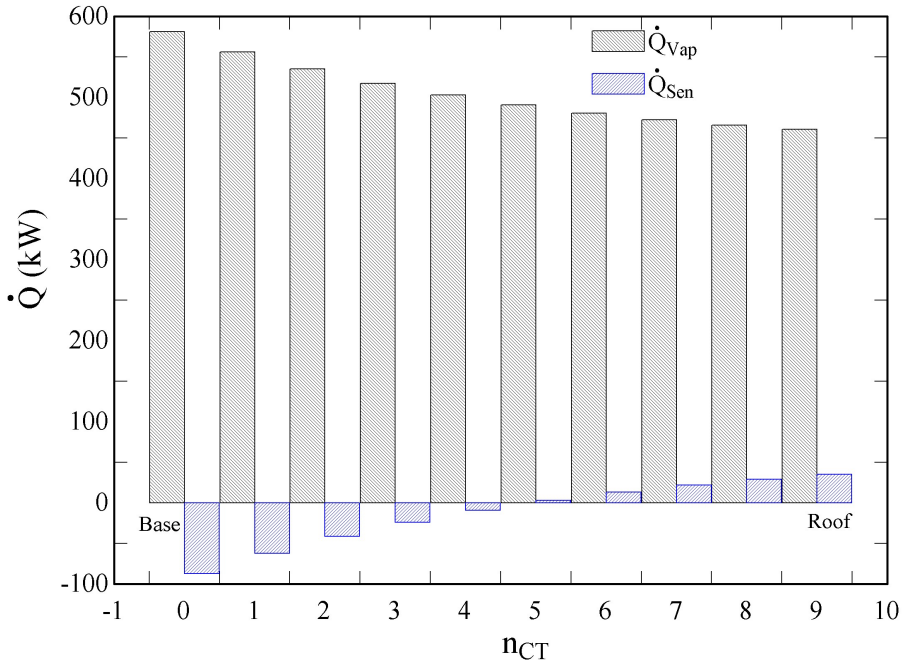

Source: Own Authorship.

Figure 76 – Water-vapour evaporating across cooling tower.

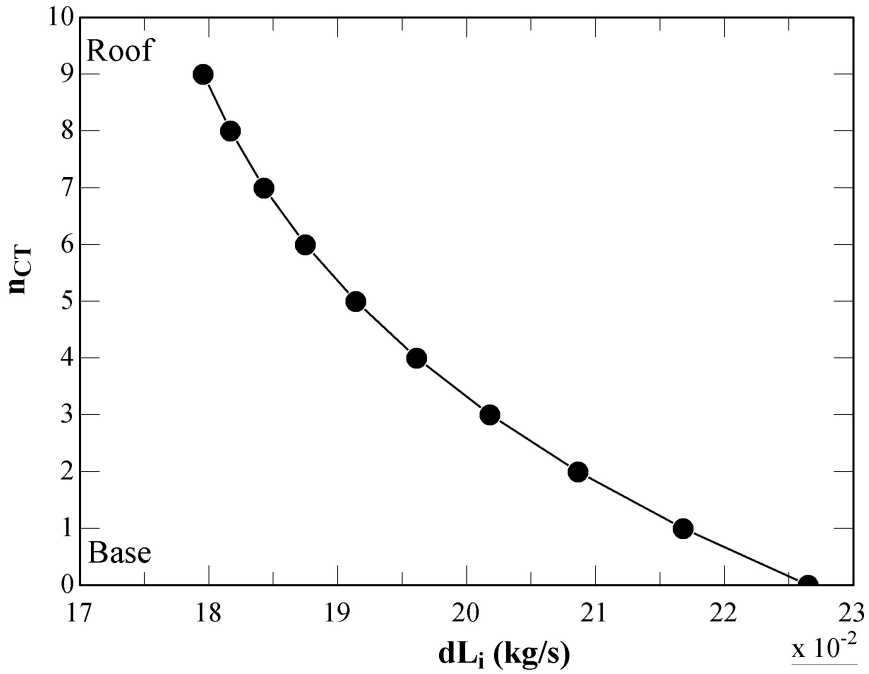

Source: Own Authorship.

The air temperature and humidity for each increment can be analysed at the psychrometric chart, as represented in Figure 77. This result is in accordance with several literature reviews, thus validating this proposed cooling tower modelling (THRELKELD, 1970; STOECKER; JONES, 1985; PERRY; GREEN; MALONEY, 1997; KLOPPERS, 2003; KRÖGER, 2004; STANFORDIII, 2016).

Figure 77 – Psychrometric chart with air humidity ratio and dry-bulb temperature across cooling tower.

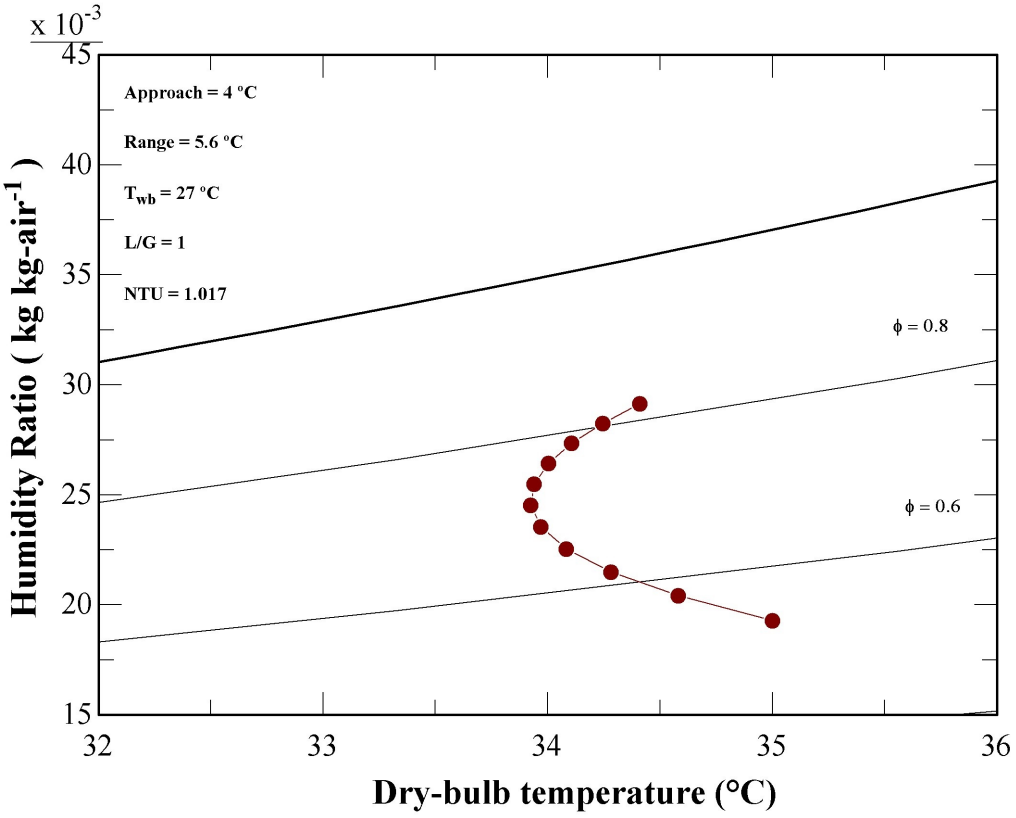

Source: Own Authorship.

In Figure 78, the NTU is reducing while increasing wet-bulb temperature, and this is explained by observing the several simulations. For the lowest wet-bulb temperature, there are more vaporization and sensible heat transfer rate across the cooling tower, rising the heat transfer area.

In Figure 79, $L\ G^{-1}$ is varied from 0.9 to 1.2, and it is verified that when increasing $L\ G^{-1}$, more heat is transferring across the cooling tower. Therefore, a bigger tower is needed to allow this heat transfer. Moreover, the thermodynamic states of air stream at the cooling tower outlet for each $L\ G^{-1}$ are approaching the saturation line.

Figure 78 – Determining thermodynamic states of air stream varying wet-bulb temperature at the cooling tower.

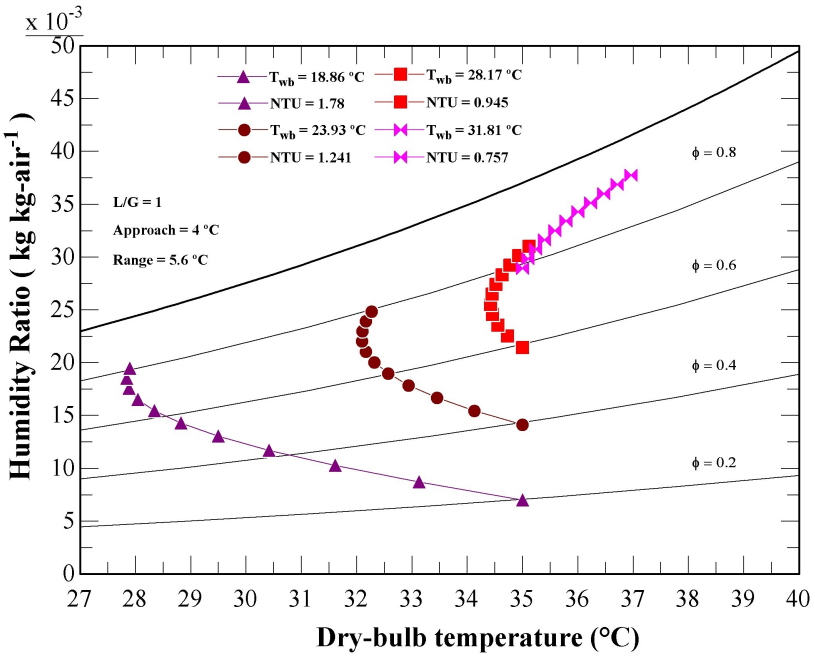

Source: Own Authorship.

Figure 79 – Determining thermodynamic states of air stream varying $L\ G^{-1}$ at the cooling tower.

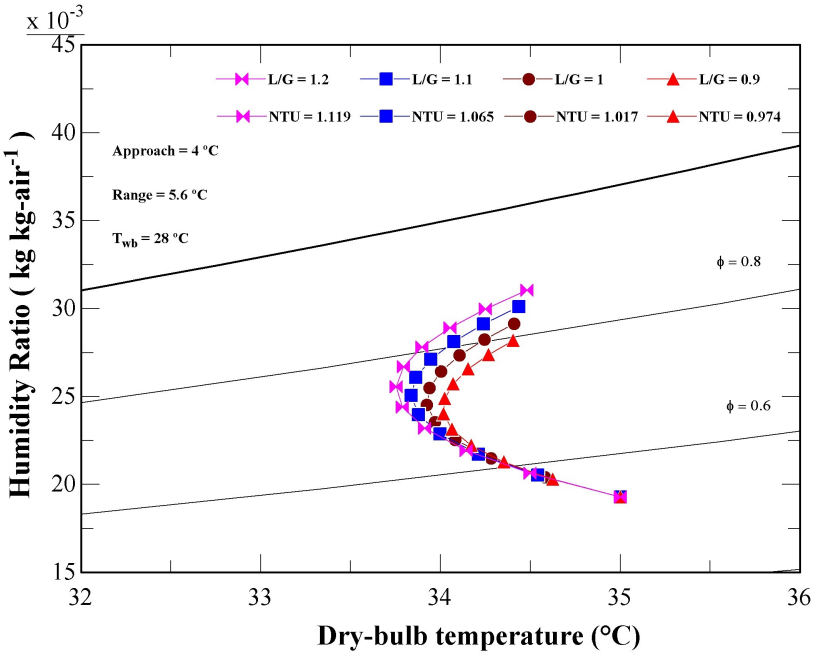

Source: Own Authorship.

A.2 Cooling Coil

Likewise in section A.1, the cooling coil modelling follows the same theoretical strategy of cooling tower equations. Then, in this section A.2, once more, mass and heat transfer using potential enthalpy difference with thermodynamic concepts are applied with linear discretization technique from Stoecker and Jones (1985). However, this technique is a simple theoretical approach and does not account with partial dry surface assumption in the cooling coil. Hence, in an effort to evaluate the dry and wet surfaces assumptions, a combination of wet and dry coil modellings are adopted from Mansour and Hassab (2012) in this master's thesis. Both methodologies are simultaneously combined, providing theoretical and correct results. The selected cooling coil here is a chilled coil which is set between the air filter and turbocharger.

Firstly, it is introduced the previous method from section A.1 and it is also defined the cooling coil as counter-flow heat exchanger, as shown in Figure 80.

Figure 80 – Discretization in cooling coil modelling.

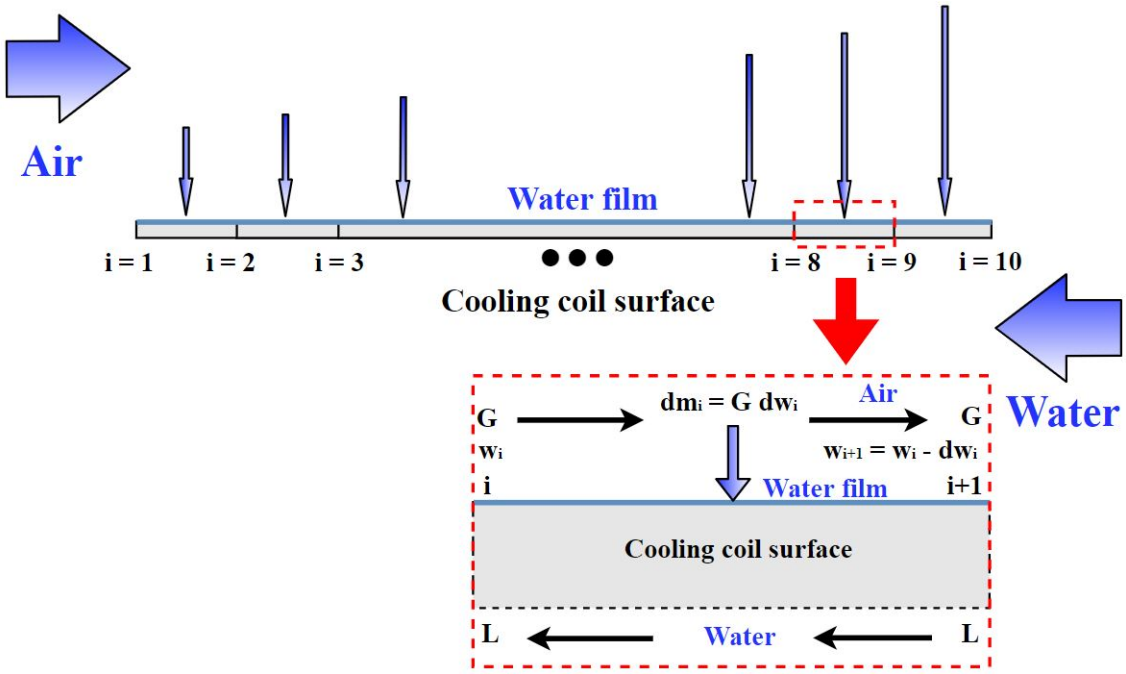

Source: Own Authorship.

For the sake of simplicity, the cooling coil modelling from Stoecker and Jones (1985) obeys a list of assumptions that are posed as follows; (i) steady state, (ii) kinetic and potential energy are negligible, (iii) no pressure losses in each discretization, (iv) humid air in contact with water film is in saturated condition, (v) cooling coil surface is completely wet from first to the last discretization, and (vi) Lewis number is unit.

Similarly, a desired number of increments (n_{CC}) is defined in this modelling. Thereupon, for each increment, the temperature ($T_{i+1,w}$) and enthalpy ($h_{i+1,w}$) for chilled water is calculated by Equation A.19 and Equation A.20, respectively.

$$T_{i+1,w} = \frac{T_{i,w} - T_{i+2,w}}{2} \tag{A.19}$$

$$h_{i+1,w} = \frac{h_{i,w} - h_{i+2,w}}{2} \tag{A.20}$$

When some parameters are known in the modelling, such as convective heat transfer coefficients in air and water (h_c and h_w), air specific heat average (c_{pm}) and area ratio (A_{out}/A_{in}), it is possible to define a relation (R) among these parameters, as presented in Equation A.21.

$$R = \frac{h_c}{c_{pm} \cdot h_w} \cdot \frac{A_{out}}{A_{in}} \tag{A.21}$$

This ratio R remains constant for each increment and it can be comprehended as the amount of heat transfer between air in contact with water film and water stream over the quantity of heat transfer between humid air stream and air in contact with water film. As consequence, the enthalpy of saturated air at the water film ($h_{i,wf}$) is directly correlated with temperature ($T_{i,wf}$), as shown in Equation A.22. Thus, enthalpy of air in contact with water film ($h_{i,wf}$) can be determined through this constant ratio R.

$$R = \frac{T_{i,wf} - T_{i,w}}{h_{i,a} - h_{i,wf}} \tag{A.22}$$

Applying the first law of thermodynamics with potential enthalpy difference definition while using humid air enthalpies, as in Equation A.23, and sensible heat transfer rate, as in Equation A.24, the heat transfer area (A_i) and air temperature ($T_{i+1,a}$) for each increment are calculated as follows.

$$G \cdot (h_{i,a} - h_{i+1,a}) = \frac{h_c \cdot A_i}{c_{pm}} \cdot \left[\frac{h_{i,a} + h_{i+1,a}}{2} - \left(\frac{h_{i,wf} + h_{i+1,wf}}{2} \right) \right] \tag{A.23}$$

$$G \cdot (T_{i,a} - T_{i+1,a}) = \frac{h_c \cdot A_i}{c_{pm}} \cdot \left[\frac{T_{i,a} + T_{i+1,a}}{2} - \left(\frac{T_{i,wf} + T_{i+1,wf}}{2} \right) \right] \tag{A.24}$$

Also, the condensed water (dm_i) for each increment can be calculated by Equation A.25.

$$dm_i = G \cdot (\omega'_{i,a} - \omega'_{i+1,a}) \tag{A.25}$$

Thus, Equation A.26 computes the total condensed water by just summing the amount of condensed water of each increment.

$$dm_{total} = \sum_{i=1}^{n_{CC}} dm_i \tag{A.26}$$

The total heat transfer rate ($\dot{Q}^{CC}_{total}$) at the cooling coil is determined by Equation A.27. The total heat transfer area (A^{CC}_{total}) of cooling coil is defined by summing all areas from each increment, as explicit in Equation A.28.

$$\dot{Q}^{CC}_{total} = G \cdot (h_{1,a} - h_{n_{CC},a}) \tag{A.27}$$

$$A^{CC}_{total} = \sum_{i=1}^{n_{CC}} A_i \tag{A.28}$$

For vaporization ($\dot{Q}^{CC}_{i,Vap}$) and sensible ($\dot{Q}^{CC}_{i,Sen}$) heat transfer rates determination, a support enthalpy is defined accordingly with Equation A.29. Hence, vaporization and sensible heat transfer rates are calculated by Equation A.30 to Equation A.32, respectively.

$$h_{i,support} = f(AirH_2O; T_{i,a}; \omega'_{i+1,a}; p_{i,a}) \tag{A.29}$$

$$\dot{Q}^{CC}_{i} = G \cdot (h_{i,a} - h_{i+1,a}) \tag{A.30}$$

$$\dot{Q}^{CC}_{i,Vap} = G \cdot (h_{i,a} - h_{i,support}) \tag{A.31}$$

$$\dot{Q}^{CC}_{i,Sen} = \dot{Q}^{CC}_{i} - \dot{Q}^{CC}_{i,Vap} \tag{A.32}$$

In order to validate this modelling, the input data are set in Table 64 and some simulations are carried out to analyse the humid air and chilled water streams, as well as, heat transfer rates and humidity ratios across the cooling coil.

Table 64 – List of input data for cooling coil modelling.

Φ'_{amb}	0.5	h_c (kW m^{-2} K^{-1})	0.055
$T_{db,amb}$ (°C)	35.0	h_w (kW m^{-2} K^{-1})	3.000
p_{amb} (atm)	1.0	A_{out}/A_{in}	16.0
n_{CC}	10	$T_{in,chilled}$ (°C)	7.0
$T_{n_{CC},wb}$ (°C)	13.0	$T_{out,chilled}$ (°C)	12.0
G (kg s^{-1})	2.5	c_{pm} (kW kg^{-1} K^{-1})	1.02

Source: Adapted from Stoecker and Jones (1985).

In Figure 81, humid air stream is transferring heat to chilled water for all increments, which is expected for this heat exchanger. Further, the temperature differences between the air stream and chilled water decrease successively across the cooling coil, presuming in less sensible heat transfer rate.

Figure 81 – Temperatures of air and water streams across cooling coil.

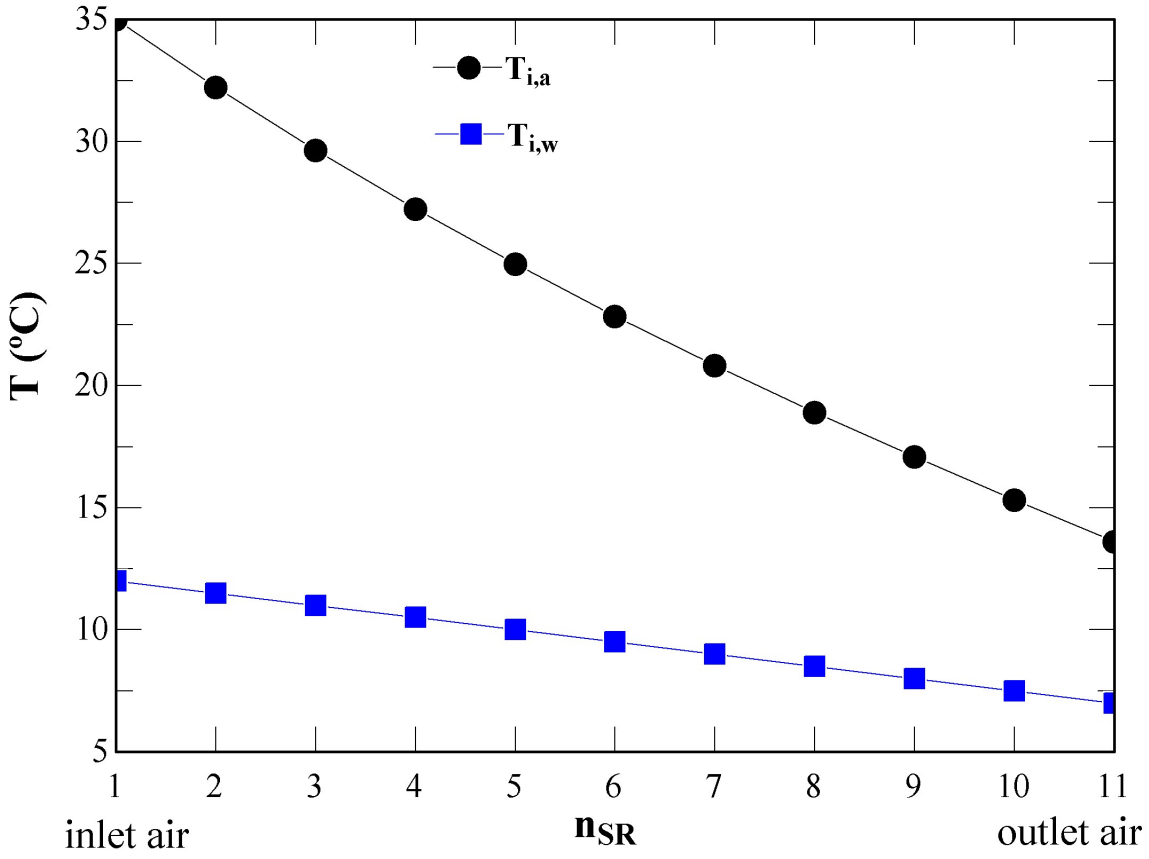

Source: Own Authorship.

Figure 82 presents vaporization and sensible heat transfer rates across the cooling coil, and it is quite interesting to notice that vaporization heat transfer rate increases for each increment while sensible heat follows the opposite behavior as supposed previously.

By analysing each increment, sensible heat transfer rate reduces in more magnitude at the beginning than at the ending of cooling coil. On the other hand, vaporization heat transfer rate rises in more significance at the beginning than at the ending of cooling coil.

Due vaporization heat is increasing for each increment, it can be seen in Figure 83 that the amount of condensed water is increasing too.

Figure 82 – Vaporization and sensible heat transfer rates across cooling coil.

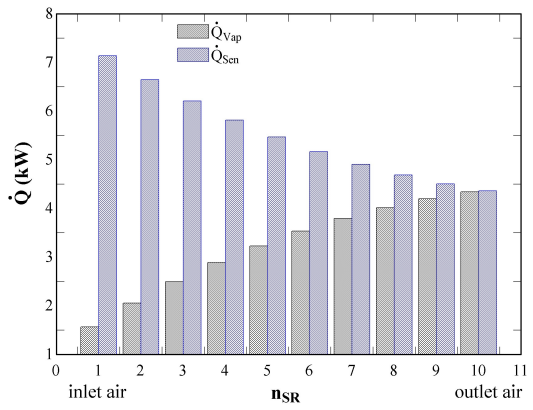

Source: Own Authorship.

Figure 83 – Liquid water condensing across cooling coil.

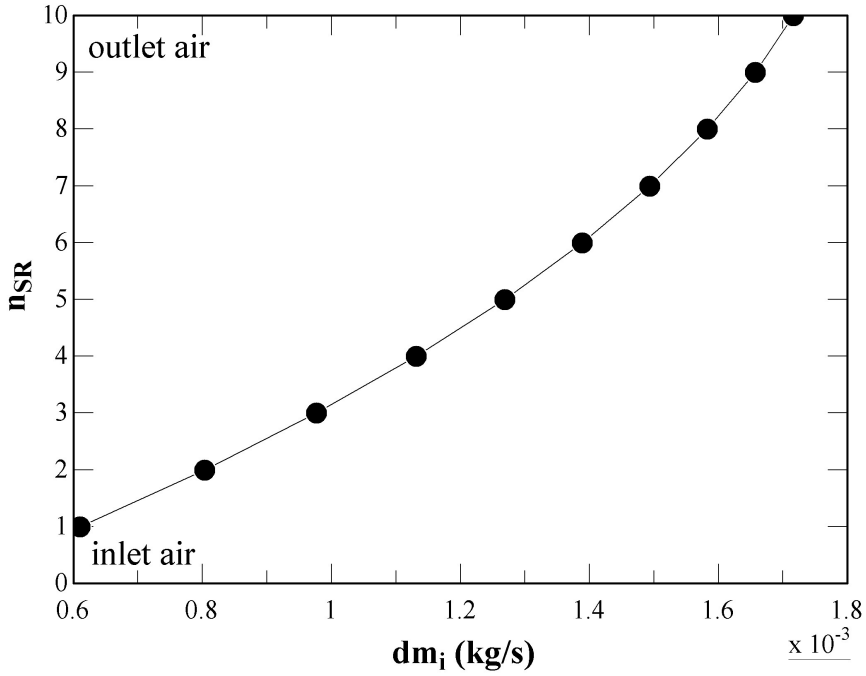

Source: Own Authorship.

At psychrometric chart in Figure 84, it is verified that the cooling coil modelling from Stoecker and Jones (1985) is presenting a theoretical agreement with dehumidification and cooling process.

Figure 84 – Psychrometric chart with air humidity ratio and dry-bulb temperature across cooling coil.

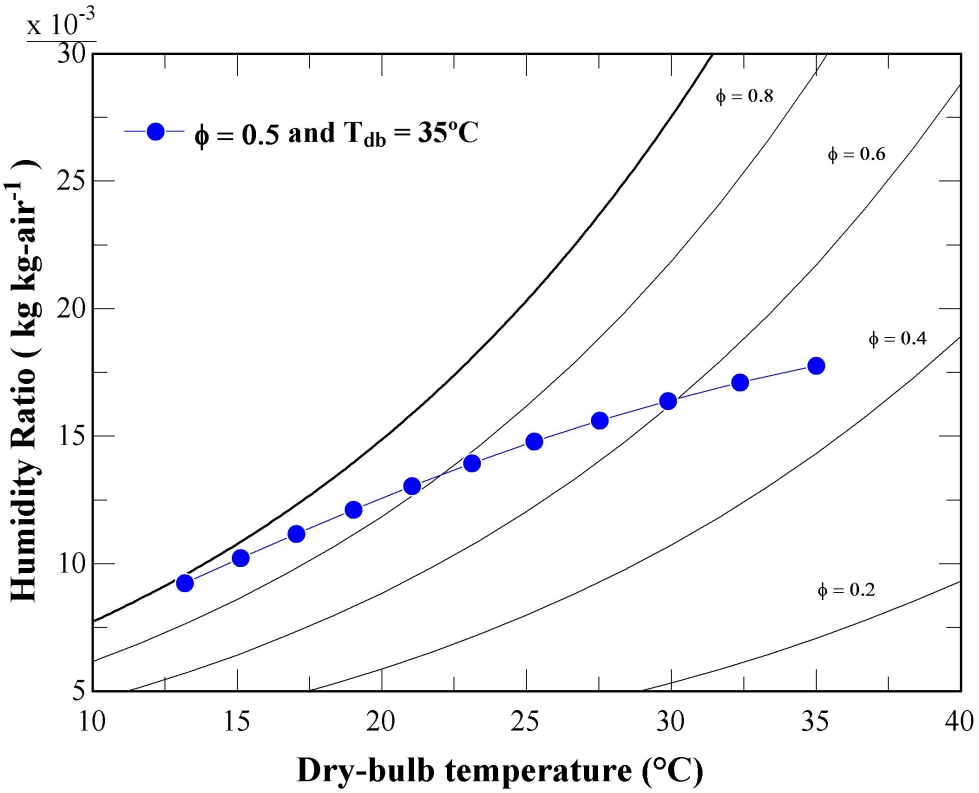

Source: Own Authorship.

For testing this modelling in distinct situations, the relative humidity is varied in an effort to analyse the thermodynamic states in air stream across the cooling coil. Hence, six more simulations are represented in Figure 85.

By comparing these results in Figure 85, a non-sense behavior occurs at the psychrometric chart for simulations with relative humidity of 0.2 and 0.3. In order to understand these wrong profiles, it is necessary to recall one of the assumptions in this theoretical modelling from Stoecker and Jones (1985). Recalling that the surface is wet for each discretization, the air stream in contact with water film at the beginning of the coil might present a higher temperature than dew-point condition. Thus, occurring a conflict of assumption with calculation, and provoking these non-sense results. Hence, to avert these wrong calculations, a dry coil modelling must be used to calculate correctly the properties.

Figure 85 – Determining thermodynamic states of air stream varying relative humidity.

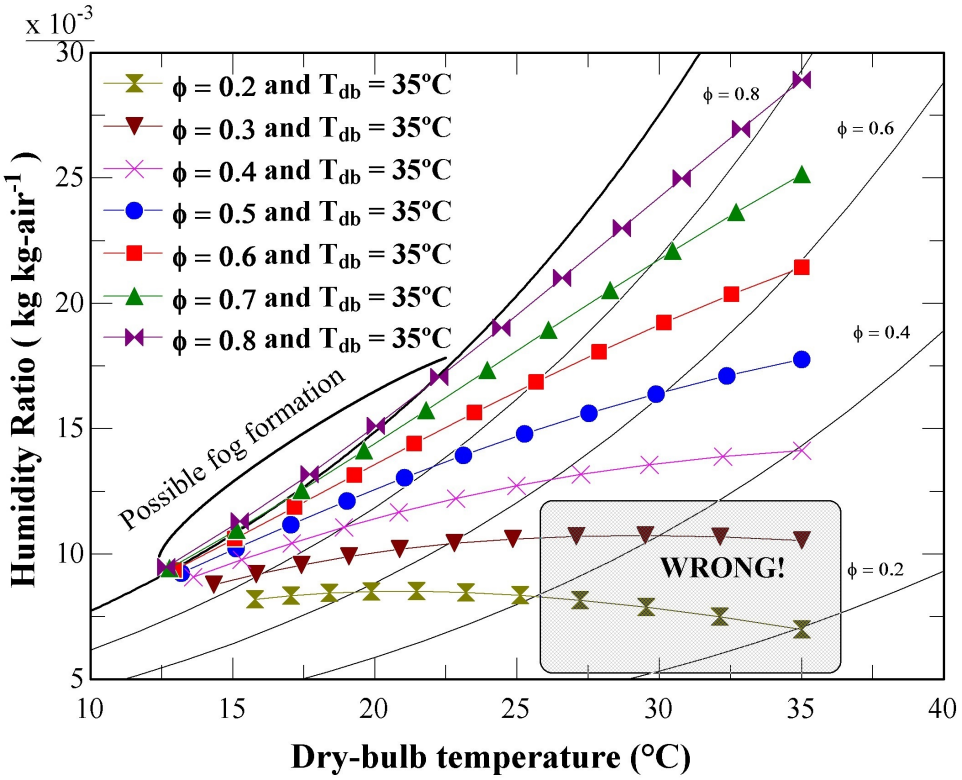

Source: Own Authorship.

The theoretical modelling predicts successfully the air stream temperature and humidity ratio for relative humidity of 0.4 to 0.8 because air in contact with water film has a temperature lower than dew-point temperature. Furthermore, it is also observed possible fog formation. This phenomenon happens when water droplets are being formed in the air stream across the cooling coil due condensation process. Depending on the application, water droplets formation at the exit of cooling coil might not be desirable at all. For the UTE LORM case study, there is a radial compressor just after the air filter, then, if the water droplets shock directly to the compressor blades it will erode and harm the compressor (KARSTADT et al., 2014).

Eventhough the possibility of fog occurrence, it is relevant to point out two possible safeguards against water droplets. Firstly, the power house is hotter than outside due heat rejection coming from engines. Thus, these supposed water droplets would evaporate subsequently as it is considerably small. Secondly, there is a joint knee right before the compressor inlet, hence, a swirl effect will spin the air stream and push the water droplets to the walls, not hitting directly the compressor blades.

Bearing in mind the previous problem in Figure 85, two more cooling coils modelling are adopted here which are wet and dry coils from Mansour and Hassab (2012). In an

effort to evaluate correctly the cooling and dehumidification process, it is firstly calculated the coil design parameters by using Equation A.33 to Equation A.37.

Equation A.33 calculates the outlet area difference (ΔA_{out}) in function of exchanger compactness (β'), longitudinal tube spacing (S_L), dry air mass flow rate, air density (ρ_{air}) and air face velocity (V_{face}).

$$\Delta A_{out} = \frac{\beta \cdot S_L \cdot G}{\rho_{air} \cdot V_{face}} \tag{A.33}$$

The next step is to define the number of transfer units in air side (NTU_{out}) by applying Equation A.34 which is in function of finned-surface weighted efficiency (η_s), air heat transfer coefficient, outlet area difference, dry air mass flow rate, and air specific heat average.

$$\Delta NTU_{out} = \frac{\eta_s \cdot h_c \cdot \Delta A_{out}}{G \cdot c_{pm}} \tag{A.34}$$

The inlet area difference (ΔA_{in}), as represented in Equation A.35, is simply determined in function of area ratio (A_{in}/A_{out}).

$$\Delta A_{in} = \frac{A_{in}}{A_{out}} \cdot \Delta A_{out} \tag{A.35}$$

The number of transfer units in water side (ΔNTU_{in}) is estimated in function of water heat transfer coefficient, inlet area difference, water mass flow rate and water specific heat (c_{pw}), as explicit in Equation A.36.

$$\Delta NTU_{in} = \frac{h_w \cdot \Delta A_{in}}{L \cdot c_{pw}} \tag{A.36}$$

The same ratio R that was used from Stoecker and Jones (1985) modelling is applied again here but also relating the number of transfer units and finned-surface weighted efficiency, as shown in Equation A.37.

$$R = \frac{h_w \cdot c_{pm} \cdot \Delta A_{in}}{h_c \cdot \eta_s \cdot \Delta A_{out}} \cdot \left(\frac{1 + \dfrac{\Delta NTU_{out}}{2}}{1 - \dfrac{\Delta NTU_{in}}{2}} \right) \tag{A.37}$$

The final procedure retains to calculate the desired number of rows (N_r) that are necessary for a defined cooling demand. Nevertheless, by using Equation A.38, temperature

of air in contact with water film is calculated at the beginning of the coil.

$$T_{i,wf} = \frac{-(R+1.4)\cdot\sqrt{(R+1.4)^2+0.184\cdot(h_{i,a}+R\cdot T_{i,w}-10.76)}}{0.092} \tag{A.38}$$

If temperature of humid air at the water film is higher than dew-point temperature, i.e. no condensation process, it must be applied Equation A.39 to Equation A.43. In short, these equations relate sensible heat transfer rate and first law of thermodynamics with heat transfer concepts.

Equation A.39 corrects the temperature of air at the water film for partially dry surface coil modelling.

$$T_{i,wf} = \frac{T_{i,a}+R\cdot T_{i,w}}{R+1} \tag{A.39}$$

The amount of heat transfer (ΔQ_i) in each row is determined by Equation A.40 as follows.

$$\Delta Q_i = \frac{h_w\cdot\Delta A_{in}}{1+\dfrac{\Delta NTU_{in}}{2}}\cdot(T_{i,wf}-T_{i,w}) \tag{A.40}$$

Applying first law of thermodynamics, Equation A.41 calculates the water temperature at the exit of each row.

$$T_{i+1,w} = T_{i,w} - \frac{\Delta Q_i}{L\cdot c_{pw}} \tag{A.41}$$

Finally, the air stream temperature and humidity ratio can be estimated by using Equation A.42 and Equation A.43, respectively.

$$T_{i+1,a} = T_{i,a} - \frac{\Delta Q_i}{G\cdot c_{pm}} \tag{A.42}$$

$$\omega'_{i+1,a} = \omega'_{i,a} \tag{A.43}$$

On the other hand, if temperature of humid air at the water film is lower than dew-point temperature, the following Equation A.44 to Equation A.47 must be used for determining the thermodynamic properties in each row. Remembering that temperature of humid air at the water film must be corrected by Equation A.38.

A correlation between the air stream enthalpy and temperature can be set by Equation A.44.

$$h_{i,a} = c_{pm}\cdot T_{i,a} + \omega'_{i,a}\cdot(2501+1.8\cdot T_{i,a}) \tag{A.44}$$

Recalling Equation A.40, it is defined the amount of heat transfer in each row. Subsequently, air stream enthalpy at the exit is calculated by Equation A.45.

$$h_{i+1,a} = h_{i,a} - \frac{\Delta Q_i}{G} \tag{A.45}$$

Finally, Equation A.46 defines the air stream temperature and Equation A.47 calculates the humidity ratio.

$$T_{i+1,a} = \left(\frac{1 - \frac{\Delta NTU_{out}}{2}}{1 + \frac{\Delta NTU_{out}}{2}} \right) \cdot T_{i,a} + \left(\frac{\Delta NTU_{out}}{1 + \frac{\Delta NTU_{out}}{2}} \right) \cdot T_{i,wf} \tag{A.46}$$

$$\omega'_{i+1,a} = \frac{h_{i+1,a} - c_{pm} \cdot T_{i+1,a}}{2501 + 1.8 \cdot T_{i+1,a}} \tag{A.47}$$

These equations from Mansour and Hassab (2012) permit to verify whether the air stream is entering below or above the dew-point temperature. Therefore, it gives properly treatment for both situations, correcting the non-sense results.

In order to validate these modellings, Stoecker and Jones (1985) method is firstly calculated by using the input data from Table 65. Subsequently, the results from this first approach is used in the improved modelling from Mansour and Hassab (2012). In summary, both methodologies are combined, allowing to determine the number of rows and other geometric dimensions.

Table 65 – List of input data for testing the wet and dry coils modelling.

$T_{wb,amb}$ (°C)	20.0	h_c (kW m^{-2} K^{-1})	0.060
$T_{db,amb}$ (°C)	32.0/25.0	h_w (kW m^{-2} K^{-1})	4.000
p_{amb} (atm)	1.0	A_{out}/A_{in}	16.0
$T_{n_{CC},wb}$ (°C)	12.5	$T_{in,chilled}$ (°C)	7.0
L (kg s^{-1})	16.202	$T_{out,chilled}$ (°C)	12.0
G (kg s^{-1})	15.523	c_{pm} (kW kg^{-1} K^{-1})	1.023
S_T (m)	0.03175	S_L (m)	0.02616
β' (m)	1060	V_{face} (m s^{-1})	2.8
η_s	0.85	V_w (m s^{-1})	1.25
d_i (m)	0.01209	ρ_a (kg m^{-3})	1.16
n_p	6	c_{pw} (kW kg^{-1} K^{-1})	4.188

Source: Adapted from Mansour and Hassab (2012)

In Figure 86, both methodologies are plotted at the psychrometric chart, and it is observed that Stoecker and Jones (1985) modelling demonstrates again an incoherence

behavior due conflicts of wet surface assumption between the first five increments. Nevertheless, Mansour and Hassab (2012) modelling corrects this incoherence in the air stream profile by applying dry coil modelling.

Figure 86 – Comparing Mansour and Hassab (2012) with Stoecker and Jones (1985) modelling when temperature of air stream at the water film is greater than dew-point temperature at the beginning of coil.

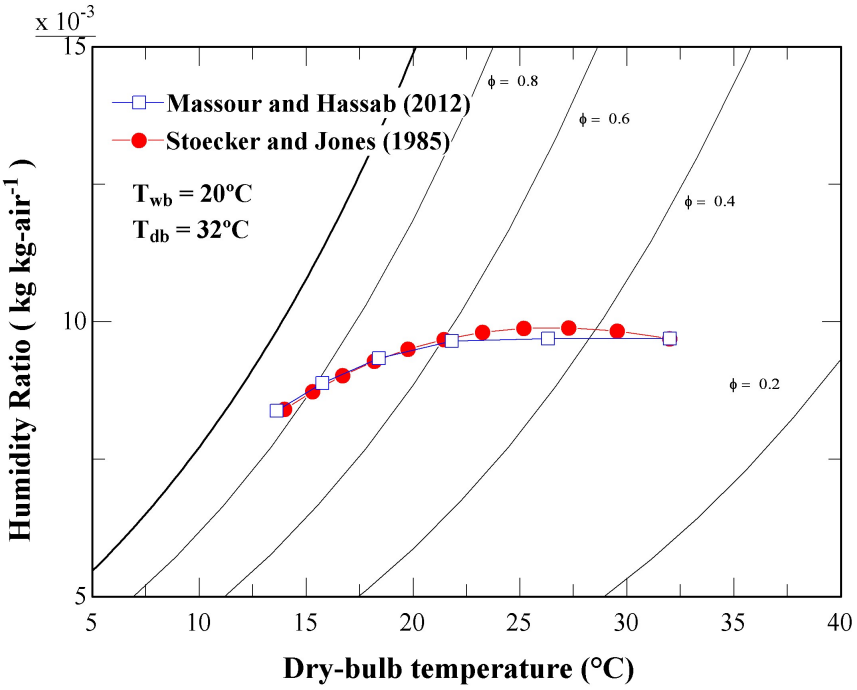

Source: Own Authorship.

Table 66 shows the results from Figure 86, during the simulation, it is targeted the chilled water temperature of 7°C as convergence criterion (MANSOUR; HASSAB, 2012). Finally, the number of rows in this example is 5.

Table 66 – Results from Figure 86.

Row	Surface	$T_{i,a}$ (°C)	$T_{i,wf}$ (°C)	$T_{i,dp}$ (°C)	$\omega'_{i,a}$ (kg kg-air^{-1})	$T_{i,w}$ (°C)
0	Dry	32.0	15.4	13.6	0.00970	12.0
1	Wet	26.3	13.5	13.6	0.00970	10.7
2	Wet	21.8	12.1	13.5	0.00965	9.6
3	Wet	18.4	10.9	13.0	0.00934	8.6
4	Wet	15.7	9.7	12.3	0.00888	7.7
5	Wet	13.6	8.7	11.4	0.00838	6.9

Source: Own Authorship

In Figure 87, for temperature of air at the water film lesser than dew-point temperature, it is verified that both methodologies present same behavior, and the number of rows is 6. The same convergence criterion is applied for Figure 87, as it is presented in Table 67.

Figure 87 – Comparing Mansour and Hassab (2012) with Stoecker and Jones (1985) modelling when temperature of air stream at the water film is lesser than dew-point temperature at the beginning of coil.

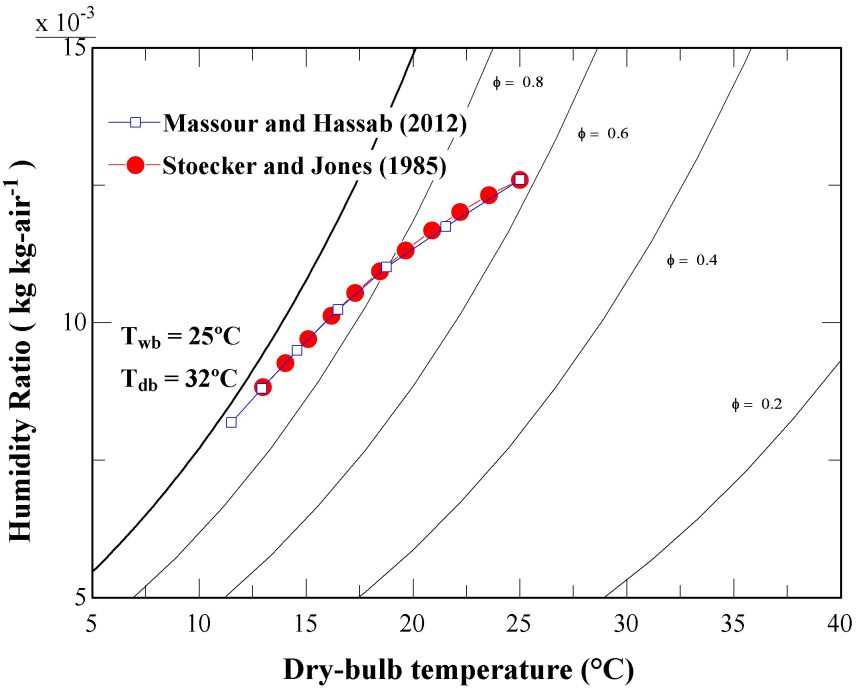

Source: Own Authorship.

Table 67 – Results from Figure 87.

Row	Surface	$T_{i,a}$ (°C)	$T_{i,wf}$ (°C)	$T_{i,dp}$ (°C)	$\omega'_{i,a}$ (kg kg-air^{-1})	$T_{i,w}$ (°C)
0	Wet	25.0	15.0	17.6	0.012600	12.0
1	Wet	21.5	13.6	16.5	0.011750	10.8
2	Wet	18.8	12.3	15.5	0.011010	9.7
3	Wet	16.5	11.0	14.4	0.010240	8.8
4	Wet	14.6	9.9	13.3	0.009498	7.9
5	Wet	12.9	8.9	12.1	0.008807	7.1
6	Wet	11.5	8.0	11.0	0.008184	6.4

Source: Own Authorship

With respect to the arrangement of copper tubes in a coil, a parallel tube-in-tube distribution is set either in staggered or non-staggered pattern, as shown in Figure 88.

Figure 88 – Schematic of chilled coil with triangular pitch.

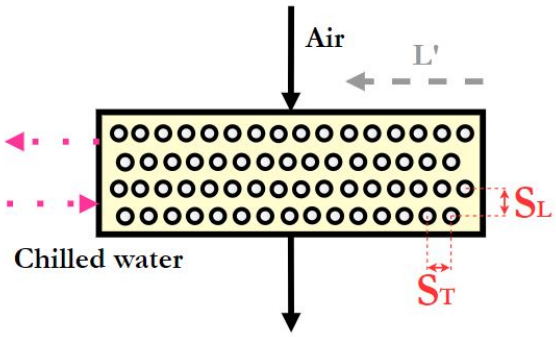

Source: Own Authorship.

When defining the pitch in a coil, for 5/8 inch tubes, it is defined a triangular pitch with 1.75 or 1.5 inch. In addition, some plate (flat-plate, wavy-plate, and star-plate fin patterns) or ripple fins are necessary to enlarge the heat transfer area (MANSOUR; HASSAB, 2012).

After simulating dry and wet coils modelling, it is possible to calculate the geometric parameters such as height (H'), length (L') and depth (D'). Hence, Equation A.48 to Equation A.54 can be used for this purpose. The Figure 89 represents the cooling coil geometric aspects.

Figure 89 – Schematic of cooling coil.

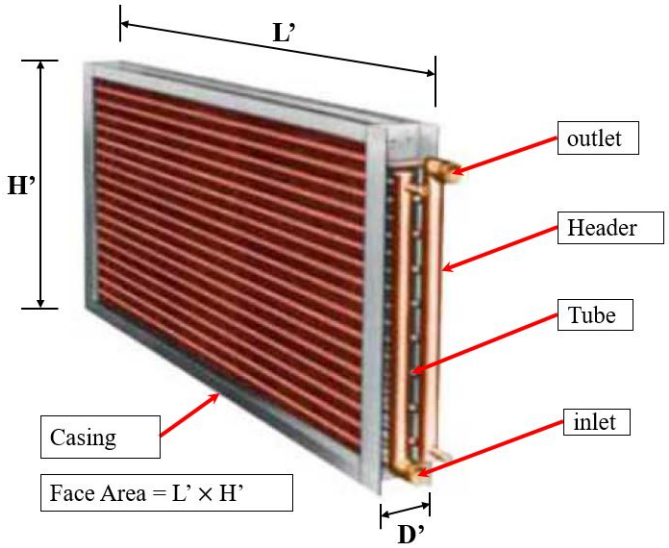

Source: Adapted from Mansour and Hassab (2012).

Equation A.48 determines the number of tubes (n_t) by using number of tube-passes

per water loop (n_p), dry air mass flow rate, water density (ρ_w), inner diameter (d_i) and water velocity (V_w).

$$n_t = \frac{4 \cdot n_p \cdot G}{\pi \cdot \rho_w \cdot d_i^2 \cdot V_w} \tag{A.48}$$

Equation A.49 uses the number of rows (n_r) and tubes to estimate the number of tuber per row (n_c).

$$n_c = \frac{n_t}{n_r} \tag{A.49}$$

Therefore, height can be computed by Equation A.50 which is in function of transversal tube spacing and number of tubes per row.

$$H' = S_T \cdot n_c \tag{A.50}$$

For estimating the length and depth, the outer area (A_{out}) and inner area (A_{in}) are calculated by using the number of rows, outlet area difference and area ratio, as explicit in Equation A.51 and Equation A.52, respectively.

$$A_{out} = n_r \cdot \Delta A_{out} \tag{A.51}$$

$$A_{in} = \frac{A_{out}}{A_{out}/A_{in}} \tag{A.52}$$

Finally, length and depth are simply calculated by Equation A.53 and Equation A.54, respectively.

$$L' = \frac{A_{in}}{\pi \cdot n_t \cdot d_{in}} \tag{A.53}$$

$$D' = n_r \cdot S_L \tag{A.54}$$

Recalling the example from Table 66, for 5 rows, it is calculated a height of 4.13 meters, length of 1.68 meters and depth of 0.13 meters.

The cooling coil modelling from Stoecker and Jones (1985) is used to calculate the amount of heat that is necessary. Thereupon, the more realistic coil modelling from Mansour and Hassab (2012) is applied to correct any incoherence and provide geometric parameters.

A.3 Turbocharger

In this section A.3, a simple thermodynamic treatment is carried out to represent two turbochargers, which is composed by single stage radial compressor and single stage axial turbine for each one. As Zabeu, Martelli and Penaranda (2018) modelled these two turbocompounds in GT-Power coding as one simple turbocharger without considering the geometric aspects, speed and compressible effects, it is carried out a similar thermodynamic modelling in EES coding for this master's thesis. However, in the end of this section A.3, a more realistic turbocharger modelling is presented based on compressible effects, triangle velocities, and geometric aspects, which is also calibrated with GT-Power results and some manufacturer information. The intention here is to investigate, and suggest for future works, a better treatment for turbocharger modelling.

For the sake of simplicity, a list of assumptions for the simple thermodynamic modelling is posed as follows; (i) steady state, (ii) adiabatic condition (iii) kinetic and potential energy are negligible, (iv) ideal gases behavior, and (v) the speed of turbocharger is not accounted as well as compressible effects.

The input data for modelling the turbocharger in EES coding is based on GT-Power database that is presented in Appendix B. For example, inlet pressure drop at the compressor upstream ($\Delta p^c_{in,0}$), total pressure at the compressor outlet ($p^c_{out,0}$), total pressures at the turbine inlet and outlet ($p^t_{in,0}$ and $p^t_{out,0}$), total temperature at the compressor outlet ($T^t_{out,0}$) and waste-gate mass flow rate ($\dot{m}_{wg}$).

In Figure 90, the total temperature at the compressor inlet is set 12.5°C (285.65 K) and an incoming pressure from cooling coil of 1 atm is assumed.

Figure 90 – Schematic of turbocharger and charge air coolers.

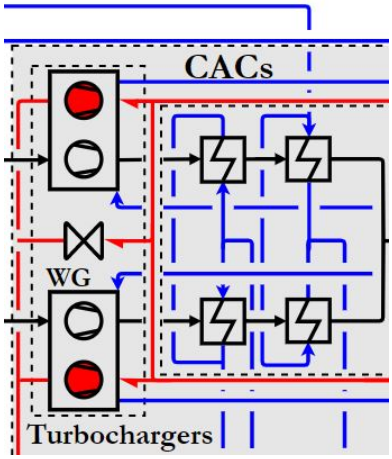

Source: Own Authorship.

The inlet total pressure is defined by Equation A.56 and its physical unit is defined as bar. Additionally, all curves fitting are in function of *BMEP*.

$$\Delta p^{c}_{in,0} = \frac{-240494 + 49880.3 \cdot BMEP + 47.448 \cdot BMEP^2 + 65.5325 \cdot BMEP^3}{10^8} \quad \text{(A.55)}$$

$$p^{c}_{in,0} = p^{CC}_{oulet,0} - \Delta p^{c}_{in,0} \quad \text{(A.56)}$$

The compressor outlet total pressure and temperature are defined accordingly to Equation A.57 and Equation A.58, respectively. Noting that the pressure is set in bar and temperature in Kelvin..

$$p^{c}_{out,0} = \frac{325948 + 164976 \cdot BMEP + 415.884 \cdot BMEP^2 + 9.49015 \cdot BMEP^3}{10^6} \quad \text{(A.57)}$$

$$T^{c}_{out,0} = \frac{249304 + 13863.6 \cdot BMEP - 234.322 \cdot BMEP^2 + 2.49308 \cdot BMEP^3}{10^3} \quad \text{(A.58)}$$

The compressor' outlet total temperature is needed to calculate the amount of heat rejection ($\dot{Q}^{CACs}_{ICE}$) on the charge air cooler, which is explicit in Equation A.59. The air mass flow rate ($\dot{m}_a$) is calculated by using air-fuel ratio (A/F) from combustion balance inside the piston-cylinder, mass and energy balance on exhaust gases, and engine efficiency. Regarding the outlet enthalpy at the charger air cooler ($h^{CACs}_{out,a}$), it is determined by calculating the charge air temperature in the intake manifold. This procedure is well detailed in section A.4.

$$\dot{Q}^{CACs}_{ICE} = \dot{m}_a \cdot (h^{CACs}_{in,a} - h^{CACs}_{out,a}) \quad \text{(A.59)}$$

In addition, for turbine inlet and outlet total pressures, two curve fitting from GT-Power database are used here to calculate the turbine pressure ratio. The physical units of both equations are set in bar.

$$p^{t}_{in,0} = \frac{481669 + 97586.4 \cdot BMEP + 1434.14 \cdot BMEP^2 + 1.17257 \cdot BMEP^3}{10^6} \quad \text{(A.60)}$$

$$p^{t}_{out,0} = \frac{994344 + 1436.76 \cdot BMEP + 37.2434 \cdot BMEP^2 - 0.142462 \cdot BMEP^3}{10^6} \quad \text{(A.61)}$$

The engine shaft power generation in function of $BMEP$ is expressed in Equation A.62 while engine efficiency is defined by Equation A.63, as follows. The shaft power output and engine efficiency are determined in kilowatts and percent, respectively.

$$\dot{W}_{ICE} = \frac{6923.49 + 434907 \cdot BMEP + 41.3413 \cdot BMEP^2 - 0.657516 \cdot BMEP^3}{10^3} \quad \text{(A.62)}$$

$$\eta_{ICE}^{brake} = \frac{37969 + 642.779 \cdot BMEP - 19.1593 \cdot BMEP^2 + 0.213254 \cdot BMEP^3}{10^3} \quad \text{(A.63)}$$

The Lower Heating Value (LHV) is determined in combustion balance, which is discussed in the next section A.4. Thus, in Equation A.64, it is computed the fuel mass flow rate in kg s^{-1}.

$$\eta_{ICE}^{brake} = \frac{\dot{W}_{ICE}}{\dot{m}_f \cdot LHV_f} \quad \text{(A.64)}$$

By calculating air-fuel ratio from combustion balance, it is defined air mass flow rate in Equation A.65.

$$\frac{\dot{m}_f}{\dot{m}_a} = A/F \quad \text{(A.65)}$$

The exhaust gases mass flow rate ($\dot{m}_g$) is determined by Equation A.66.

$$\dot{m}_a + \dot{m}_f = \dot{m}_g \quad \text{(A.66)}$$

Hence, the following Equation A.67 to Equation A.73 are used to determine total temperatures at the exit of turbine ($T_{out,g}^{t}$), exit of waste-gate valve ($T_{out,g}^{wg}$) and outlet temperature at the junction from both gases streams ($T_{out,g}^{ICE}$).

The waste-gate mass flow rate is extracted from GT-Power database, which is represented in Equation A.67. The physical unit is defined in kg s^{-1}.

$$\dot{m}_g^{wg} = \frac{-1535.55 + 232.208 \cdot BMEP - 7.2635 \cdot BMEP^2 + 0.023447 \cdot BMEP^3}{10^3} \quad \text{(A.67)}$$

Here, it is defined the turbine mass flow rate ($\dot{m}_g^t$) by applying Equation A.68.

$$\dot{m}_g^{wg} + \dot{m}_g^t = \dot{m}_g \quad \text{(A.68)}$$

The compressor power demand is now estimated by Equation A.69, and equalized with turbine power production, as defined in Equation A.70.

$$\dot{W}_a^c = \dot{m}_a \cdot (h_{out,a}^c - h_{in,a}^c) \tag{A.69}$$

$$\dot{W}_g^t = \dot{W}_a^c \tag{A.70}$$

There are two equation and three variables, we need one more equation to calculate the exit temperatures. Thus, it is important to analyse the energy balance in W20V34SG engine which is discussed properly in next section A.4.

$$\dot{W}_g^t = \dot{m}_g^t \cdot (h_{in,g}^t - h_{out,g}^t) \tag{A.71}$$

$$h_{out,g}^{wg} = h_{in,g}^{wg} = h_{in,g}^t \tag{A.72}$$

$$\dot{m}_g^{wg} \cdot h_{out,g}^{wg} + \dot{m}_g^t \cdot h_{out,g}^t = \dot{m}_g \cdot h_{out,g}^{ICE} \tag{A.73}$$

Basically, it is determined the percentage amount of heat losses through exhaust gases, as shown in Equation A.74 to Equation A.76. Therefore, $h_{out,g}^{ICE}$ is estimated by using these equations.

$$Losses_{\%}^{gases} = 1 - \sum Losses_{\%}^{i} \tag{A.74}$$

$$Losses_{\%}^{gases} = \frac{\dot{Q}_{out,g}^{ICE}}{\dot{m}_f \cdot LHV_f} \tag{A.75}$$

$$\dot{Q}_{out,g}^{ICE} = \dot{m}_g \cdot (h_{out,g}^{ICE} - h_{ref,g}) \tag{A.76}$$

This a simple modelling that responds thermodynamically the temperatures calculation and works pretty well. One of the reasons why it is used this simple modelling regards to no availability of compressor and turbine maps to guide the turbocharger operation. Therefore, the turbocharger is modelled assuming conservative approaches.

Approaching by Compressible Effects, Triangle Velocities and Geometric Aspects

In this extra section, it is presented a more complex modelling, because it is quite important to realize that neglecting the compressible effects carry an error. Therefore, it is discussed here an analytical approach to treat the turbocharger with compressible effects, using triangle velocities and geometric characteristics. This frame work is based on well established principles of turbomachinery technology available in the literature (BASKHARONE, 2006; DIXON; HALL, 2013; KORPELA, 2011; TURTON, 2012). The goal is to compare the results from this second approach with GT-Power results.

A list of assumptions is also necessary to simplify this second modelling; (i) steady state, (ii) adiabatic condition, (iii) specific heat and coefficient k are constant, (iv) potential energy is neglected, (v) ideal gases behavior, (vi) free vortex in radial direction inside the compressor, and (vii) compressible effects are accounted in the modelling, as well as, triangle velocities and the geometric aspects.

In short, in consonance with some literature, the governing equations of compressible phenomena are presented below in function of Mach number (M_j), total and static properties ($T_{j,0}$, $p_{j,0}$, $\rho_{j,0}$, T_j, p_j and ρ_j), speed of sound (a_j), and fluid characteristics (k_j, $\bar{R}_j$ and $\bar{M}_j$). Subscripts 0 refers to total property while subscript j assigns each thermodynamic state.

$$\frac{T_{j,0}}{T_j} = 1 + \frac{(k_j - 1) \cdot M_j^2}{2} \tag{A.77}$$

$$\frac{p_{j,0}}{p_j} = \left[1 + \frac{(k_j - 1) \cdot M_j^2}{2}\right]^{\frac{k_j}{k_j - 1}} \tag{A.78}$$

$$\frac{\rho_{j,0}}{\rho_j} = \left[1 + \frac{(k_j - 1) \cdot M_j^2}{2}\right]^{\frac{1}{k_j - 1}} \tag{A.79}$$

$$a_j = \sqrt{k_j \cdot R_j \cdot T_j} \tag{A.80}$$

$$M_j = \frac{V_j}{a_j} \tag{A.81}$$

$$R_j = \frac{\bar{R}_j}{\bar{M}_j} \tag{A.82}$$

The ratio k for air is adopted around 1.4, while for exhaust gases, the coefficient k must be calculated assuming an average between the inlet and outlet ks of thermodynamic

states in the turbine, as it is presented in Equation A.83. Thus, Equation A.84 calculates each k by dividing specific heat $c_{p,j}$ over $c_{v,j}$.

$$k_g^t = \frac{k_{in}^t + k_{out}^t}{2} \tag{A.83}$$

$$k_j^t = \frac{c_{p,j}}{c_{v,j}} \tag{A.84}$$

With reference to the governing equations for each component in the turbocharger, they are separated and organized in Table 68. The subscript i refers to compressor or turbine component.

Table 68 – Governing equations for air compressor and gas turbine.

Parameter	Radial compressor	Axial turbine
η_{ts}^i	$\dfrac{\left(\dfrac{p_{out}^c}{p_{in,0}^c}\right)^{\dfrac{k_a-1}{k_a}} - 1}{\dfrac{T_{out,0}^c}{T_{in,0}^c} - 1}$	$\dfrac{1 - \dfrac{T_{out,0}^t}{T_{in,0}^t}}{1 - \left(\dfrac{p_{out}^t}{p_{in,0}^t}\right)^{\dfrac{k_g-1}{k_g}}}$
η_{tt}^i	$\dfrac{\pi_c^{\dfrac{k_a-1}{k_a}} - 1}{\tau_c - 1}$	$\dfrac{1-\tau_t}{1-\pi_t^{\dfrac{k_g-1}{k_g}}}$
SR_i	$\dfrac{\Delta h_{static}^c}{\Delta h_{total}^c}$	$\dfrac{\Delta h_{static}^t}{\Delta h_{total}^t}$
A_j^i	$(r_{j,tip}^c)^2 - (r_{j,hub}^c)^2$	$(Pe_{j,tip}^t + Pe_{j,hub}^t) \cdot \dfrac{r_{j,tip}^t - r_{j,hub}^t}{2}$
	$2 \cdot \pi \cdot r_j^c \cdot b_j^c$	
$\dot{m}_j^i$	$\rho_a \cdot V_j^c \cdot A_j^c$	$\rho_g \cdot V_j^t \cdot A_j^t$
π_i	$\dfrac{p_{out,0}^c}{p_{in,0}^c}$	$\dfrac{p_{in,0}^t}{p_{out,0}^t}$
τ_i	$\dfrac{T_{out,0}^c}{T_{in,0}^c}$	$\dfrac{T_{in,0}^t}{T_{out,0}^t}$

Source: Baskharone (2006)

Figure 91 represents the radial compressor and axial turbine geometries, each thermodynamic state is calculated in this turbocharger. Moreover, the radial compressor is a backward curved configuration while axial turbine is a single stage structure.

Figure 91 – Schematic of compressor and turbine geometries.

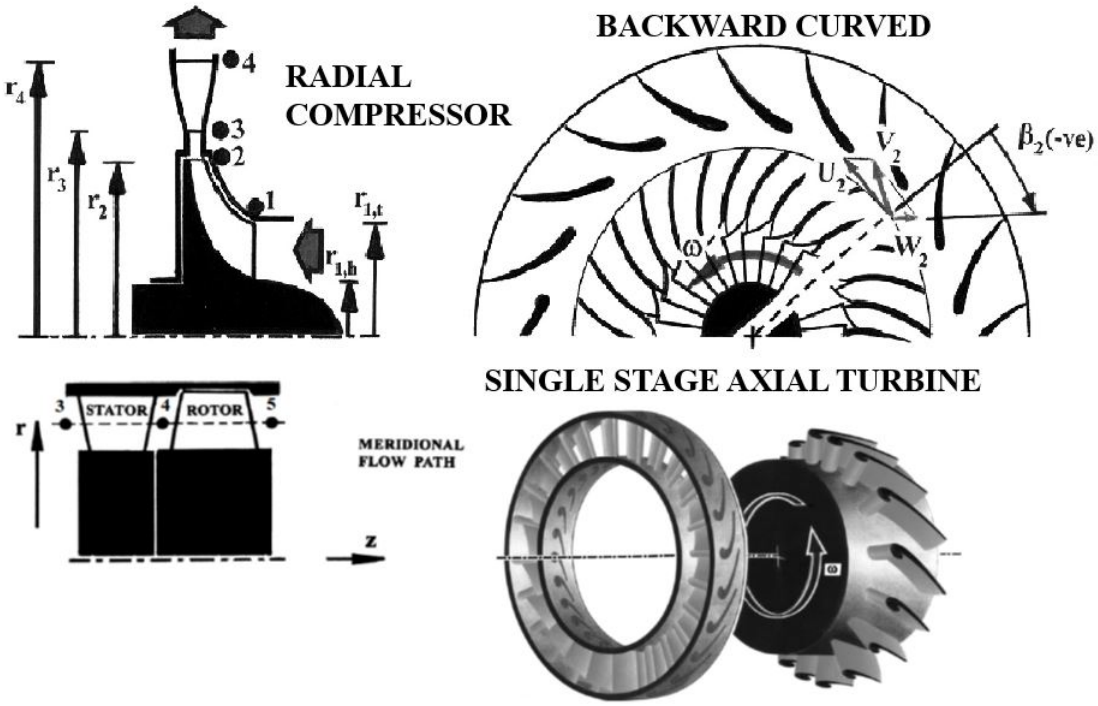

Source: Adapted from Baskharone (2006).

The geometric characteristics are defined in Table 69, notwithstanding it is relevant to note that some information are approximated by analysing some available technical drawings.

Table 69 – Geometric characteristics.

Parameter	Radial compressor	Axial turbine
$n_{diffuser.vanes}$ and $n_{nozzle.vanes}$	16	24
$n_{impeller.blades}$ and $n_{rotor.blades}$	18	53
$r^i_{1/3,tip}$ (m)	0.11	0.26
$r^i_{1/3,hub}$ (m)	0.04	0.20
r^c_2 (m)	0.16	-
r^c_3 (m)	0.18	-
r^c_4 (m)	0.25	-
e^t_{rotor} (m)	-	0.003
$e^t_{in,nozzle.vanes}$ (m)	-	0.013
$e_{out,nozzle.vanes}$ (m)	-	0.001

Source: Adapted from UTE LORM.

As the turbocharger must meet the W20V34SG engine operating requirements such as low air flow restriction in the intake path, a backward curved configuration matches this application, as it can be seen in Figure 92. This is explained because it is not desirable to increase the outlet temperature while rising the outlet pressure. Reminding that there are two CACs just after the radial compressor, then, it is attractive to meet a low compressed air temperature at the compressor exit, hence, not overloading the CAC.

Figure 92 – Temperature ratio behavior for each exit configuration at the impeller.

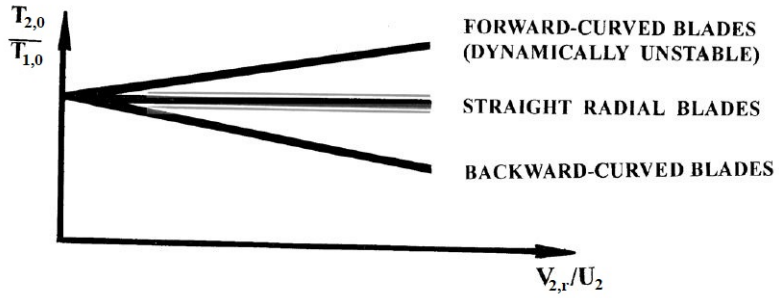

Source: Adapted from Baskharone (2006).

The usage of triangle velocities technique is necessary because kinetic energy is not neglected in this modelling. And an essential parameter called as stage reaction (SR_i) must be analysed for each component. These stages reactions are computed by acknowledging the velocities.

For radial compressor, Equation A.85 to Equation A.87 estimate the stage reaction in this component.

$$\Delta h^c_{static} = \frac{(\bar{W}^c_1)^2 - (W^c_2)^2 + (U^c_2)^2 - (\bar{U}^c_1)^2}{2} \tag{A.85}$$

$$\Delta h^c_{dyn} = \frac{(V^c_2)^2 - (\bar{V}^c_1)^2}{2} \tag{A.86}$$

$$\Delta h^c_{total} = \Delta h^c_{static} + \Delta h^c_{dyn} \tag{A.87}$$

The stage reaction in the turbine is calculated by Equation A.88 and Equation A.89.

$$\Delta h^t_{static} = \frac{(W^t_5)^2 - (W^t_4)^2}{2} \tag{A.88}$$

$$\Delta h^t_{total} = \frac{(W^t_5)^2 - (W^t_4)^2 + (V^t_4)^2 - (V^t_5)^2}{2} \tag{A.89}$$

Hence, in Figure 93 and Figure 94, it is presented the triangle velocities for radial compressor and axial turbine, respectively.

Figure 93 – Radial compressor triangle velocities.

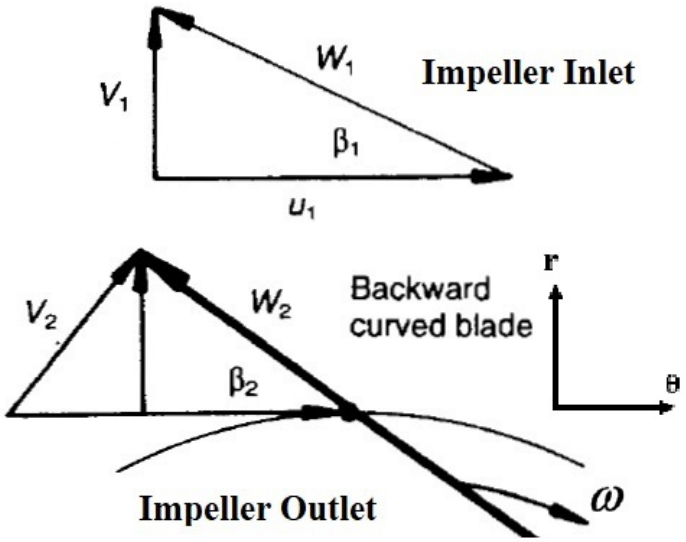

Source: Adapted from Turton (2012).

Figure 94 – Axial turbine triangle velocities.

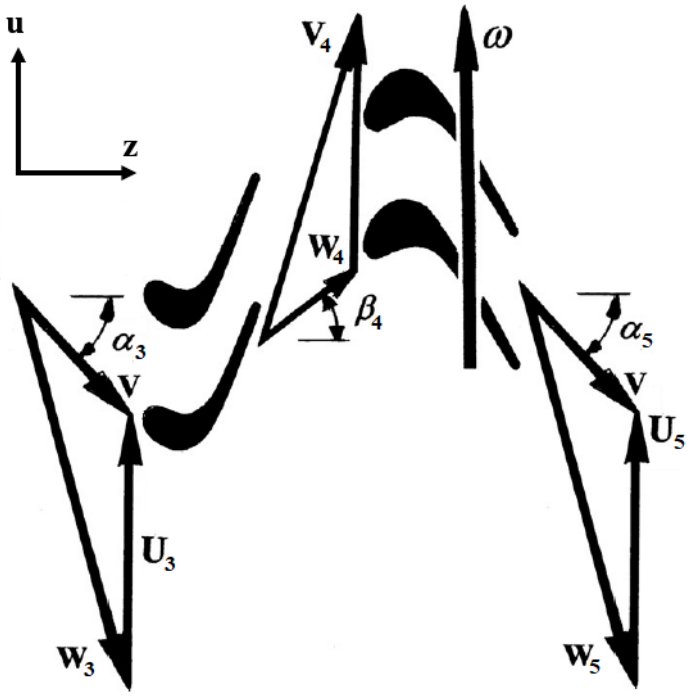

Source: Adapted from Baskharone (2006).

The following vectorial Equation A.90 is applied for each triangle velocity. Further, for the sake of simplicity, the absolute flow angle on the compressor inlet (α_1^c) is null, i.e. it means that air stream is flowing perpendicular to the impeller. For turbine, the inlet and outlet absolute flow angles (α_3^t and α_5^t) are assumed null too.

$$\hat{V}_j^i = \hat{W}_j^i + \hat{U}_j^i \tag{A.90}$$

The speed can be evaluated by Equation A.91 and Equation A.92.

$$U_j^i = \omega_i \cdot \bar{r}_j^i \tag{A.91}$$

$$\omega_i = \frac{2 \cdot \pi \cdot N_i}{60} \tag{A.92}$$

Regarding the radial compressor, each velocity in r-direction and θ-direction are represented by Equation A.93 to Equation A.96.

$$V_{j,\theta}^c = V_j^c \cdot \cos \alpha_j^c \tag{A.93}$$

$$V_{j,r}^c = V_j^c \cdot \sin \alpha_j^c \tag{A.94}$$

$$W_{j,\theta}^c = W_j^c \cdot \cos \beta_j^c \tag{A.95}$$

$$W_{j,r}^c = W_j^c \cdot \sin \beta_j^c \tag{A.96}$$

The same equations are repeated for turbine triangle velocities but in z-direction and u-direction, as explicit in Equation A.97 to Equation A.100.

$$V_{j,z}^t = V_j^t \cdot \cos \alpha_j^t \tag{A.97}$$

$$V_{j,u}^t = V_j^t \cdot \sin \alpha_j^t \tag{A.98}$$

$$W_{j,z}^t = W_j^t \cdot \cos \beta_j^t \tag{A.99}$$

$$W_{j,u}^t = W_j^t \cdot \sin \beta_j^t \tag{A.100}$$

When evaluating the turbine, it is necessary to define the flow parameter ($FP^t_{i,0}$) which is represented by Equation A.101 and Equation A.102. Both equations relate thermodynamic and kinetic properties with geometric aspects.

$$FP^t_{j,0} = \frac{\dot{m}_t \cdot \sqrt{T^t_{j,0} \cdot \frac{R_g}{k_g}}}{p^t_{j,0} \cdot A_{j,t} \cdot cos(\alpha^t_j)} \tag{A.101}$$

$$FP^t_{j,0} = M_{j,t} \cdot \left(1 + \frac{k_g - 1}{2} \cdot M^2_{j,t}\right)^{\frac{(k_g+1)}{2 \cdot (1-k_g)}} \tag{A.102}$$

After defining the governing equations as well as other auxiliary equations to correlate kinetic energy with thermodynamic properties and geometric characteristics, it is important to discuss the first calibration in the impeller outlet relative angle, known as β_2.

When dealing with radial compressor, in this case, backward configuration, the relative angle β_2 must be set for calculation purposes. However, this relative angle is not given even from manufacturer. Thus, this relative angle is calibrated in this modelling by assuming some operating conditions, i.e. reverse engineering.

Regarding the operating condition, this radial compressor does not present supersonic flow inside the compressor. As it has a diffuser, if the incoming flow stream achieves supersonic speed, this device will work as a supersonic nozzle, increasing the velocity while decreasing the pressure. Thereupon, in an effort to avert this situation, the Mach number on point 3 must be lesser than unit, i.e. the diffuser will work in subsonic flow, which implicates in increasing the pressure while decreasing the velocity.

In Figure 95, the pressure ratio and total temperature at the impeller outlet are plotted in function of relative angle β_2. The first calibration is set by respecting the boundaries conditions from manufacturer and UTE LORM operating conditions. The maximum pressure ratio is 5:1 with maximum speed of 29500 RPM.

The chart of pressure ratio in function of β_2 allows to determine this relative angle in Figure 95. Considering an approximated pressure ratio of 3.8, β_2 is -45°, which is inside the backward curved region. Furthermore, it also implicates in total temperature at the impeller exit lesser than 200°C (473.15 K), respecting the manufacturer limits.

By analysing Figure 96, it is checked that the Mach number at the diffuser is not in supersonic flow. Therefore, this first calibration respects all operating conditions in this radial compressor. For generating these charts in function of relative angle, it was adopted impeller efficiency around 0.8192, and speed of 26150 RPM with an air mass flow rate of 6.7 kg s^{-1} in one radial compressor.

Figure 95 – Calibrating relative angle at the exit of impeller.

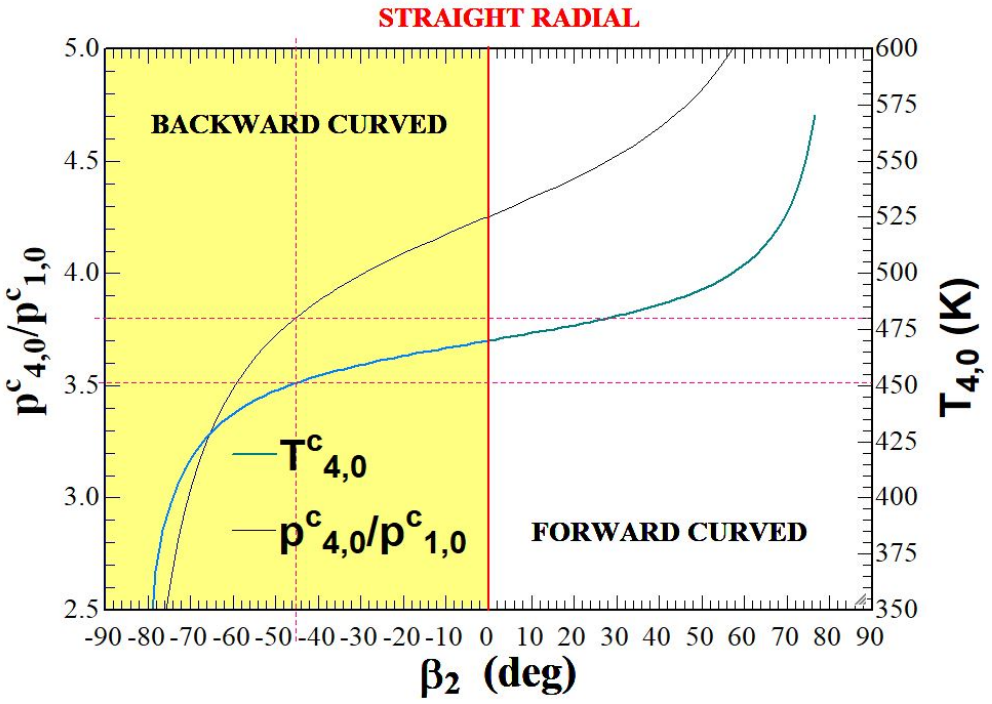

Source: Own Authorship.

Figure 96 – Checking the Mach numbers for relative angle at the exit of impeller.

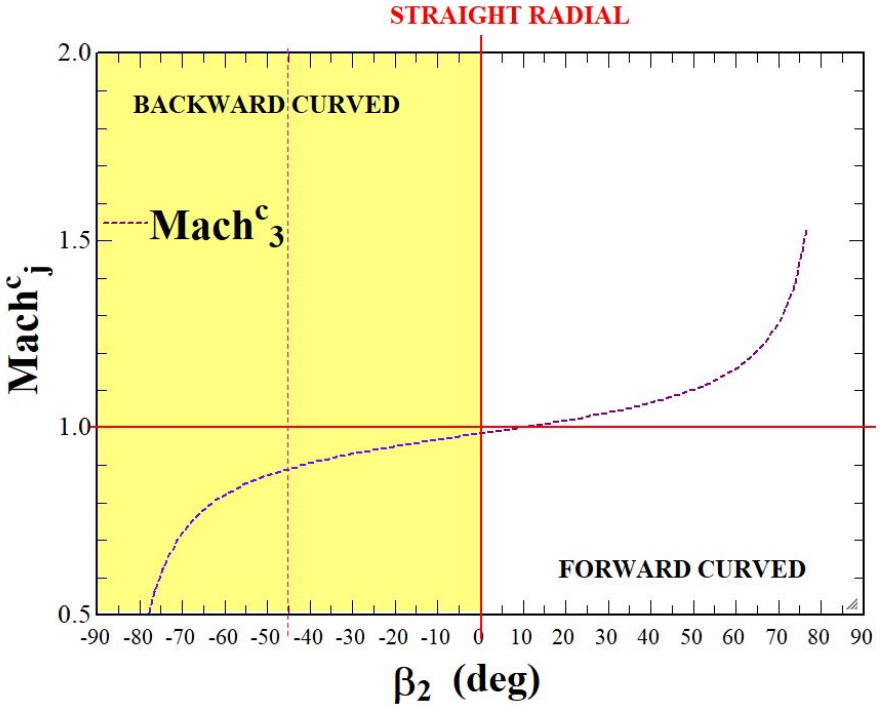

Source: Own Authorship.

As GT-Power software gives some results in different *BMEPs*, there are some database of turbocharger modelling that can be used as a backup information. Thus, a second calibration using *BMEP* of 20 bar is carried out in this framework. The previous curve fittings from Equation A.55, Equation A.57, Equation A.60 to Equation A.63 are used as parameters in this second modelling, assisting in the calibration. Moreover, three more curve fitting equations based on GT-Power are used here as parameters too, as represented in Equation A.103 to Equation A.105. The temperatures are set in Kelvin, pressures in bar, and mass flow rates in kg s^{-1}.

$$T_1^c = \frac{286388 - 67.6281 \cdot BMEP + 0.682831 \cdot BMEP^2 - 0.0493137 \cdot BMEP^3}{10^3} \quad \text{(A.103)}$$

$$T_{3,0}^t = \frac{731442 + 2516.12 \cdot BMEP - 32.5323 \cdot BMEP^2 + 0.20383 \cdot BMEP^3}{10^3} \quad \text{(A.104)}$$

$$\dot{m}_{air}^c = \frac{762937 + 665159 \cdot BMEP - 975.639 \cdot BMEP^2 + 25.6431 \cdot BMEP^3}{2 \cdot 10^6} \quad \text{(A.105)}$$

Basically, the total temperature at the impeller outlet in the radial compressor of 452.8 K, waste-gate mass flow rate of 0.3908 kg s^{-1}, compressor and turbine total-to-static efficiencies around 0.8 were targeted simultaneously. The compressor impeller efficiency (η_{imp}) as well as turbine polytropic efficiency (η_p), tip and hub radius are slightly calibrated to match these previous values from GT-Power for *BMEP* of 20 bar.

The first comparison regards to waste-gate mass flow rates, as presented in Figure 97. First of all, when assuming compressible effects and using more complex relations to determine the turbocharger operating behavior, it is observed that waste-gate mass flow rate is higher than GT-Power result. Hence, the waste-gate valve is more open, additionally, the turbine mass flow rate in this proposed modelling is lesser than turbine mass flow rate from GT-Power, as explicit in Figure 98.

These difference can be explained due a levering on stage reaction in turbine which is presented in Figure 99. The reaction is rising slightly when *BMEP* is increasing, which means that less exhaust gases are necessary in the turbine.

Another crucial advantage of using these more complex equations from this proposed methodology is regarded to estimate the operating speed and how much work is required for each *BMEP*. In Figure 100, it is shown both of these results.

Figure 97 – Comparison of waste-gate mass flow rate in function of *BMEP*.

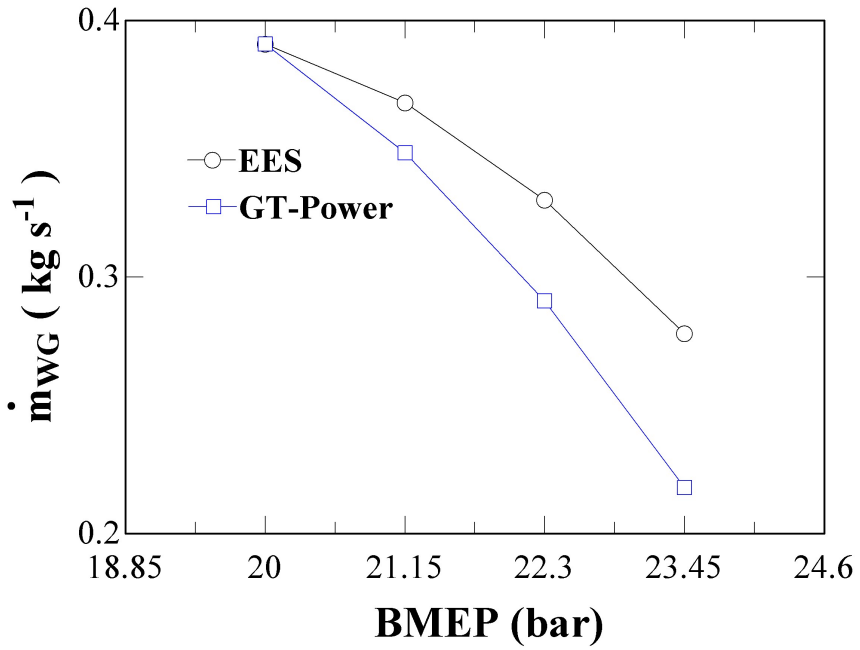

Source: Own authorship.

Figure 98 – Comparison of turbine mass flow rate in function of *BMEP*.

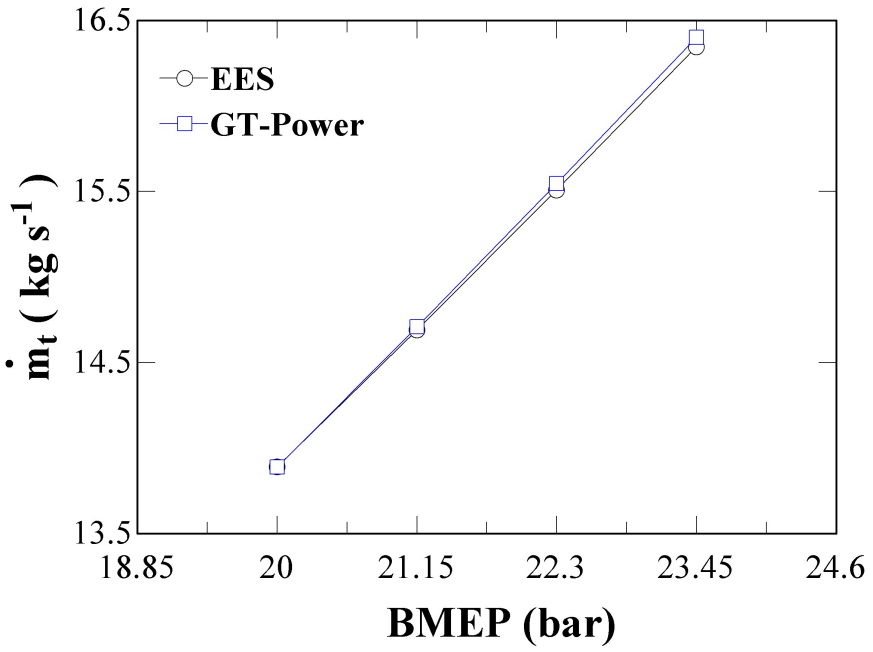

Source: Own authorship.

Figure 99 – Stage reaction profile in function of *BMEP*.

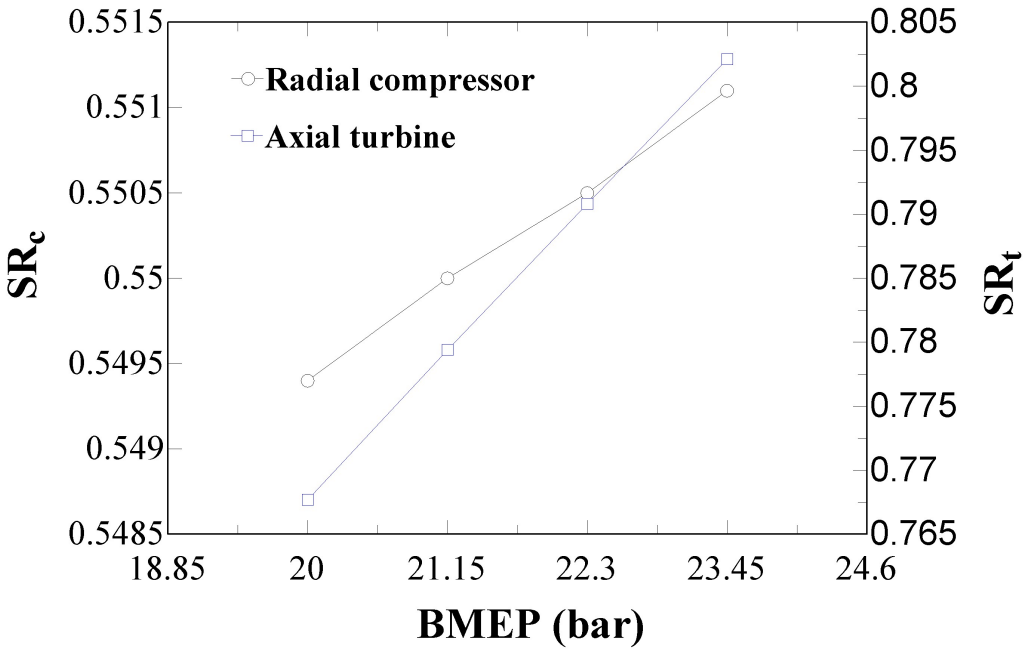

Source: Own authorship.

Figure 100 – Turbocharger speed and work.

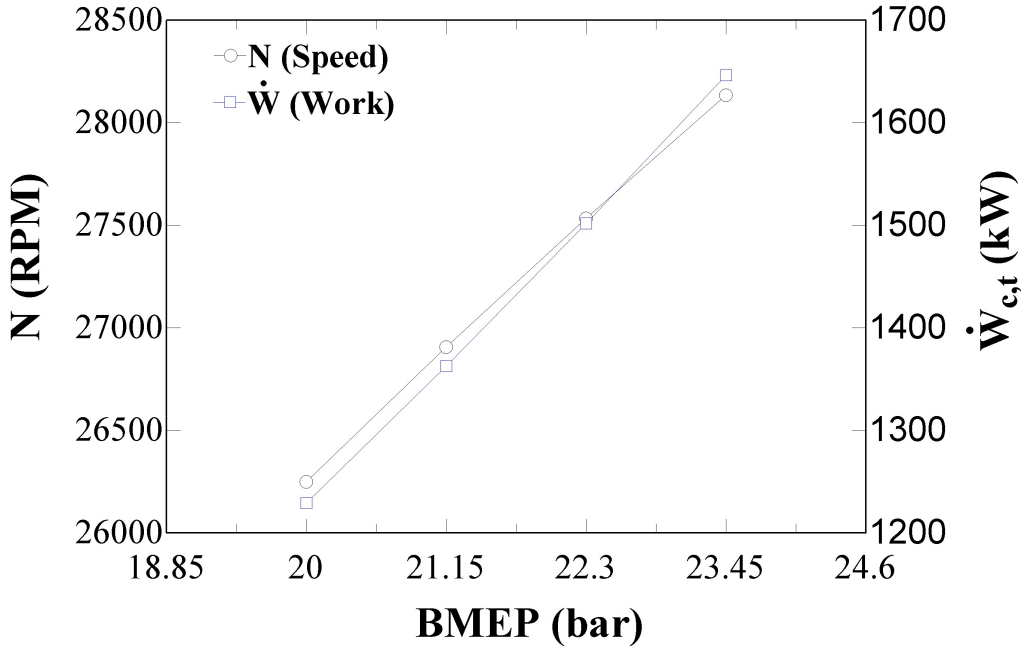

Source: Own authorship.

The total-to-static efficiencies are calculated in each *BMEP* for both compressor and turbine. It is essential to state that these efficiencies are not constant as it was defined in the simple turbocharger modelling. Nevertheless, they change slightly with *BMEP*, as represented in Figure 101. The turbine total-to-static efficiency is more sensible than compressor efficiency in function of *BMEP*. Moreover, the turbine efficiency decreases while compressor efficiency rises for each *BMEP*.

Figure 101 – Turbocharger total-to-static efficiencies in function of *BMEP*.

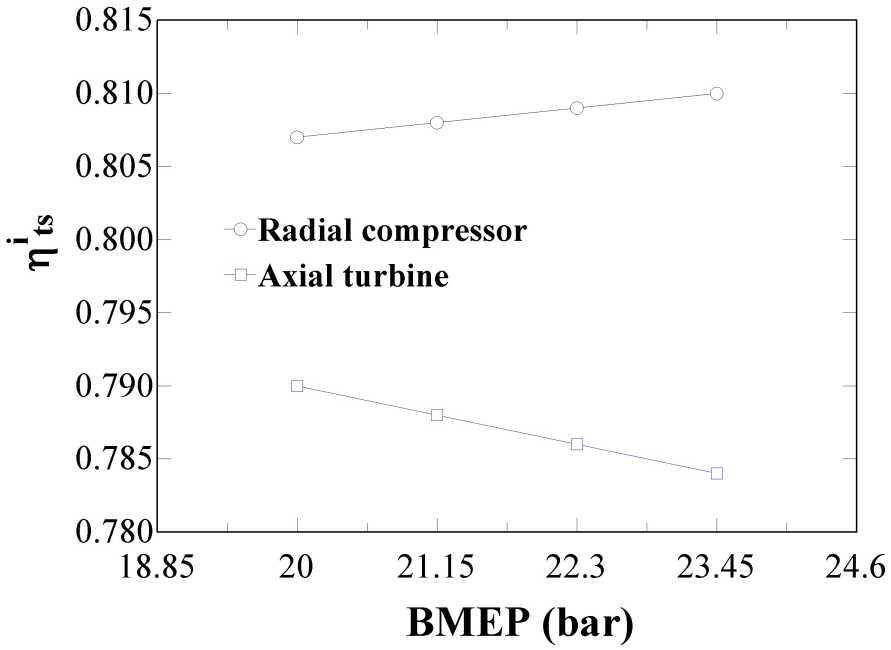

Source: Own authorship.

Despite the fact that these efficiency profiles seem to change slightly in each *BMEP*, the operating characteristics are affected directly by these efficiencies.

The temperature at the compressor outlet is following GT-Power result with a small difference, which makes sense since it was used the database as input in this modelling and compressor efficiency did not change abruptly. Further, the compressor power demand in this modelling is approximately equal to GT-Power result.

In Figure 102, the outlet temperature at the turbine component from this methodology is lesser than GT-Power result. This behavior makes sense since turbine is losing efficiency, and less mass rate is entering in the turbine. Hence, the enthalpy difference in exhaust gases increases to keep the same amount of work. As consequence, the temperature of exhaust gases at the junction of waste-gate with turbine outlet changes in a same manner, which is shown in Figure 103.

Figure 102 – Turbocharger total temperatures in function of *BMEP*.

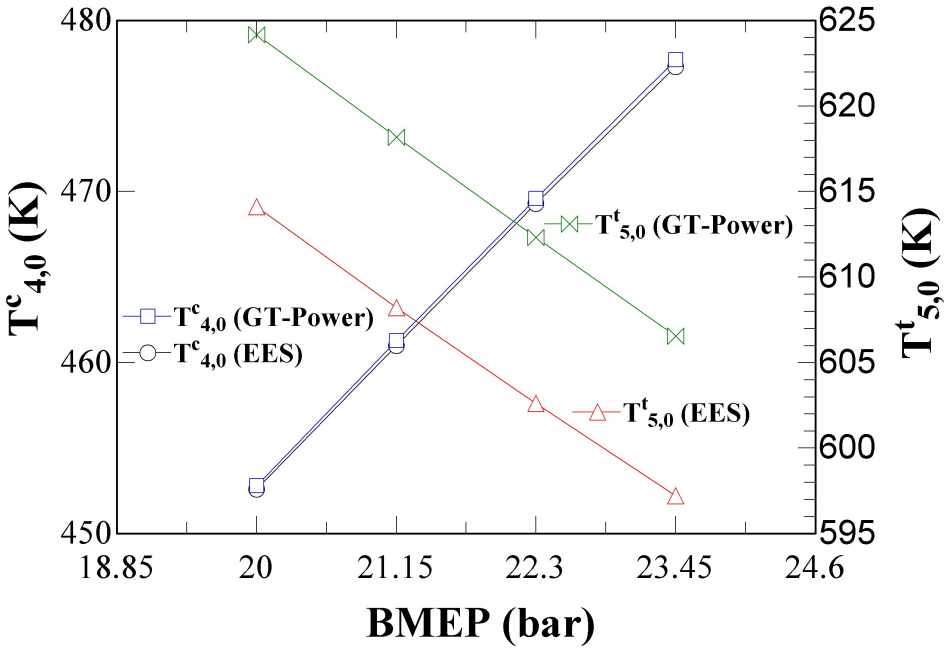

Source: Own authorship.

Figure 103 – Turbocharger total temperatures in function of *BMEP* at the junction of waste-gate with turbine exit.

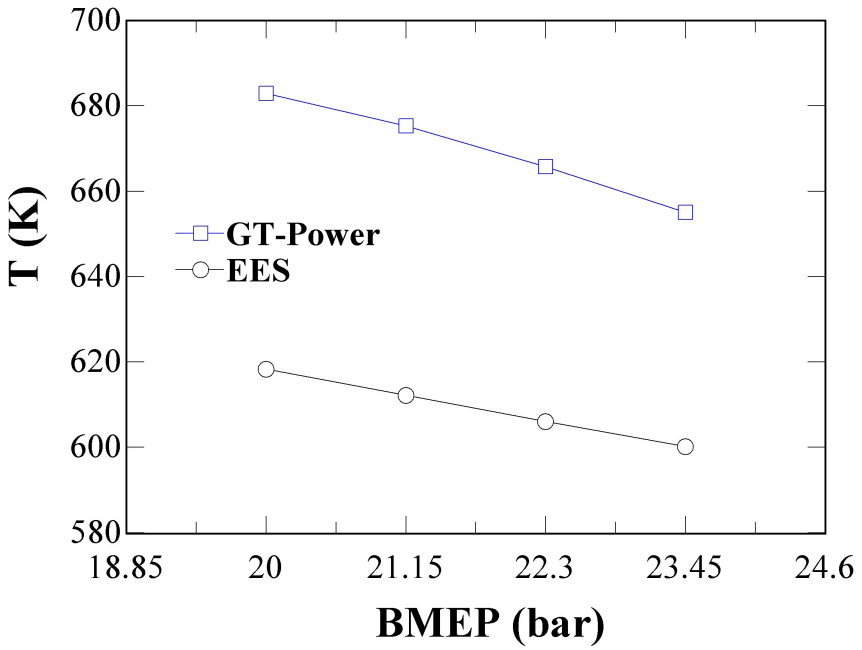

Source: Own authorship.

In summary, this methodology has been developed in an effort to instigate how to approach the turbocharger as a real machine, accounting with compressible effects by combining triangle velocities and geometric aspects. Of course, this modelling has a lot of simplifications and basic assumptions that interfere considerably in the final results. Nevertheless, it is interesting to note that more complex relations are required to evaluate this turbocharger. This methodology is not considered in this master's thesis due to high complexities, which increases significantly the optimization problem. Hence, it is suggested for future works to utilize this methodology and compare with this master's thesis.

A.4 Thermal System integrated with Wärtsilä Engine

This subsection A.4 provides the integration between the W20V34SG engine with superstructure of absorption chillers by applying conservation laws and combustion balance into piston-cylinders. Moreover, as the *BMEP* is increasing over the rated condition, the heat losses on W20V34SG engine must follow proportionally the shaft power generation.

First of all, the discussion here begins with combustion balance into piston-cylinders due the necessity to evaluate the Lower Heating Value (LHV_f) of the fuel, which is natural gas, as well as, the chemical composition of exhaust gases. The molar mass of the fuel ($\bar{M}_f$) can be determined by applying Equation A.106.

$$\bar{M}_f = \sum_{i=1}^{8} n_i \cdot \bar{M}_i \tag{A.106}$$

Table 70 presents the results from complete combustion model with excess of humid air.

Table 70 – Natural gas chemical compositions.

		Fuel		
i	$species_i$	n_i (mole)	$\bar{M}_i$ (kg kmole^{-1})	LHV_i (kJ kg^{-1})
1	CH_4	0.9079	16.04	50023
2	C_2H_6	0.0569	30.07	47508
3	C_3H_8	0.0159	44.10	46330
4	C_4H_{10}	0.0034	58.12	45348
5	C_5H_{12}	0.0004	72.15	44974
6	C_6H_{14}	0.0000	86.17	44742
7	CO_2	0.0088	44.01	0
8	N_2	0.0066	28.01	0

Source: EES software and Zabeu, Martelli and Penaranda (2018).

The LHV_f can be determined by applying Equation A.107 that is extracted from Moran et al. (2013).

$$LHV_f = \sum_{i=1}^{8} \frac{n_i \cdot LHV_i \cdot \bar{M}_i}{\bar{M}_f} \tag{A.107}$$

Equation A.108 is representing the combustion process inside the piston-cylinders, reminding that air is humid, thus, taking into account the excess of air and humidity.

$$[fuel + air \rightarrow gases]_{piston-cylinders} \tag{A.108}$$

In order to estimate the chemical composition of ambient air, the following Equation A.109 must be applied.

$$y_v = \frac{\Phi'_{amb} \cdot p_{sat}(T_{amb})}{p_{amb}} \tag{A.109}$$

One essential detail must be noted here, the humid air is suffering dehumidification and cooling process across cooling coil. Hence, it is fundamental to correct the chemical composition right after it is leaving the cooling coil. Equation A.109 must be used again but considering the properties at the coil outlet, as represented in Equation A.110. Table 71 contains the number of moles for humid air at the coil outlet. A quick reminder about this detail on exergy analysis, the chemical composition on air stream at the cooling tower also needs to be corrected due to humidification process.

$$y_v^{CC} = \frac{\Phi'^{CC}_{out} \cdot p_{sat}(T^{CC}_{out})}{p^{CC}_{out}} \tag{A.110}$$

Table 71 – Chemical composition of humid air at the coil outlet.

i	$species_i$	$y_{dry,i}$	y_i (% Vol.)		n_i (mole)	
9	H_2O	0	$100 \cdot y_v^{CC}$	1.45	$y_i\ y_{13}^{-1}$	0.070
10	CO_2	0.03	$y_{dry,i} \cdot (1 - y_v^{CC})$	0.03	$y_i\ y_{13}^{-1}$	0.001
11	Ar	0.93	$y_{dry,i} \cdot (1 - y_v^{CC})$	0.92	$y_i\ y_{13}^{-1}$	0.044
12	N_2	78.09	$y_{dry,i} \cdot (1 - y_v^{CC})$	76.96	$y_i\ y_{13}^{-1}$	3.727
13	O_2	20.95	$y_{dry,i} \cdot (1 - y_v^{CC})$	20.65	1	1

Source: Adapted from Moran et al. (2013).

As the chemical molar composition of humid air is defined, the next procedure regards to execute the complete combustion balance. Firstly, the stoichiometric complete

combustion balance is carried out to find the molar coefficients without considering excess of air and humidity, as explicit in Equation A.111.

$$\sum_{i=1}^{8} n_i \cdot species_i + A' \cdot O_2 \rightarrow \sum_{i=14}^{17} n_{stoich,i} \cdot species_i \tag{A.111}$$

After calculating the stoichiometric molar coefficients, the complete combustion with excess of air and humidity can be evaluated by Equation A.112. The A' is determined around 2.1198.

$$\sum_{i=1}^{8} n_i \cdot species_i + \lambda \cdot A' \cdot \sum_{i=9}^{13} n_i \cdot species_i \rightarrow \sum_{i=14}^{18} n_i \cdot species_i \tag{A.112}$$

The excess of air (λ) into piston-cylinders is set 2 which is in accordance with Zabeu, Martelli and Penaranda (2018). This value was tested for W20V34SG engine in several $BMEPs$ with distinct λ at the UTE LORM. Moreover, Petrassi (2012) provides a combustion map in function of $BMEP$ and excess of air, as described in Figure 104.

Figure 104 – Combustion map of W20V34SG engine in function of λ and $BMEP$.

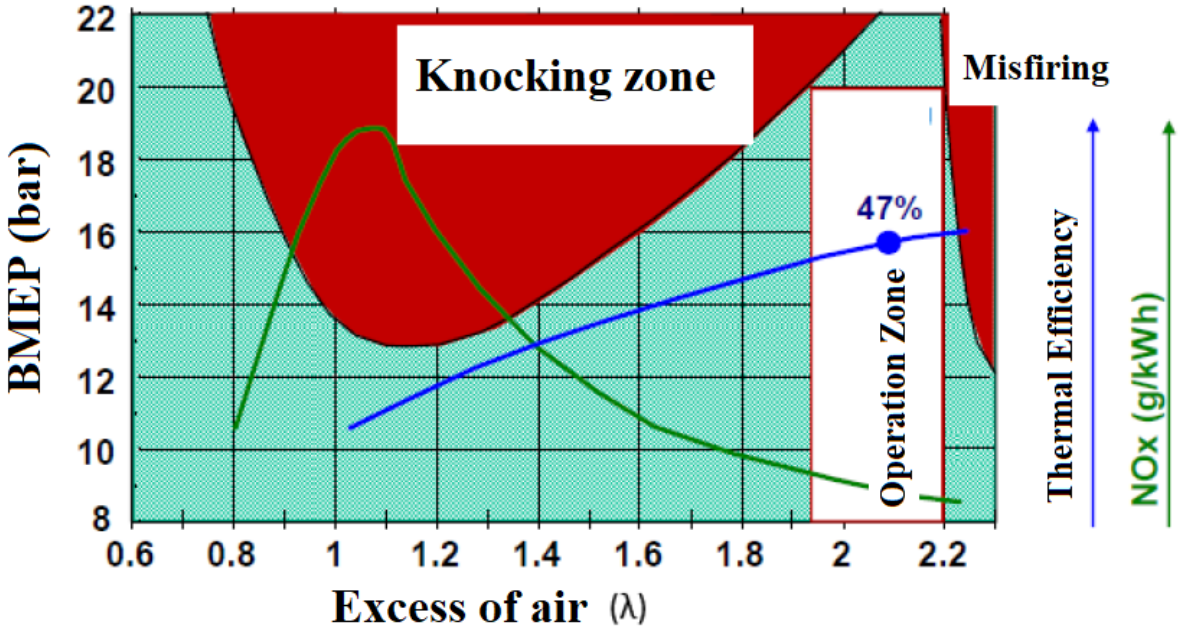

Source: Adapted from Petrassi (2012).

The air-fuel ratio (A/F) can be calculated by using Equation A.113.

$$A/F = \frac{\lambda \cdot A' \cdot \sum_{i=9}^{13} n_i \cdot \bar{M}_i}{\sum_{i=1}^{8} n_i \cdot \bar{M}_i} \tag{A.113}$$

Table 72 – Stoichiometric and complete combustion model with excess of humid air.

			Stoichiometric	Complete Combustion with Excess of humid air		
			Fuel**			
i	$species_i$		n_i (mole)		n_i (mole)	y_i (% mole)
1	CH_4		0.9079		0.9079	90.79
2	C_2H_6		0.0569		0.0569	5.69
3	C_3H_8		0.0159		0.0159	1.59
4	C_4H_{10}		0.0034		0.0034	0.34
5	C_5H_{12}		0.0004		0.0004	0.04
6	C_6H_{14}		0.0000		0.0000	0.00
7	CO_2		0.0088		0.0088	0.88
8	N_2		0.0066		0.0066	0.66
	Oxygen				Humid Air	
i	$species_i$		$n_{stoich,i}$ (mole)		n_i (mole)	y_i (% mole)
9	H_2O		0	$\lambda \cdot A'$	0.070	1.45
10	CO_2		0	$\lambda \cdot A'$	0.001	0.03
11	Ar		0	$\lambda \cdot A'$	0.044	0.92
12	N_2		0	$\lambda \cdot A'$	3.727	76.96
13	O_2	A'	1	$\lambda \cdot A'$	1	20.65
			Exhaust Gases			
i	$species_i$		$n_{stoich,i}$ (mole)		n_i (mole)	y_i (% mole)
14	H_2O		2.0695		2.367	11.00
15	CO_2		1.0938		1.100	5.10
16	Ar		0.0000		0.188	0.90
17	N_2		0.0066		15.809	73.20
18	O_2		0.0000		2.120	9.80

Source: Adapted from **Zabeu, Martelli and Penaranda (2018).

Recalling in section A.3, the fuel mass flow rate is determined by applying Equation A.64. Thus, acknowledging the LHV_f and $\dot{m}_f$, it is also possible to estimate the amount of heat of natural gas ($\dot{Q}_{NG}$), as represented in Equation A.114.

$$\dot{Q}_{NG} = \dot{m}_f \cdot LHV_f \tag{A.114}$$

Furthermore, the heat rejection at the charge air cooler is defined in section A.3 as the heat transfer between compressor outlet and intake manifold. In order to evaluate the intake manifold temperature, it is used psychrometric properties from EES software. The humidity ratio is calculated at the coil outlet, and it remains constant at the intake

manifold too.

$$\omega_a'^{IM} = \omega_{out,a}'^{CC} \tag{A.115}$$

The pressure at the intake manifold is extracted from GT-Power simulations as a curve fitting equation in function of *BMEP*, which is explicit in Equation A.116. The R^2 of this regression equation is 100% with a root mean square (*RMS*) of 1.59 $\cdot 10^{-12}$, the physical unit is set in bar.

$$p_a^{IM} = \frac{360712 + 156977 \cdot BMEP + 598.09 \cdot BMEP^2 + 5.39163 \cdot BMEP^3}{10^6} \tag{A.116}$$

A control condition of 2°C above dew-point temperature ($T_{dp,a}^{IM}$) is set to avoid condensation at the intake manifold ($T_{db,a}^{IM}$), as represented in Equation A.117.

$$T_{db,a}^{IM} = T_{dp,a}^{IM} + 2 \tag{A.117}$$

The intake manifold dew-point temperature can be evaluated by using Equation A.118.

$$T_{dp,a}^{IM} = T(AirH_2O; T_{db,a}^{IM}; \omega_a'^{IM}; p_a^{IM}) \tag{A.118}$$

The outlet air enthalpy at the CACs ($h_{out,a}^{CACs}$) is equal to intake manifold enthalpy, as follows.

$$h_{out,a}^{CACs} = h_{db,a}^{IM} \tag{A.119}$$

By calculating intake manifold dry-bulb temperature ($T_{db,a}^{IM}$), it is possible to determine the heat rejection on charge air coolers ($\dot{Q}_{ICE}^{CACs}$). Subsequently, the percentage of heat losses for CACs ($Losses_{\%}^{CACs}$) is also estimated by applying Equation A.120.

$$Losses_{\%}^{CACs} = \frac{\dot{Q}_{ICE}^{CACs}}{\dot{Q}_{NG}} \tag{A.120}$$

With respect to the other losses from W20V34SG engine, e.g. lube oil, radiation and convection, and engine block, it is used some data from Wärtsilä brochure at the Annex B to predict the heat rejection above 20 bar of *BMEP* in function of shaft power. Hence, Equation A.121 to Equation A.124 are applied here.

$$Losses_{\%}^{LO} = \frac{106069}{10^6} - \frac{9.55417}{10^6} \cdot \dot{W}_{ICE} + \frac{4.34115}{10^{10}} \cdot \dot{W}_{ICE}^2 - \frac{6.82689}{10^{15}} \cdot \dot{W}_{ICE}^3 \tag{A.121}$$

$$Losses_{\%}^{r/c} = \frac{546701}{10^7} - \frac{104.364}{10^7} \cdot \dot{W}_{ICE} + \frac{9.50631}{10^{10}} \cdot \dot{W}_{ICE}^2 - \frac{3.09460}{10^{14}} \cdot \dot{W}_{ICE}^3 \quad \text{(A.122)}$$

$$Losses_{\%}^{block} = \frac{1192801}{10^7} - \frac{3.10373}{10^9} \cdot \dot{W}_{ICE}^2 + \frac{4.11766}{10^{13}} \cdot \dot{W}_{ICE}^3 - \frac{1.52987}{10^{17}} \cdot W_{ICE}^4 \quad \text{(A.123)}$$

Using conservation of energy, the sum of these losses must be 1. Thus, Equation A.124 calculates the percentage of losses in exhaust gases.

$$Losses_{\%}^{gases} = 1 - (Losses_{\%}^{block} + Losses_{\%}^{r/c} + Losses_{\%}^{LO} + Losses_{\%}^{CACs} + \eta_{ICE}^{brake}) \quad \text{(A.124)}$$

The heat rejection of each part can be estimated by just multiplying the total amount of heat of natural gas with each percentage, as shown in Equation A.125 to Equation A.127.

$$\dot{Q}_{ICE}^{block} = Losses_{\%}^{block} \cdot \dot{Q}_{NG} \quad \text{(A.125)}$$

$$\dot{Q}_{ICE}^{r/c} = Losses_{\%}^{r/c} \cdot \dot{Q}_{NG} \quad \text{(A.126)}$$

$$\dot{Q}_{ICE}^{LO} = Losses_{\%}^{LO} \cdot \dot{Q}_{NG} \quad \text{(A.127)}$$

The cooling water at the LT circuit must be analysed by applying conservation of energy, the total amount of heat rejection in this circuit is equal to CACs and lube oil heat transfer rates, as represented in Equation A.128 to Equation A.130. The water mass flow rate at the LT circuit ($\dot{m}_{LT,w}$) is assumed 23.772 kg s^{-1} with a pressure at the CACs inlet around 4 bar, as represented in Figure 105.

$$\dot{Q}_{LT,w}^{rejection} = \dot{Q}_{ICE}^{LO} + \dot{Q}_{ICE}^{CACs} \quad \text{(A.128)}$$

$$\dot{Q}_{LT,w}^{rejection} = \dot{m}_{LT,w} \cdot (h_{out,w}^{CACs} - h_{in,w}^{CACs}) \quad \text{(A.129)}$$

$$\dot{Q}_{ICE}^{LO} + \dot{Q}_{ICE}^{CACs} = \dot{m}_{LT,w} \cdot (h_{out,w}^{CACs} - h_{in,w}^{CACs}) \quad \text{(A.130)}$$

Another consideration is set here about the three-way valve (3WV), it is defined the inlet temperature at the CACs 2°C below dew-point temperature, as explicit in Equation A.131.

$$T_{in,w}^{CACs} = T_{dp,a}^{IM} - 2 \tag{A.131}$$

Figure 105 – Schematic of HT/LT water circuit.

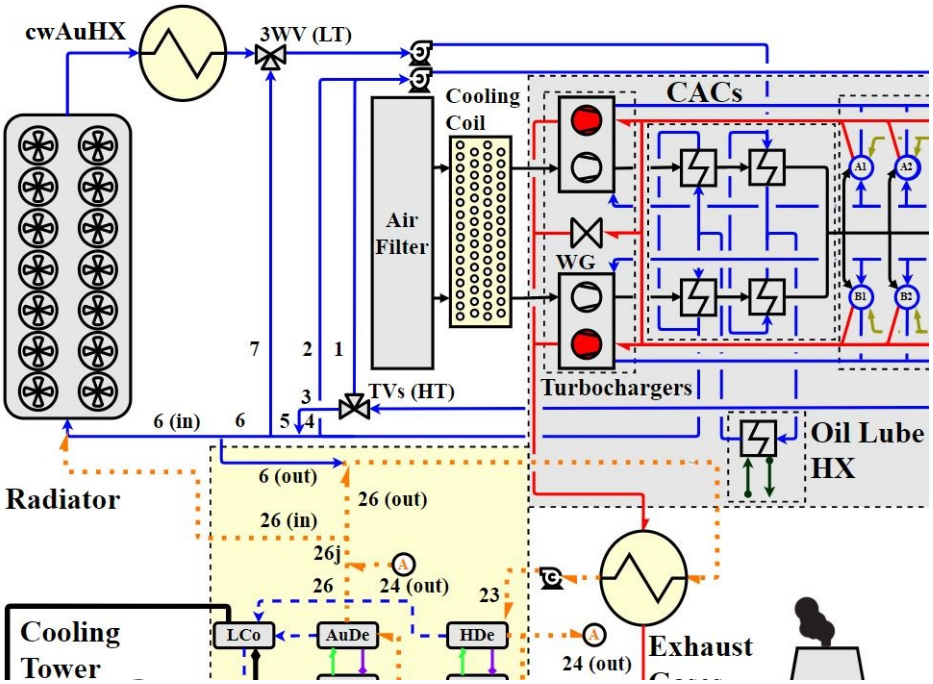

Source: Own Authorship.

The total amount of heat rejection that radiator plus chilled water auxiliary heat exchanger must release to the environment is defined by Equation A.132 and Equation A.133. Also, the incoming water stream in three-way valve at the LT circuit (3WV-LT) is considered 4°C below dew-point of the intake manifold, as explicit in Equation A.134.

$$\dot{Q}_{total,w}^{rejection} = \dot{Q}_{ICE}^{block} + \dot{Q}_{ICE}^{CACs} + \dot{Q}_{ICE}^{LO} \tag{A.132}$$

$$\dot{Q}_{total,w}^{rejection} = \dot{m}_{w}^{rad} \cdot (h_{in,w}^{rad} - h_{out,w}^{cwAuHX}) \tag{A.133}$$

$$T_{out,w}^{cwAuHX} = T_{dp,a}^{IM} - 4 \tag{A.134}$$

The thermodynamic state at the inlet of engine block circuit is defined as 76°C with a absolute pressure around 4 bar. Then, the thermodynamic state at the outlet of

engine block circuit ($h_{out,w}^{block}$) can be calculated by applying first law of thermodynamics, as it can be seen in Equation A.135.

$$\dot{Q}_{ICE}^{block} = \dot{m}_{HT,w} \cdot (h_{out,w}^{block} - h_{in,w}^{block}) \tag{A.135}$$

The following Equation A.136 to Equation A.148 are used to estimate the water mass flow rates as well as the thermodynamic properties at the radiator circuit and in each splitting and junction of HT/LT water circuit.

The first equation here is in regard to the mass balance at the engine block circuit (HT water circuit) which is described in Equation A.136. Also, Equation A.137 represents the first law of thermodynamics in this junction.

$$\dot{m}_{HT,w} = \dot{m}_{1,w} + \dot{m}_{2,w} \tag{A.136}$$

$$\dot{m}_{HT,w} \cdot h_{in,w}^{block} = \dot{m}_{1,w} \cdot h_{1,w} + \dot{m}_{2,w} \cdot h_{2,w} \tag{A.137}$$

The point 5 receives water stream from point 3 and 4. It can be assumed that point 5 has the same mass flow rate of LT water circuit. Thus, Equation A.138 represents the conservation of mass between points 3 and 4, while Equation A.139 also represents mass balance between points 4 and 2. Moreover, point 5 is divided in point 6 and 7, which is explicit in Equation A.140.

$$\dot{m}_{LT,w} = \dot{m}_{5,w} = \dot{m}_{4,w} + \dot{m}_{3,w} \tag{A.138}$$

$$\dot{m}_{LT,w} = \dot{m}_{5,w} = \dot{m}_{4,w} + \dot{m}_{2,w} \tag{A.139}$$

$$\dot{m}_{LT,w} = \dot{m}_{5,w} = \dot{m}_{6,w} + \dot{m}_{7,w} \tag{A.140}$$

first law of thermodynamics can be used here again to correlate the thermodynamic properties of points 3, 4 and 5, as shown in Equation A.141.

$$\dot{m}_{5,w} \cdot h_{5,w} = \dot{m}_{3,w} \cdot h_{3,w} + \dot{m}_{4,w} \cdot h_{4,w} \tag{A.141}$$

At three-way valve in LT circuit (3WV-LT), an energy balance is also applied, as represented in Equation A.142.

$$\dot{m}_{out,w}^{cwAuHX} \cdot h_{out,w}^{cwAuHX} + \dot{m}_{7,w} \cdot h_{7,w} = \dot{m}_{LT,w} \cdot h_{in,w}^{CACs} \tag{A.142}$$

After point 6, there is another splitting that dictates how much of water stream from LT circuit is going to be recovered by the superstructure. Hence, Equation A.143 to Equation A.148 are required to evaluate the mass flow rate as well as thermodynamic properties in each point. Furthermore, a decision variable is considered in this set of equations, which is the splitting in point 6 (b_5).

$$\dot{m}_{out,6,w} = b_{5,w} \cdot \dot{m}_{6,w} \tag{A.143}$$

$$\dot{m}_{6,w} = \dot{m}_{in,6,w} + \dot{m}_{out,6,w} \tag{A.144}$$

$$\dot{m}_{23} = \dot{m}_{out,6,w} + \dot{m}_{out,26,w} \tag{A.145}$$

$$\dot{m}_{23} \cdot h_{in,w}^{EHX} = \dot{m}_{6,out,w} \cdot h_{6,w} + \dot{m}_{out,26,w} \cdot h_{out,26,w} \tag{A.146}$$

$$\dot{m}_{23} = \dot{m}_{26,j} = \dot{m}_{out,26,w} + \dot{m}_{in,26,w} \tag{A.147}$$

$$\dot{m}_{6,w} \cdot h_{in,w}^{rad} = \dot{m}_{6,in,w} \cdot h_{6,w} + \dot{m}_{in,26,w} \cdot h_{26,j} \tag{A.148}$$

The exhaust gases heat exchanger is also presented here as a simple energy balance with conservation of mass. Thus, some techniques as log mean temperature difference is recalled to calculate the heat transfer area of this equipment. Figure 105 is representing this heat exchanger producing hot water to drive the superstructure of absorption chiller.

The Equation A.149 to Equation A.153 represent the first law of thermodynamics and log mean temperature difference calculation. The temperature at the exit of exhaust gases heat exchanger on water side ($T_{out,w}^{EHX}$) is considered 95°C with a pressure of 4 bar, also, the overall heat transfer coefficient ($U_{w,g}^{EHX}$) is assumed around 50 W m^{-2} K^{-1}.

$$\dot{Q}_{w}^{EHX} = \dot{m}_{23} \cdot (h_{out,w}^{EHX} - h_{in,w}^{EHX}) \tag{A.149}$$

$$\dot{Q}_{g}^{EHX} = \dot{m}_{g} \cdot (h_{in,g}^{EHX} - h_{out,g}^{EHX}) \tag{A.150}$$

$$\dot{Q}_{g}^{EHX} = \dot{Q}_{w}^{EHX} \tag{A.151}$$

$$\Delta T_{lm}^{EHX} = \frac{(T_{in,g}^{EHX} - T_{out,w}^{EHX}) - (T_{out,g}^{EHX} - T_{in,w}^{EHX})}{ln\left(\frac{T_{in,g}^{EHX} - T_{out,w}^{EHX}}{T_{out,g}^{EHX} - T_{in,w}^{EHX}}\right)} \tag{A.152}$$

$$\dot{Q}_{w,g}^{EHX} = U_{w,g}^{EHX} \cdot A_{w,g}^{EHX} \cdot \Delta T_{lm}^{EHX} \tag{A.153}$$

The next component to be discussed here is the radiator, this equipment has the goal to exchange heat between the water and air streams, maintaining the water circuit under safe operating condition for the engine in means of thermal stability. In an effort to model the radiator, Table 73 contains the necessary database from UTE LORM.

Table 73 – Radiator design parameters.

n_{fans}	14
$T_{in,w}$ (°C)	72.9
$T_{out,w}$ (°C)	39.8
$\dot{V}_w$ (m^3 h^{-1})	120.0
$T_{in,a}$ (°C)	35.0
$T_{out,a}$ (°C)	55.6
Φ'_a	0.8
$\dot{m}_a$ (kg s^{-1})	210.2
$A_{w,a}^{rad}$ (m^2)	10126
$U_{w,a}^{rad}$ (W m^{-2} K^{-1})	46.59
$\dot{Q}_{w,a}^{rad}$ (kW)	4600.0
$\dot{W}_{design}^{rad}$ @60Hz (kW)	5.55
$\dot{W}_{ele,design}^{rad}$ @60Hz (kW)	6.61
N_{design}^{rad} (RPM)	865.0

Source: UTE LORM.

An important observation about radiator is related to the overall heat transfer coefficient. During the R&D project, it was noticed that the radiator was not functioning properly. Thereupon, an investigation was carried out to discover why the radiator was not responding accordingly with the manufacturer brochure. It was encountered that the real overall heat transfer coefficient was much below the designing condition. In short, it was verified by some simulations that the corrected overall heat transfer coefficient was almost half of the design parameter (22.68 W m^{-2} K^{-1}) and a corrected air mass flow rate at the radiator around 126.6 kg s^{-1}. This can be explained due the high usage of radiator without cleaning and giving a proper maintenance.

Similarly to exhaust gases heat exchanger, the radiator is also modelled as a simple energy balance with conservation of mass and log mean temperature difference calculation,

as explicit in Equation A.154 to Equation A.158.

$$\dot{Q}_{w}^{rad} = \dot{m}_{w}^{rad} \cdot (h_{in,w}^{rad} - h_{out,w}^{rad}) \tag{A.154}$$

$$\dot{Q}_{a}^{rad} = \dot{m}_{a}^{rad} \cdot (h_{out,a}^{rad} - h_{in,a}^{rad}) \tag{A.155}$$

$$\dot{Q}_{a}^{rad} = \dot{Q}_{w}^{rad} \tag{A.156}$$

$$\Delta T_{lm}^{rad} = \frac{(T_{in,w}^{rad} - T_{out,a}^{rad}) - (T_{out,w}^{rad} - T_{in,a}^{rad})}{ln\left(\frac{T_{in,w}^{rad} - T_{out,a}^{rad}}{T_{out,w}^{rad} - T_{in,a}^{rad}}\right)} \tag{A.157}$$

$$\dot{Q}_{w,a}^{rad} = U_{w,a}^{rad} \cdot A_{w,a}^{rad} \cdot \Delta T_{lm}^{rad} \tag{A.158}$$

In this master's thesis, one of the objectives is to evaluate possible savings in shaft energy demand at the 14 fans. Thus, similarities rules for fan devices can be used here (FOX; PRITCHARD; MCDONALD, 2012), as it can be seen in Equation A.159 to Equation A.161. For the sake of simplicity, the radiator inverter efficiency (η_{ele}^{rad}) is assumed unit.

$$\dot{m}_{a}^{rad} = \rho_{a}^{rad} \cdot \dot{V}_{fan}^{rad} \tag{A.159}$$

$$\frac{\dot{V}_{fan}^{rad}}{\dot{V}_{design}^{rad}} = \frac{N_{fan}^{rad}}{N_{design}^{rad}} \tag{A.160}$$

$$\frac{\dot{W}_{fan}^{rad}}{\dot{W}_{design}^{rad}} = \left(\frac{N_{fan}^{rad}}{N_{design}^{rad}}\right)^{3} \tag{A.161}$$

$$\dot{W}_{ele}^{rad} = \frac{\dot{W}_{fan}^{rad}}{\eta_{ele}^{rad}} \tag{A.162}$$

The chilled water auxiliary heat exchanger is also modelled as a simple energy balance with conservation of mass and log mean temperature difference calculation, as it can be seen in Equation A.163 to Equation A.167. The inlet and outlet temperatures of chilled water ($T_{in,cw}^{cwAuHX}$ and $T_{out,cw}^{cwAuHX}$) are 7 and 12°C, respectively. The overall heat transfer coefficient for this equipment is assumed 1000 W m^{-2} K^{-1}.

$$\dot{Q}_{w}^{cwAuHX} = \dot{m}_{w}^{cwAuHX} \cdot (h_{in,w}^{cwAuHX} - h_{out,w}^{cwAuHX}) \tag{A.163}$$

$$\dot{Q}_{cw}^{cwAuHX} = \dot{m}_{cw}^{cwAuHX} \cdot (h_{out,cw}^{cwAuHX} - h_{in,cw}^{cwAuHX}) \tag{A.164}$$

$$\dot{Q}_{cw}^{cwAuHX} = \dot{Q}_{w}^{cwAuHX} \tag{A.165}$$

$$\Delta T_{lm}^{cwAuHX} = \frac{(T_{in,w}^{cwAuHX} - T_{out,cw}^{cwAuHX}) - (T_{out,w}^{cwAuHX} - T_{in,cw}^{cwAuHX})}{ln\left(\frac{T_{in,w}^{cwAuHX} - T_{out,cw}^{cwAuHX}}{T_{out,w}^{cwAuHX} - T_{in,cw}^{cwAuHX}}\right)} \tag{A.166}$$

$$\dot{Q}_{w,cw}^{cwAuHX} = U_{w,cw}^{cwAuHX} \cdot A_{w,cw}^{cwAuHX} \cdot \Delta T_{lm}^{cwAuHX} \tag{A.167}$$

At last, the electric generator coupled with W20V34SG engine, as shown in Figure 106, is also represented mathematically here as a curve fitting based on manufacturer brochure database.

Figure 106 – Electric generator coupled with W20V34SG engine.

Source: Own Authorship.

Equation A.168 and Equation A.169 define the electric power output at the generator.

$$\eta_{eg}^{ICE} = const_0 + \sum_{k=1}^{2} const_k \cdot d_k + \sum_{k=1}^{2} const_k \cdot d_k^{const_{k+2}} \tag{A.168}$$

$$\dot{W}_{ele}^{ICE} = \dot{W}_{ICE} \cdot \eta_{eg}^{ICE} \tag{A.169}$$

Concerning the Equation A.168, Table 74 contains necessary data for this curve fitting.

Table 74 – List of coefficients for electric generator curve fitting.

$const_k$	Value	d_k
0	919E-3	-
1	27.66E-3	$p.f. = 1$
2	555E-9	$\dot{W}_{ele}^{ICE}$
3	5.796E-3	-
4	-129.2E-3	-

Source: UTE LORM.

All the presented modellings are necessary to integrate the whole superstructure of absorption chiller with one W20V34SG engine. Hence, all equations must be set and connected to permit the calculation of all results.

APPENDIX B – GT - Power Software Simulation

In this master's thesis, it is not carried out a detailed modelling for the ICE in EES software due to its high complexity and transient problem. Then, in this Appendix B, a previous R&D project (ANEEL PD-6932-0115-2014) from Zabeu, Martelli and Penaranda (2018) is consulted and adapted for this present work. They modelled the same Wärtsilä 20V34SG engine in the GT-Power software by using some literature assumptions and operating conditions from the site. For instance, a well-known book from Heywood (2018) contains great amount of information about internal combustion engines.

The objective of using GT-Power simulation separately from EES is to investigate 11 internal parameters of ICE in an effort to predict how far it is feasible to push forward the *BMEP*, reaching nearly 10 MW of shaft power output without harming the engine. Concerning to provide the ICE operation behavior under the new circumstances, pressure drops on the intake air of compressor upstream and on the exhaust gases system are taken into account, respecting the manufacturer limits of 2 and 5 kPa, respectively.

It is listed in Table 75 the 11 internal parameters that was observed during the simulations.

Table 75 – List of internal parameters from GT-Power ICE modelling.

1	Average of maximum cylinder pressures (bar)
2	Average pressure at the charge air (bar)
3	brake efficiency (%)
4	brake specific fuel consumption (g kWh^{-1})
5	Compressor average outlet pressure (bar)
6	Compressor average outlet temperature (K)
7	Pressure drop on intake air admission (bar)
8	Shaft power (kW)
9	Turbine average inlet total pressure (bar)
10	Turbine average outlet pressure (bar)
11	Waste-gate average mass flow rate (kg s^{-1})

Source: Adapted from Zabeu, Martelli and Penaranda (2018).

The assumptions in ICE modelling using GT-Power software are: (i) assuming ambient air at 12.5°C with atmospheric pressure of 1 bar, (ii) inserting pressure losses on the intake air at the compressor upstream and exhaust gases system, (iii) putting a simple charge air cooler to account pressure losses on air stream, (iv) varying the *BMEP*

in a range of 20 to 23.45 bar, i.e. reaching a shaft power output around 10 MW (ZABEU; MARTELLI; PENARANDA, 2008).

Regarding the knocking phenomena, it is not modelled in this present thesis. However, there is a theoretical hypothesis in regard to this intake air cooling application, which is an engine operation at reduced knocking conditions due cooled intake air combined with a $BMEP$ under safe operating condition while respecting the engine operating limits. Of course, this assumption will be investigated, tested and validated through experiments on future works at the UTE LORM when the integration between the new thermal system and the engine is completely finished.

In Figure 107, an important technological parameter, known as average of maximum cylinder pressures ($P_{cyl,MAX}$), is below the maximum manufacturer allowed pressure ($P_{Manufacturer,MAX}$) of 186 bar. The maximum pressure dictates a safe operating condition into piston-cylinders, thus, overpassing this upper limit will compromise the engine safety operation (ZABEU; MARTELLI; PENARANDA, 2008).

Figure 107 – Average of maximum cylinder pressures.

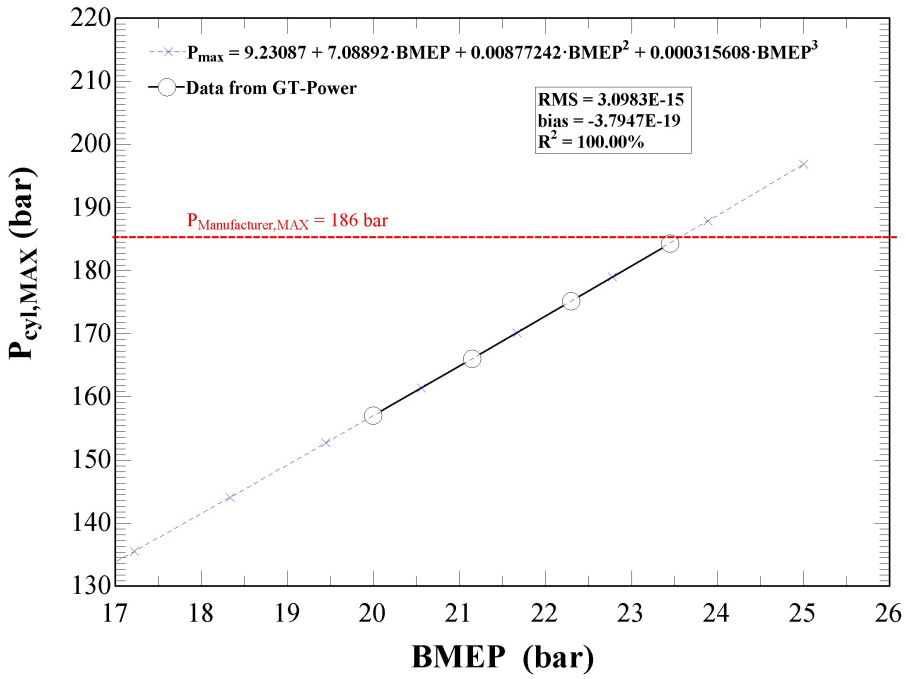

Source: Own Authorship.

Another crucial parameter that might affect negatively the engine operating condition is the waste-gate flow rate. This parameter must be always slightly open due control purposes at the turbocharger.

In GT-Power simulations, when varying $BMEP$ over a range of 20 to 23.45 bar,

as represented in Figure 108, it is verified that the waste-gate almost closes but not completely.

Hence, although the mass flow rate is quite small, it is not losing control, consequently, not interfering negatively in engine operating condition.

Figure 108 – Waste-gate flow rate.

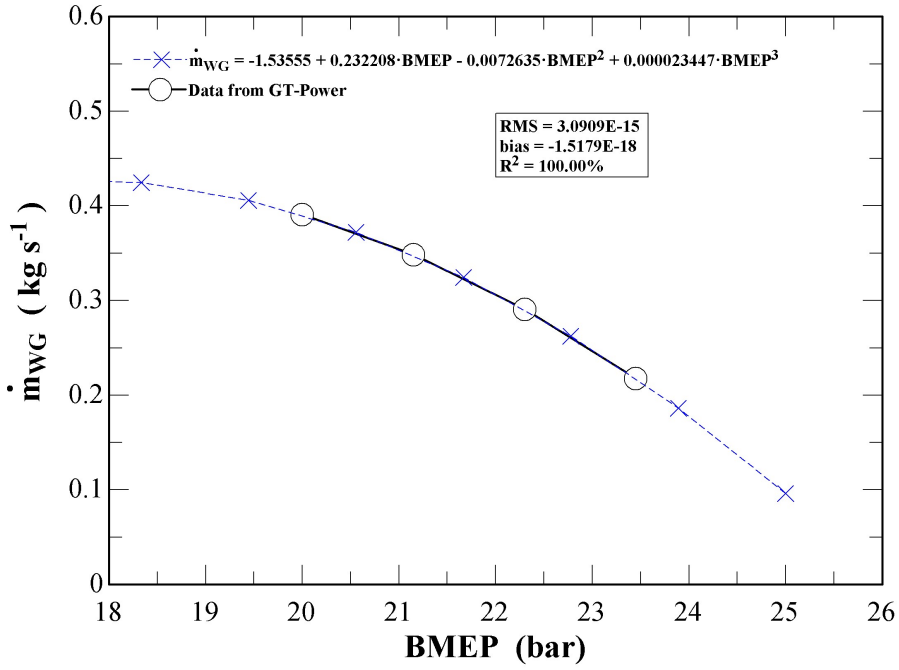

Source: Own Authorship.

By observing brake efficiency and specific fuel consumption from GT-Power simulations in Figure 109 and Figure 110, respectively, it can be seen as expected that brake efficiency rises while specific fuel consumption decreases for high *BMEP*s.

The shaft power is represented in Figure 111, this parameter is fundamental for determining air and fuel flow rates, and energy balance in the ICE for high *BMEP*s.

There are other necessary information from GT-Power simulations that are used in the turbocharger, ICE and cooling water circuit modellings, thus it is presented consecutively from Figure 112 to Figure 117.

Figure 109 – brake efficiency.

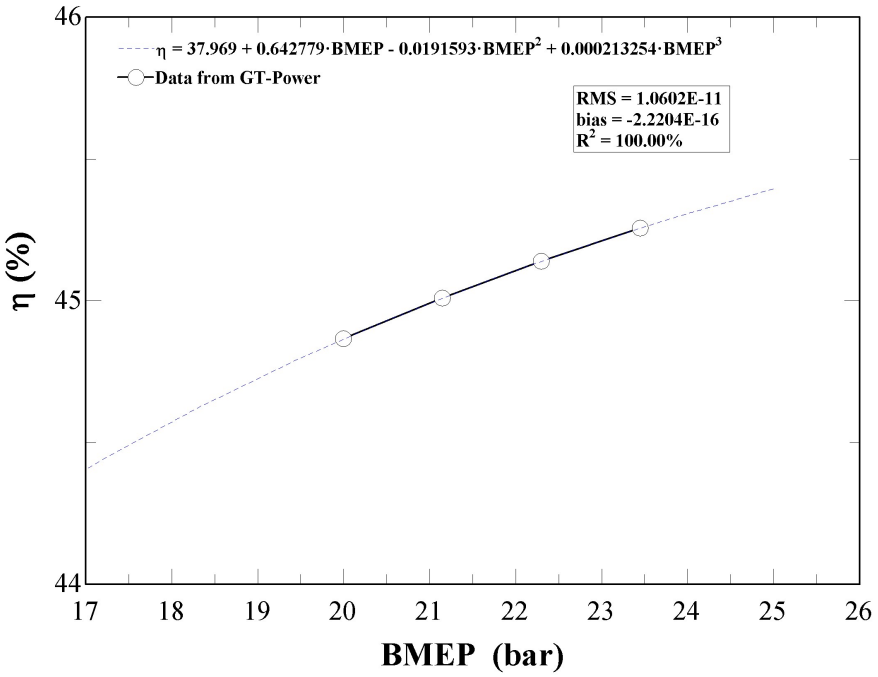

Source: Own Authorship.

Figure 110 – brake specific fuel consumption.

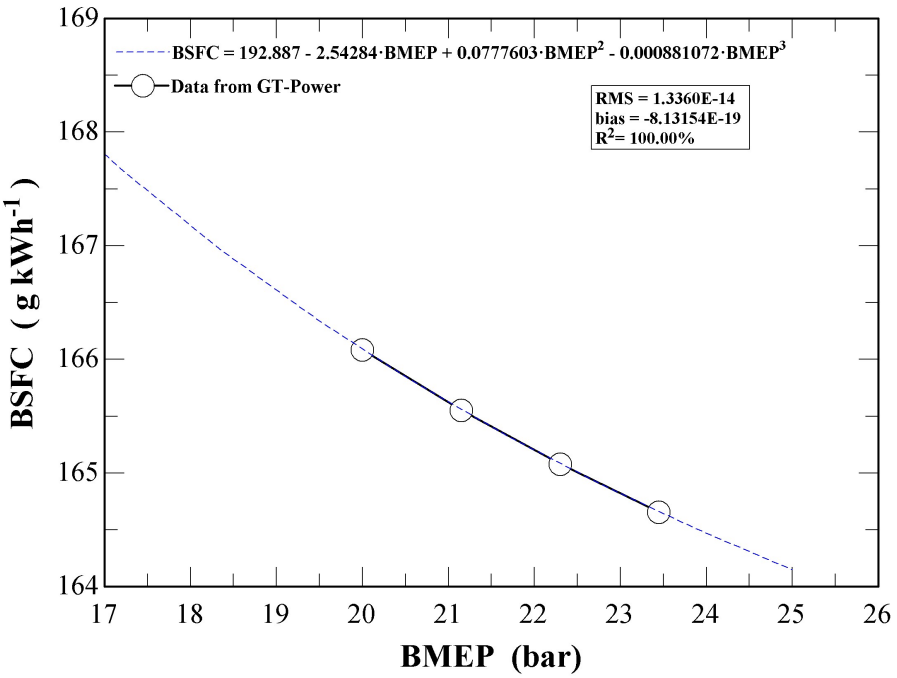

Source: Own Authorship.

Figure 111 – Shaft power output.

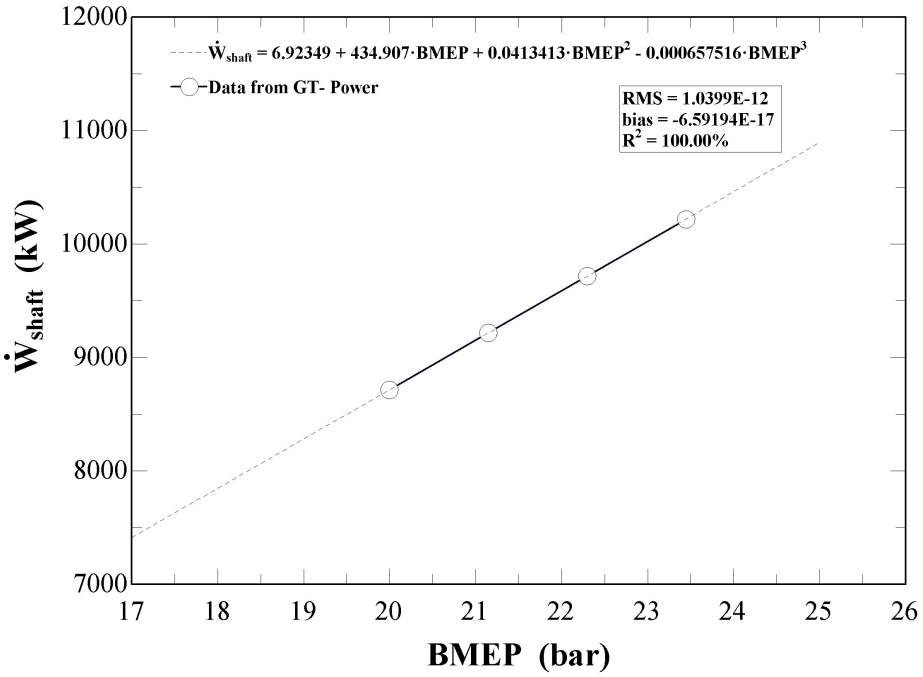

Source: Own Authorship.

Figure 112 – Average pressure at the charge air.

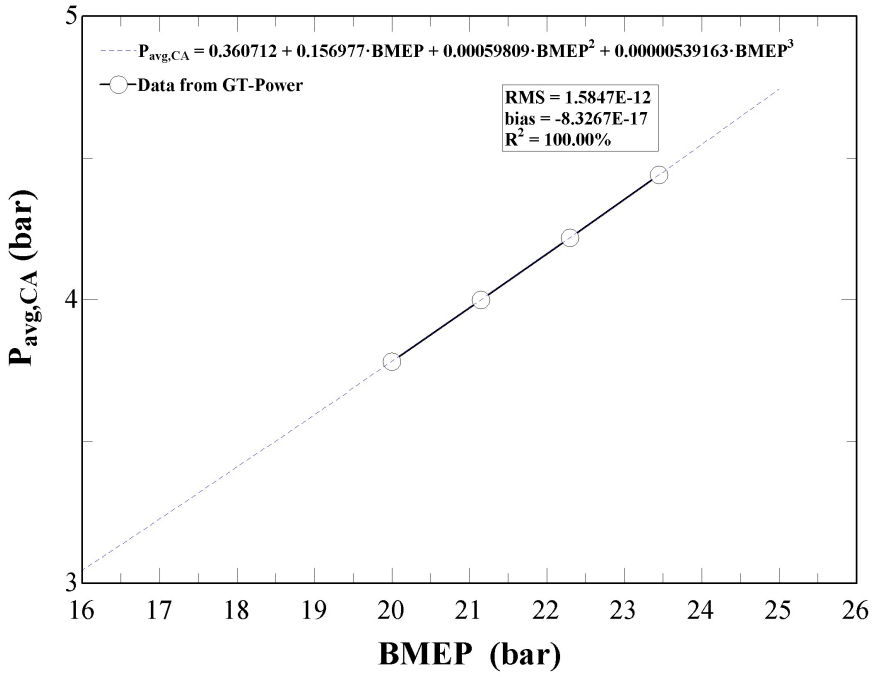

Source: Own Authorship.

Figure 113 – Total pressure average at the compressor outlet.

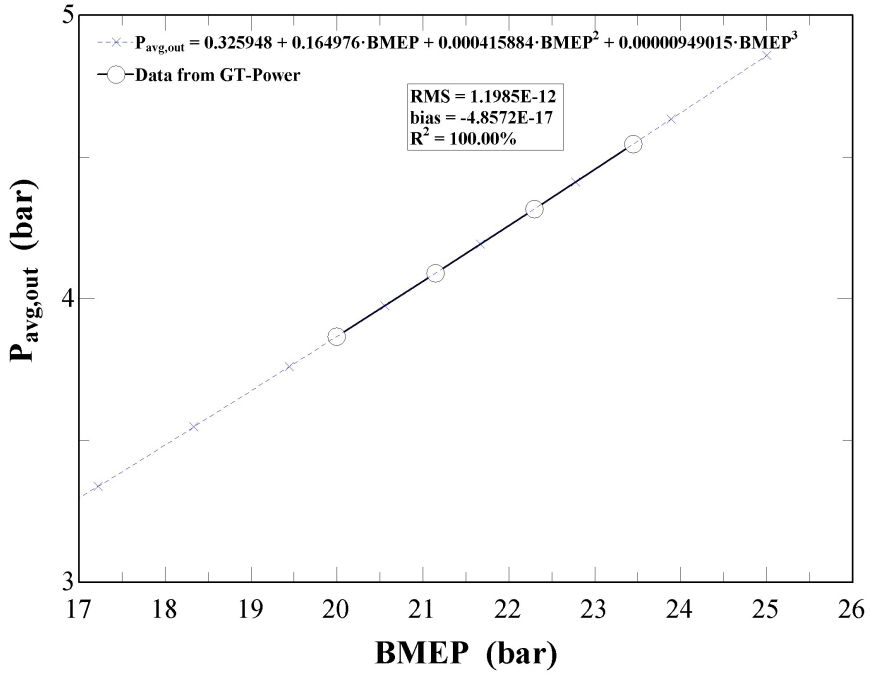

Source: Own Authorship.

Figure 114 – Total temperature average at the compressor outlet.

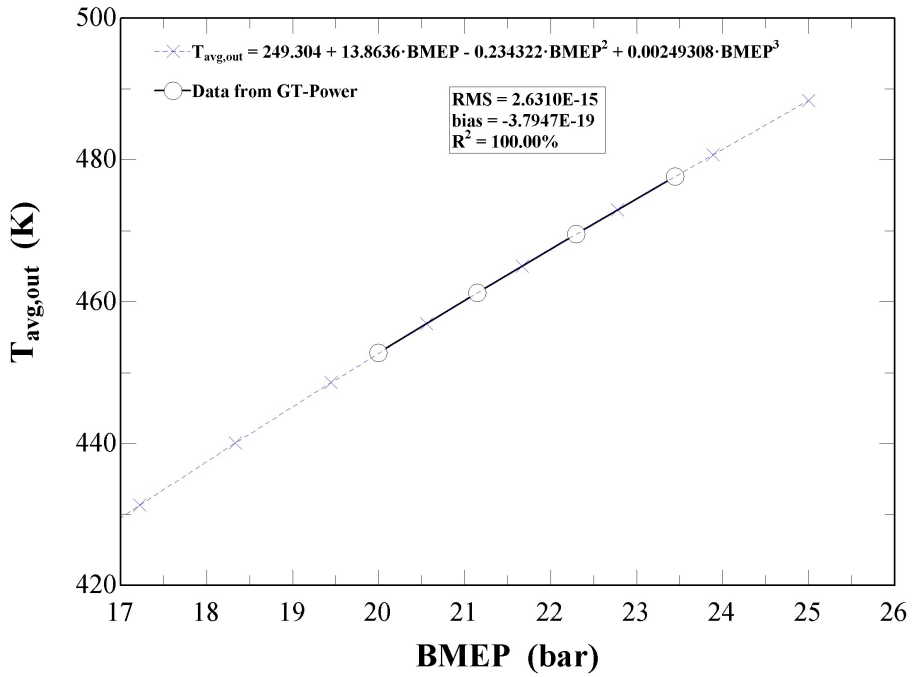

Source: Own Authorship.

Figure 115 – Pressure drop on intake air.

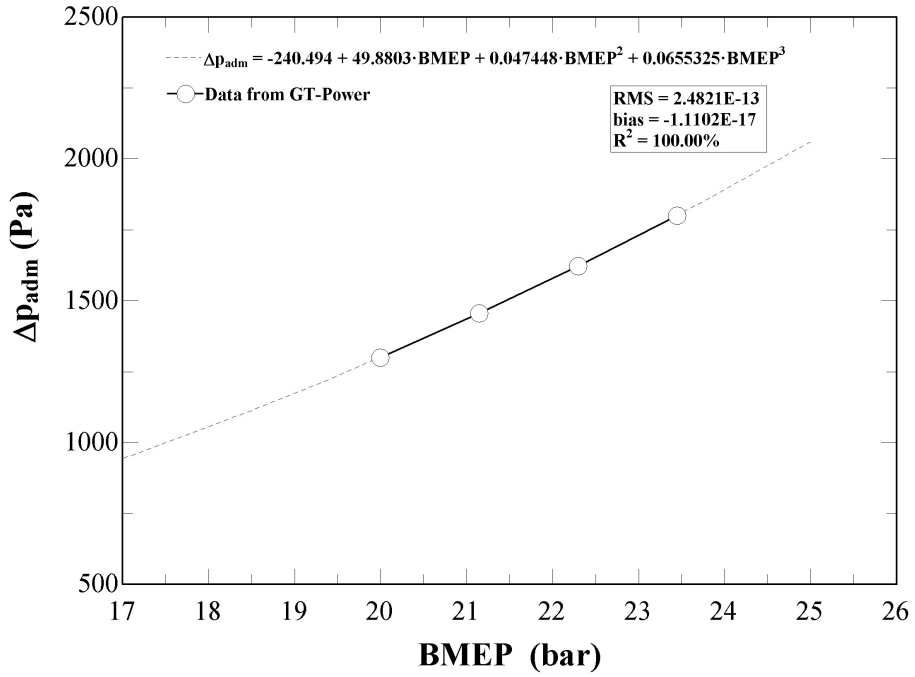

Source: Own Authorship.

Figure 116 – Total pressure average at the turbine outlet.

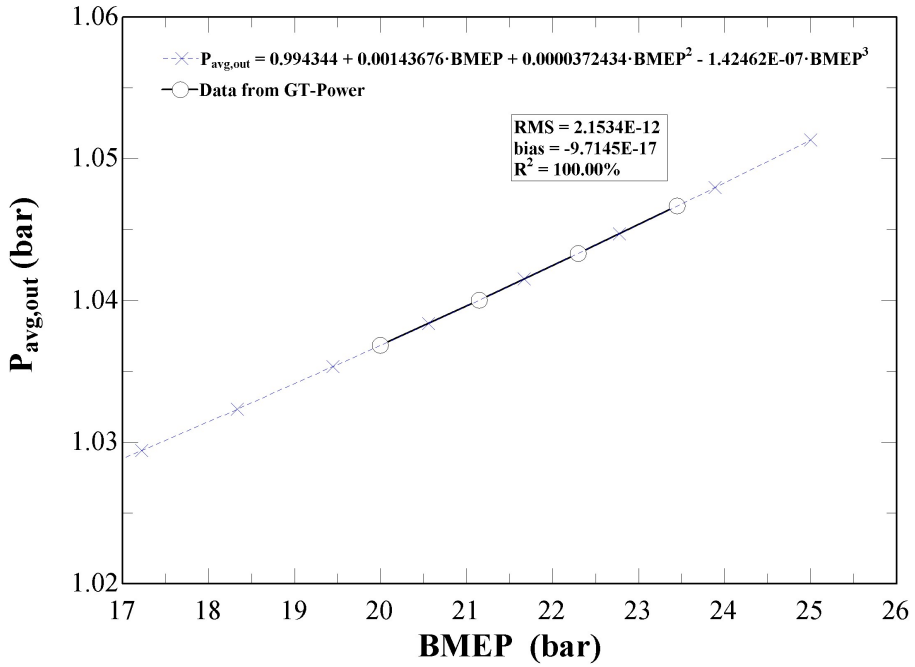

Source: Own Authorship.

Figure 117 – Total pressure average at the turbine inlet.

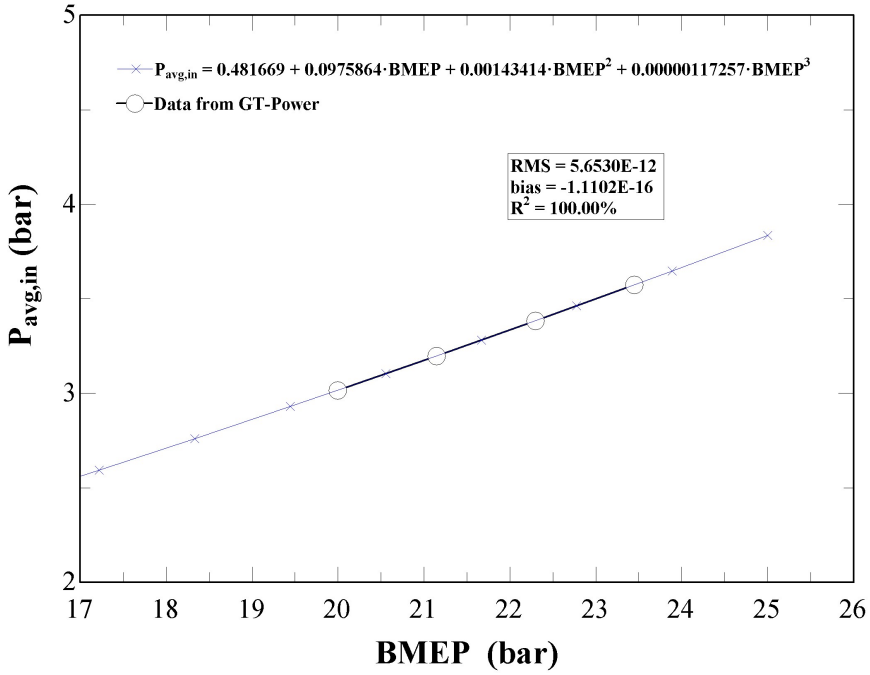

Source: Own Authorship.

Turbocharger Modelling with Compressible Effects

These three curve fitting are required to assist the proposed turbocharger modelling while assuming more complex considerations and compressible governing equations. However, it is important to remind here that for the sake of simplicity, this proposed method is suggested for future works.

Figure 119 represents the inlet total temperature at the turbine, it is used as input data in order to develop a fair comparison by stating a same reference basis.

Figure 118 – Total temperature average at the turbine inlet.

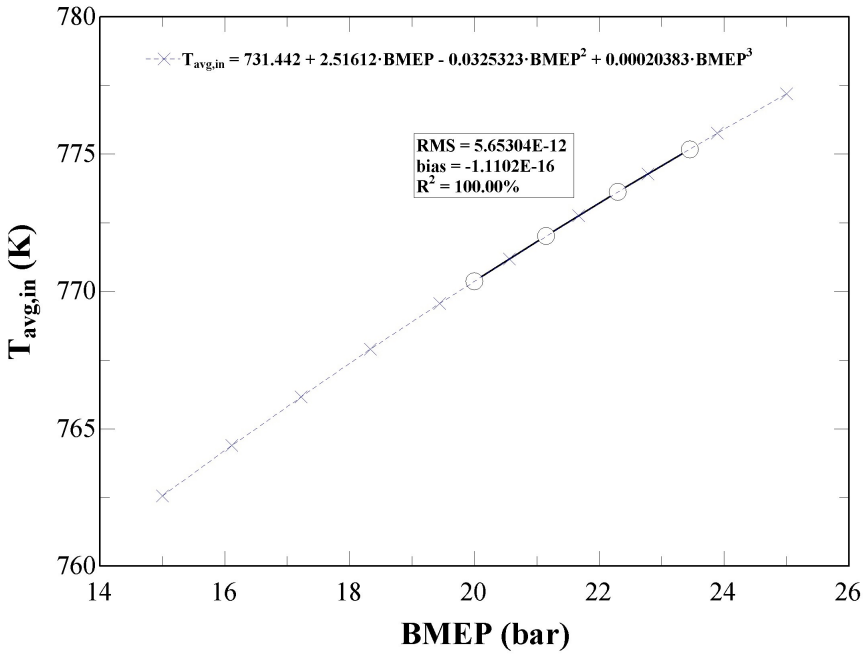

Source: Own Authorship.

The following Figure 119 and Figure 120 are correlated to air mass flow rate and average outlet total temperature at the junction after waste-gate, respectively. Both of them are used to calibrate the turbocharger modelling which assumes more complex correlations and assumptions. Furthermore, the previous curve fittings are also applied here as input data in function of *BMEP*. Reminding that the comparison must have a same reference basis.

Figure 119 – Average of air mass flow rate.

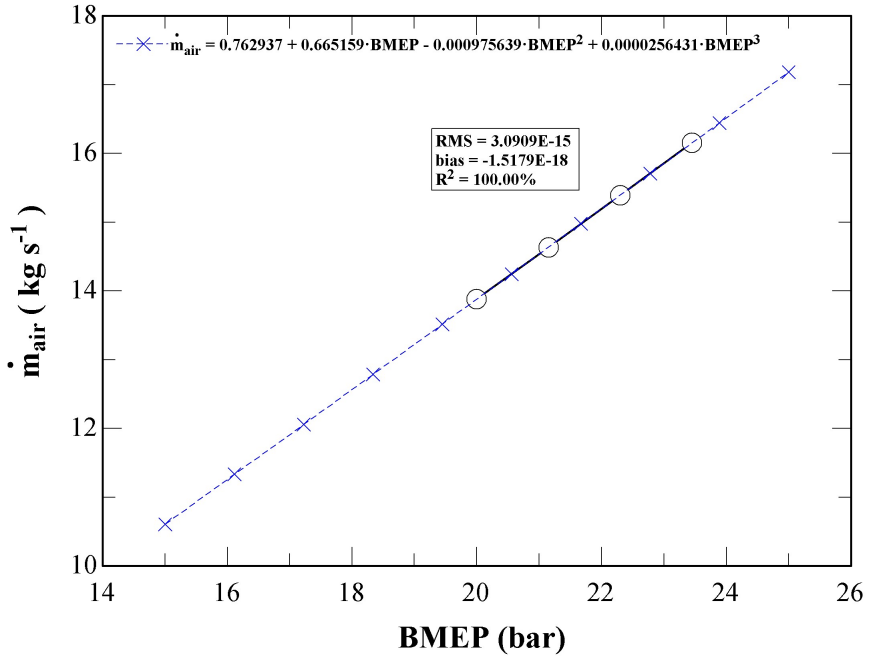

Source: Own Authorship.

Figure 120 – Total temperature average at the engine outlet.

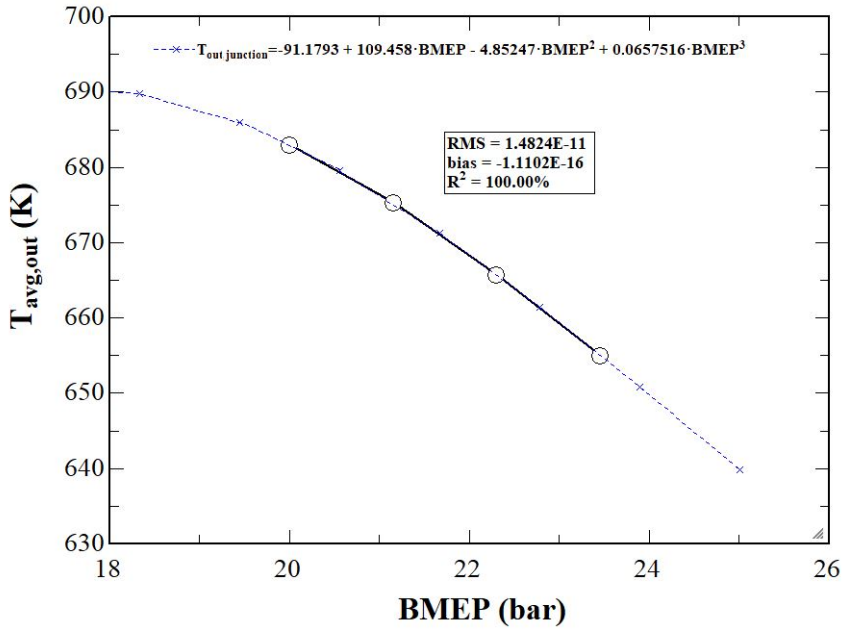

Source: Own Authorship.

APPENDIX C – Chemical Exergy Calculation

In this Appendix C, it is presented in detail all necessary calculations to obtain chemical exergy of the fuel as well as LiBr-H_2O working fluid. The thermodynamic reference state is defined as 25°C and 1 atm.

C.1 LiBr-H_2O

In an effort to determinate the activities of LiBr-H_2O as well as other coefficients, chemical exergy calculation based on Palacios-Bereche, Gonzales and Nebra (2012) is executed here.

The following Equation C.1 and Equation C.2 calculate the coefficient a_i and b_i by consulting Table 76, respectively. Also, each equation is in function of temperature (T) and the coefficients a_{ij} or b_{ij}.

$$a_i = \sum_{j=0}^{2} a_{ij} \cdot T^{-j} \tag{C.1}$$

$$b_i = \sum_{j=0}^{2} b_{ij} \cdot T^{-j} \tag{C.2}$$

Table 76 – Coefficients for calculating a_i and b_i.

	j = 0	j = 1	j = 2
a_{1j}	-2.19631551E+01	4.93723160E+03	-6.55484060E+05
a_{2j}	-3.81047520E+03	2.61153450E+06	-3.66996910E+08
a_{3j}	1.22808540E+05	-7.71879230E+07	1.03985600E+10
a_{4j}	-1.47167370E+06	9.19528480E+08	-1.18945020E+11
a_{5j}	7.76582130E+06	-4.93756660E+09	6.31755470E+11
a_{6j}	-1.51189220E+07	9.83997440E+09	-1.27378980E+12
b_{1j}	-4.41786540E-05	3.11489920E-02	-4.36112260E+00
b_{2j}	3.07939920E-04	-1.86320980E-01	2.73871370E+01
b_{3j}	-4.08079430E-04	2.16079550E-01	-2.51759710E+01

Source: Kim and Infante Ferreira (2006).

The determination of activities follows three steps, firstly it is calculated the molality (m) in function of mass fraction or mole fraction of LiBr-H_2O (x_{LiBr} and y_{LiBr})

and molar mass of each species ($\bar{M}_{LiBr}$ and $\bar{M}_{H_2O}$), as it is represented in Equation C.3. At second step, the osmotic coefficient (Φ) is estimated by Equation C.4. It depends on coefficients a_i and b_i, molality, pressure, and dissociation number for the solute (ν) which is assumed 2 (PALACIOS-BERECHE; GONZALES; NEBRA, 2012).

$$m = \frac{x_{LiBr}}{(1 - x_{LiBr}) \cdot \bar{M}_{LiBr}} = \frac{y_{LiBr}}{(1 - y_{LiBr}) \cdot \bar{M}_{H_2O}} \tag{C.3}$$

$$\Phi = 1 + \sum_{i=1}^{6} a_i \cdot m^{i/2} + \frac{p}{2 \cdot \nu} \cdot \sum_{i=1}^{2} i \cdot b_i \cdot m^{i/2} \tag{C.4}$$

In the final step, it is determined the activity for each species in the solution (a_{H_2O} and a_{LiBr}), H_2O and LiBr, respectively. By applying Equation C.5 to Equation C.7, it is calculated the activities.

$$ln(a_{H_2O}) = -\Phi \cdot \nu \cdot m \cdot \bar{M}_{H_2O} \tag{C.5}$$

$$ln(a_{LiBr}) = -\nu \cdot \left[ln(m) + \sum_{i=1}^{6} \frac{i+2}{i} \cdot \left(a_i + i \cdot \frac{p \cdot b_i}{2 \cdot \nu} \right) \cdot m^{i/2} \right]_{m}^{m_{sat}} \tag{C.6}$$

$$b_3 = b_4 = b_5 = b_6 = 0 \tag{C.7}$$

The Figure 121 represents the activities of LiBr and H_2O in function of solution mass concentration. By using the previous equations, it is possible to observe that the activity of each species presents opposite behavior. For instance, when the mass fraction is increased, the activity of H_2O decays simultaneously. The activity of LiBr rises abruptly after the solution mass fraction is above 0.56.

In Figure 122, it can be verified the behavior of standard chemical exergy, exergy destruction due dissolution process, and chemical total exergy. These results are in line with the mentioned chemical exergy calculation from Palacios-Bereche, Gonzales and Nebra (2012).

Figure 121 – Activities of LiBr-H_2O

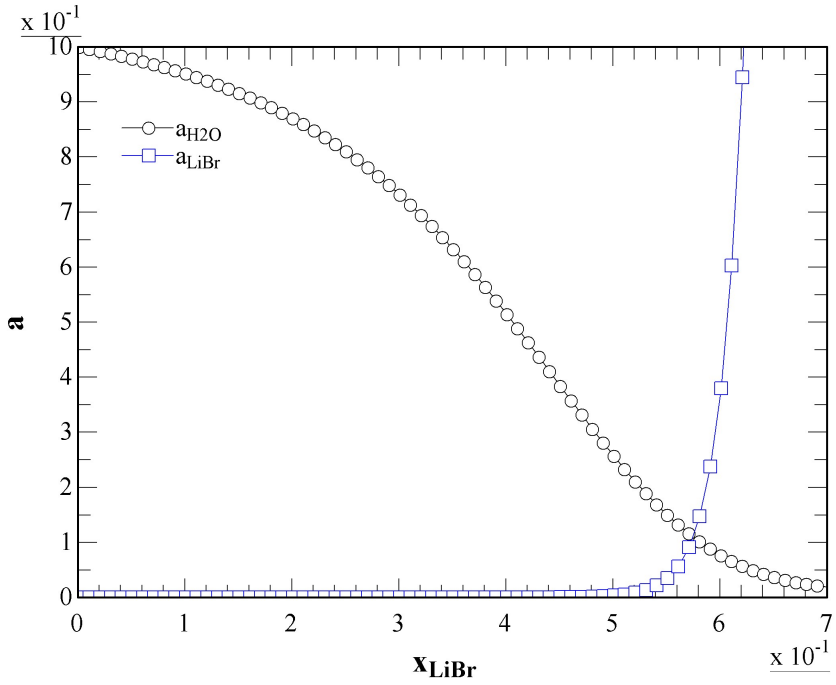

Source: Own Authorship.

Figure 122 – Chemical exergy of LiBr-H_2O

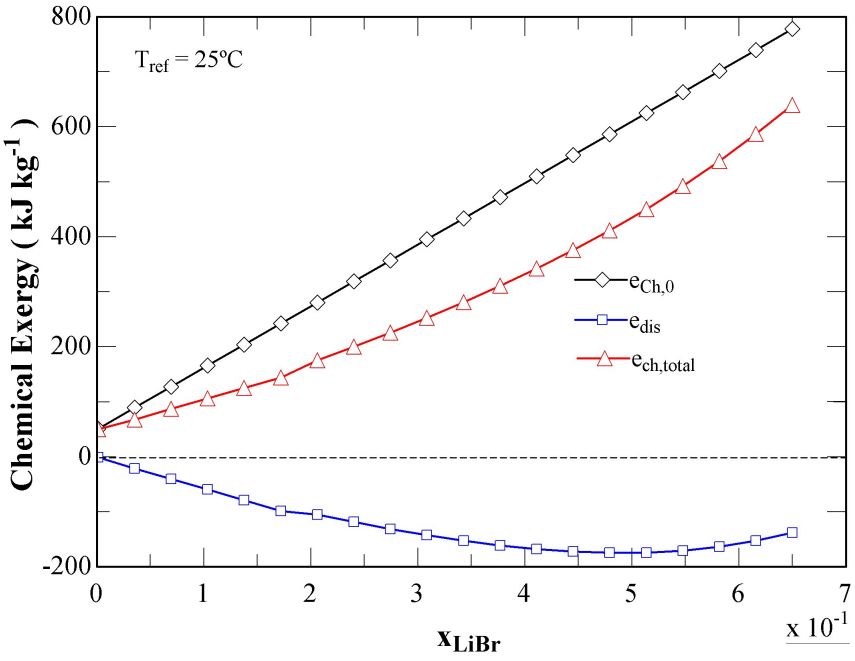

Source: Own Authorship.

C.2 Fuel

The chemical exergy of fuel is computed based on Moran et al. (2013) methodology. First of all, it is important to recall the stoichiometric complete combustion balance, as shown in Equation C.8.

$$\sum_{i=1}^{8} n_i \cdot species_i + A' \cdot O_2 \rightarrow \sum_{i=14}^{17} n_{stoich,i} \cdot species_i \tag{C.8}$$

In order to calculate the chemical exergy of the fuel, Table 77 has the thermodynamic properties from EES software, chemical composition of natural gas and reference humid air. Reminding that the reference condition is set in 25°C and 1 atm.

Table 77 – Thermodynamic properties, chemical compositions of natural gas and reference humid air.

	Fuel**		EES thermodynamic properties		
i	$species_i$	n_i (mole)	$\bar{h}_i$ (kJ kmole^{-1})	$\bar{s}_i$ (kJ kmole^{-1} K^{-1})	$\bar{M}_i$ (kg kmole^{-1})
1	CH_4	0.9079	-74595	186.251	16.04
2	C_2H_6	0.0569	-83846	229.098	30.07
3	C_3H_8	0.0159	-104674	270.189	44.10
4	C_4H_{10}	0.0034	-125782	309.753	58.12
5	C_5H_{12}	0.0004	-146751	349.430	72.15
6	C_6H_{14}	0.0000	-166910	388.717	86.17
7	CO_2	0.0088	-393486	213.665	44.01
8	N_2	0.0066	0	191.489	28.01
Saturated humid air* ($\Phi'_{st} = 1.0$)					
i	$species_i$	$y_{st,i}$ (% Vol.)	$n_{stoich,i}$ (mole)	$\bar{h}_i$ (kJ kmole^{-1})	$\bar{s}_i$ (kJ kmole^{-1} K^{-1})
9	H_2O	3.12	0	-241811	188.709
10	CO_2	0.03	0	-393486	213.665
11	Ar	0.83	0	0	154.835
12	N_2	75.67	0	0	191.489
13	O_2	20.35	A'	0	205.028
	Exhaust Gases				
i	$species_i$		$n_{stoich,i}$ (mole)	$\bar{h}_i$ (kJ kmole^{-1})	$\bar{s}_i$ (kJ kmole^{-1} K^{-1})
14	H_2O		2.0695	-241811	188.709
15	CO_2		1.0938	-393486	213.665
16	Ar		0.0000	0	154.835
17	N_2		0.0066	0	191.489
18	O_2		0.0000	0	205.028

Source: Adapted from *Moran et al. (2013) and **Zabeu, Martelli and Penaranda (2018).

The chemical exergy for natural gas in molar basis can be estimated by applying Equation C.9, which is in function of enthalpy formation ($\bar{h}_i$) as well as entropy formation ($\bar{s}_i$) of each species.

Moreover, it is necessary to calculate the stoichiometric number of moles for each reagent (A') and product ($n_{stoich,i}$). The A' is equal to 2.1198. Finally, the reference humid air ($y_{st,i}$) must be accounted during the calculations. Hence, Equation C.9 to Equation C.14 are applied here. The variable $\bar{R}$ is the universal gas constant, which value is 8.314 kJ kmole^{-1} K^{-1}.

$$\bar{e}_{ch,f} = \bar{h}_{Rea} - \bar{h}_{Pro} - T_0 \cdot (\bar{s}_{Rea} - \bar{s}_{Pro}) + T_0 \cdot \bar{R} \cdot ln\left(\frac{y_{st,13}^{A'}}{y_{st,9}^{n_{stoich,14}} \cdot y_{st,10}^{n_{stoich,15}} \cdot y_{st,12}^{n_{stoich,17}}}\right) \quad \text{(C.9)}$$

$$\bar{h}_{Rea} = \sum_{i=1}^{8} n_i \cdot \bar{h}_i + A' \cdot \bar{h}_{13} \quad \text{(C.10)}$$

$$\bar{h}_{Pro} = \sum_{i=14}^{17} n_{stoich,i} \cdot \bar{h}_i \quad \text{(C.11)}$$

$$\bar{s}_{Rea} = \sum_{i=1}^{8} n_i \cdot \bar{s}_i + A' \cdot \bar{s}_{13} \quad \text{(C.12)}$$

$$\bar{s}_{Pro} = \sum_{i=14}^{17} n_{stoich,i} \cdot \bar{s}_i \quad \text{(C.13)}$$

The molar mass of natural gas ($\bar{M}_f$) is determined around 17.7762 kg kmole^{-1} and the molar chemical exergy of natural gas is 884,173.581 kJ kmole^{-1}, thereby, resulting in 49739.121 kJ kg^{-1}.

$$e_{ch,f} = \frac{\bar{e}_{ch,f}}{\bar{M}_f} \quad \text{(C.14)}$$

The total amount of chemical exergy for natural gas in UTE LORM case study is determined by Equation C.15.

$$\dot{E}_f = \dot{m}_f \cdot e_{ch,f} \quad \text{(C.15)}$$

As the fuel mass flow rate is 0.4708 kg s^{-1}, the chemical exergy of natural gas can be estimated, resulting in 23417 kW.

APPENDIX D – Historic Environment Records at Linhares

In this Appendix D, historic environment records from 01/26/2019 to 01/25/2020 are extracted from INMET (2020), aiming to support how to define the critical ambient conditions for sizing and designing the thermal system integrated to Wärtsilä 20V34SG engine at the UTE LORM. In order to organize these huge database of ambient conditions from Linhares, EES software is used to create Figure 123 to Figure 131, facilitating the analysis.

When analysing these amount of database from INMET (2020), it can be seen that the dry-bulb, wet-bulb, dew-point temperatures and relative humidity changes across the year. For cooling towers and cooling coils, the ambient wet-bulb temperature affects directly the sizing of these heat exchangers as well as the designing aspects. Due to this reason, by analysing Figure 124 to Figure 131, it is considered the harshest wet-bulb temperature along the year which is 27.81°C with a dry-bulb temperature of 31.1°C and relative humidity of 0.78. The atmospheric pressure is assumed 1 atm.

Figure 123 – Atmospheric pressure 01/26/2019 to 01/25/2020.

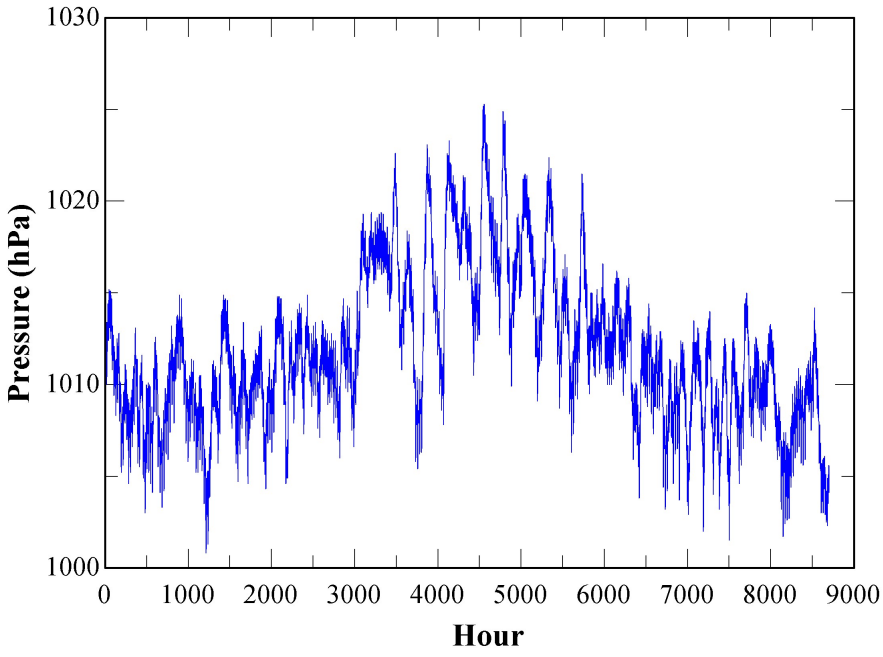

Source: INMET (2020).

Figure 124 – Dry-bulb temperature from 01/26/2019 to 01/25/2020.

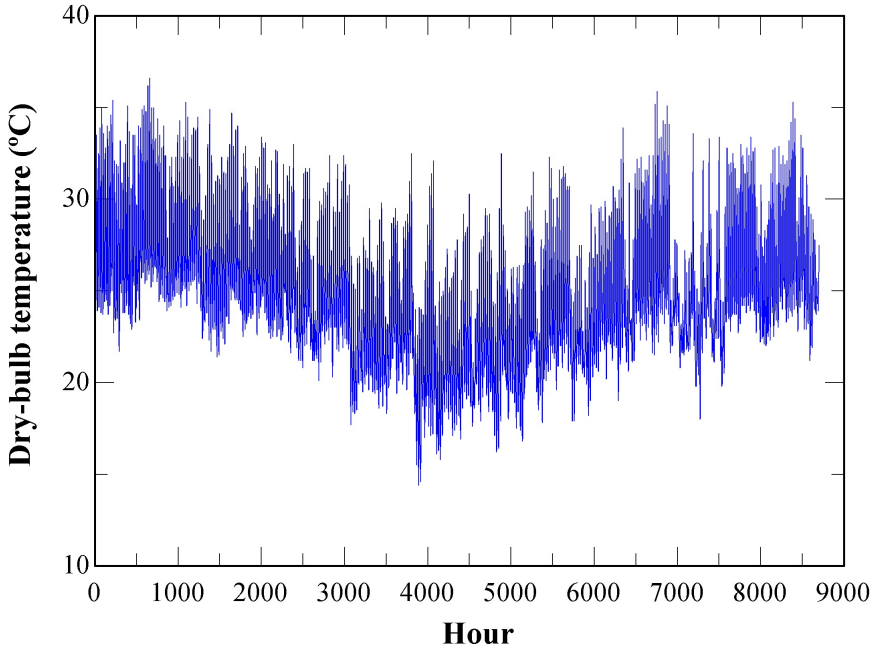

Source: INMET (2020).

Figure 125 – Wet-bulb temperature from 01/26/2019 to 01/25/2020.

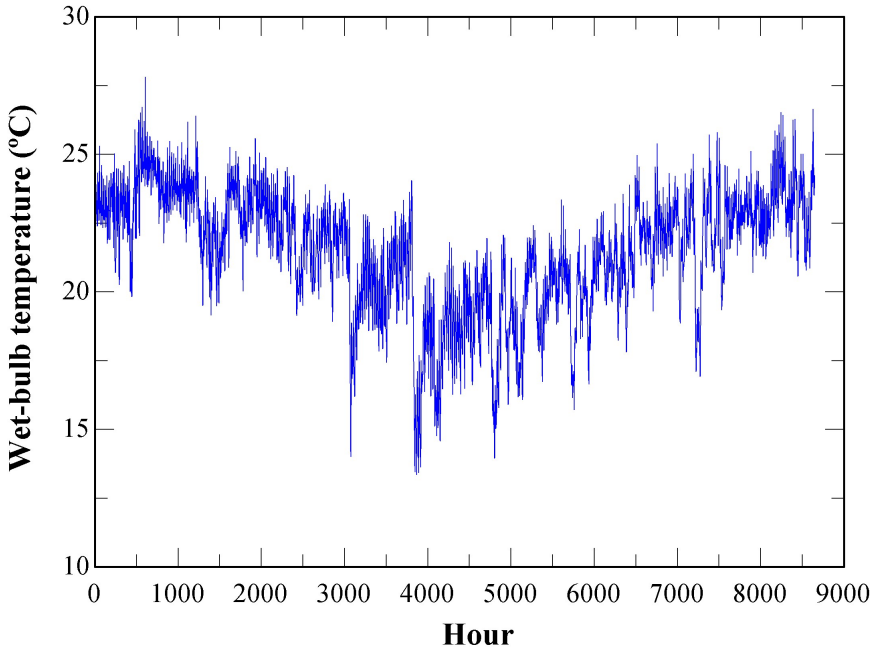

Source: INMET (2020).

Figure 126 – Dew-Point temperature from 01/26/2019 to 01/25/2020.

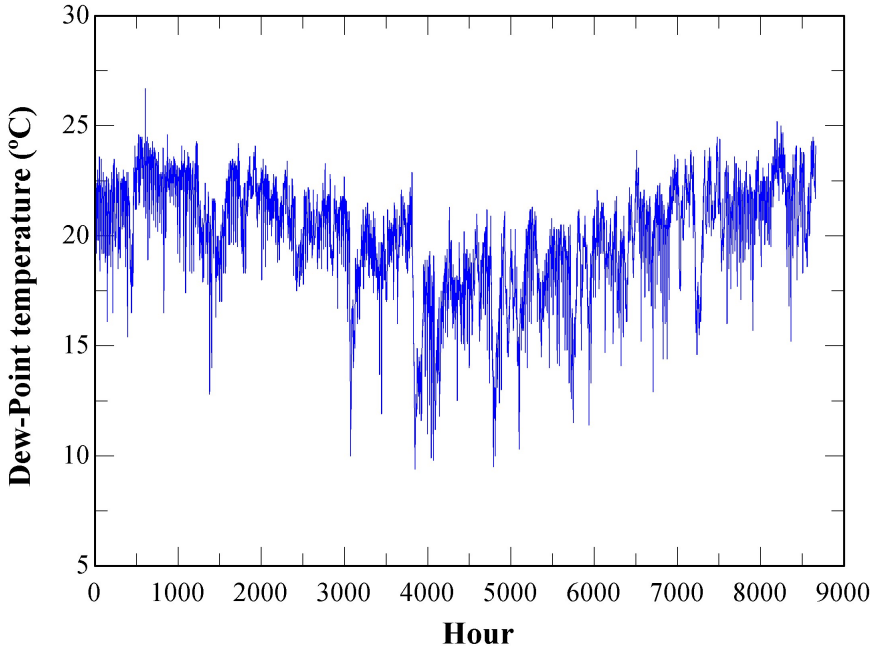

Source: INMET (2020).

Figure 127 – Relative humidity from 01/26/2019 to 01/25/2020.

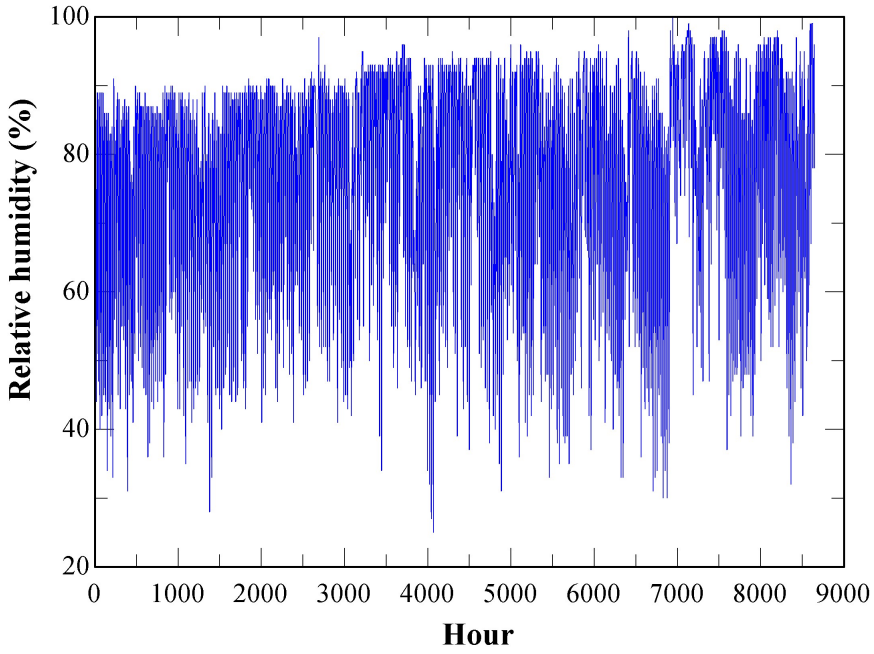

Source: INMET (2020).

Figure 128 – Humidity ratio from 01/26/2019 to 01/25/2020.

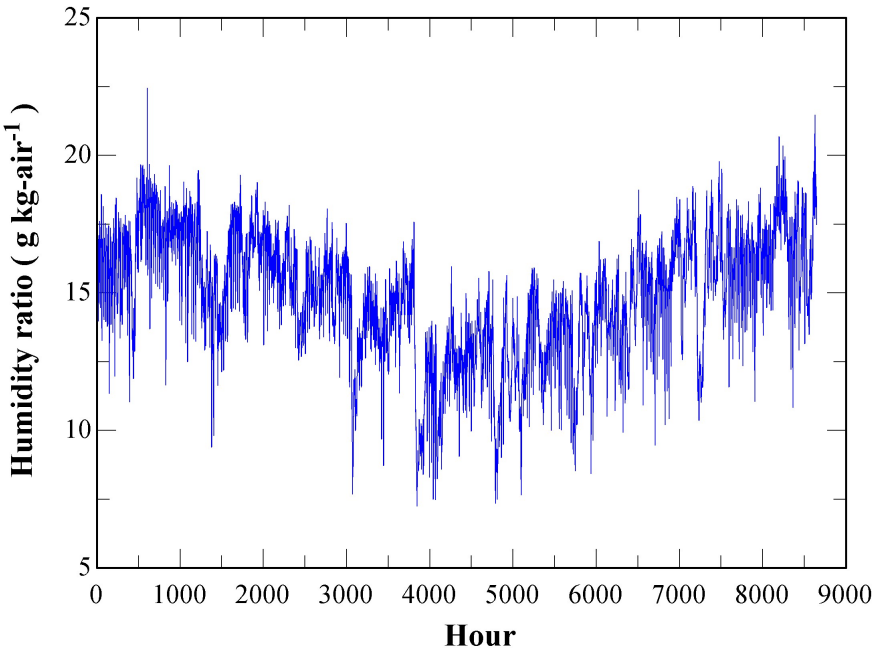

Source: INMET (2020).

Figure 129 – Humid air enthalpy from 01/26/2019 to 01/25/2020.

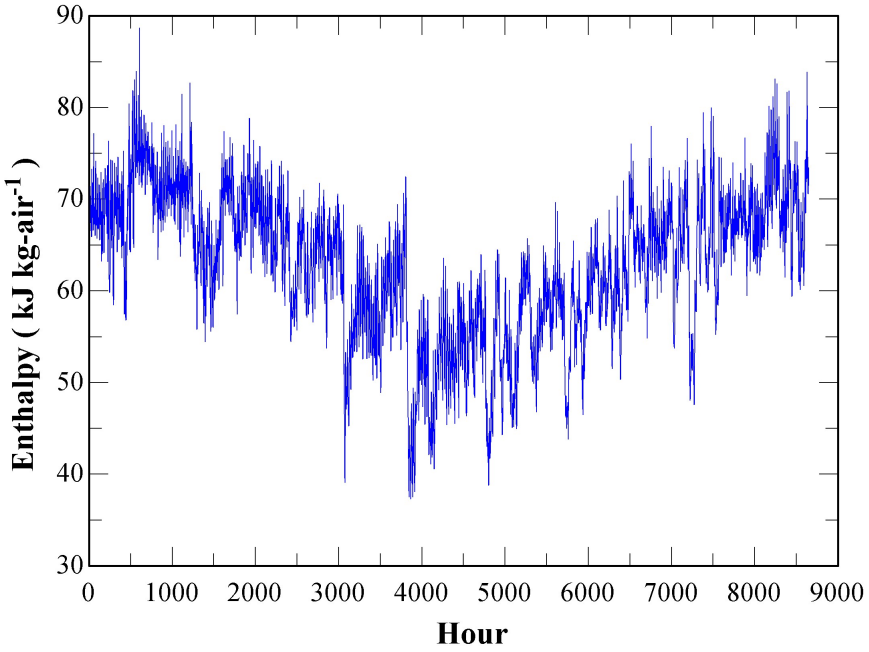

Source: INMET (2020).

Annex

ANNEX A – Price of Natural Gas for Thermoelectric Power Plants in Brazil

Figure 130 – Price of natural gas in Brazilian thermoelectric section.

AGÊNCIA DE REGULAÇÃO DE SERVIÇOS PÚBLICOS DO ESPÍRITO SANTO

ANEXO II

TABELA CONTENDO PRC (PARCELA DE RESERVA DE CAPACIDADE) E PUC (PARCELA DE USO DE CAPACIDADE) DO SEGMENTO TERMOELÉTRICO

VÁLIDA A PARTIR DE 01/05/2018

Os valores não incluem ICMS, PIS e COFINS, e serão aplicados conforme a legislação vigente.

Segmento Termoelétrico

Classe	Volume m³/mês		PARCELA DE RESERVA DE CAPACIDADE - PRC (R$/Mês)	PARCELA DE USO DE CAPACIDADE - PUC (R$/Mês)
1	-	15.000,00	3.213,92	0,1800
2	15.000,01	45.000,00	3.528,82	0,1590
3	45.000,01	300.000,00	5.271,03	0,1203
4	300.000,01	900.000,00	10.324,24	0,1035
5	900.000,01	3.000.000,00	29.443,44	0,0822
6	3.000.000,01	9.000.000,00	85.632,03	0,0635
7	9.000.000,01	15.000.000,00	133.275,85	0,0487
8	15.000.000,01	30.000.000,00	144.327,00	0,0404
9	30.000.000,01	60.000.000,00	159.136,70	0,0302
10	Acima de 60.000.000,01		227.338,15	0,0212

A Fórmula de Cálculo da Margem é:
MD = PRC + (PUC X CM), onde:
MD = Margem de Distribuição;
PRC = Parcela de Reserva de Capacidade em R$;
PUC= Parcela de Uso da Capacidade, aplicada na mesma faixa definida no PRC em R$/m³;
CM = Consumo Mensal Medido em m³.

A Quantidade Diária Contratada (QDC) definirá em que faixa de volume será aplicada a tabela.
A Formula de Cálculo da Tarifa é:
TG = PS +MD, onde:
TG = Tarifa do Gás, ex-tributos e encargos financeiros;
PS = Parcela do Supridor vigente à época;
MD = Margem de Distribuição.

Serão ainda adicionados os tributos ICMS, PIS, COFINS, nas alíquotas vigentes à época.

Source: ARSP (2019).

The price of natural gas in this present thesis is determined by the following Equation A.1 to Equation A.5. The number of days per month is defined approximately

as 30:1.

$$\dot{V}_{f,month} = \frac{\dot{m}_f \cdot 3600 \cdot 24 \cdot 30}{\rho_f} \tag{A.1}$$

As the Figure 130 is defined for standard ambient condition of 0°C and 1 atm (IUPAC) and the natural gas is delivered in the same standard conditions, it is not necessary to normalize the volume flow at the UTE LORM.

However, if the fuel is not delivered in the same conditions, Equation A.2 is utilized for normalization. As the mass flow rate of the fuel ($\dot{m}_f$) is 0.4708 kg s^{-1} with a density (ρ_f) of 0.712 kg m^{-3}. The volume of fuel ($\dot{V}_{f,month}$) is calculated around 1,713,853 m^3 $month^{-1}$.

$$\dot{V}_{f,month,normalized} = \dot{V}_{f,month} \cdot \frac{p_f}{T_f + 273.15} \cdot \frac{273.15}{1.01325} \tag{A.2}$$

The fuel cost of one month (Z_f) is estimated around 31,664.00 US$ $month^{-1}$ by Equation A.3.

$$Z_f = Cost_{fixed} + Cost_{variable} \cdot \dot{V}_{f,month,normalized} \tag{A.3}$$

The fuel cost rate ($\dot{Z}_{fuel}$) is determined by Equation A.4, which uses the fuel cost (Z_f) from Figure 130 and it is divided by the number of hours in one month.

$$\dot{Z}_f = \frac{Z_f}{30 \cdot 24} \tag{A.4}$$

Finally, the capital cost of the fuel per kilogram (P_f) is calculated by Equation A.5. Of course, it is important to remind here that the monetary conversion system is R$ 5.38 to US$ 1.00.

$$P_f = \frac{\dot{Z}_f}{\dot{m}_{fuel} \cdot 3600} \tag{A.5}$$

By using these previous equations, the capital cost of the fuel per kilogram is calculated around 0.026 US$ kg^{-1} of fuel.

ANNEX B – Wärtsilä Manufacturer Brochure

Figure 131 – Technical data of Wärtsilä 20V34SG engine.

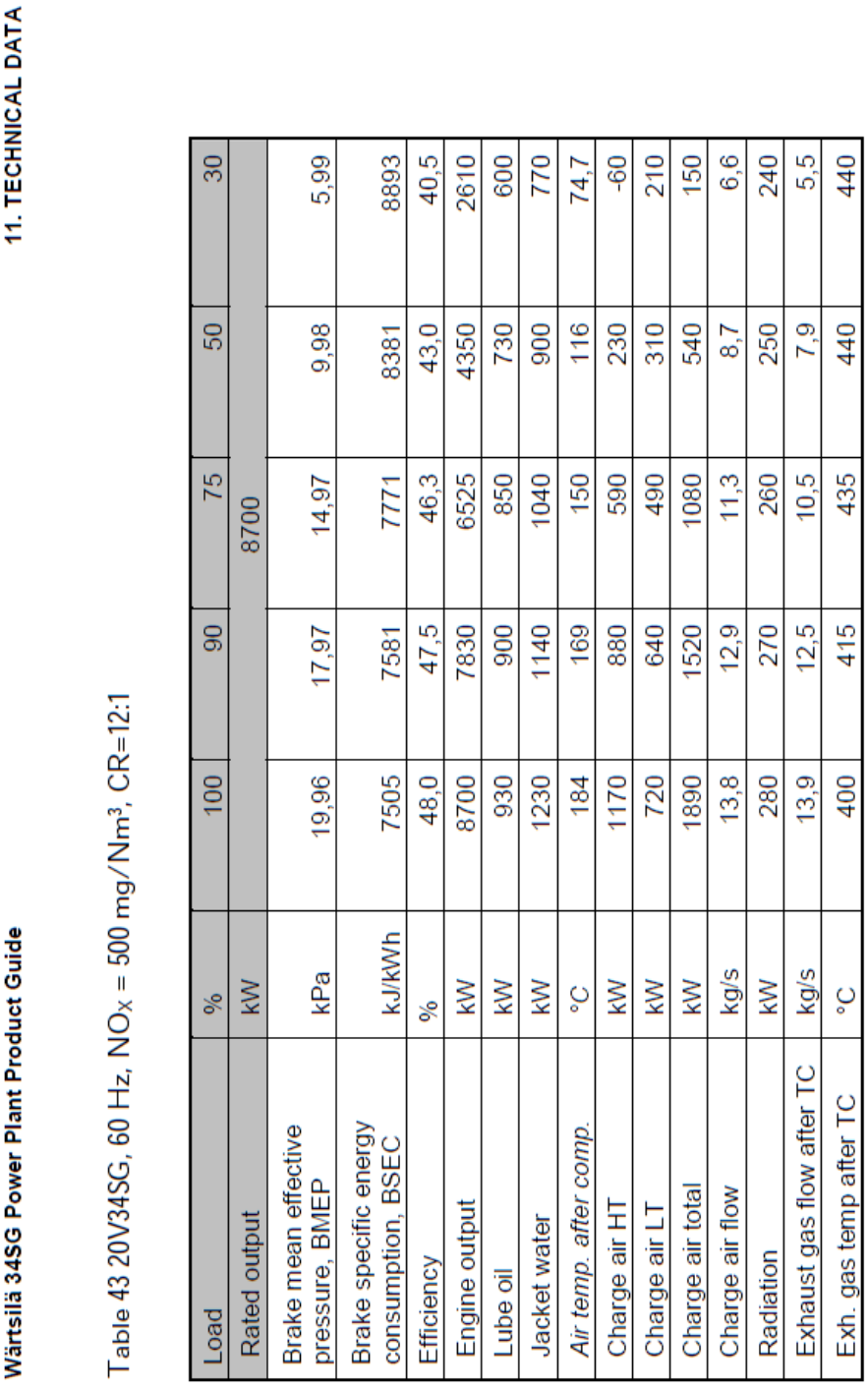

Wärtsilä 34SG Power Plant Product Guide **11. TECHNICAL DATA**

Table 43 20V34SG, 60 Hz, NO_X = 500 mg/Nm³, CR=12:1

Load	%	100	90	75	50	30
Rated output	kW	8700				
Brake mean effective pressure, BMEP	kPa	19,96	17,97	14,97	9,98	5,99
Brake specific energy consumption, BSEC	kJ/kWh	7505	7581	7771	8381	8893
Efficiency	%	48,0	47,5	46,3	43,0	40,5
Engine output	kW	8700	7830	6525	4350	2610
Lube oil	kW	930	900	850	730	600
Jacket water	kW	1230	1140	1040	900	770
Air temp. after comp.	°C	184	169	150	116	74,7
Charge air HT	kW	1170	880	590	230	-60
Charge air LT	kW	720	640	490	310	210
Charge air total	kW	1890	1520	1080	540	150
Charge air flow	kg/s	13,8	12,9	11,3	8,7	6,6
Radiation	kW	280	270	260	250	240
Exhaust gas flow after TC	kg/s	13,9	12,5	10,5	7,9	5,5
Exh. gas temp after TC	°C	400	415	435	440	440

Source: Wärtsilä (2008).